

Growth and Characterization of Some Magnetic Oxide Semiconductor Nanofilms by Electrodeposition Method

By

**Umeokwonna Nicholas Sunday
2007537004P**

**Department of Physics and Industrial Physics
Faculty of Physical Sciences
Nnamdi Azikiwe University, Awka**

Being a PhD Dissertation

**Submitted in partial fulfillment of the requirements for
the award of Doctor of Philosophy (PhD) degree in Solid
State Physics.**

Supervisor: Prof. A.J. Ekpunobi

August, 2017.

CERTIFICATION

This is to certify that this research was independently carried out by Umeokwonna Nicholas Sunday and has not been submitted or used for any degree or certificate. This work has met all the standards as stipulated by the school of Postgraduate studies and Department of Physics and Industrial Physics Nnamdi Azikiwe University, Awka.

.....
Prof A. J. Ekpunobi
(Supervisor)
.....

.....
Date

.....
Prof P.I. Ekwo
(Co supervisor)
.....

.....
Date

.....
Dr T.N. Obiekezie
(Head of Department)
.....

.....
Date

.....
Prof. A.J. Ekpunobi
(Dean, Faculty of Physical Sciences)
.....

.....
Date

.....
Prof. I.H. Odimegwu
(Dean, School of Postgraduate Studies)
.....

.....
Date

.....
Prof. F.I. Ezema
(External Examiner)

.....
Date

DEDICATION

This work is dedicated to Ezesokwu Umeokwonna family.

ACKNOWLEDGEMENTS

My thanks go to the Almighty God who made this dream a reality. I thank my supervisor Prof. A.J. Ekpunobi for his guidance and commitment towards the accomplishment of this research. To my second supervisor Prof P.I Ekwo, I say a big thank you. I appreciate the cooperation of the Head of Department; Dr T.N. Obiekezie. My thanks go to Prof. A.O.C. Nwokoye, Dr D. N. Okoli, and other lecturers of the Department of Physics and Industrial Physics, Nnamdi Azikiwe University, Awka.

I praise God for the role He used my spiritual director, Rev Fr Anthony Nwachukwu to play in making this dream a reality.

I thank in a special way, my senior brother Nze Ezechukwu G.C. Umeokwonna for his advice and encouragement. Special thanks to Prof. Laz Ezenwaka for the special role God used him to play in my academic carrier. My thanks go to my dear wife for her support and encouragement. I appreciate the prayers of my children and that of other members of our family. The moral support of Mr Paschal Onwukwalu is appreciated. Thanks to Mr Attah Daniel Baati, then at EMDI Akure for the successful characterization of the samples. Special appreciation goes to Prof. F.I. Ezema for access to the Crystal Growth Laboratory of University of Nigeria Nsukka where the samples were grown. I appreciate the efforts of the staff of Engineering Materials Development Institute (EMDI) Akure, Naseni Center of Excellence in Nanotechnology and Advanced Materials Akure, and Sheda Science and Technology Complex (SHESCO) Abuja for characterization of the samples. I recognize the cooperation of some academics in the persons of C.I. Elekalachi, Dr U.V Okpala, Dr Mrs E.I Ottih, Dr S.I. Olisakwe and Mrs P.C Okafor.

ABSTRACT

Some magnetic oxide semiconductors; NiCo₂O₄, MgCo₂O₄, CdCo₂O₄ and AgCoO₂ were grown by electrodeposition method. Effect of deposition time, deposition voltage and percentage cobalt as dopant on the optical properties were determined. The samples were optically characterized using UV-VIS spectrophotometer in the UV-VIS-NIR regions of electromagnetic spectrum. Results show that NiCo₂O₄ has band gap that decreased from 3.8eV to 1.0eV as percentage cobalt dopant increased, maximum absorbance of 3.5% in UV region and maximum transmittance of 99.4% in the visible region. MgCo₂O₄ has bandgap that decreased from 4.4eV to 2.6eV as percentage cobalt dopant increased, maximum absorbance of 8% in UV region and maximum transmittance of approximately 100% in NIR. CdCo₂O₄ has bandgap that decreased from 2.2eV to 1.5eV as percentage cobalt dopant increased, maximum absorbance of 15% in UV region and maximum transmittance of 98.7% in NIR. AgCoO₂ has bandgap that increased from 2.6eV to 4.1eV as percentage cobalt dopant increased, maximum absorbance of 6% for 3% Co doped in UV-VIS-NIR regions and maximum transmittance of 98.5% for 23% Co doped in NIR region. Magnetic property was characterized with Microsense VSM system. Thickness of the films was characterized with profilometer while compositional property was done by X-ray fluorescence spectrometer. Results of the study show that the optical properties of the films viz; absorbance, reflectance, refractive index, extinction coefficient, complex dielectric constant and optical conductivities of NiCo₂O₄, MgCo₂O₄, CdCo₂O₄ increased as deposition time, deposition voltage and percentage cobalt dopant increased, but in case of AgCoO₂ they increased as deposition voltage and deposition time increased but decreased as percentage cobalt dopant increased. However the transmittance of the films NiCo₂O₄, MgCo₂O₄ and CdCo₂O₄ decreased as deposition voltage, deposition time and percentage cobalt dopant increased but in case of AgCoO₂, it decreased as deposition voltage and deposition time increased but increased as percentage cobalt dopant increased. Thickness of NiCo₂O₄, MgCo₂O₄ and CdCo₂O₄ films increased as percentage cobalt dopant, deposition voltage and deposition time increased but in case of AgCoO₂ it increased as deposition voltage and deposition time increased but decreased as percentage cobalt dopant increased.

TABLE OF CONTENTS

Page		
Title page		i
Certification page		ii
Dedication		iii
Acknowledgements		iv
Abstract		v
Table of contents		vi
Definition of terms		ix
List of tables		x
List of figures		xi
CHAPTER ONE		1
1. INTRODUCTION		1
1.1 Background of study		1
1.2 Explanation of terms		4
1.3 Statement of problems		11
1.4 Significance of study		12
1.5 Aim and objectives		12
1.6 Scope of study		12
CHAPTER TWO		14
2. LITERATURE REVIEW		14
2.1 Nanofilm		14
2.2 Semiconductor		17
2.4 Doping		24
2.5 Absorbance		29

2.6	Optical conductivity	32
2.7	Extinction coefficient	33
2.8	Reflectance	33
2.9	Transmittance	33
2.10	Refractive index	34
2.11	Complex dielectric constant	35
2.12	Applications of nanofilm semiconductors	36
2.13	Thinfilm/Nanofilm deposition techniques	58
2.14	Spintronics	70
2.15	Transparent conducting oxides	79
2.16	Review of related works	82
2.17	Effect of annealing on crystalline and magnetic properties of semiconductor thin films	105
2.18	Effect of dopant concentration on bandgap of semiconductor thin films	110
2.19	Effect of thickness on bandgap	110
2.20	Effect of cobalt doping on thickness of thin films	111
2.21	Bandgap bowing parameter	112
2.22	Magnetic susceptibility	113
	CHAPTER THREE	116
	3. MATERIALS AND METHOD	116
3.1	Overview	116
3.2	Slide preparation	116
3.3	Electrodeposition apparatus	117
3.4	Deposition of nickel coxide nanofilm	117
3.5	Deposition of magnesium oxide nanofilm	118

3.6 Deposition of cadmium oxide nanofilm	118
3.7 Deposition of silver oxide nanofilm	118
3.8 Deposition of nickel cobalt oxide nanofilms	119
3.9 Deposition of magnesium cobalt oxide nanofilms	121
3.10 Deposition of cadmium cobalt oxide nanofilms	123
3.11 Deposition of silver cobalt oxide nanofilms	125
3.12 Optical characterization of the nanofilms	127
3.13 Compositional characterization	127
3.14 Thickness characterization	127
3.15 Magnetic property characterization	128
3.16: Mathematical tools for analysis of optical properties	129
3.17 Pictures of deposited samples	130
CHAPTER FOUR	131
4. RESULTS AND DISCUSSIONS	131
4.1 Analysis of nickel cobalt oxide nanofilms	131
4.2 Analysis of magnesium cobalt oxide nano films	167
4.3 Analysis of cadmium cobalt oxide nanofilms	201
4.4 Analysis of silver cobalt oxide nanofilms	236
CHAPTER FIVE	272
5. CONCLUSIONS AND RECOMMENDATIONS FOR FURTHER STUDIES	272
5.1 Summary	272
5.2 Conclusions	273
5.3 Contributions to knowledge	273
5.4 Recommendations for further studies	274
References	275

DEFINITION OF TERMS

UV: Ultraviolet

VIS : Visible

NIR; Near infra red

RT: Room temperature

RF or rf: radio frequency

DMS: Dilute magnetic semiconductor

LED: Light emitting diode

ITO: Indium tin oxide

a.u. : arbitrary unit

MEMS : Micro-electro-mechanical systems

RAM : Random access memory

pH : potential Hydrogen

VSM : Vibrating system magnetometer

LIST OF TABLES	Page
2.1: Classification of materials	114
2.2: Classification of magnetic materials according to magnetic susceptibility	115
3.1: Deposition of NiO nanofilm	117
3.2: Deposition of MgO nanofilm	118
3.3: Deposition of CdO nanofilm	118
3.4: Deposition of AgO nanofilm	119
3.5 Variation of percentage doping for $NiCo_2O_4$ nanofilms	120
3.6 Variation of deposition voltage for $NiCo_2O_4$ nanofilms	120
3.7 Variation of deposition time for $NiCo_2O_4$ nanofilms	121
3.8 Variation of percentage doping for $MgCo_2O_4$ nanofilms	122
3.9: Variation of deposition voltage for $MgCO_2O_4$ nanofilm	122
3.10: Variation of deposition time for $MgCO_2O_4$ nanofilm	123
3.11: Variation of percentage doping for $CdCO_2O_4$ nanofilm	124
3.12: Variation of deposition voltage for $CdCO_2O_4$ nanofilm	124
3.13: Variation of deposition time for $CdCO_2O_4$ nanofilm	125
3.14: Variation of percentage doping for $AgCoO_2$ nanofilm	126
13.15: Variation of deposition voltage for $AgCoO_2$ nanofilm	126
3.16: Variation of deposition time for $AgCoO_2$ nanofilm	127
4.1: Variation of bandgap with percentage doping for cobalt doped $NiCO_2O_4$ nanofilm	134
4.2: Compositional analysis for $NiCo_2O_4$ at various percentage doping with cobalt	166
4.3: Variation of bandgap with percentage doping for cobalt doped magnesium oxide	168
4.4: Compositional analysis for magnesium cobalt oxide nanofilms at various percentage doping with cobalt	200

4.5: Variation of bandgap of cobalt doped cadmium oxide with percentage doping	202
4.6: Compositional analysis for cadmium cobalt oxide nanofilm at various percentage doping with cobalt	236
4.7: Variation of bandgap with percentage doping for cobalt doped silver cobalt oxide nanofilm.	238
4.8: Compositional analysis for AgCoO_2 at various percentage doping with cobalt	272

LIST OF FIGURES

2.1: Schematic representation of the alignment in polycrystalline thin films.	16
2.2 (a) Simple form of band structure (b) Simplified form of band structure	20
2.3: The absorption coefficient for several semiconductor materials	31
2.4: Fluorescence spectra of CdTe quantum dots of various sizes	40
2.5: Production of visible light through energy transfer from thin layers of quantum wells to crystals above the layers	41
2.6: Electron spins up and spins down	77
2.7: New forms of memory	78
2.8: I-V characteristics with the p-n diode structure of the p-NiO/n-ITO junction.	88
2.9: Transmittance spectra of the p-NiO/n-ITO junction	89
3.1: Electrodeposition apparatus	117
3.8: Pictures of deposited nanofilms	130
4.1: Graph of absorption coefficient squared versus photon energy for nickel cobalt oxide nanofilm.(3% doping with cobalt).	135
4.2: Graph of absorption coefficient squared versus photon energy for nickel cobalt oxide nanofilm(8% doping with cobalt)	133
4.3:Graph of absorption coefficient squared versus photon energy for nickel cobalt oxide nanofilm (13% doping with cobalt).	134
4.4: Graph of absorption coefficient squared versus photon energy for nickel cobalt oxide nanofilm (18% doping with cobalt).	134
4.5: Graph of absorption coefficient squared versus photon energy for NiCo ₂ O ₄ nanofilm (23% doping with cobalt).	135
4.6: Graph of absorption coefficient squared versus photon energy for undoped nickel oxide nanofilm.	135

4.7: Variation of bandgap with percentage doping for NiCo ₂ O ₄	136
4.8: Variation of bandgap with thickness for NiCo ₂ O ₄ nanofilm.	136
4.9 : Variation of thickness with percentage doping with cobalt for NiCo ₂ O ₄ nanofilm	137
4.10: Variation of bandgap bowing parameter for NiCo ₂ O ₄ nanofilm	137
4.11 Variation of absorbance with wavelength for NiCo ₂ O ₄ nanofilms for different percentages doping.	140
4.12: Variation of percentage transmittance with wavelength for different percentages doping	140
4.13: Variation of reflectance with wavelength for NiCo ₂ O ₄ nanofilm for different percentages doping.	141
4.14: Variation of refractive index with wavelength for NiCo ₂ O ₄ nanofilm for different percentages doping.	141
4.15: Variation of extinction coefficient with wavelength for NiCo ₂ O ₄ nanofilm. for different percentages doping.	142
4.16: Variation of complex dielectric constant with wavelength for NiCo ₂ O ₄ nanofilm for different percentages doping.	142
4.17: Variation of optical conductivity with wavelength for NiCo ₂ O ₄ nanofilm for different percentages doping.	143
4. 18: Variation of absorbance with wavelength for NiCo ₂ O ₄ nanofilm for different thicknesses.	145
4.19: Variation of transmittance with wavelength for NiCo ₂ O ₄ nanofilm for different thicknesses.	145
4.20: Variation of reflectance with wavelength for NiCo ₂ O ₄ nanofilm for different thicknesses.	146

4.21: Variation of refractive index with wavelength for NiCo ₂ O ₄ nanofilm for different thicknesses.	146
4.22: Variation of extinction coefficient with wavelength for NiCo ₂ O ₄ nanofilms for different thicknesses.	147
4.23: Variation of complex dielectric constant with wavelength for NiCo ₂ O ₄ nanofilm for different thicknesses.	147
4.24: Variation of optical conductivity with wavelength for NiCo ₂ O nanofilm for different thicknesses.	148
4.25: Variation of absorbance with wavelength for NiCo ₂ O ₄ nanofilm for different deposition times.	150
4.26: Variation of transmittance with wavelength for NiCo ₂ O ₄ nanofilm for different deposition times.	150
4.27: Variation of reflectance with wavelength for NiCo ₂ O ₄ nanofilm for different deposition times.	151
4.28: Variation of refractive index with wavelength for NiCo ₂ O ₄ nanofilm for different deposition times.	151
4. 29: Variation of extinction coefficient with wavelength for NiCo ₂ O ₄ nanofilm for different deposition times.	152
4.30: Variation of complex dielectric constant with wavelength for NiCo ₂ O ₄ nanofilm for different deposition times.	152
4.31: Variation of optical conductivity with wavelength for NiCo ₂ O ₄ nanofilm for different deposition times.	153
4.32: Variation of absorbance with wavelength for NiCo ₂ O ₄ nanofilm for different deposition voltages.	155

4.33: Variation of transmittance with wavelength for NiCo ₂ O ₄ nanofilm for different deposition voltages.	155
4.34: Variation of reflectance with wavelength for NiCo ₂ O ₄ nanofilm for different deposition voltages.	156
4.35: Variation of refractive index with wavelength for NiCo ₂ O ₄ nanofilm for different deposition voltages.	156
4.36: Variation of extinction coefficient with wavelength for NiCo ₂ O ₄ nanofilm for different deposition voltages.	157
4.37: Variation of complex dielectric constant with wavelength for NiCo ₂ O ₄ nanofilm for different deposition voltages.	157
4.38: Variation of optical conductivity with wavelength for NiCo ₂ O ₄ nanofilm. for different deposition voltages.	158
4.39: Variation of magnetic saturation of pinned layer with percentage doping with cobalt.	160
4.40: Variation of magnetic saturation of free layer with percentage doping with cobalt for NiCo ₂ O ₄ nanofilm.	160
4.41: Variation of magnetization with applied voltage for NiCo ₂ O ₄ nanofilm (3% doping)	162
4.42: Variation of magnetization with applied voltage for NiCo ₂ O ₄ nanofilm (8% doping)	162
4.43: Variation of magnetization with applied voltage for NiCo ₂ O ₄ nanofilm (13% doping)	163
4.44: Variation of magnetization with applied voltage for NiCo ₂ O ₄ nanofilm (18% doping)	163
4.45: Variation of magnetization with applied voltage for NiCo ₂ O ₄ nanofilm (23% doping)	164
4.46: Variation of magnetic susceptibility with percentage doping with cobalt for NiCo ₂ O ₄	164
4.47: Absorption coefficient squared versus photon energy, 3% Co doped MgCo ₂ O ₄ nanofilm.	168
4.48: Absorption coefficient squared versus photon energy, 8% Co doped MgCo ₂ O ₄ nanofilm	168
4.49: Absorption coefficient squared versus photon energy, 13% Co doped MgCo ₂ O ₄ nanofilm	169

4. 50: Absorption coefficient squared versus photon energy, 18% Co doped MgCo ₂ O ₄ nanofilm	169
4.51: Absorption coefficient squared versus photon energy, 23% Co doped MgCo ₂ O ₄ nanofilm	170
4. 52: Absorption coefficient squared versus photon energy for MgO nanofilm .	170
4. 53: Variation of bandgap with percentage doping for MgCo ₂ O ₄ nanofilm.	171
4. 54: Variation of bandgap with thickness for MgCo ₂ O ₄ nanofilms.	171
4.55: Variation of thickness with percentage doping for MgCo ₂ O ₄	172
4.56 Variation of bandgap bowing parameter with percentage doping for MgCo ₂ O ₄ nanofilm.	172
4.57: Variation of absorbance with wavelength for MgCo ₂ O ₄ nanofilm for different percentages doping with cobalt.	175
4. 58: Variation of transmittance with wavelength for MgCo ₂ O ₄ nanofilm for different percentages doping with cobalt.	175
4.59: Variation of reflectance with wavelength for cobalt doped MgCo ₂ O ₄ nanofilm for different percentages doping with cobalt.	176
4.60: Variation of refractive index with wavelength for MgCo ₂ O ₄ nanofilm for different percentages doping with cobalt.	176
4.61: Variation of extinction coefficient with wavelength for MgCo ₂ O ₄ nanofilm for different percentages doping with cobalt.	177
4.62: Variation of complex dielectric constant with wavelength for MgCo ₂ O ₄ nanofilm for different percentages doping with cobalt.	177
4.63: Variation of optical conductivity with wavelength for MgCo ₂ O ₄ nanofilm for different percentages doping with cobalt.	178
4.64: Variation of absorbance with wavelength for MgCo ₂ O ₄ nanofilms for different thicknesses.	180

4.65: Variation of transmittance with wavelength for MgCo ₂ O ₄ nanofilm for different thicknesses.	180
4.66: Variation of reflectance with wavelength for MgCo ₂ O ₄ nanofilm for different thicknesses.	181
4.67: Variation of refractive index with wavelength for MgCo ₂ O ₄ nanofilm for different thicknesses.	181
4.68: Variation of extinction coefficient with wavelength for MgCo ₂ O ₄ nanofilm for different thicknesses.	182
4.69: Variation of complex dielectric constant with wavelength for MgCo ₂ O ₄ nanofilm for different thicknesses.	182
4.70: Variation of optical conductivity with wavelength for MgCo ₂ O ₄ nanofilm for different thicknesses.	183
4.71: Variation of absorbance with wavelength for MgCo ₂ O ₄ nanofilm for different deposition times.	185
4.72: Variation of percentage transmittance with wavelength for MgCo ₂ O ₄ nanofilm for different deposition times.	185
4.73: Variation of reflectance with wavelength for MgCo ₂ O ₄ nanofilm for different deposition times.	186
4.74: Variation of refractive index with wavelength for MgCo ₂ O ₄ nanofilm for different deposition times.	186
4.75: Variation of extinction coefficient with wavelength for MgCo ₂ O ₄ nanofilm for different deposition times.	187
4.76: Variation of complex dielectric constant with wavelength for MgCo ₂ O ₄ nanofilm for different deposition times.	187

4.77: Variation of optical conductivity with wavelength for MgCo ₂ O ₄ nanofilm for different deposition times.	188
4.78: Variation of absorbance with wavelength for MgCo ₂ O ₄ nanofilm for different deposition voltages.	190
4.79: Variation of transmittance with wavelength for MgCo ₂ O ₄ nanofilm for different deposition voltages.	190
4.80: Variation of reflectance with wavelength for MgCo ₂ O ₄ nanofilm for different deposition voltages.	191
4.81: Variation of refractive index with wavelength for MgCo ₂ O ₄ nanofilm for different deposition voltages.	191
4.82: Variation of extinction coefficient with wavelength for MgCo ₂ O ₄ nanofilm for different deposition voltages.	192
4.83: Variation of complex dielectric constant with wavelength for MgCo ₂ O ₄ nanofilm for different deposition voltages.	192
4.84: Variation of optical conductivity with wavelength for MgCo ₂ O ₄ nanofilm for different deposition voltages.	193
4.85: Variation of magnetic saturation of pinned layer with percentage doping with cobalt for MgCo ₂ O ₄	195
4.86: Variation of magnetic saturation of free layer with percentage doping with cobalt for MgCo ₂ O ₄	195
4.87: Variation of magnetization with applied voltage for MgCo ₂ O ₄ nanofilm (3% doping)	197
4.88: Variation of magnetization with applied voltage for MgCo ₂ O ₄ nanofilm (8% doping)	197
4.89: Variation of magnetization with applied voltage for MgCo ₂ O ₄ nanofilm (13% doping)	198
4.90: Variation of magnetization with applied voltage for MgCo ₂ O ₄ nanofilm (18% doping)	198
4.91: Variation of magnetization with applied voltage for MgCo ₂ O ₄ nanofilm (23% doping)	199

4.92: Variation of magnetic susceptibility with percentage doping with cobalt for MgCo ₂ O ₄ Nanofilm	199
4.93: Graph of absorption coefficient squared versus photon energy for 3% cobalt doped cadmium cobalt oxide nanofilm.	203
4.94: Graph of absorption coefficient squared versus photon energy for 8% Co doped CdCo ₂ O ₄ nanofilm	203
4.95: Graph of absorption coefficient squared versus photon energy for 13% cobalt doped cadmium cobalt oxide nanofilm.	204
4.96: Graph of absorption coefficient squared versus photon energy for 18% cobalt doped cadmium cobalt oxide nanofilm.	204
4.97: Graph of absorption coefficient squared versus photon energy for 23% Co doped CdCo ₂ O ₄ nanofilm.	204
4.98: Graph of absorption coefficient squared versus photon energy for undoped cadmium oxide nanofilm.	205
4.99 Variation of bandgap with percentage doping for cobalt doped CdCo ₂ O ₄ nanofilm.	206
4.100: Variation of bandgap with thickness for cobalt doped CdCo ₂ O ₄ nanofilm.	206
4.101: Variation of thickness with percentage doping with cobalt for CdCo ₂ O ₄ nanofilm	207
4.102 Variation of bandgap bowing parameter with percentage doping for cobalt doped CdCo ₂ O ₄ nanofilm.	207
4.103: Variation of absorbance with wavelength for CdCo ₂ O ₄ nanofilm for different percentages doping with cobalt.	210
4.104: Variation of transmittance with wavelength for CdCo ₂ O ₄ nanofilm for different percentages doping with cobalt.	210
4.105: Variation of reflectance with wavelength for CdCo ₂ O ₄ nanofilm for different percentages doping with cobalt.	211

4.106: Variation of refractive index with wavelength for CdCo ₂ O ₄ nanofilm for different percentages doping with cobalt.	211
4.107: Variation of extinction coefficient with wavelength for CdCo ₂ O ₄ nanofilm for different percentages doping with cobalt.	212
4.108: Variation of complex dielectric constant with wavelength for CdCo ₂ O ₄ nanofilm for different percentages doping with cobalt.	212
4.109: Variation of optical conductivity with wavelength for CdCo ₂ O ₄ nanofilm for different percentages doping with cobalt.	213
4.110: Variation of absorbance with wavelength for CdCo ₂ O ₄ nanofilm for different thicknesses.	215
4.111: Variation of transmittance with wavelength for CdCo ₂ O ₄ nanofilm for different thicknesses.	215
4.112: Variation of reflectance with wavelength for CdCo ₂ O ₄ nanofilm for different thicknesses.	216
4.113: Variation of refractive index with wavelength for CdCo ₂ O ₄ nanofilm for different thicknesses.	216
4.114: Variation of extinction coefficient with wavelength for CdCo ₂ O ₄ nanofilm for different thicknesses.	217
4.115: Variation of complex dielectric constant with wavelength for CdCo ₂ O ₄ nanofilm for different thicknesses.	217
4.116: Variation of optical conductivity with wavelength for CdCo ₂ O ₄ nanofilm for different thicknesses	218
4.117: Variation of absorbance with wavelength for CdCo ₂ O ₄ nanofilm for different deposition voltages.	220

4.118: Variation of transmittance with wavelength for CdCo ₂ O ₄ nanofilm for different deposition voltages.	220
4.119: Variation of reflectance with wavelength for CdCo ₂ O ₄ nanofilm for different deposition voltages.	221
4.120: Variation of refractive index with wavelength for CdCo ₂ O ₄ nanofilm for different deposition voltages.	221
4.121: Variation of extinction coefficient with wavelength for CdCo ₂ O ₄ nanofilm for different deposition voltages.	222
4.122: Variation of complex dielectric constant with wavelength for CdCo ₂ O ₄ nanofilm for different deposition voltages.	222
4.123: Variation of optical conductivity with wavelength for CdCo ₂ O ₄ nanofilm for different deposition voltages.	223
4.124: Variation of absorbance with wavelength for CdCo ₂ O ₄ nanofilm for different deposition times.	225
4.125: Variation of transmittance with wavelength for CdCo ₂ O ₄ nanofilm for different deposition times.	225
4.126: Variation of reflectance with wavelength for CdCo ₂ O ₄ nanofilm for different deposition times.	226
4.127: Variation of refractive index with wavelength for CdCo ₂ O ₄ nanofilm for different deposition times.	226
4.128: Variation of extinction coefficient with wavelength for CdCo ₂ O ₄ nanofilm for different deposition times.	227
4.129: Variation of complex dielectric constant with wavelength for CdCo ₂ O ₄ nanofilm for different deposition times.	227

4. 130: Variation of optical conductivity with wavelength for CdCo ₂ O ₄ nanofilm for different deposition times.	228
4.131: Variation of remanent magnetization with percentage doping with cobalt for CdCo ₂ O ₄ nanofilm	231
4.132: Variation of saturation magnetization with percentage doping with cobalt for CdCo ₂ O ₄ nanofilm	230
4.133: Variation of magnetization with applied voltage for CdCo ₂ O ₄ nanofilm(3% doping)	232
4.134: Variation of magnetization with applied voltage for CdCo ₂ O ₄ nanofilm(8% doping)	232
4.135: Variation of magnetization with applied voltage for CdCo ₂ O ₄ nanofilm(13% doping)	233
4.136: Variation of magnetization with applied voltage for CdCo ₂ O ₄ nanofilm(18% doping)	233
4.137: Variation of magnetization with applied voltage for CdCo ₂ O ₄ nanofilm(23% doping)	234
4.138: Variation of magnetic susceptibility with percentage doping for CdCo ₂ O ₄ nanofilm	234
4.139: Absorption coefficient versus photon energy for 3% Co doped AgCoO ₂ nanofilm.	238
4.140: Absorption coefficient versus photon energy for 8% Co doped AgCoO ₂ nanofilm.	238
4.141: Absorption coefficient versus photon energy for 13% Co doped AgCoO ₂ nanofilm.	239
4.142: Absorption coefficient versus photon energy for 18% Co doped AgCoO ₂ nanofilm.	239
4.143: Absorption coefficient versus photon energy for 23% Co doped AgCoO ₂ nanofilm.	240
4.144: Absorption coefficient versus photon energy for undoped Silver Oxide (Ag ₂ O) nanofilm.	240
4.145: Variation of bandgap with percentage doping for Co doped AgCoO ₂ nanofilm.	241
4.146: Variation of bandgap with thickness for Co doped AgCoO ₂ nanofilm	241
4.147: Variation of thickness with percentage doping with cobalt for AgCoO ₂ nanofilm	242
4.148 Variation of bandgap bowing parameter with percentage doping for Co doped AgCoO ₂ nanofilm.	242
4.149: Variation of absorbance with wavelength for AgCoO nanofilms for different percentages doping with cobalt.	245

4.150: Variation of transmittance with wavelength for AgCoO ₂ nanofilms for different percentages doping with cobalt.	245
4.151: Variation of reflectance with wavelength for AgCoO nanofilm for different percentages doping with cobalt.	246
4.152: Variation of refractive index with wavelength for AgCoO ₂ nanofilm for different percentages doping with cobalt.	246
4.153: Variation of extinction coefficient with wavelength for AgCoO ₂ nanofilm. for different percentages doping with cobalt.	247
4.154: Variation of complex dielectric constant with wavelength for AgCoO ₂ nanofilm. for different percentages doping with cobalt.	247
4.155: Variation of optical conductivity with wavelength for (AgCoO ₂) nanofilm for different percentages doping with cobalt.	248
4.156: Variation of absorbance with wavelength for AgCoO ₂ nanofilm for different thicknesses.	250
4.157: Variation of transmittance with wavelength for AgCoO ₂ nanofilm for different thicknesses.	250
4.158: Variation of reflectance with wavelength for AgCoO ₂ nanofilm for different thicknesses.	251
4.159: Variation of refractive index with wavelength for AgCoO ₂ nanofilm for different thicknesses.	251
4.160: Variation of extinction coefficient with wavelength for AgCoO ₂ nanofilm for different thicknesses.	252
4.161: Variation of complex dielectric constant with wavelength for AgCoO ₂ nanofilm for different thicknesses.	252

4.162: Variation of optical conductivity with wavelength for AgCoO ₂ nanofilm for different thicknesses.	253
4.163: Variation of absorbance with wavelength for AgCoO ₂ nanofilm for different deposition times.	255
4.164: Variation of percentage transmittance with wavelength for AgCoO ₂ nanofilms for different deposition times.	255
4.165: Variation of reflectance with wavelength for AgCoO ₂ nanofilms for different deposition times.	256
4.166: Variation of refractive index with wavelength for AgCoO ₂ nanofilms for different deposition times.	256
4.167: Variation of extinction coefficient with wavelength for AgCoO ₂ nanofilms for different deposition times.	257
4.168: Variation of complex dielectric constant with wavelength for AgCoO ₂ nanofilms for different deposition times.	257
4.169: Variation of optical conductivity with wavelength for AgCoO ₂ nanofilms for different deposition times.	258
4.170: Variation of absorbance with wavelength for AgCoO ₂ nanofilms for different deposition voltages.	261
4.171: Variation of transmittance with wavelength for AgCoO ₂ nanofilms for different deposition voltages.	261
4.172: Variation of reflectance with wavelength for AgCoO ₂ nanofilms for different deposition voltages.	262
4.173: Variation of refractive index with wavelength for AgCoO ₂ nanofilms for different deposition voltages.	262

4.174: Variation of extinction coefficient with wavelength for AgCoO ₂ nanofilms for different deposition voltages.	263
4.175: Variation of complex dielectric constant with wavelength for AgCoO ₂ nanofilms for different deposition voltages.	263
4.176: Variation of optical conductivity with wavelength for AgCoO ₂ nanofilms for different deposition voltages.	264
4.177: Variation of magnetic saturation of pinned layer with percentage doping with cobalt for AgCoO ₂ nanofilm	266
4.178: Variation of magnetic saturation of free layer with percentage doping with cobalt for AgCoO ₂ nanofilm	266
4.179: Variation of magnetization with applied voltage for AgCoO ₂ nanofilm(3% doping)	268
4.180: Variation of magnetization with applied voltage for AgCoO ₂ nanofilm(8% doping)	268
4.181: Variation of magnetization with applied voltage for AgCoO ₂ nanofilm(13% doping)	269
4.182: Variation of magnetization with applied voltage for AgCoO ₂ nanofilm(18% doping)	269
4.183: Variation of magnetization with applied voltage for AgCoO ₂ nanofilm(23% doping)	270
4.184 Variation of magnetic susceptibility with percentage doping with cobalt for AgCoO ₂ nanofilm	270

CHAPTER ONE

INTRODUCTION

1.1 Background of study

Magnetic semiconductors are semiconductor compounds in which a fraction of the constituent ions are magnetic. These compounds provide a rich experimental and theoretical laboratory for testing many important ideas of condensed matter Physics. The central issue in magnetic semiconductor research is the interaction between semiconductor band electrons (e.g., charge carriers or impurity states) and magnetic moments of the ions. This interaction results in a range of electronic phenomena –such as giant magnetoresistance, strong magneto-optical rotation, magnetically driven semiconductor metal transition and magnetic polaron effects – all of which are absent in ordinary semiconductors. The simultaneous presence of semiconducting and magnetic properties in these compounds along with the ability to independently control them offers the potential for a variety of technological and scientific opportunities. Magnetic semiconductors are expected to have a variety of applications given the technological importance of both semiconductor devices and magnetic materials in communications, logic and memory. Currently, the most actively investigated systems are diluted magnetic semiconductors (DMS) (Furdyna *et al.*, 1991). In the field of dilute magnetic semiconductors(DMS), host non magnetic II-VI and III-V semiconductors are doped to a typically very dilute extent with magnetic elements from transition metal 3d or rare Earth 4f series; such examples include $Zn_{1-x}Co_xO$ and $Zn_{1-x}Ni_xO$ (Ziatko, 2010). Diluted magnetic semiconductors(DMS), are potential high performance candidates and are II-VI, IV-VI, II-V and III-V compounds in which a sizable number of magnetic ions (eg, Mn^{2+} , Fe^{2+} , Co^{2+}) offer a variety of co-operative effects via spin-spin exchange interaction (Chuu *et al.*, 1997). One of the primary goals of research in DMS

material is to develop a ferromagnetic semiconductor with an ordering temperature well above room temperature. The avenue that has been pursued most intensively is to develop regular III-V, or II-VI semiconductors with a magnetic element such as Mn or Co. In general, the magnetic (3d) atoms in DMS materials are located on substitutional and /or interstitial sites of the semiconducting host and most attention has been focused on III-V and II-VI semiconductors where underlying lattice has wurzite or zinc blende structure. An important fact is that for II-VI semiconductors, a larger concentration lattice up to ~ 35% magnetic atoms can be absorbed which should be compared to ~8% for III-V semiconductors (Sato *et al.*, 2010) .

The possibility of using electrons' spins in addition to their charge in information technology has created much enthusiasm for a new field of electronics popularly known as spintronics. An intensely studied approach to obtaining spin-polarized carriers for data-storage devices is the use of diluted magnetic semiconductors created by doping ions like Mn, Fe, or Co having a net spin into a semiconducting host such as GaAs, ZnO, or GaN (Edmonds *et al.*, 2006). The discovery of Giant magnetoresistive effect (GMR) is considered the beginning of the new spin based electronics. Important applications of GMR include magnetic field sensors, read heads for hard drives, galvanic isolators and magnetoresistive random access memory (MRAM),(Wolf, *et al.*, 2001). MRAM is likely to replace commonly used flash memory such as SD cards and compact flash first, as it is faster and doesn't suffer from flash memory's limited lifespan. As electronics approaches the limits of silicon, spintronic components will play an important role in ensuring we enjoy steady performance gains, faster, and higher-capacity storage at lower power and cost,(Atsufumi, 2015).Compared to conventional semiconductor devices, where only the charge of electrons is used, some predicted advantages of spintronics are, increased speed of data

processing, increased integration density, nonvolatility of data storage, and low electric power consumption (Wolf, *et al.*, 2001).

Most wide band gap materials are insulating, while most conducting materials are opaque to light at visible wavelengths. In this sense, wide band gap oxide semiconductors (ZnO, TiO₂, In₂O₃, etc.) are unique because they are good conductors due to the presence of native defects while simultaneously being transparent in the visible region (King and Veal, 2011). Current magnetic devices, such as read heads for magnetic data storage, are mainly based on ferromagnetic metals. The first step towards magnetic property modification is searching materials with reproducible and stable room temperature ferromagnetism. The long term goal of the oxide ferromagnetic semiconductor study is to produce novel spin-based multifunctional devices, such as magnetic tunnel junctions, spin field effect transistors, and spin light emitting diodes, wherein nonvolatile information storage, high processing speed, and low energy consumption could all be achieved simultaneously, (Tian *et al.*, 2013). Information mass storage devices, giant magnetoresistance (GMR), spin valve sensors, giant tunneling magnetoresistance (GTMR), racetrack memory, quantum computing, microdrives are all outcome of spintronics. NiCo₂O₄ being magnetic, by virtue cobalt presence, MgCo₂O₄, CdCo₂O₄ and AgCoO₂ are dilute magnetic semiconductors, and as such are veritable materials for spintronics, hence could be useful in the afore mentioned applications. Doped semiconductors could be prepared by many deposition methods such as electrodeposition, sol-gel method, thermal evaporation, chemical bath, spin coating, electron beam evaporation, pulsed layer deposition, silar method, vacuum evaporation, sputtering, spray pyrolysis, etc.

1.2. EXPLANATION OF TERMS

1.2.1 Crystal growth

The process of crystal growth can be summarized into four steps viz: Transport of atoms through solution, attachment of atoms to the surface, movement of atoms on the surface and attachment of atoms to edges and kinks (Lasaga, 1998; In Cubillas and Anderson, 2010). The formation of a new crystalline entity from a solution starts through the nucleation process. Nucleation is the series of atomic or molecular processes by which the atoms or molecules of a reactant phase rearrange into a cluster of the product phase large enough as to have the ability to grow irreversibly to a macroscopically large size. The cluster is defined as the nucleus (Kashchiev, 2000; In Cubillas and Anderson, 2010) or critical nuclei. Nucleation can be homogeneous, in the absence of foreign particles or crystals in the solution or heterogeneous in the presence of foreign particles in the solution. Both types of nucleation are collectively known as primary nucleation. Secondary nucleation takes place when nucleation is induced by the presence of crystals of same substance (Cubillas and Anderson, 2010).

1.2.2 Characterization

Characterization as used in material science refers to the broad and general process by which a material's structure and properties are probed and measured. It is a fundamental process in the field of material science without which no scientific understanding of engineering materials could be obtained. The scope of the term often differs; some definitions limit the term's use to techniques which study microscopic structure and properties of the material (Leng, 2009; In Wikipedia, 2017) while others use the term to refer to any material's analysis process including macroscopic techniques such as mechanical testing, thermal analysis and density calculation (Zhang, 2008; In Wikipedia, 2017). Some examples of characterization techniques are : UV-

VIS-NIR spectroscopy for measurement of absorbance and transmittance of light through the material (Soares, 2014), X-ray fluorescence spectroscopy for identification and quantification of various elements present in a material (Guthrie and Ferguson, 2012). X-ray diffraction spectroscopy (XRD), for investigation of crystalline structures of materials(Sardela, 2014), Auger electron spectroscopy (AES) for elemental composition of surface layers, Rutherford backscattering (RBS) for elemental composition of deeper layers (Salik, *et al.*, 1986).Vibrating sample magnetometry for measurement of magnetic properties (Spinu *et al.*,2013).

1.2.3 Oxide semiconductors

Oxide semiconductors are very promising family of materials for electronic device applications, displaying unique physical properties. Their bandgaps range from the infrared (IR) over the visible and into the ultraviolet (UV) regions of the electromagnetic spectrum. They are most often easily made n-type, making them attractive materials for transparent conducting oxides (TCOs),(Gordon,2000;In Lyons *et al.*, 2013), photodetectors(Irvin *et al.*,2010;In Lyons *et al.*, 2013) and transparent thin film transistors(Normura *et al.*, 2013;In Lyons *et al.*, 2013). Other properties such as large exciton binding energies and the availability of large substrates, give them potential advantages over other materials such as nitride semiconductors. A common characteristic of many oxide semiconductors is that their electrical conductivity has proved difficult to control. Unlike more traditional semiconductors such as Si, Ge, or GaAs, oxides are often grown or deposited with less sophisticated growth techniques, leading to lower crystal quality and higher concentration of unintentional impurities (McCluskey and Jokela, 2007;In Lyons *et al.*, 2013). Most semiconducting oxides are naturally n-type and have proved difficult to reliably dope p-type; far fewer oxide materials are p-type (Lyons *et al.*, 2013).

1.2.4 Magnetic semiconductors

These are semiconductors containing magnetic element such as cobalt, nickel, iron, gadolinium, dysprosium (Eisberg and Resnick, 1974), Manganese, (Sato *et al.*, 2010) etc. Magnetic semiconductor could be ferromagnetic, antiferromagnetic or ferrimagnetic depending on the component elements and spin orientations of the dipole moments. A magnetic semiconductor in which the spin dipole moments are parallel aligned is ferromagnetic while it is antiferromagnetic if the spin dipole moments are anti parallel aligned. In ferrimagnetic semiconductors, there is anti parallel alignment of unequal dipole moments. They contain Fe^{3+} as one of the component metallic ions. They have room temperature spontaneous magnetization and positive, high magnetic susceptibility, though less than that of ferromagnetic. Ferromagnetic semiconductors have room temperature spontaneous magnetization and magnetic susceptibility is large and positive. Antiferromagnetic semiconductors have no room temperature spontaneous magnetization and the magnetic susceptibility is very small and positive (Kittel, 2005; Eisberg and Resnick, 1974)

1.2.5 Nanofilm

Nanofilm is a film that has one of its dimensions in the nano range(nanoscale). Nanoscale is (1 to 100nm, i.e., 1×10^{-9} to $1 \times 10^{-7}m$). There are a number of advantages that nanofilm technology pose. Nanofilm products will be more durable and last longer due to their strength and therefore are smart economic choice when buying merchandise. Nanofilm products promote the reuse of materials more often as well as recycling (Horneyak, *et al.*, 2009). Most benefits of nanotechnology depend on the fact that it is possible to tailor the essential structures of materials at the nanoscale to achieve specific properties. Using nanotechnology, materials can effectively

be made stronger, lighter, more durable, more reactive ,better electrical conductors (Nano National Initiative, 2016).

1.2.6 Electrodeposition

It is possible to grow many materials such as semiconductors, semimetals (i.e. topological insulators - TI) and metals by electrodeposition. Metal salts of the desired material are dissolved in an aqueous solution (electrolyte). Deposition is performed by the application of a current or potential between two conducting electrodes submerged in the electrolyte and connected through a potentiostat. In this way, it is relatively easy to deposit films on one of the electrodes, cathode, by the cathodic reduction of the dissolved metal cations. The dimensions of the film are the same as the cathode and the thickness is controlled by the deposition time. Thin-films from sub-nanometer to tens of microns are commonly made,(Wade,T. and Clochard M., 2017).The recent upsurge of interest in electrodeposition is due to three main factors/technologies (i) Metal deposition for the fabrication of integrated circuits (ii) Deposition of magnetic recording devices (iii) Deposition of multilayer structures. Electrodeposition techniques are increasingly used for the production of micromechanical sensors, actuators, motors or electronic devices requiring the ability to produce flat deposits in thick, multilevel microstructures (Muresan and Varvara, 2005)

1.2.7 Applications of wide bandgap Semiconductors

Wide bandgap semiconductors are materials that have bandgap significantly greater than those of Silicon 1.1eV. They have the following applications:

1. Wide bandgap semiconductor materials allow power electronic components to be smaller, faster, more reliable, and more efficient than their silicon (Si)-based counterparts. These capabilities make it possible to reduce weight, volume, and life-cycle costs in a wide range of

power applications. Harnessing these capabilities can lead to dramatic energy savings in industrial processing and consumer appliances, accelerate widespread use of electric vehicles and fuel cells, and help integrate renewable energy onto the electric grid.

2. Wide bandgap semiconductors permit devices to operate at much higher temperatures, voltages, and frequencies—making the power electronic modules using these materials significantly more powerful and energy efficient than those made from conventional semiconductor materials.

3. Wide bandgap materials also emit light in the visible color range, an optical property useful for applications in solid-state lighting. For example Gallium nitride (GaN) is an enabling material behind the ultra-high efficiency of light emitting diodes (LEDs).

4. Wide bandgap semiconductors are expected to pave the way for exciting innovations in power electronics, solid-state lighting, and other diverse applications across multiple industrial and clean energy sectors. Realizing the energy-saving potential of wide bandgap semiconductors will require the development of cutting-edge manufacturing processes that can produce high-quality wide bandgap materials, devices, and modules at an affordable cost.

5. Wide bandgap materials have the potential to enable cutting-edge electronic and optical devices with vastly superior performance compared to current technology. Specific energy-related benefits are as listed.

Electronic devices

(i) Reduced energy losses: Eliminates up to 90% of the power losses that currently occur during AC-to-DC and DC-to-AC electricity conversion.

(ii) Higher-voltage operation: Handles voltages more than 10 times higher than Si-based devices, greatly enhancing performance in high-power applications.

(iii) Higher-temperature operation: Operates at temperatures over 300°C (twice the maximum temperature of Si-based devices). This tolerance for higher operating temperature results in better overall system reliability, enables smaller and lighter systems with reduced lifecycle energy use, and creates opportunities for new applications.

(iv) Higher frequencies: Operates at frequencies at least 10 times higher than Si-based devices, making possible more compact, less costly product designs and opening up a range of new applications, such as radio frequency (RF) amplifiers.

(v) Improved power quality: Ensures more reliable and consistent power electronic device operation.

Optical devices

(i) Greater lighting efficiency: Wide bandgap -based LEDs produce more than 10 times more light per watt of input energy than comparable incandescent bulbs and extend service life by 30 times or more.

As manufacturing capabilities improve and market applications expand, costs are expected to decrease, making Wide bandgap -based devices competitive with less expensive Si-based devices.

(ii) Industrial Motors: Wide bandgap materials will enable higher-efficiency, variable-speed drives in motors—pumps, fans, compressors, and high voltage alternating current systems—used across manufacturing. Motor systems use 69% of the electricity consumed in U.S. manufacturing.

(iii) Electronics: Wide bandgap materials are already used in large, high-efficiency data centers and show promise as compact power supplies for consumer electronics.

(iv) Grid integration: Wide bandgap -based inverters can convert the DC electricity generated from solar and wind energy into the AC electricity used in homes and businesses —while reducing losses by 50%.

(v) Utility applications: Wide bandgap have the potential to reduce transformer size by a factor of ten or more. Wide bandgap -based power electronics could also accelerate development of high-voltage DC power lines, which will operate more efficiently than existing high-voltage AC transmission lines.

(vi) Electric vehicles and plug-in hybrids: Wide bandgap materials are expected to cut electricity losses by 66% during vehicle battery recharging. They also offer greater efficiency in converting AC to DC power and in operating the electric traction drive during vehicle use.

The ability of these electronics to tolerate higher operating temperatures could reduce the size of an automotive cooling system by 60% or even eliminate the secondary liquid cooling system.

(vii) Military: Wide bandgap semiconductors have great potential as an enabling material in high-density power applications, satellite communications, and high-frequency and high-power radar.

(viii) Geothermal: Wide bandgap -based electronic sensors can withstand the harsh, high-pressure, and high-temperature environments of geothermal wells.

(ix) Lighting: At today’s energy prices, LED lighting is expected to save \$250 billion in cumulative energy costs by 2030

(x) Broad Economic Impacts

Wide bandgap semiconductors are a foundational technology that promises to transform multiple industries and markets. Low-cost, high-performance power electronics are expected to become integral to everything from household appliances and consumer goods to military systems,

vehicles, and a modernized grid that incorporates renewable energy. The Wide bandgap share of the global lighting market alone is projected to reach \$84 billion by 2020.

The ability to design and manufacture innovative wide bandgap -enabled devices cost effectively will create a strong foundation of domestic materials technology expertise and give U.S. manufacturers early entry and, therefore, a competitive edge in key global markets. Extensive use of these devices will save U.S. businesses and consumers billions of dollars in energy costs (U.S. Department of Energy, 2013)

1.3 STATEMENT OF PROBLEMS

The need for solutions to some unresolved issues as stated hereafter constituted the problems prompting this research.

Firstly, the non magnetic oxide semiconductors have few applications whereas the magnetic oxide semiconductors have more improved optoelectronic applications. Magnetic oxide semiconductors have applications in spintronics which the non magnetic oxide semiconductors do not have, hence the need for more magnetic semiconductors. In order to proffer solutions to the above problems, magnetic oxide nanofilms of cobalt doped NiCo_2O_4 , MgCo_2O_4 , CdCo_2O_4 and AgCoO_2 were selected for deposition. This research is intended to ascertain the effect of percentage doping on the optical and magnetic properties of the films, the effect of deposition voltage, deposition time and thickness on the optical properties. The determination of the structural properties and possible applications of the films.

1.4

SIGNIFICANCE OF STUDY

This research based on growth of nanofilms of NiCo_2O_4 , MgCo_2O_4 , CdCo_2O_4 and AgCoO_2 is another step forward in the development of nanotechnology in magnetic semiconductors. The work will serve as a basis for further research in other properties of the semiconductor nanofilms, and subsequently discovery of their new applications. It will serve as a reference point to other researchers. Results of the work will contribute immensely to the development of optoelectronic industry relying on such properties of the films. It will provide source of information to prospective researchers in semiconductor nanofilms. This research has contributions to knowledge on doped magnetic and dilute magnetic semiconductors. It has exposed their growth conditions, properties, possible applications and new areas of research about them.

1.5

AIM AND OBJECTIVES

Aim

This research is aimed at Growth and Characterization of Some Magnetic Oxide Semiconductor Nanofilms by Electrodeposition Method and their possible Applications.

Objectives

The objectives include:

1. To grow cobalt doped nanofilms of NiO , MgO , CdO and Ag_2O by electrodeposition method
2. To carry out optical, magnetic and compositional characterization of the films
3. To ascertain possible applications of the films

1.6

SCOPE OF STUDY

This work is geared to study the effect of the following on the properties of the films;

Effect of percentage doping on the optical properties of the films.

Effect of deposition voltage on the optical properties of the films.

Effect of deposition time on the optical properties of the films.

Effect of percentage doping on the magnetic property of the films.

Analysis of compositional property of the films.

Possible applications of the films in terms of optical and magnetic properties.

CHAPTER TWO

LITERATURE REVIEW

2.1 Nanofilm

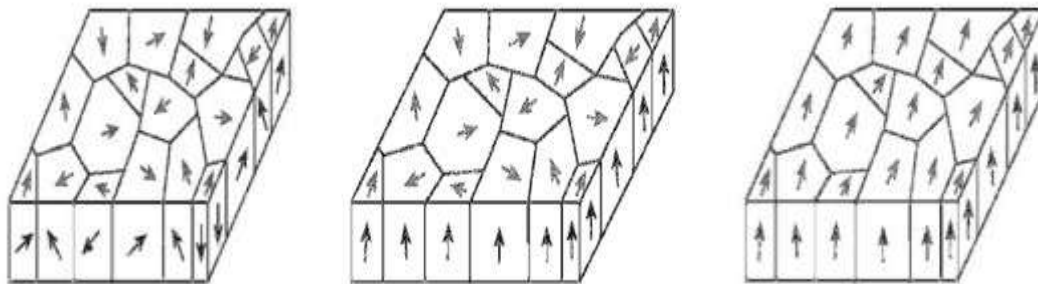
United States National Nanotechnology Initiative defined nanotechnology as science, engineering and technology conducted at the nanoscale which is about 1 to 100 nanometers (1×10^{-9} to 1×10^{-7} m). Nanoscience and nanotechnology are the study and application of extremely small things and can be used across all the other science fields, such as chemistry, biology, physics, materials science and engineering.

Nanoscale science and nanotechnology involves imaging, measuring, modeling, and manipulating matter at this length scale. At the nanoscale, the physical, chemical, and biological properties of materials can differ in fundamental and useful ways from the properties of individual atoms and molecules or bulk matter.

Nanofilm is that which has thickness within the nanoscale. Film properties and functionality depend crucially on the crystallinity, i.e., on whether a film is crystalline or amorphous. Amorphous films are in general less dense and thus exhibit inferior mechanical strength as compared to their crystalline counterparts (Jaan *et al.*, 2005; In Saraiva, 2012). On the other hand, due to the absence of grain boundaries, amorphous films are less prone to diffusion, chemical attack, oxidation and corrosion (Smith, 1995; In Saraiva, 2012). Furthermore, the lack of long-range order results in isotropic properties, which is frequently not the case for crystalline films. The combination of amorphous and crystalline structure in the same film can also be beneficial. This is the

case in the so called nanocomposite films in which control of the relative size and separation of nanosized crystals embedded in an amorphous matrix can result in films with superior mechanical, electrical and tribological performance (Patscheider *et al.*, 2011; In Saraiva, 2012). Film synthesis at conditions of limited atomic assembly kinetics, realized at relatively low growth temperatures and large arrival rates of the film forming species, leads to amorphous structures in materials with relatively large crystallization energy barriers (Ohring, 2002; In Saraiva, 2012). Bombardment by energetic species, frequently encountered in plasma-assisted physical vapor deposition techniques (e.g. magnetron sputtering) has also been shown to be crucial for the structure formation (Patscheider *et al.*, 2011; In Saraiva, 2012). Moreover, intentional and non-intentional addition of impurity species which segregate at the grain boundaries may hinder or promote grain growth and thus determine the structure formation (Barna and Adamik, 1998; In Saraiva, 2012). Another way to control structure formation is by mixing two materials that exhibit different crystalline structures. In the case of relatively low concentration of the impurity phase in the host lattice, a solid solution may form. However, further increase in the impurity phase content often leads to formation of amorphous structure. Although as observed in many systems, the origin of the later behaviour on a fundamental electronic level is still not understood. The presence of atoms with size and valence electron number different from those of the host atoms may affect electronic charge distribution and consequently the bond strength and type. These factors are in turn known to be crucial for the stability of a certain atomic configuration.

A polycrystalline film consists of many crystallites called grains of various size, shape and orientation. Each crystallite is a single crystal with anisotropic properties due to its periodic atomic arrangement in three-dimensional space. In most cases, crystallites have an anisotropic orientation distribution. This anisotropic distribution is referred to as a preferred orientation or a texture. A film having all crystallites fully randomly oriented is said to have no texture. Depending on the degree of the preferred orientation, a film is referred to as having a weak, moderate or strong texture. The texture in thin films can be classified into different types. The first case is simply the absence of any preferential orientation: All grains have a completely random orientation, and this is named random texture (see figure 2.1a).



(a) Non Aligned

(b) Uniaxial Alignment

(c) Biaxial alignment

Figure 2.1: Schematic representation of the alignment in polycrystalline thin films. (a) Non aligned; (b)Uniaxial alignment and (c) Biaxial alignment(Saraiva, 2012).

If all the grains have the alignment of one crystal plane in common, parallel to the substrate and no additional constraints on the orientation exist, the films are said to have uniaxial alignment (see figure 2.1b), exhibiting an out-of-plane orientation. This texture is called fiber texture. In the case that the grains have the alignment of one crystal plane in common, but not parallel to the substrate, an off-normal fiber texture exists and is called axiotaxy. Furthermore, when one crystallographic axis is parallel to the substrate normal and a second crystallographic axis which is parallel to the substrate is also aligned, there is in-plane and out-of-plane alignment (see figure 2.1c). A thin film which possesses preferential out-of-plane and in-plane alignment is said to be biaxially aligned. When the orientation of the grains in the film is uniquely defined with respect to the substrate, only one single orientation of the grains occurs.

For a substrate which is a single crystal, one uses the term epitaxy. The properties of polycrystalline materials are determined by the combination of the single crystal's properties, the boundary between crystallites and the orientation distribution of the crystallites within the material. Therefore, it is important to understand the crystalline structure and microstructure of the thin films (Saraiva, 2012).

2.2 Semiconductor

A semiconductor is a material which has [electrical conductivity](#) to a degree between that of a conductor (such as copper) and that of an [insulator](#) (such as glass). Size of band gap determines whether a material is a conductor (band gap 0eV), semiconductor (bandgap

<4 eV) or insulator (bandgap>4eV) (Bremner, 2009). Semiconductors are assumed to have bandgaps from 0 ~ 4eV and insulators > 4eV (Cohen and Chelikowsky, 2012).

. Semiconductors are the foundation of modern [electronics](#) including [transistors](#), [solar cells](#), [light-emitting diodes](#) (LEDs), [quantum dots](#) and digital and analog [integrated circuits](#). A semiconductor may have a number of unique properties, one of which is the ability to change conductivity by the addition of impurities ("[doping](#)") or by interaction with another phenomenon such as an [electric field](#) or [light](#). This ability makes a semiconductor very useful for constructing a device that can amplify, switch, or convert an energy input, (Wikipedia, 2014).

Semiconductors are mainly classified into two categories: Intrinsic and Extrinsic. An intrinsic semiconductor material is chemically very pure and possesses poor conductivity. It has equal numbers of negative carriers (electrons) and positive carriers (holes). An extrinsic semiconductor is an improved intrinsic semiconductor with small amount of impurities added by a process known as doping which alters the electrical properties of the semiconductor and improves its conductivity. Introducing impurities into the semiconductor materials (doping process) can control their conductivity. Doping process produces two groups of semiconductors: The negative charge conductor (n-type) and the positive charge conductor (p-type). Semiconductors are available as either elements or compounds. Silicon and Germanium are the most common elemental semiconductors. Compound Semiconductors include InSb, InAs, GaP, GaSb, GaAs, SiC, GaN. Si and Ge both have a crystalline structure called the diamond lattice. That is, each

atom has its four nearest neighbours at the corners of a regular tetrahedron with the atom itself being at the center. In addition to the pure element semiconductors, many alloys and compounds are semiconductors. The advantage of compound semiconductor is that they provide the device engineer with a wide range of energy gaps and mobilities, so that materials are available with properties that meet specific requirements. Some of these semiconductors are therefore called wide bandgap semiconductors, (Scribd, 2013).

2.3 Band gap

Band gap is the difference in energy between the lowest points of the conduction band (conduction band edge) and the highest point of the valence band (valence band edge), (Kittel, 2005). Band gap is the most important parameter in the characterization of materials since it determines the optical (Xin-Zheng and Jian-Bai, 2002), electrical (Benramache *et al.*, 2014) and electronic (Detlef 2014) properties of the material.

A semiconductor for which the conduction band lowest valley occurs at the same k value as the valence band maximum is called direct transition semiconductor while that in which the conduction band lowest valley occurs at a value of k different from the valence band maximum is called indirect gap semiconductor (Animalu, 1977), as illustrated in figure 2.2 .

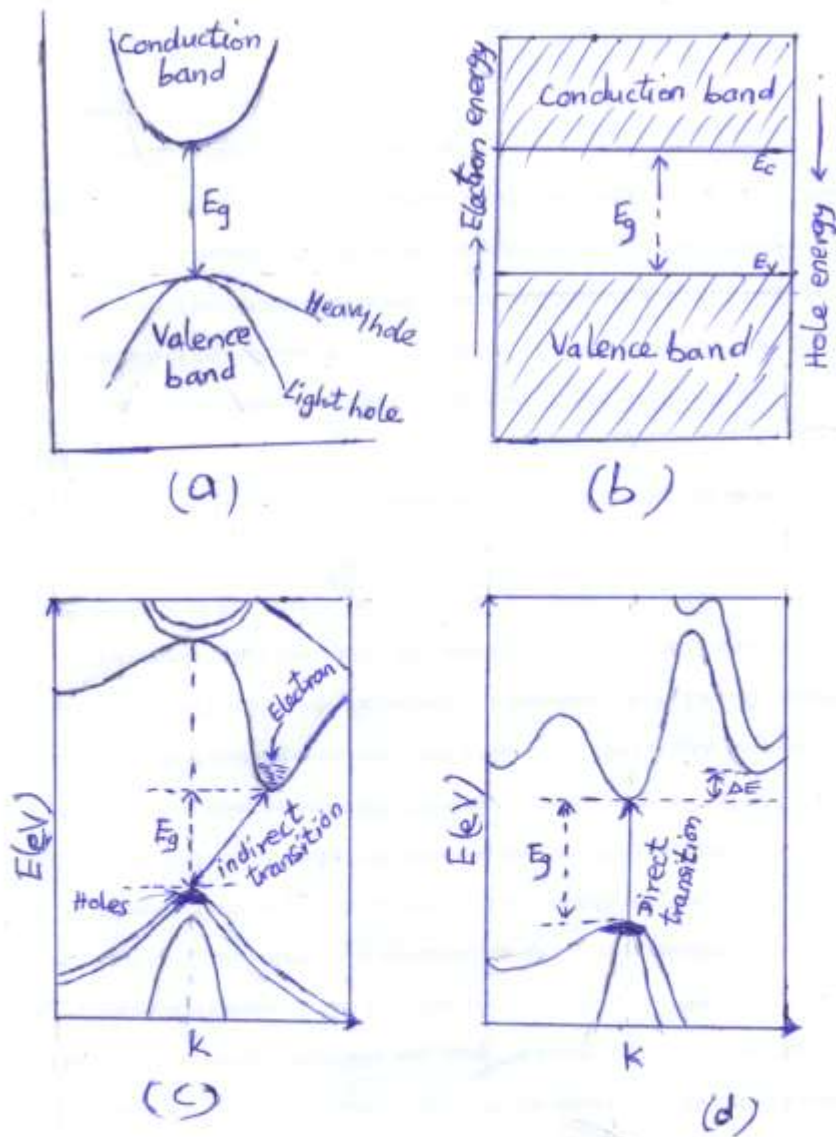


Figure : 2.2 (a) Simple form of band structure (b) Simplified form of band structure
 (c) Indirect transition (indirect bandgap) (d) Direct transition (direct bandgap),
 (Chopra and Das , 1983)

When electrons and holes recombine radiatively, an optical transition occurs between the crystal orbitals at the bottom of the conduction band and at the top of the valence band. For this transition to be allowed, conservation of momentum as well as energy needs to be satisfied. Since part of light normally of interest to us, infrared, ultraviolet or visible, has a very long wavelength compared to the unit cell length of the solids, its momentum, K_{hv} can be neglected. Hence, for an allowed transition, it is essential to satisfy $\Delta K = K_{electron} - K_{hole} = K_{hv} \approx 0$. In other words, radiative recombination of electrons and holes is forbidden in semiconductors with an indirect band gap. For solid with a direct band gap, light emission may be allowed, (Reynolds and Collins, 1981; In Seo and Hoffman, 1999). Light absorption and emission in a semiconductor is known to be heavily dependent on the detailed band structure of the semiconductor. Direct bandgap semiconductors, i.e semiconductors for which the minimum of the conduction band occurs at the same wave vector, k , as the maximum of the valence band, have a stronger absorption of light as characterized by a larger absorption coefficient. They are also the favored semiconductors when fabricating light emitting devices. Indirect bandgap semiconductors, i.e. semiconductors for which the minimum of the conduction band does not occur at the same wave vector as the maximum of the valence band, are known to have a smaller absorption coefficient and are rarely used in light emitting devices. The direct bandgap semiconductor, has a vertically aligned conduction and valence band, Absorption of a photon is obtained if an empty state in the conduction band is available for which the energy and momentum equals that of an electron in the

valence band plus that of the incident photon. Photons have little momentum relative of their energy since they travel at the speed of light. The electron therefore makes an almost vertical transition on the $E-k$ diagram. For an indirect bandgap semiconductor, the conduction band is not vertically aligned to the valence band.. Therefore a simply interaction of an incident photon with an electron in the valence band will not provide the correct energy and momentum corresponding to that of an empty state in the conduction band. As a result absorption of light requires the help of another particle, namely a phonon. Since a phonon, i.e a particle associated with lattice vibrations, has a relatively low velocity close to the speed of sound in the material, it has a small energy and large momentum compared to that of a photon. Conservation of both energy and momentum can therefore be obtained in the absorption process if a phonon is created or an existing phonon participates. The minimum photon energy that can be absorbed is slightly below the bandgap energy in the case of phonon absorption and has to be slightly above the bandgap energy in the case of phonon emission. Since the absorption process in an indirect bandgap semiconductor involves a phonon in addition to the electron and photon, the probability of having an interaction take place involving all three particles will be lower than a simple electron-photon interaction in a direct bandgap semiconductor. As a result one finds that absorption is much stronger in a direct bandgap material. Similarly, in the case of light emission, a direct bandgap material is also more likely to emit a photon than an indirect bandgap material. While indirect bandgap materials are occasionally used for some LEDs, they result in a low conversion

efficiency. Direct bandgap materials are used exclusively for semiconductor laser diodes,(Zeghbrouck, 2011). Absorption coefficient for direct transition is defined mathematically as;

$$\alpha \propto (h\nu - E_g)^n \quad (2.1)$$

Where $n = 1/2$ for allowed direct transition, $n = 3/2$ for forbidden direct transition, $h\nu$ is photon energy and E_g is the bandgap. In the case of amorphous films, the relation could also be expressed in the form (Harbeke, 1972 ; Moss,1961):

$$(\alpha h\nu) \propto (h\nu - E_g)^n \quad (2.2)$$

For direct bandgap, absorption coefficient is related with the formular(Cemre, 2013)

$$\alpha = A(h\nu - E_g)^{\frac{1}{2}} \quad (2.3)$$

The following relational expression for obtaining bandgap holds.

$$(\alpha h\nu)^n = A(h\nu - E_g) \quad (2.4)$$

Where h is Planck's constant, ν is frequency of vibration, α is absorption coefficient, E_g is band gap, A is proportional constant .The value of the exponent n denotes the nature of the sample transition.

For direct allowed transition, $n = 1/2$, For direct forbidden transition , $n = 3/2$

For indirect allowed transition, $n = 2$, For indirect forbidden transition , $n = 3$

When the graph of $\alpha^{\frac{1}{n}}$ or $(\alpha h\nu)^n$ as the case may be, is plotted against $h\nu$, the value associated with the point of intersection of the line tangent to the plotted curve inflection point with the horizontal axis ($h\nu$ axis) becomes the band gap (E_g) value (Tauc, 1972;

In Shimadzu, A428). In thin films the particle size of crystallites is of the order of film thickness and proportional to thickness of films. Since grain size influences the energy level of electrons, the band gap will be dependent on thickness of films. Since in thin films, the average grain size is proportional to thickness of films, it is expected that the band gap of thin semiconducting films will increase quadratically if charges are accumulated at grain boundaries. The decrease in the band gap with the increase in film thickness in our study indicates there is no charge accumulation at grain boundaries in silver telluride thin films (Pandiarman *et al.*, 2011). Increase in grain size has a decreasing effect on bandgap (Ramana *et al.*, 2003).

2.4 Doping

In [semiconductor](#) production, doping intentionally introduces impurities into an extremely pure (also referred to as [intrinsic](#)) semiconductor for the purpose of modulating its electrical properties. The impurities are dependent upon the type of semiconductor. Lightly and moderately doped semiconductors are referred to as [extrinsic](#). A semiconductor doped to such high levels that it acts more like a [conductor](#) than a semiconductor is referred to as [degenerate](#). Doping a semiconductor crystal introduces allowed energy states within the band gap but very close to the energy band that corresponds to the dopant type. In other words, donor impurities create states near the conduction band while acceptors create states near the valence band. The gap between these energy states and the nearest energy band is usually referred to as dopant-

site bonding energy or E_B and is relatively small. For example, the E_B for [boron](#) in silicon bulk is 0.045 eV compared with silicon's band gap of about 1.12 eV. Because E_B is so small, it takes little energy to ionize the dopant atoms and create free carriers in the conduction or valence bands. Usually the thermal energy available at room temperature is sufficient to ionize most of the dopants.

Dopants also have the important effect of shifting the energy bands relative to the [Fermi level](#). The energy band that corresponds with the dopant with the greatest concentration ends up closer to the Fermi level. Since the Fermi level must remain constant in a system in [thermodynamic equilibrium](#), stacking layers of materials with different properties leads to many useful electrical properties if the interfaces can be made clean enough. For example, the [p-n junction](#)'s properties are due to the energy [band bending](#) that happens as a result of the necessity to line up the bands in contacting regions of p-type and n-type material, (Wikipedia, 2013).

The sensitive dependence of a semiconductor's electronic, optical, and magnetic properties on dopants has provided an extensive range of tunable phenomena to explore and apply to devices. Recently it has become possible to move past the tunable properties of an ensemble of dopants and to identify the effects of a solitary dopant on commercial device performance as well as locally on the fundamental properties of a semiconductor. New applications have become available that require the discrete character of a single dopant such as single-spin devices in the area of quantum information or single-dopant transistors. Dramatic advances in the past decade towards observing, controllably

creating and manipulating single dopants as well as their application in novel devices have allowed opening the new field of solotronics (solitary dopant optoelectronics),(Koeraad and Flatte,2011).

For the [Group IV](#) semiconductors such as [diamond](#), [silicon](#), [germanium](#), [silicon carbide](#), and [silicon germanium](#), the most common dopants are [acceptors](#) from [Group III](#) or [donors](#) from [Group V](#) elements. [Boron](#), [arsenic](#), [phosphorus](#), and occasionally [gallium](#) are used to dope silicon. Boron is the [p-type dopant](#) of choice for silicon integrated circuit production because it diffuses at a rate that makes junction depths easily controllable. Phosphorus is typically used for bulk-doping of silicon wafers, while arsenic is used to diffuse junctions, because it diffuses more slowly than phosphorus and is thus more controllable.

By doping pure silicon with [Group V](#) elements such as phosphorus, extra [valence electrons](#) are added that become unbonded from individual atoms and allow the compound to be an electrically conductive [n-type semiconductor](#). Doping with [Group III](#) elements, which are missing in the fourth valence electron creates "broken bonds" (holes) in the silicon lattice that are free to move. The result is an electrically conductive [p-type semiconductor](#). In this context, a [Group V](#) element is said to behave as an electron donor and a [group III](#) element as an acceptor. This is a key concept in the physics of a [diode](#) (Wikipedia, 2013).

Very heavily doped semiconductor behaves more like a good conductor (metal) and thus exhibits more linear positive thermal coefficient. Such effect is used for instance in

[sensistors](#)(Dharma *et al.*, 2008; In Wikipedia, 2013). Lower dosage of doping is used in other types (NTC or PTC) [thermistors](#) (Wikipedia, 2013).

A one dimensional doping profile in a semiconductor can be considered to be δ -function like if the thickness of the doped layer is smaller as compared to other relevant length scales. Doping distribution whose width is narrower than the electron de Broglie wavelength is δ -function like. The δ -doping technique represents the ultimate limit for scaling of doping profiles. Such scaling of the dimensions of a semiconductor structure is of importance for semiconductor devices. As the spatial lateral and vertical dimensions of devices shrink, the switching speed and the power consumption of the device decrease, (Schubert, 1990). Over the last few years and in pace with the continuous reduction of the spatial dimensions of semiconductor hereostructures and devices, the size of dopant distributions has been decreased dramatically. One of the more promising doping techniques at the atomic level is clearly delta (δ) doping where the dopants are confined to one or a few atomic monolayers, (Proetto, 1996).

2.4.1 Cationic doping

The doping of a cation to metal oxide is known as cationic doping; e.g. Al, V, Cr, Mn, Fe, Ni (Borgarello *et al.*,1982; In Arshid *et al.*, 2012) , Co, (Wang *et al.*,2008; In Arshid *et al.*, 2012) are used as cationic dopant(s) to ZnO and/or TiO .

2.4.2 Anionic doping:

The doping of an anion to metal oxide is known as anionic doping; e.g. N, C, and S (Kerr *et al.*, 2007; In Arshid *et al.*, 2012) are used as anionic dopant(s) to ZnO/TiO₂. Each type of dopant has a unique impact on crystal lattice of metal oxide. For example, cationic doping leads to localised d-states in the band gap of TiO₂ which usually act as recombination centres for photo excited electrons and holes leading to lower photocatalytic activity (Choi *et al.*, 1994; In Arshid *et al.*, 2012). It might also unfavourably shift the conduction band below the redox potential of adsorbates, rendering the material inactive for photocatalysis. In contrast, anionic doping results in p-states near the valence band similar to other deep donor levels in the semiconductor (Sato, 1986; In Arshid *et al.*, 2012).

2.4.3 Impact of dopant on the semiconductors

It is of great significance to develop a material that can absorb both UV irradiation and visible light to widen the range of a photocatalyst. In almost all photocatalytic materials, the band gap of the semiconductor metal oxide plays a pivotal role in triggering the photoreaction after UV-induced electron-hole pair (Chang *et al.*, 2000; In Arshid *et al.*, 2012). In undoped TiO₂ and ZnO materials, the energy associated with visible light is not enough to initiate the photoreaction. Many studies have been cited showing that doping of a metal or transition element can cause a hyper-chromic shift in the optical absorption of semiconductor metal oxide (Collis *et al.*, 2006; In Arshid *et al.*, 2012). Usually doping

is done to create tail states within the band gap (Ullah and Dutta, 2008; In Arshid *et al.*, 2012), to increase surface defects (Collis *et al.*, 2006; In Arshid *et al.*, 2012) which ultimately increase the surface area (a mandatory aspect if there is to be a significant increase in photocatalytic activity); and/or to alter the electrical properties (Vanheusden *et al.*, 1995; In Arshid *et al.*, 2012), of the semiconductor metal oxide (such ZnO and TiO₂). The doped metal or transition element causes the following changes in the electrical structure : Incorporation of localised dopant levels near the valence band and the conduction band, band gap narrowing resulting from the broadening of the valence band, localised dopant levels and electronic changes to the conduction band, electronic transition from localised levels near the valence band to their corresponding excited states (Serpone, 2006; In Arshid *et al.*, 2012). Another aspect of doping in semiconductor metal oxides is the thermal instability and its tendency towards charge-carrier recombination centers that could reduce the overall UV-induced electron and/or hole taken up by their respective accepting species (Qui and Burda, 2007; In Arshid *et al.*, 2012).

2.5 ABSORBANCE

Absorbance (also called optical density) is a quantitative expression of absorption of light by different materials (Perkampus, 1992) .

Absorbance is defined according to the formular (Tempus, 2012)

$$\text{Abs}(\lambda) = \text{Log} \frac{I_o(\lambda)}{I(\lambda)} = -\text{Log} T(\lambda) \quad (2.5)$$

Where T is transmittance , I_o and I are incident and transmitted radiations respecively.

2.5.1 Absorption coefficient as a function of the energy of the impinging light.

The absorption coefficient α , is a property of a material which defines the amount of light absorbed by it. The inverse of the absorption coefficient, α^{-1} , is the average distance traveled by a photon before it gets absorbed.

Photon energy,

$$E = \frac{hc}{\lambda} \quad (2.6)$$

where E is photon energy, h is Planck's constant, c is speed of light and λ is wavelength (Katarzyna, 2014).

The absorption coefficient determines how far into a material, light of a particular wavelength can penetrate before it is absorbed. In a material with a low absorption coefficient, light is only poorly absorbed, and if the material is thin enough, it will appear transparent to that wavelength. The absorption coefficient depends on the material and also on the wavelength of light being absorbed. Semiconductor materials have a sharp edge in their absorption coefficient, since light which has energy below the band gap does not have sufficient energy to excite an electron into the conduction band from the valence band. Consequently this light is not absorbed. The absorption coefficient for several semiconductor materials is shown in figure 2.3

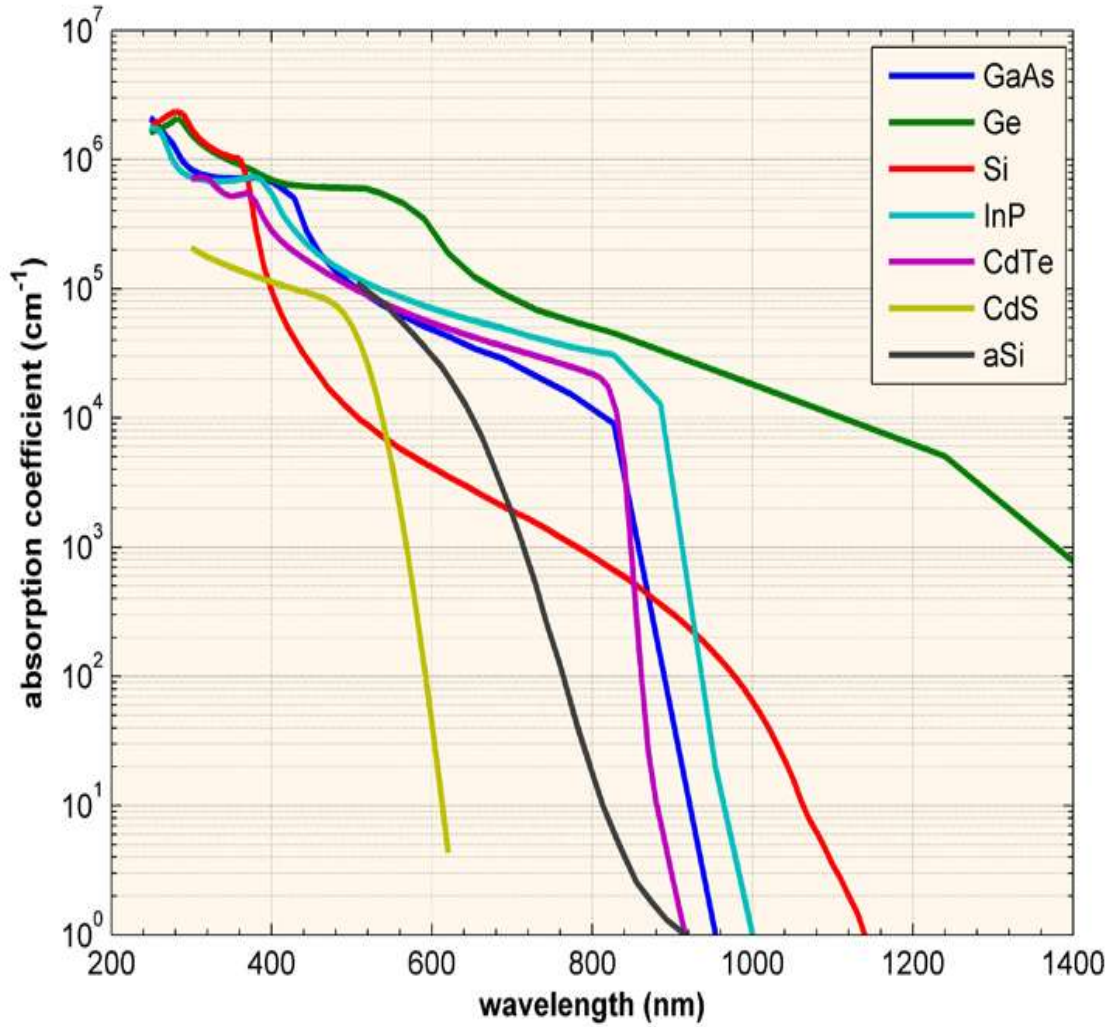


Figure 2.3: The absorption coefficient for several semiconductor materials (Honsberg and Bowden, 2014)

The absorption coefficient, α , in a variety of semiconductor materials at 300K as a function of the vacuum wavelength of light.

The graph of fig. 2.3 shows that even for those photons which have an energy above the band gap, the absorption coefficient is not constant, but still depends strongly on

wavelength. The probability of absorbing a photon depends on the likelihood of having a photon and an electron interact in such a way as to move from one energy band to another. For photons which have energy very close to that of the band gap, the absorption is relatively low since only those electrons directly at the valence band edge can interact with the photon to cause absorption. As the photon energy increases, not just the electrons already having energy close to that of the band gap, can interact with the photon. Therefore, a larger number of electrons can interact with the photon and result in the photon being absorbed.

The absorption coefficient, α , is related to the extinction coefficient, k , by the following formula:

$$\alpha = \frac{4\pi k}{\lambda} \quad (2.7)$$

where λ is the wavelength. If λ is in nm, multiply by 10^7 to get the absorption coefficient in the units of cm^{-1} (Honsberg and Bowden, 2014).

2.6 Optical conductivity (σ_o)

The optical response of a material is mainly studied in terms of the optical conductivity (σ), and is given by the relation,

$$\sigma_o = \frac{\alpha n c}{4\pi} \quad (2.8)$$

where c is the velocity of light, α is absorption coefficient and n is refractive index, (Pankove, 1975; In Sharma and Katyal, 2007) . It can be seen clearly that the optical

conductivity directly depends on the absorption coefficient and the refractive index of material (Sharma and Katyal, 2007).

2.7 Extinction Coefficient

The extinction coefficient is a measure of the fraction of light lost due to scattering and absorption per unit distance of the penetration medium. It can be estimated from the values of α and λ using the relation given by (Forouhi, and Bloomer, 1988; In Bakr *et al.*, 2011)

$$k = \frac{\alpha\lambda}{4\pi} \quad (2.9)$$

2.8 Reflectance

Reflectance is the fraction of incident power that is reflected from an interface, (Hieronymi, 2016).

If T is the Transmittance and A is the absorbance of the film then, the reflectance of the film can be found by using the relationship given by (Rubby and Suman, 2011)

$$\begin{aligned} A + T + R &= 1, \\ R &= 1 - (A + T) \end{aligned} \quad (2.10)$$

2.9 Transmittance

Transmittance is a fraction of incident light of a specific wavelength which passes via a sample, (AZO Optics, 2014). Transmission spectra of a sample is given by

$$T(\lambda) = \frac{I(\lambda)}{I_o(\lambda)} \quad (2.11)$$

Where $I_o(\lambda)$ is the intensity of light illuminating the sample , $I(\lambda)$ is the intensity of the light transmitted through the sample, (Tempus, 2012).

2.10 Refractive index (n)

Refractive index may also be defined in terms of velocity of light. The absolute or vacuum refractive index of any medium is the ratio of the velocity of light in vacuum to the velocity of light in that medium, (Gaur and Gupta, 2001).

$$n = \frac{c}{v} \quad (2.12)$$

Where n is absolute refractive index, c is velocity of light in vacuum and v is velocity of light in the medium. As the magnitude of refractive index of a medium is only very slightly altered when the incident light is in air instead of a vacuum, experiments to determine the absolute refractive index are usually performed with the light incident from air into the medium. Hence we can take $_{\text{air}}n_{\text{glass}}$ as equal to $_{\text{vacuum}}n_{\text{glass}}$ for most practical purposes, (Nelkon and Parker, 1982)

The refractive of the film can be calculated from reflectance formula,

$$R = \frac{(n-1)^2}{(n+1)^2} \quad (2.13)$$

Where, R is the normal reflectance , (Nadeem and Ahmed, 2000; In Rubby and Suman, 2011).

Using this relation in (2.19), refractive index n can be determined by the formula

$$n = \frac{1+\sqrt{R}}{1-\sqrt{R}} \quad (2.14)$$

2.11 Complex dielectric constant (ϵ_c)

The complex dielectric constant is a fundamental intrinsic property of the material. The real part of the dielectric constant shows how much it will slow down the speed of light in the material, whereas the imaginary part shows how a dielectric material absorbs energy from an electric field due to dipole motion. The knowledge of the real and the imaginary parts of the dielectric constant provides information about the loss factor which is the ratio of the imaginary part to the real part of the dielectric constant.

The real and the imaginary parts of the dielectric constant can be estimated using the relations, (Goswami, 2005; In Bakr *et al.*, 2011)

$$\epsilon_r = n^2 - k^2 \quad (2.15)$$

$$\epsilon_i = 2nk \quad (2.16)$$

The real and imaginary parts of dielectric constant are related by;

$$\epsilon_c = \epsilon_r + \epsilon_i = (n + ik)^2 \quad (2.17)$$

Where ϵ_r is the real part and is the normal dielectric constant , ϵ_i is the imaginary part and represents the the absorption associated with radiation by free carrier (Chopra,1969; In Nadeem and Ahmed ,2000).

2.12 Applications of nanofilm semiconductors

Nanofilm semiconductors are veritable materials for optoelectronic applications. Some examples are discussed as follows.

2.12.1 Solar-cell Covers

Solar-cell covers remove the incident solar energy that does not contribute to the electrical output of the cell and protect it from possible deterioration of its performance through the action of ultraviolet radiation. The blue solar-cell covers protect the cell only from the adverse effects of ultraviolet radiation (Reynard and Andrew, 1966) .

Photovoltaic solar cells, which convert a portion of the incident solar radiation into electrical energy, are an important, even critical, source of electrical power in space craft. However, the efficiency of the conversion process is reduced at elevated temperatures and is permanently degraded by ionizing radiation. To maintain high conversion efficiency, solar cells on space craft are cooled by radiation from transparent glass or glass-like covers, which also may shield the cells from ionizing radiation. Radiation that is not reflected by a solar cell or its cover is absorbed and converted into both electrical power and heat. The heat raises the cell temperature and lowers the efficiency for conversion of absorbed radiation into electrical power. Thus, absorbed radiation of wavelengths for which there is a high spectral response will cause a net increase in the electrical output of the cell, but absorbed radiation of wavelengths for which there is a low spectral response will cause a net decrease in electrical output.

Many solar cells are formed of silicon, which has a spectral response between 350 nanometers (nm) and 1100 nm. That is, only incident radiation with wavelengths between 350 and 1100 nm is converted to electrical current in the silicon cell. Another solar cell material, gallium arsenide (GaAs), has a spectral response between about 350 and 900 nm.

Protective solar cell covers are attached to solar cells with transparent adhesive or cement. Typically, the adhesives are degraded by ultraviolet (UV) radiation of wavelengths in the 300-350 nm region, especially the region between 300 and 320 nm.

To protect the cover cements from UV degradation, most solar cell covers are or include material which is opaque to radiation in this region. The opacity of solar cell covers may be provided by absorption in the glass or glass-like substrate or by the addition of a coating to the surface of the cover. For example, cerium-doped glasses, such as Pilkington's CMX glass or Corning's 0213 glass, absorb wavelengths shorter than about 350 nm and may be used for such covers. To further improve the electrical output of solar cells, optical coatings may be used to reflect spectral portions of the incident solar radiation which the cell does not convert to electricity. Without optical coatings, solar radiation outside the spectral response region (radiation with wavelengths longer or shorter than that of the spectral response region) may be absorbed by the cover or the cell causing the temperature of the cell to rise and the conversion efficiency to decrease. Multilayer optical coatings are commonly used on covers for silicon solar cells to reflect the ultraviolet wavelengths between 300 and 350 nm.

Applied to solar cell covers, the Thelen coatings reflect an ultraviolet band with wavelengths shorter than about 400 nm and an infrared band with wavelengths longer than about 1100 nm. The short-and long-wavelengths limits of the transmission band, i.e. 400 and 1100 nm, are fixed by the indices of the thin film materials used in Thelen's design

In another aspect, our invention is embodied in a solar-cell cover which reflects infrared and blue or ultraviolet radiation, or infrared radiation. Combined with solar cells, the new cover provides increased electrical output, presently of several percent compared to previous cover and cell combinations, by reducing the cell operating temperature. The new cover reflects portions of solar radiation with wavelengths that are shorter than and longer than the wavelengths which are effectively converted to electrical energy by state-of-the-art solar cells, (Beauchamp and Tuttle-Hart, 1995).

2.12.2 Quantum dot

Quantum dot is a [nanocrystal](#) made of [semiconductor](#) materials that are small enough to exhibit quantum mechanical properties. Specifically, its [excitons](#) are [confined](#) in all three [spatial dimensions](#). The electronic properties of these materials are intermediate between those of bulk semiconductors and of discrete [molecules](#), (Brus, 2007; In Wikipedia, 2014). Researchers have studied applications for quantum dots in [transistors](#), [solar cells](#), [LEDs](#), and [diode lasers](#). They have also investigated quantum dots as [agents](#) for [medical imaging](#) and as possible [qubits](#) in [quantum computing](#). Electronic characteristics of a

quantum dot are closely related to its size and shape. For example, the [band gap](#) in a quantum dot which determines the frequency range of emitted light is inversely related to its size. In fluorescent dye applications the frequency of emitted light increases as the size of the quantum dot decreases. Consequently, the color of emitted light shifts from red to blue when the size of the quantum dot is made smaller. This allows the excitation and emission of quantum dots to be highly tunable. Since the size of a quantum dot may be set when it is made, its conductive properties may be carefully controlled. Quantum dot assemblies consisting of many different sizes, such as [gradient multi-layer nanofilms](#), can be made to exhibit a range of desirable emission properties,(Wikipedia, 2014). An immediate optical feature of colloidal quantum dots is their color. While the material which makes up a quantum dot defines its intrinsic energy signature, the nanocrystal's quantum confined size is more significant at energies near the [band gap](#). Thus quantum dots of the same material, but with different sizes, can emit light of different colors. The physical reason is the [quantum confinement](#) effect. The larger the dot the [redder](#) (lower energy) its [fluorescence spectrum](#). Conversely, smaller dots emit [bluer](#) (higher energy) light. The coloration is directly related to the energy levels of the quantum dot. Quantitatively speaking, the [bandgap energy](#) that determines the energy (and hence color) of the fluorescent light is inversely proportional to the size of the quantum dot. Larger quantum dots have more energy levels which are also more closely spaced. This allows the quantum dot to absorb photons containing less energy, i.e., those closer to the red end of the spectrum. Recent articles in [Nanotechnology](#) and in other journals

have begun to suggest that the shape of the quantum dot may be a factor in the coloration as well, but as yet not enough information is available. It was shown, (VanDriel, 2005; In Wikipedia, 2014)) that the lifetime of fluorescence is determined by the size of the quantum dot. Larger dots have more closely spaced energy levels in which the electron-hole pair can be trapped. Therefore, electron-hole pairs in larger dots live longer causing larger dots to show a longer lifetime. As with any crystalline semiconductor, a quantum dot's electronic [wave functions](#) extends over the [crystal lattice](#). Similar to a molecule, a quantum dot has both a [quantized energy spectrum](#) and a quantized [density of electronic states](#) near the edge of the band gap.

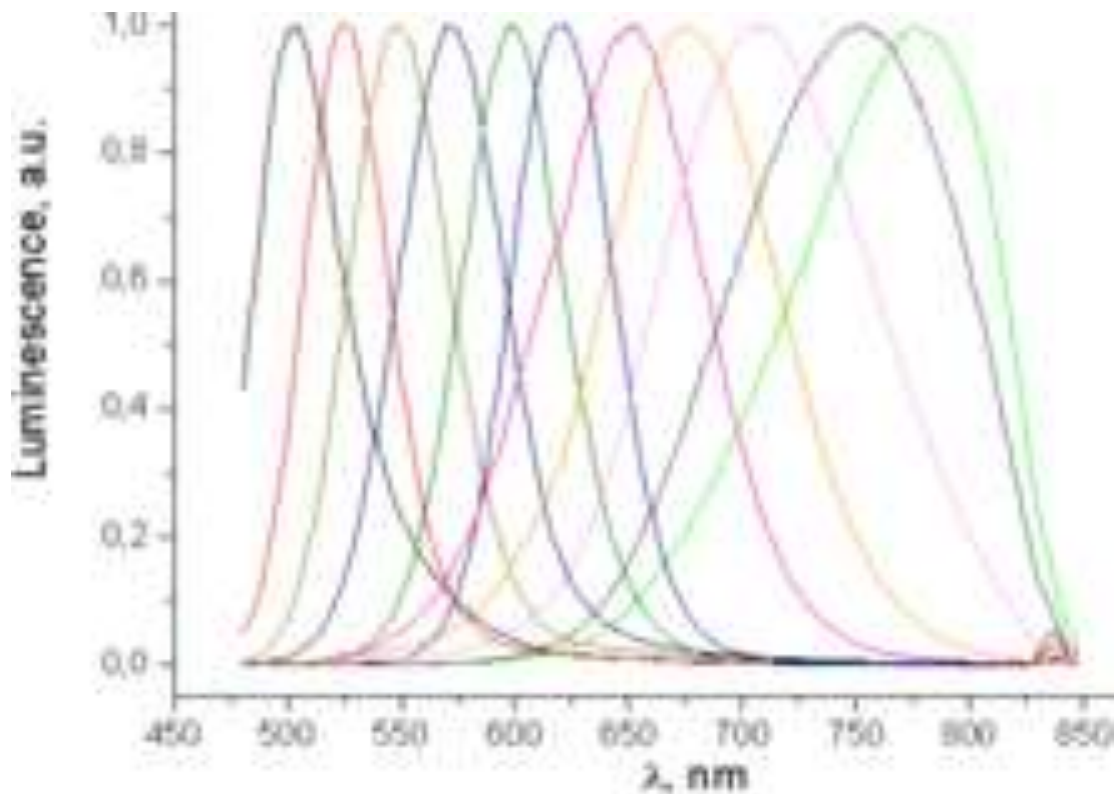


Figure 2.4: Fluorescence spectra of CdTe quantum dots of various size(VanDriel, 2005)

Fluorescence spectra of CdTe quantum dots of various sizes is shown in fig. 2.4. Different sized quantum dots emit different color light due to quantum confinement (VanDriel, 2005).

Quantum dots are particularly significant for optical applications due to their high [extinction coefficient](#), (Leatherdale *et al.*, 2002; In Wikipedia, 2014). In electronic applications they have been proven to operate like a [single electron transistor](#) and show the [Coulomb blockade](#) effect. Quantum dots have also been suggested as implementations of [qubits](#) for [quantum information processing](#).

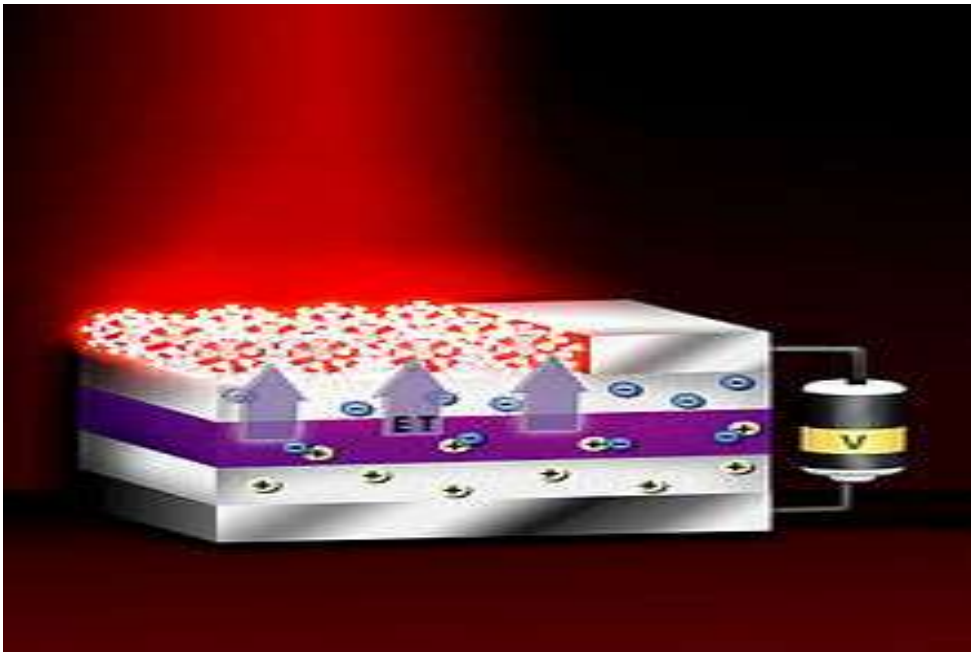


Figure 2.5: Production of visible light through energy transfer from thin layers of quantum wells to crystals above the layers, (Achermann *et al.*, 2004; In Wikipedia, 2014).

Researchers at [Los Alamos National Laboratory](#) have developed a device that efficiently produces [visible light](#), through energy transfer from thin layers of quantum wells to crystals above the layers as shown in fig. 2.5, (Achermann *et al.*, 2004; In Wikipedia,

2014). Being [zero-dimensional](#), quantum dots have a sharper [density of states](#) than higher-dimensional structures. As a result, they have superior transport and optical properties, and are being researched for use in [diode lasers](#), amplifiers, and biological sensors. Quantum dots may be excited within a locally enhanced electromagnetic field produced by gold nanoparticles, which can then be observed from the surface [plasmon resonance](#) in the photoluminescent excitation spectrum of (CdSe)ZnS nanocrystals. High-quality quantum dots are well suited for optical encoding and multiplexing applications due to their broad excitation profiles and narrow/symmetric emission spectra. The new generations of quantum dots have far-reaching potential for the study of intracellular processes at the single-molecule level, high-resolution cellular imaging, long-term in vivo observation of cell trafficking, tumor targeting, and diagnostics

1 Computing

Quantum dot technology is one of the most promising candidates for use in solid-state [quantum computation](#). By applying small voltages to the leads, the flow of electrons through the quantum dot can be controlled and thereby precise measurements of the spin and other properties therein can be made. With several [entangled](#) quantum dots, or [qubits](#), plus a way of performing operations, quantum calculations and the [computers](#) that would perform them might be possible,(Wikipedia, 2014).

2 Biology

In modern biological analysis, various kinds of [organic dyes](#) are used. However, with each passing year, more flexibility is being required of these dyes, and the traditional dyes are often unable to meet the expectations (Walling and Novak, 2009; In Wikipedia, 2014). To this end, quantum dots have quickly filled in the role, being found to be superior to traditional organic dyes on several counts; One of the most immediately obvious being brightness [owing to the high extinction co-efficient combined with a comparable quantum yield to fluorescent dyes (Michalet *et al.*, 2005; In Wikipedia, 2014), as well as their stability (allowing much less [photobleaching](#)). It has been estimated that quantum dots are 20 times brighter and 100 times more stable than traditional fluorescent reporters, (Walling and Novak, 2009; In Wikipedia, 2014. For single-particle tracking, the irregular [blinking of quantum dots](#) is a minor drawback.

The usage of quantum dots for highly sensitive cellular imaging has seen major advances over the past decade,(Spie, 2014; In Wikipedia, 2014). The improved photostability of quantum dots, for example, allows the acquisition of many consecutive focal-plane images that can be reconstructed into a high-resolution three-dimensional image (Tokumasu *et al.*, 2005; In Wikipedia, 2014). Another application that takes advantage of the extraordinary photostability of quantum dot probes is the real-time tracking of molecules and cells over extended periods of time (Dahan *et al.*, 2003; In Wikipedia, 2014). Antibodies, streptavidin (Howarth *et al.*, 2008; In Wikipedia, 2014), peptides (Akerman *et al.*, 2002; In Wikipedia, 2014), DNA (Farlow *et al.*, 2013; In Wikipedia,

2014), nucleic acid [aptamers](#) (Dwarakanath *et al.*, 2004; In Wikipedia, 2014), or small-molecule ligands, (Zherebetsky *et al.*, 2014; In Wikipedia, 2014) can be used to target quantum dots to specific proteins on cells. Researchers were able to observe quantum dots in lymph nodes of mice for more than 4 months (Ballou *et al.*, 2004; In Wikipedia, 2014).

Semiconductor quantum dots have also been employed for [in vitro](#) imaging of pre-labeled cells. The ability to image single-cell migration in real time is expected to be important to several research areas such as [embryogenesis](#), [cancer metastasis](#), [stem cell](#) therapeutics, and [lymphocyte immunology](#). Scientists have proven that quantum dots are dramatically better than existing methods for delivering a gene-silencing tool known as [siRNA](#), into cells (Newswise, 2008; In Wikipedia, 2014).

First attempts have been made to use quantum dots for tumor targeting under [in vivo](#) conditions. There exist two basic targeting schemes: Active targeting and passive targeting. In the case of active targeting, quantum dots are functionalized with tumor-specific binding sites to selectively bind to tumor cells. Passive targeting uses the enhanced permeation and retention of tumor cells for the delivery of quantum dot probes. Fast-growing tumor cells typically have more permeable membranes than healthy cells, allowing the leakage of small nanoparticles into the cell body. Moreover, tumor cells lack an effective lymphatic drainage system, which leads to subsequent nanoparticle-accumulation.

One of the remaining issues with quantum dot probes is their potential in vivo toxicity. For example, CdSe nanocrystals are highly toxic to cultured cells under UV illumination. The energy of UV irradiation is close to that of the [covalent](#) chemical bond energy of CdSe nanocrystals. As a result, semiconductor particles can be dissolved in a process known as [photolysis](#) to release toxic cadmium ions into the culture medium. However in the absence of UV irradiation, quantum dots with a stable polymer coating have been found to be essentially nontoxic (Ballou *et al.*, 2004; In Wikipedia, 2014). [Hydrogel encapsulation of quantum dots](#) allows for quantum dots to be introduced into a stable aqueous solution reducing the possibility of cadmium leakage. Then again, only little is known about the excretion process of quantum dots from living organisms (Choi *et al.*, 2007; In Wikipedia, 2014). These and other questions must be carefully examined before quantum dot applications in tumor or [vascular](#) imaging can be approved for human clinical use.

Another potential cutting-edge application of quantum dots is being researched with quantum dots acting as the inorganic [fluorophore](#) for intra-operative detection of tumors using [fluorescence spectroscopy](#).

3 Photovoltaic devices (Quantum dot solar cell)

Quantum dots may be able to increase the efficiency and reduce the cost of today's typical silicon [photovoltaic cells](#). Experimental proof from 2004, (Schaller and Klimov, 2004; In Wikipedia, 2014) Quantum dots of lead selenide can produce more than one

exciton from one high energy photon via the process of carrier multiplication or [multiple exciton generation](#) (MEG). This compares favorably to today's photovoltaic cells which can only manage one exciton per high-energy photon, with high kinetic energy carriers losing their energy as heat. Quantum dot photovoltaics would theoretically be cheaper to manufacture, as they can be made using simple chemical reactions.

4 Light emitting devices

There are several inquiries into using quantum dots as [light-emitting diodes](#) to make displays and other light sources such as "QD-LED" displays, and "QD-WLED" (White LED). In June 2006, QD Vision announced technical success in making a proof-of-concept [quantum dot display](#) and show a bright emission in the visible and near infra-red region of the spectrum. Quantum dots are valued for displays, because they emit light in very specific [gaussian distributions](#). This can result in a display that more accurately renders the colors that the human eye can perceive. Quantum dots also require very little power since they are not color filtered. Additionally, since the discovery of "white-light emitting" QD, general solid-state lighting applications appear closer than ever(Vanderbilt.edu, 2013; In Wikipedia, 2014). A color liquid crystal display (LCD) for example, it is usually [backlit](#) by [fluorescent lamps](#) (CCFLs) or [conventional white LEDs](#) that are color filtered to produce red, green, and blue pixels. A better solution is using a conventional blue-emitting LED as light source and converting part of the emitted light into *pure* green and red light by the appropriate quantum dots placed in front of the blue

LED. This type of white light as backlight of an LCD panel allows for the best color gamut at lower cost than a RGB LED combination using three LEDs.

Quantum dot displays that intrinsically produce [monochromatic](#) light can be more efficient, since more of the light produced reaches the eye. QD-LEDs can be fabricated on a silicon substrate, which allows integration of light sources onto silicon-based [integrated circuits](#) or [microelectromechanical systems](#). A QD-LED integrated at a scanning microscopy tip was used to demonstrate fluorescence near-field scanning optical microscopy ([NSOM](#)) imaging (Hoshino *et al.*, 2012; In Wikipedia, 2014).

5 Photodetector devices

Quantum dot photodetectors (QDPs) can be fabricated either via solution-processing (Konstantatos and Sargent, 2009; In Wikipedia, 2014), or from conventional single-crystalline semiconductors (Vaillancourt *et al.*, 2011; In Wikipedia, 2014). Conventional single-crystalline semiconductor QDPs are precluded from integration with flexible organic electronics due to the incompatibility of their growth conditions with the process windows required by organic semiconductors. On the other hand, solution-processed QDPs can be readily integrated with an almost infinite variety of substrates, and also post processed atop other integrated circuits. Such [colloidal](#) QDPs have potential applications in surveillance, machine vision, industrial inspection, [spectroscopy](#), and fluorescent biomedical imaging.

2.12.3 Photolithography

Generally, lithography is used to transfer a specific pattern onto a photosensitive surface. A photolithography method comprising: projecting photons through at least one patterned photomask to form a corresponding pattern on a wafer, at least in part coated with a photoresist layer including semiconductor nano-sized particles; causing some of the said nano-sized particles to absorb at least a portion of said patterned photons. Some of the said nano-sized particles upon absorption, transfer out at least one of an electron and/or a hole, thereby changing solubility of portions of said photoresist layer in part, in response to the said transferred out electrons and/or holes based on the pattern. Further processing of the photoresist layer with changed solubility forms a patterned structure on the wafer (Zhiyun *et al.*, 2011). This technology herein relates to photolithography, and more particularly to applications of semiconductor nano-sized particles in photolithography. It also relates more particularly to applications of semiconductor nano-sized particles as highly refractive media in immersion lithography, as anti-reflection coating, as pellicle, and as sensitizer in UV photoresists. Lithography can be applied to transfer a variety of patterns including, for example, painting, printing, and the likes. More recently, lithographic techniques have become widespread for use in "microfabrication"--a major (but non-limiting) example of which is the manufacture of integrated circuits such as computer chips. In a typical micro fabrication operation, lithography is used to define patterns for miniature electrical circuits. Lithography defines a pattern specifying the location of metal, insulators, doped regions, and other

features of a circuit printed on a silicon wafer or other substrate. The resulting circuit can perform any of a number of different functions. For example, an entire computer can be placed on a chip. A primary lithography system includes a wafer stepper, a photomask and photoresist. A wafer stepper generally consists of a ultraviolet (UV) light source, a photomask holder, an optical system for projecting and demagnifying the image of the mask onto a photoresist-coated wafer, and a stage to move the wafer. Conventional lithography also generally requires a photomask--a quartz substrate with chrome patterns on one surface. The chrome patterns form a perfect master of the pattern to be inscribed on one layer of a chip. Also it requires photoresist to receive the light pattern generated by the mask. Improvements in lithography have been mainly responsible for the explosive growth of computers in particular and the semiconductor industry in general. The major improvements in lithography are mainly as a result of decrease in the minimum feature size (improvement in resolution. This improvement allows for an increase in the number of transistors on a single chip (and in the speed at which these transistors can operate). For example, the computer circuitry that would have filled an entire room in 1960's technology can now be placed on a silicon "die" the size of a thumbnail. A device, the size of a wristwatch can contain more computing power than the largest computers of several decades ago (Zhiyun *et al.*, 2011).

2.12.4 Semiconductor nano-sized particles

Nano-sized particles are loosely defined as powders with small diameters for example

ranging from a few hundred nanometers or less down to a few angstroms. Since they have generally been the only focus of research in the last two decades, there is little standardization and they take many different names including quantum dot, quantum sphere, quantum crystallite, nano-crystal, micro-crystal, colloidal particle, nano-cluster, Q-particle or artificial atom. Due to their small size, they often possess dramatically different physical properties compared to their bulk counterparts. Nano-sized particles have a wide range of applications including metallurgy, chemical sensors, pharmaceuticals, painting, and cosmetics. As a result of the rapid development in synthesis methods in the last two decades, they have now entered into microelectronic and optical applications. Nano-sized particles with sizes less than 5 nm have been synthesized from a variety of semiconductors, examples include C, Si, Ge, CuCl, CuBr, CuI, AgCl, AgBr, AgI, Ag₂S, CaO, MgO, ZnO, ZnS, HgS, ZnSe, CdS, CdSe, CdTe, HgTe, PbS, BN, AN, GaN, GaP, GaAs, GaSb, InP, InAs, In_xGa_{1-x}As, SiC, Si_{1-x}Ge_x, Si₃N₄, ZrN, CaF₂, YF₃, Al₂O₃, SiO₂, TiO₂, Cu₂O, Zr₂O₃, SnO₂, YSi₂, GaInP₂, Cd₃P₂, Fe₂S, Cu₂S, CuIn₂S₂, MoS₂, In₂S₃, Bi₂S₃, CuIn₂Se₂, In₂Se₃, HgI₂, PbI₂, Lanthanide oxides, etc. They have revealed very interesting optical properties. Semiconductor materials have the so called bandgaps. The electron band below the bandgap is called valence band (VB) and the electron band above the bandgap is called conduction band (CB). The manifestation of a bandgap in optical absorption is that only photons with energy larger than the bandgap are absorbed. A photon with sufficient energy excites an electron from the top of valence band to the bottom of conduction band, leaving an

empty state, a hole, at the top of the valence band . There are several major advantages of using semiconductor nano-sized particles in photolithography. First, the bandgap of semiconductor nano-sized particles can be tailored by their size, (Zhiyun *et al.*, 2011). In a certain range the smaller the size, the larger the bandgap. The bandgap determines the working wavelength. Second, the refractive index can be very high near the bandgap. Actually some semiconductors have the highest refractive indices. For example wurzite TiO_2 has a refractive index of 2.4, and wurzite GaN has a refractive index about 2.6 near the bandgap. The refractive indices of common optical materials such as fused silica and quartz used in the UV lithography are around 1.5. This high refractive index is desirable for highly refractive medium immersion lithography and optical coating. Third, nano-sized particles can be easily coated onto optics or wafers in the form of a thin film. They are, therefore, very simple to handle and produce much less contamination. Because of the polycrystalline nature of nano-sized particle films, there is less concern about matching the thermal expansion coefficients between the coating and the optics. Applying nano-sized particles by coating provides least disturbance to the existing lithography system. Fourth, semiconductors nano-sized particles can reach sizes much smaller than the working wavelength. Currently, a large number of semiconductors can be fabricated into nano-sized particles smaller than 5 nm in diameter. Hence the scattering from the nanoparticles is negligible and size fluctuation of nano-sized particles does not affect the final scattered and transmitted light. Fifth, in a broad sense, semiconductors can possess bandgaps as high as 12 eV, corresponding to a wavelength

of 100 nm. For 157 nm lithography and beyond, few materials can withstand the radiation except certain semiconductors. Nano-sized particles offer a solution for the optics in these wavelengths. Lastly, many semiconductor nano-sized particles can be produced rather inexpensively. Therefore, the overall cost will likely be lower than conventional methods, (Zhiyun *et al.*, 2011) .

2.12.5 Elemental semiconductors

The important elemental semiconductors are group IV materials such as silicon (Si) and germanium (Ge). These group IV elemental materials all have diamond crystal structure, i.e., each atom is in a tetrahedral configuration with four nearest atoms and thus they are also referred to as tetrahedrally-bonded semiconductors. Another group IV elemental semiconductor having such a structure is α -Sn ($E_g = 0.08\text{eV}$), which is also referred to as gray Sn. Other elemental semiconductors having various structures differing from diamond structure include group III element boron, group V material, phosphorous and group VI materials such as sulphur (S), selenium (Se) and tellurium (Te). It should be emphasized that currently Si is the most important material used in electronic devices (e.g., integrated circuits). Some of the important advantages of Si over other semiconductors are (i) a relative ease of passivating the surface by oxidizing it in a controlled manner and forming a layer of stable native oxide that substantially reduces the surface recombination velocity. (ii) its hardness that allows large wafers to be handled safely (iii) its thermal stability up to 1100°C , that allows high temperature

processing, related to diffusion, oxidation, and annealing (iv) its relatively low cost. The basic limitations of Si are due to (i) the magnitude and type of its energy gap (i.e., the value of $E_g = 1.12\text{eV}$ and the fact that it is an indirect energy gap material which limit the optoelectronic applications of this material and (ii) the relatively lower carrier mobility (as compared to e.g., GaAs) . However, emerging materials based on Si nanostructures (e.g., Si nanocrystals, quantum wires and dots, and porous Si) and $\text{Si}_x\text{Ge}_{1-x}$ layers grown on Si substrate, appear to be promising materials in various applications. In nanostructures, quantum confinement of carriers leads to (i) increased electron-hole wave function overlap (and hence increased photon emission efficiency) and (ii) high energy shift(i.e., blue shift) of the emission peak (Yacobi, 2004).

2.12.6 Compound Semiconductors

Compound semiconductors, usually based on a combination of Group 111-V or 11-VI elements, have had a significant impact on our everyday lives. A wide variety of applications exist, including use in satellite TV receivers, optical fiber communications, CD-players, bar code readers and full-color electroluminescent advertising displays. Metalorganic chemical vapor deposition (MOCVD), which uses a volatile metalorganic compound to deposit solid semiconductor films, has become one of the preferred industrial techniques for the fabrication of sophisticated devices from 111-V and 11-VI materials, and the application of metalorganic chemistry has played a vital role (Jones and O'Brien, 1997).Compound semiconductors have been an integral part of everyday

life. Recent progress on their potential as sensing devices in biological and chemical environments, and high –efficiency power devices demonstrates their impact on energy and environment. Compound semiconductor based photovoltaic systems are emerging as an economical means of generating renewable energy through the use of concentrator technologies. However, while solid state lighting devices have shown energy saving and environmental benefits, much still needs to be done to realize their full potential (Shahepour-Sandvik *et al.*,(Eds.), 2009).

2.12.7 Sensors

Sensor is a device that detects or measures a physical quantity. Among the types of energy that can be sensed are those classed as radiant, mechanical, gravitational, electrical, thermal and magnetic. Sensors can be classed as active or passive. An active or self generating sensor is one that can generate a signal without the need for an external power supply, example, photovoltaic cells, thermocouples and piezoelectric devices. The more common passive sensors need an external source of energy, (Sinclair, 2001).

The purpose of a sensor is to respond to some kind of an input physical property(stimulus) and to convert it into an electrical signal which is compatible with electronic circuits. A sensor is a translator of a generally non electrical value into an electrical value. By electrical, it is meant a signal which can be channelled, amplified and modulated by electronic devices. The sensors output signal may be in the form of voltage, current or charge. These may be further described in terms of amplitude,

frequency, phase or digital code. Any sensor is an energy converter. No matter what you try to measure, you always deal with energy transfer from the object of measurement to the sensor, (Fraden, 2004)

2.12.8 Nanowires

Nanowires are hair-like, one-dimensional (1D) nanomaterials with diameters in the sub-one hundred nanometer scale and lengths ranging from several hundreds of nm to as high as a few cm. Owing to their nanoscale dimensions in the radial direction, they have size confinement effects that give them novel physical properties as compared to bulk materials. Their one-dimensional geometry on the nanometer scale provides an extremely high surface area with a nanoscale radius of curvature and great mechanical flexibility with near theoretical strength. These properties are advantageous in many chemical and mechanical applications. The geometry also provides anisotropic properties that should be interesting from the point of view of nanomaterials science and engineering. Their length, reaching as high as the cm scale, makes them easy to manipulate for device fabrication (Choi, 2012).

Nanowires are promising materials for advanced optoelectronics. In addition to the unique aspects of their physical, chemical, and mechanical properties, the size of these materials is comparable to visible light in wavelength from 400 to 650 nm.

This implies that nanowires can be used to handle light on a nanometer scale and thus can be used as building blocks for advanced optoelectronics. Indeed, novel methods of the manipulation of light with nanowires, including nanoscale Fabry–Perrot mode

stimulated emission, wave guiding of photons, random lasing action, highly efficient luminescence, and extremely sensitive photodetection, have recently been demonstrated. The concept of many advanced nanowire-based optoelectronic devices including light-emitting diodes (LEDs), lasers, optical sensors, photo diodes, and photovoltaic cells have also been demonstrated. The physical and chemical states of nanowires dominate their optical properties. The length and diameter of nanowires as well as their alignment, affect the emission and absorption properties. The composition, impurity, or doping level, defect concentration, crystal structure, growth direction, and nature of the facets are also critical to the emission and/or stimulated emission and absorption. It should be noted that these physical and chemical states are closely related to the growth of nanowires. Therefore, one must fully understand the growth behavior of nanowires and develop rational, reliable growth processes to exploit the potential of nanowires in optoelectronics (Choi, 2012).

2.12.9 Other Uses

Semiconductors are used in the production of [transistors](#), diodes, and [computer memory](#) devices and serve as the foundational component of every piece of modern day electronic equipment. This technology has completely changed the world in which we live by providing better, faster, and cheaper electronic devices. Semiconductor applications are widely used throughout the electronic, integrated circuit, and computer industries. Electronic equipment and various consumer products also depend upon different types of

semiconductors. Much of today's modern military equipment, research laboratory instrumentation, and manufacturing industries rely on semiconductors. Not all semiconductors are fit for use in computers. Computer semiconductors must be manufactured in a specific way to ensure that they have the correct properties. In 2011, two-thirds of semiconductor applications involve the manufacturing of [integrated circuits](#) which are used in electronic devices such as personal computers, netbooks, laptops, tablet computers, calculators and other devices. Continued improvement in the manufacturing process of semiconductors is the main reason that the prices of computers and other similar electronics continue to decrease.

Television sets and a host of other consumer electronic devices make up a large portion of different semiconductor applications. Every consumer electronic device, from a simple toaster that can sense when toast is too brown to the most technologically advanced home theater system, uses this technology. Without semiconductors, modern day electronic devices and many of the functions and features that people take for granted would not exist. For example, the computers and integrated circuits that are part of some home appliances, like microwave ovens, televisions sets, digital thermostats, and refrigerators rely on semiconductor applications (Kayo, 2014). Many different electronic devices depend on semiconductors that are used to make the integrated circuits and the computer chips necessary to perform various advanced functions like temperature control, digital recording, and signal reception.

Some other semiconductor applications include military equipment, weapons, laboratory equipment, and various electronic devices used in industrial control systems. For example, the electronic components and circuitry used to guide a missile to a specific target rely on the accurate functioning of semiconductors. Devices used in research to measure the presence of a single atom or molecule could not function without advanced semiconductor applications. The electronic devices that allow humans to interface with various types of industrial equipment are also heavily reliant on this technology. Electronic devices used in industrial control systems that take several thousand readings each second and are connected to a network of computers handling data at the speed of light would not be possible without semiconductor technology (Kayo, 2014).

2.13 Thinfilm/Nanofilm deposition techniques .

Deposition techniques fall into two categories depending on whether the process is primarily chemical or physical.

1. Depositions that happen because of a chemical reaction:

a. Chemical Vapor Deposition (CVD)

b. Electrodeposition

c. Epitaxy

d. Thermal oxidation, (MEMSnet, 2013)

e. Spray pyrolysis

f. [Chemical solution deposition](#) (CSD) or [Chemical bath deposition](#) (CBD)

g. Sol gel method

h. SILAR method(Gosavi, 2010)

These processes exploit the creation of solid materials directly from chemical reactions in gas and/or liquid compositions or with the substrate material. The solid material is usually not the only product formed by the reaction. By-products can include gases, liquids and even other solids.

2. Depositions that happen because of a physical reaction:

a. Physical Vapor Deposition (PVD)

b. Evaporation

c. Sputtering

d. Casting (MEMSnet, 2013)

e. Spin coating, (Cruz *et al.*,2012)

f. Pulsed laser deposition, (Rafael *et al.*, 2005)

Common for all these processes is that the material deposited is physically moved on to the substrate. In other words, there is no chemical reaction which forms the material on the substrate. This is not completely correct for casting processes, though it is more convenient to think of them that way , (MEMSnet, 2013).

2.13.1 Chemical Vapor Deposition (CVD)

In this process, the substrate is placed inside a reactor to which a number of gases are supplied. The fundamental principle of the process is that a chemical reaction takes place

between the source gases. The product of that reaction is a solid material which condenses on all surfaces inside the reactor.

The two most important CVD technologies in MEMS are the Low Pressure CVD (LPCVD) and Plasma Enhanced CVD (PECVD). The LPCVD process produces layers with excellent uniformity of thickness and material characteristics. The main problems with the process are the high deposition temperature (higher than 600°C) and the relatively slow deposition rate.

The PECVD process can operate at lower temperatures (down to 300° C), thanks to the extra energy supplied to the gas molecules by the plasma in the reactor. However, the quality of the films tends to be inferior to processes running at higher temperatures. Secondly, most PECVD deposition systems can only deposit the material on one side of the wafers, on 1 to 4 wafers at a time. LPCVD systems deposit films on both sides of at least 25 wafers at a time, (MEMSnet, 2013). CVD has a number of advantages as a method of depositing thinfilms. One of the primary advantages is that CVD films are generally quite conformal, ie, that the film thickness on the sidewalls of features is comparable to the thickness on the top. This means that films can be applied to elaborately shaped pieces including the insides and undersides of features and that high aspect ratio holes and other features can be completely filled. Another advantage is that in addition to the wide variety of materials that can be deposited, they can be deposited with very high purity. This results from the relative ease with which impurities are removed from gaseous precursors using distillation techniques. Other advantage includes

relatively high deposition rates and the fact that CVD often doesn't require as high a vacuum as PVD processes. However, CVD has a number of disadvantages, one of the primary disadvantages lies in the properties of the precursors. Ideally, the precursors need to be volatile at near room temperatures. This is non-trivial for a number of elements in the periodic table, although the use of metal organic precursors has eased this situation. CVD precursors can also be highly toxic, explosive or corrosive. The by products of CVD can also be hazardous. Another disadvantage is the fact that these films are usually deposited at elevated temperatures. This puts some restrictions on the kinds of substrates that can be coated. More importantly it leads to stresses in films deposited on materials with different thermal expansion coefficients which can cause mechanical instabilities in the deposited films, (Creighton and Ho, 2001). CVD processes are ideal to use when a thin film with good step coverage is desired. A variety of materials can be deposited with this technology. However, some of them are less popular with fabs because of hazardous by-products formed during processing. The quality of the material varies from process to process, however a good rule of thumb is that higher process temperature yields a material with higher quality and less defects, (MEMSnet, 2013).

Types includes;

CVD – Chemical Vapor Deposition

APCVD – Atmospheric Pressure Chemical Vapor Deposition

LPCVD – Low Pressure Chemical Vapor Deposition

PECVD – Plasma Enhanced Chemical Vapor Deposition

2.13.2 Electrodeposition

This process is also known as "electroplating" and is typically restricted to electrically conductive materials. There are basically two technologies for plating: Electroplating and Electroless plating. In the electroplating process the substrate is placed in a liquid solution (electrolyte). When an electrical potential is applied between a conducting area on the substrate and a counter electrode (usually platinum) in the liquid, a chemical redox process takes place resulting in the formation of a layer of material on the substrate and usually some gas generation at the counter electrode.

In the electroless plating process a more complex chemical solution is used, in which deposition happens spontaneously on any surface which forms a sufficiently high electrochemical potential with the solution. This process is desirable since it does not require any external electrical potential and contact to the substrate during processing. Unfortunately, it is also more difficult to control with regards to film thickness and uniformity. Electrodeposition process is well suited for making films of metals. The deposition is best controlled when used with an external electrical potential, however, it requires electrical contact to the substrate when immersed in the liquid bath. In any process, the surface of the substrate must have an electrically conducting coating before the deposition can be done (MEMSnet, 2013).

2.13.3 Epitaxy

This technology is quite similar to what happens in CVD processes, however, if the substrate is an ordered semiconductor crystal (i.e. silicon, gallium arsenide), it is possible for this process to continue building on the substrate with the same crystallographic orientation, with the substrate acting as a seed for the deposition. If an amorphous/polycrystalline substrate surface is used, the film will also be amorphous or polycrystalline.

There are several technologies for creating the conditions inside a reactor needed to support epitaxial growth, of which the most important is Vapor Phase Epitaxy (VPE). In this process, a number of gases are introduced in an induction heated reactor where only the substrate is heated. The temperature of the substrate typically must be at least 50% of the melting point of the material to be deposited. An advantage of epitaxy is the high growth rate of material, which allows the formation of films with considerable thickness (>100Å). Epitaxy is a widely used technology for producing silicon on insulator (SOI) substrates. The technology is primarily used for deposition of silicon.

The process can be used to form films of silicon with thicknesses of ~1µm to >100µm. Some processes require high temperature exposure of the substrate, whereas others do not require significant heating of the substrate. Some processes can even be used to perform selective deposition, depending on the surface of the substrate (MEMSnet,2013).

Molecular beam epitaxy is a technology used for the deposition of thin film compound semiconductors, metals or insulators that allows a precise control of compositional profiles by using a process far from the thermodynamic equilibrium. The term epitaxy originates from the Greek roots; epi and taxis which means to arrange upon. In other words, the epitaxy is the arrangement of one or more thermal particles atop a heated and ordered crystalline substrate to form a thin layer whose crystallinity matches that of the substrate even though the composition of the materials may differ. Again the term beam means that the evaporated elements (atoms, and/or molecules) do not interact with each other or with vacuum chamber gases until they impinge the substrate because of their long mean free paths which are involved in the deposition process, (Lorenzo, 2013).

2.13.4 Thermal oxidation

This is one of the most basic deposition technologies. It is simply, oxidation of the substrate surface in an oxygen rich atmosphere. The temperature is raised to 800°C-1100° C to speed up the process. This is also the only deposition technology which actually consumes some of the substrate as it proceeds. The growth of the film is spurred by diffusion of oxygen into the substrate, which means that the film growth is actually downwards into the substrate. As the thickness of the oxidized layer increases, the diffusion of oxygen to the substrate becomes more difficult leading to a parabolic relationship between film thickness and oxidation time for films thicker than ~100nm. This process is naturally limited to materials that can be oxidized, and it can only form films that are oxides of that material. This is the classical process used to form silicon

dioxide on a silicon substrate. This is a simple process, which unfortunately produces films with somewhat limited use in MEMS components. It is typically used to form films that are used for electrical insulation or that are used for other process purposes later in a process sequence (MEMSnet, 2013).

2.13.5 Spray pyrolysis

Spray pyrolysis technique involves spraying a solution, usually aqueous containing soluble salts of the constituent atoms of the desired compound onto a substrate maintained at elevated temperatures. The sprayed droplets reaching the hot substrate surface undergoes pyrolytic (endothermic) decomposition and forms a single crystallite or a cluster of crystallites of the product. The other volatile by-products and excess solvent escape in the vapour phase. The substrate provides the thermal energy for the thermal decomposition and subsequent recombination of the constituent species followed by sintering and recrystallization of the clusters of crystallites giving rise to a coherent film, (Chopra and Das, 1983). ZnO thin films were deposited by this method (Lehraki *et al.*, 2012).

2.13.6 Chemical solution deposition (CSD) or Chemical bath deposition (CBD)

Chemical bath deposition (CBD) is a simple and low cost thin film deposition method that works at low temperatures and ambient pressures. It requires only a solution that contains precursor ions or complexes and a substrate on which films are deposited. The solution and substrate need not be conductive. One disadvantage of this method is that the solution is wasted after every deposition, (Guojun, 2010). In the work, Synthesis and

characterization of Al doped CdS thin films grown by chemical bath deposition method and its application to remove dye by photocatalytic treatment, this method was used (Patil *et al.*, 2011).

2.13.7 Sol gel method

Sol-gel process involves the transition of a liquid (sol, mostly colloidal) into a solid (gel) phase. This method enables fabrication of ceramic or glass materials in a wide variety of forms, ultrafine or spherical shaped powders, thin film coatings, ceramic fibres, micro porous inorganic membranes, monolithic ceramics and glasses or extremely porous aerogel. Thin films can be produced on a piece of substrate by spin coating or dip coating, (Gosavi, 2010). In the work, Antimicrobial activity of thin solid films of silver doped hydroxyapatite this method was used (Simona *et al.*, 2014).

2.13.8 Successive Ionic Layer Adsorption and Reaction (SILAR) Method:

SILAR is a modified chemical method based on immersion of substrates into separately placed cationic and anionic precursors and rinsing between every immersion with ion exchange water to avoid homogeneous precipitation in the solution, (Pathan *et al.*, 2002). SILAR can be used to deposit compound materials on a variety of substrates such as insulators, semiconductors, metals. One SILAR cycle contains four steps: (a) the substrate is immersed into first reaction containing the aqueous cation precursor, (b) rinsed with water, (c) immersed into the anion solution, and (d) rinsed with water (Guzeldir *et al.*, 2012). CdSe thin film was prepared by this method (Pathan *et al.*, 2002).

2.13.9 Physical Vapor Deposition (PVD)

PVD covers a number of deposition technologies in which material is released from a source and transferred to the substrate. The two most important technologies are evaporation and sputtering. PVD comprises the standard technologies for deposition of metals. It is far more common than CVD for metals since it can be performed at lower process risk and cheaper in regards to materials cost. The quality of the films are inferior to CVD, which for metals means higher resistivity and for insulators more defects and traps. The step coverage is also not as good as CVD (MEMSnet, 2013).

2.13.10 Evaporation .

In evaporation the substrate is placed inside a vacuum chamber, in which a block (source) of the material to be deposited is also located. The source material is then heated to the point where it starts to boil and evaporate. A vacuum is required to allow the molecules to evaporate freely in the chamber, and they subsequently condense on all surfaces. This principle is the same for all evaporation technologies, only the method used to heat (evaporate) the source material differs. There are two popular evaporation technologies, which are e-beam evaporation and resistive evaporation each referring to the heating method.

In e-beam evaporation, an electron beam is aimed at the source material causing local heating and evaporation. In resistive evaporation, a tungsten boat, containing the source material, is heated electrically with a high current to make the material evaporate. Many materials are restrictive in terms of which evaporation method can be used (i.e.

aluminum is quite difficult to evaporate using resistive heating), which typically relates to the phase transition properties of that material (MEMSnet, 2013). Electron beam evaporation was used to deposit Mo doped ZnTe thin films (Shailaja *et al.*, 2014).

2.13.11 Sputtering

This technique involves the creation of vapour species (atoms) through the bombardment of the surface of the target material by high energetic and non reactive ions from a low pressure plasma thereby causing the erosion of the material atoms or cluster of atoms from the target and subsequent deposition of the atoms (films) on a substrate. The ejection of atoms is made possible by the momentum transfer between the impinging ions and the atoms of the target surface. The sputtering atoms are condensed on a substrate to form a film (Chopra and Das, 1983). Thin films of In doped CdS thin films were deposited using this method (Islam *et al.*, 2013).

2.13.12 Casting

In this process the material to be deposited is dissolved in liquid form in a solvent. The material can be applied to the substrate by spraying or spinning. Once the solvent is evaporated, a thin film of the material remains on the substrate. This is particularly useful for polymer materials, which may be easily dissolved in organic solvents, and it is the common method used to apply photoresist to substrates (in photolithography). The thicknesses that can be cast on a substrate range all the way from a single monolayer of molecules (adhesion promotion) to tens of micrometers. In recent years, the casting

technology has also been applied to form films of glass materials on substrates. Casting is a simple technology which can be used for a variety of materials (mostly polymers). The control on film thickness depends on exact conditions, but can be sustained within +/-10% in a wide range. For photolithography casting method is advised, which is an integral part of that technology. There are also other interesting materials such as polyimide and spin-on glass which can be applied by casting (MEMSnet, 2013).

2.13.13 Spin coating

Spin coating technique consists in the deposition of a small quantity of a solution at the centre of a substrate which is rotated at high speed in order to spread the slip by centrifugal force. The rotation is continued while the excess solution is removed with the spinning until the desired thickness is obtained, Basile and Galluci's study (as cited in Cruz *et al.*, 2012). There are two ways to apply the solution; the static application is the deposition of a small amount of solution in the middle of the substrate or close to it and then begins to spin. In the dynamic application, the solution will be placed on the substrate while it is rotated at low speed. The final thickness is a function of the rotational speed, concentration of solution, molecular weight and time. It also depends on how much the solution is applied to the substrate as well as drying rate both of which are affected by viscosity of the solution, (Cruz *et al.*, 2012). Nickel doped zinc oxide thin films were deposited using this method (Thakur *et al.*, 2013).

2.13.14 Pulsed laser deposition (PLD)

Pulsed laser deposition is a [thin film deposition](#) (specifically a [physical vapor deposition](#), PVD) technique where a high-power pulsed [laser](#) beam is focused inside a [vacuum](#) chamber to strike a target of the material that is to be deposited. This material is vaporized from the target (in a plasma plume) which deposits it as a [thin film](#) on a substrate (such as a silicon wafer facing the target). This process can occur in [ultra high vacuum](#) or in the presence of a background gas, such as oxygen which is commonly used when depositing oxides to fully oxygenate the deposited films. While the basic-setup is simple relative to many other deposition techniques, the physical phenomena of laser-target interaction and film growth are quite complex. When the laser pulse is absorbed by the target, energy is first converted to electronic excitation and then into thermal, chemical and mechanical energy resulting in evaporation, [ablation](#), [plasma](#) formation and even [exfoliation](#). The ejected species expand into the surrounding vacuum in the form of a plume containing many energetic species including [atoms](#), [molecules](#), [electrons](#), [ions](#), clusters, particulates and molten globules, before depositing on the typically hot substrate (Douglas and Graham, as cited in Wikipedia). Europium doped Zinc oxide thin films were deposited by this method (Rafael *et al.*, 2005).

2.14 Spintronics

It is widely believed that DMS are ideal material for spintronics. The term "spintronics" stands for spin transition electronics. As well known today, integrated circuits and high-

frequency devices, used for information processing and communications, have had great success through controlling the charge of electrons in semiconductors. Mass storage of information (indispensable for information technology) is carried out by magnetic recording (hard disks, magnetic disks...) using electronic spins in ferromagnetic materials. It is then quite natural to ask if both the charge and spin of electrons can be used at the same time to enhance the performance of devices. This is the main idea of spintronics, which is widely expected to be the future solution to downsize current microelectronic devices into size of even nanometers. The realization of functional spintronic devices requires materials with ferromagnetic ordering at operational temperatures compatible with existing semiconductor materials. Being a ferromagnetic semiconductor with favorable experimental properties, dilute magnetic semiconductors will promisingly suit this need. Two major criteria are considered to select the most promising materials for semiconductor spintronics. First, the ferromagnetism should be retained up to practical temperatures namely room temperature. Second, it would be a major advantage if there are already an existing technology base for the material in other applications. As early as late 1960 to early 1970, oxide doped with Eu^{2+} and spinel structured composite, for example, ZnCr_2Se_4 are studied as magnetic semiconductors. However, structures of those composites are different from Si or GaAs. The crystals are very hard to produce in experiment, their low Curie temperature T_c (50K or lower), strong insulation and poor semiconducting transport property further hampered their value in application (Zheng, 2008). The possibility of using electrons' spins in addition to

their charge, in information technology has created much enthusiasm for a new field of electronics popularly known as "spintronics." An intensely studied approach to obtaining spin-polarized carriers for data-storage devices is the use of diluted magnetic semiconductors created by doping ions like Mn, Fe, or Co having a net spin into a semiconducting host such as GaAs, ZnO, or GaN (Edmonds *et al.*, 2006). One advantage of spin over charge is that spin can be easily manipulated by externally applied magnetic fields, a property already in use in magnetic storage technology. Another more subtle (but potentially significant) property of spin is its long coherence or relaxation time—once created, it tends to stay that way for a long time, unlike charge states which are easily destroyed by scattering or collision with defects, impurities or other charges. These characteristics open the possibility of developing devices that could be much smaller, consume less electricity and be more powerful for certain computations than is possible with electron-charge based systems, (Das-Sarma, 2001).

2.14.1 The Application of Spintronics

The word spintronics—short for spin electronics—was coined in the 1990s to describe devices that take advantage of “spin,” a quantum-mechanical property of an electron that takes only two values: spin-up and spin-down. Spintronics research flowered following the discovery of the giant magnetoresistance (GMR) effect in the late 1980s. IBM Almaden Research Center researchers realized that GMR could be used to make more sensitive hard disk drive read heads. Parkin discovered the fundamental underlying spintronics phenomena that made the spin valve a reality while researching novel

properties of superlattices formed from combinations of various magnetic and non-magnetic materials based on flowing charge currents through these superlattices.

By working at the atomic scale, he discovered that by sandwiching a non-magnetic layer of material between two magnetic layers, where each of the layers was just a few atoms thick, and by applying small magnetic fields, the current flowing through the sandwich could significantly be changed. The reason was that within the magnetic layers, the electrical current, which was composed of negatively charged electrons, became spin-polarized. All the electrons' spins became oriented either "up" or "down," depending on the magnetic orientation of these layers—just like nanoscopic compass needles, which point to either the North or South Pole. Small magnetic fields reorient these compass needles. This effectively created the ability to turn the spin-polarized current, on or off just like a valve.

The spin valve also created the ability to detect more minute magnetic impulses when flown over a magnetic hard drive. This ability allowed for vastly more data to be written to and stored on a hard drive than was possible before the discovery of GMR.

The first use of spin-valve sensors in hard disk drive read heads was in the IBM[®] Deskstar 16GP Titan, which was released in late 1997 with 16.8 GB of storage. Now, every single hard disk drive on the market, many ranging up to terabytes and more of storage features are read head based on Parkin's discoveries. Today, though, the read head no longer uses GMR but something called giant tunneling magnetoresistance, based on different physics that are still spintronic (Parkin *et al.*, 2007).

The huge increases in digital storage made possible by giant magnetoresistance (GMR), made consumer audio and video iPods, as well as Google-style data centers, a reality.

The first mass-produced spintronic device has already revolutionized the hard-disk drive industry. Introduced in 1997, the giant magnetoresistive (GMR) head, developed at the IBM Almaden lab, is a super-sensitive magnetic-field sensor that enabled a 40-fold increase in data density over the past seven years. Another multilayered spintronic structure is at the heart of the high-speed, nonvolatile magnetic random access memory (MRAM), currently being developed by a handful of companies.”

Magnetoresistive random access memory (MRAM) is expected to revolutionize the memory market and contribute to the development of advanced and versatile computing and personal devices. Promising advances such as instantly bootable computers, MRAM could well be the next big thing in spintronics. Quantum computation is perhaps one of the most exciting potential applications of spintronics. However, harnessing the power of the quantum states to enable information processing and storage is not easy. The evolution of MRAMs and various spin-based technologies could be critically important in facilitating the development of the first quantum computer. Think of one combined unit that integrates logic, storage, and communication for computing. We envision using a mixture of optical, electronic, and photonic techniques to prepare and manipulate spin-based information (Parkin *et al.*, 2007). The spin could be stored in semiconductors, run at frequencies many times faster than today’s technology and work at room temperature and all in a single nanostructure. Then imagine millions of these nanostructures working

together in a device small by human standards. What such devices will do is up to scientists and engineers to determine. But the most exciting prospects are the revolutionary ones rather than simple extrapolations of today's technology.

These huge increases in storage capacity made possible the evolution of giant data centers in the "cloud." Perhaps most importantly, the ability to store and access huge amounts of data in worldwide networks helped create the information-based world of today. In 2005 alone, the amount of data that could be stored by all the spin-valve-enabled hard drives sold, equaled all of the analog data, available in the world at that time approximately 100 exabytes. Since 2007, the basic spin valve has evolved to a related thin-layered structure magnetic tunnel junction that displays giant tunneling magnetoresistance (TMR), a phenomenon where electrons tunnel through a thin insulator. The non-magnetic layer in a GMR spin valve has been replaced by this insulator, which, when formed from magnesium oxide, is a spin filter that only allows electrons of one spin direction through it, like a gatekeeper (Parkin *et al.*, 2007). The current that flows through magnesium oxide is composed of electrons that are almost 100 percent spin-up or spin-down, depending on the magnetic orientation of the surrounding magnetic layers. This means that the TMR signal is much larger than that from a GMR spin valve. Indeed it is almost 100 times larger. TMR is also the basis of magnetic random access memory (MRAM), a new type of non-volatile memory that uses magnetic moments to retain data instead of electrical charges.

Stuart Parkin is now leading a team of IBM researchers in studying Racetrack Memory, a radically different non-volatile memory technology proposed by Parkin in 2004 that is based on a recently discovered spintronics phenomena. Racetrack memory uses currents of spin-oriented electrons to move magnetic regions along magnetic racetracks - nanoscopic magnetic wires. Racetrack memory is one of a number of new technologies being explored that could offer higher storage density than comparable devices such as flash memory, and eventually replace disk drives with a solid-state memory device.

Throughout its history, IBM has collaborated with external entities, including universities, organizations and other corporations to advance research in a variety of technologies. In 2004, the IBM-Stanford Spintronic Science and Applications Center (SpinAps) was established in California. Within SpinAps, scientists and engineers from IBM Almaden Research Center are working together with Stanford faculty, students and post-doctoral fellows to study the theoretical and practical fundamentals of spintronics, and to develop advanced technologies built on those fundamentals.

Spintronics may also enable the leap into quantum computing where units of quantum information known as “qubits” can occupy spin-up and spin-down states simultaneously, and so allow for massive increases in computational power (Parkin *et al.*, 2007). The spin orientation of an electron pair in an atom is as shown in fig. 2.6.

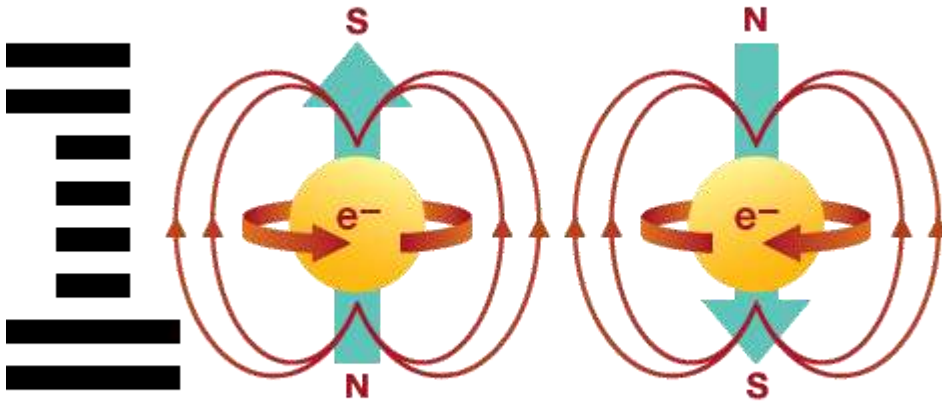


Figure 2.6: Electron spin-up and spin-down (Parkin *et al.*, 2007)

The discovery and application by IBM researcher Stuart Parkin and his colleagues of a spin valve, essentially the capability to alter the magnetic state of materials at the atomic level, changed the landscape of magnetic data storage by dramatically increasing storage capacity. This helped pave the way for some of today's most popular devices and online applications. The first use of spin-valve sensors in hard disk drive read heads was in the IBM Deskstar 16GP Titan, which was released in 1997 with 16.8 GB of storage. In 2007, Hitachi, which bought IBM's hard drive division in 2003, released the Deskstar 7K1000, the first 1 TB hard disk drive. Today, the Hitachi Deskstar 7K3000 provides up to 3 TB of storage.

IBM introduced the microdrive in 1999, the smallest hard drive to date, with a capacity of 170 MB on a single, 1-inch platter. Hitachi, which later bought IBM's hard drive business, expanded the microdrive to 8 GB by 2006. Offering more capacity and lower cost per gigabyte than flash memory, the microdrive was used in many personal digital devices during the past decade, including Apple's iPod Mini and iPod Classic, Palm's LifeDrive personal digital assistant, and various mp3 players, digital cameras, printers and mobile phones.

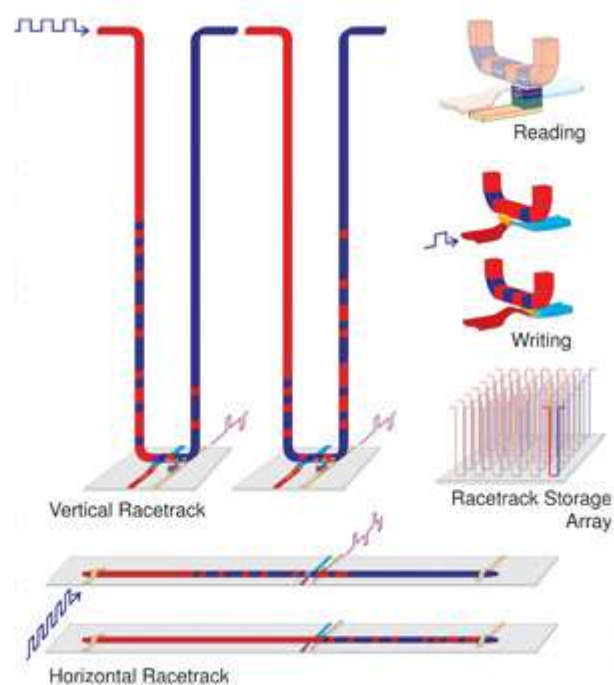


Figure 2.7: New forms of memory (Parkin *et al.*, 2007)

Researchers at the IBM-Stanford Spintronic Science and Applications Center are exploring new spintronic devices that take us beyond the realm of the simple GMR

(giant magnetoresistive) spin valve, including magnetic random access memory (MRAM), spin injectors for spin logic applications and the development of a new storage-memory technology called racetrack memory as shown in fig. 2.7 (Parkin *et al.*, 2007).

2.15 Transparent conducting oxides

A transparent conducting oxide coating, abbreviated TCO, is a doped metal oxide thin film predominantly used in optoelectronic devices, for example flat panel displays and photovoltaics (including inorganic and organic devices as well as dye-sensitized solar cells). Most TCOs are manufactured with polycrystalline or amorphous microstructures. On the average, the aforementioned applications use electrode materials that have >80% transmittance of incident light as well as conductivities $>10^3$ S/cm for efficient carrier transport (Beneq, 2010).

Transparent conducting oxides (TCOs) are electrical conductive materials with comparably low absorption of electromagnetic waves within the visible region of the spectrum. They are usually prepared with thin film technologies and used in optoelectrical devices such as solar cells, displays, opto-electrical interfaces and circuitries. Glass fibers are nearly lossless conductors of light, but electrical insulators; silicon and compound semiconductors are wavelength dependent optical resistors (generating mobile electrons), but dopant dependent electrical conductors. Transparent conducting oxides are highly flexible intermediate states with both these characteristics. Their conductivity can be tuned from insulating via semiconducting to conducting as well as

their transparency adjusted. As they can be produced as n-type and p-type conductives, they open a wide range of power saving opto-electrical circuitries and technological applications. As n-type TCOs are of special importance for thin film solar cell production, ITO and the reasonably priced aluminum-doped zinc oxide (ZnO:Al) are examples. As transparent conducting oxides are usually compound semiconductors—where the nonmetal part is oxygen—they are discussed along their metal elements. Metals were used as compound materials or dopants (with just a few percent content) (Andreas, 2012).

In transparent conducting oxides (TCOs), the nonmetal part, B, consists of oxygen in combination with different metals or metal-combinations, A, lead to compound semiconductors, $AyBz$, with different opto-electrical characteristics. These opto-electrical characteristics can be changed by doping, $AyBz:D$ ($D = \text{dopant}$), with metals, metalloids or nonmetals. Hence, metals can be part of the compound semiconductor itself, A, or can be a dopant, D (Andreas, 2012). Transparent conducting oxides (TCO) are critical component of many organic electronic devices including organic solar cells and light-emitting diodes (Li, *et al.*, 2014). In general, TCO thin films that are in practical use as transparent electrodes are polycrystalline or amorphous, except for single crystals grown epitaxially and exhibit a resistivity of the order of $10^3 \Omega\text{cm}$ or less and an average transmittance above 80% in the visible range. Thus TCO semiconductors suitable for use as thin film transparent electrodes should have a carrier concentration of the order 10^{20}cm^{-3} or higher and a bandgap energy above approximately 3eV (Minami,

2005). Recent developments in optoelectronic device applications have frequently required improvements in the physical and chemical properties of TCO films used as thin film transparent electrodes. In order to develop TCO films suitable for specialized applications, previously proposed material developments using multicomponent oxides has recently been attracting much attention as source of new TCO semiconductors (Minami, 1999; In Minami, 2005). TCO is a wide band-gap semiconductor that has a relatively high concentration of free electrons in its conduction band. These arise either from defects in the material or from extrinsic dopants, the impurity levels of which lie near the conduction band edge. The high-electron-carrier concentration (the materials will be assumed to be n-type unless otherwise specified) causes absorption of electromagnetic radiation in both the visible and infrared portions of the spectrum. For the present purposes, it is the former that is the more important. Because a TCO must necessarily represent a compromise between electrical conductivity and optical transmittance, a careful balance between the properties is required. Reduction of the resistivity involves either an increase in the carrier concentration or in the mobility. Increasing the former also leads to an increase in the visible absorption. Increasing the mobility, however, has no deleterious effect and is probably the best direction to follow. To achieve a high-carrier mobility will necessarily improve the optical properties (Coutts *et al.*, 1999).

2.16 Review of related works

Some related works are reviewed with a view to having insight into the main work and provide a basis for some comparison of results.

2.16.1 Optical, electrical and structural studies of nickel cobalt oxide nanoparticles

Optical, electrical and structural studies of nickel cobalt oxide nanoparticles by co-precipitation method, the effect of sintering on the particle size was studied. Also studied was the effect of temperature and frequency on the dielectric behavior and AC electrical conductivity for nanosized nickel cobalt spinel oxide sample prepared by same method. The particle size was determined from X-ray diffraction studies and Tem image. The surface morphology was revealed by SEM image. The effect of sintering on the particle size was analyzed and the absorption spectra of the material in the UV-VIS-NIR range was done. An absorption band was observed to occur at 350nm and another one around 650nm. Analysis of the absorption spectra for the nickel cobalt oxide sintered at 500⁰C, 700⁰C and 900⁰C was found to have a direct bandgap ranging from 1.827 to 1.61eV. The electrons were highly localized in nanoparticles and interaction between those localized states gave rise to the observed bandgap. The dielectric permittivity of nanosized nickel cobalt spinel oxide sample was evaluated from the observed capacitance values in the frequency range 100kHz to 5mHz and in the temperature range of 300 to 403K. It was seen that with decreasing frequency, the dielectric constant increased much more obviously than that of conventional materials. As the temperature increased more and more dipoles were oriented resulting in an increase in the values of

dipole moment. Space charge polarization and rotation direction polarization played a crucial role in the dielectric behavior of this nano sized material (Nisha *et al.*, 2008).

2.16.2 Spectroscopic ellipsometry characterization of electrochromic tungsten oxide and nickel oxide thin films made by sputter deposition

Electrochromic films of tungsten oxide and nickel oxide were made by reactive dc magnetron sputtering and were characterized by X-ray diffraction, rutherford backscattering spectrometry, scanning electron microscopy, and atomic force microscopy. The optical properties were investigated in detail by spectroscopic ellipsometry and spectrophotometry, using a multiple-sample approach. The W-oxide film was modeled as a homogeneous isotropic layer, whereas the Ni-oxide film was modeled as an anisotropic layer with the optical axis perpendicular to the surface. Parametric models of the two layers were then used to derive complex refractive index in the 300–1700 nm range, film thickness, and surface roughness. A band gap of 3.15 eV was found for the W-oxide film, using a Tauc–Lorentz parameterization. For the Ni-oxide film, taken to have direct optical transitions, bandgaps along the optical axis, perpendicular to it, and in an isotropic intermediate layer at the bottom of the film were found to be 3.95, 3.97, and 3.63 eV, respectively. Parameterization for the Ni oxide was made by use of the Lorentz model (Valyukh *et al.*, 2010).

2.16.3 Temperature effect on the electrical properties of undoped NiO thin films

Undoped NiO thin films were prepared onto glass substrate by e-beam evaporation of the element Ni in vacuum at $\sim 2 \times 10^{-4}$ Pa. The as-deposited Ni films were then oxidized in

air by heating for about 2 h at a temperature of 470 K and then the oxidized Ni films were turned into NiO thin films. From the deposition time and film thickness after annealing in air, an effective deposition rate of NiO thin films was about 6.67 nm s^{-1} .

X-ray diffraction (XRD) study showed that the NiO films were amorphous in nature. SEM studies of the surface morphology of NiO films exhibited a smooth and homogeneous growth on the entire surface. The elemental composition of NiO films was estimated by energy dispersive analysis of X-rays (EDAX) method. The effects of temperature on the electrical properties of NiO thin films were studied in details. The heating and cooling cycles of the samples were reversible in the investigated temperature range after successive heat-treatment in air. Thickness dependence of conductivity was well in conformity with the Fuchs–Sondheimer theory. Temperature dependence of electrical conductivity showed a semiconducting behavior with activation energy. The thickness dependence of activation energy as well as thermopower studies was done within 293–473 K temperature range, respectively. Thermopower study indicated the NiO films as a p-type semiconductor. Optical study in the wavelength range $0.3 < \lambda < 1.2 \text{ }\mu\text{m}$ range exhibited a high transmittance in the visible as well as in the near infra-red. By calculation from the optical data, the NiO sample exhibited a band gap of 3.11 eV, which agrees well with earlier reported values. These studies may be of importance for the application of this material in energy efficient surface coating devices (Hakim *et al.*, 2009).

2.16.4 Optical properties of chemical bath deposited nickel oxide (NiO_x) thin films

Thin films of NiO_x were deposited on glass slide from aqueous solutions of nickel chloride and ammonia. Ammonia was employed as complexing agent in the presence of hydroxyl solution. The film was studied using X-ray diffraction, photomicrograph for the structure and absorption spectroscopy for its optical properties. The optical characterization showed that the film had band gap that ranged between 2.10eV and 3.90eV, and thickness that ranged between 0.061μm and 0.346μm. The average transmittance of the films were found to be between 50% and 91% in the UV-VIS-NIR regions. The films could be effective as optical coatings for poultry houses (Ezema *et al.*, 2008).

2.16.5 Spray pyrolytic synthesis of large area NiO_x thin films from aqueous nickel acetate solutions.

Non-stoichiometric nickel oxide thin films were prepared by pyrolytic decomposition of aerosol droplets of aqueous nickel acetate solution. Conventional un-nebulized spray pyrolysis system was used for the synthesis of thin films. The fine droplets were atomized by employing compressed air as carrier gas and allowed to decompose onto pre-heated Sn doped In₂O₃ (ITO) coated glass. The preparative parameters such as substrate temperature, solution concentration, distance from spray-nozzle to substrate, pressure of carrier air, etc., were optimized to obtain large area, uniform thin films. The appropriate substrate temperature was selected after thermo-gravimetric analysis of

nickel acetate. The temperature range of 330–420 °C was investigated for pyrolysis. Structural studies using X-ray diffraction (XRD) showed the formation of cubic NiO. Morphological aspects of the films as-prepared and air annealed films were studied by employing scanning electron microscopy. The optical absorption studies gave direct band gap equal to 3.61 eV. The compositional analysis was carried out from the elemental depth profiles employing Auger electron spectroscopy. These indicated the formation of non-stoichiometric nickel oxide thin films (Desai *et al.*, 2006).

2.16.6 Structural and optical properties of nickel oxide thin films prepared by chemical bath deposition and by spray pyrolysis techniques

Nickel oxide thin films were prepared by chemical bath deposition (CBD) and by chemical spray pyrolysis from the same precursor onto glass substrate. Analysis of the work showed that the sprayed NiO thin films were polycrystalline in cubic phase structure with (111) preferred orientation. While the chemical bath deposited as a nickel hydroxide phase and transferred to polycrystalline NiO with annealing. The annealed CBD-films were polycrystalline with cubic phase structure and preferred orientation (200). Sprayed and CBD NiO films had optical transmittance in the visible region 70% and 46 %, respectively. Sprayed and CBD NiO thin films had optical band gaps of 3.54eV and 3.62 eV, respectively. Sprayed NiO thin films can be used as transparent materials in invisible electronics applications,(Gomaa *et al* 2016).

2.16.7 p-Type transparent NiO thin films by e-beam evaporation technique

Nickel oxide (NiO) semiconductors thin films were prepared by e-beam evaporation technique at different substrate temperatures ranging from room temperature to 400⁰C on glass substrate. Glancing incident X-ray diffraction depict that with the increase in substrate temperature, the preferred orientation changed from (111) to (200) direction. Atomic force microscopy was used to investigate the surface morphology of the NiO thin films. The transmittance of NiO thin film increased with substrate temperature. NiO thin film was also deposited on n-type indium tin oxide (ITO) thin films to investigate the diode characteristic of p-NiO/n-ITO junction. The value of the bandgap (E_g) varied in the range 3.76 to 3.79 eV as the substrate temperature increased from RT to 400⁰ C. The change in the optical band gap was due to the change in stoichiometry and crystallinity in the film (Patel *et al.*, 2011).

1 p-n junction characteristics

In order to examine the p-type semi-conducting behavior of NiO thin films, a p-n junction formed by depositing it on n-ITO coated glass substrate held at 400⁰C substrate temperature was done. I-V characteristic and the transmittance spectra of the p-NiO/n-ITO junction are illustrated in Fig.2.10 and 2.11 respectively..

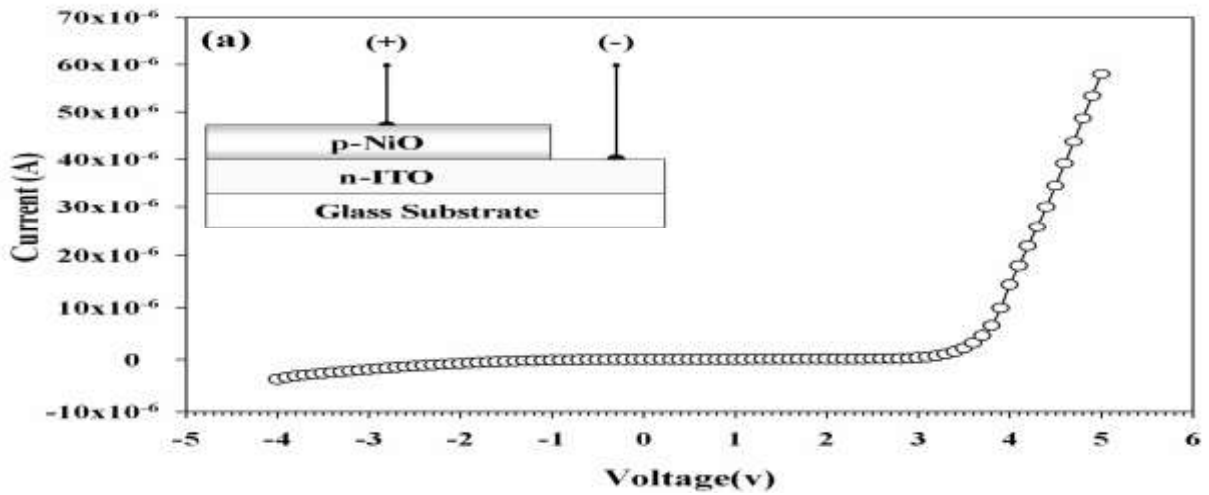


Figure 2.8: I-V characteristics with the p-n diode structure of the p-NiO/n-ITO junction (Patel *et al.*, 2011).

Fig. 2.8 shows a typical rectifying behavior of thin film p-n junction diode which exhibited a threshold voltage of 3.4 V. The inserted image shows the p-NiO/n-ITO/Glass multilayered structure

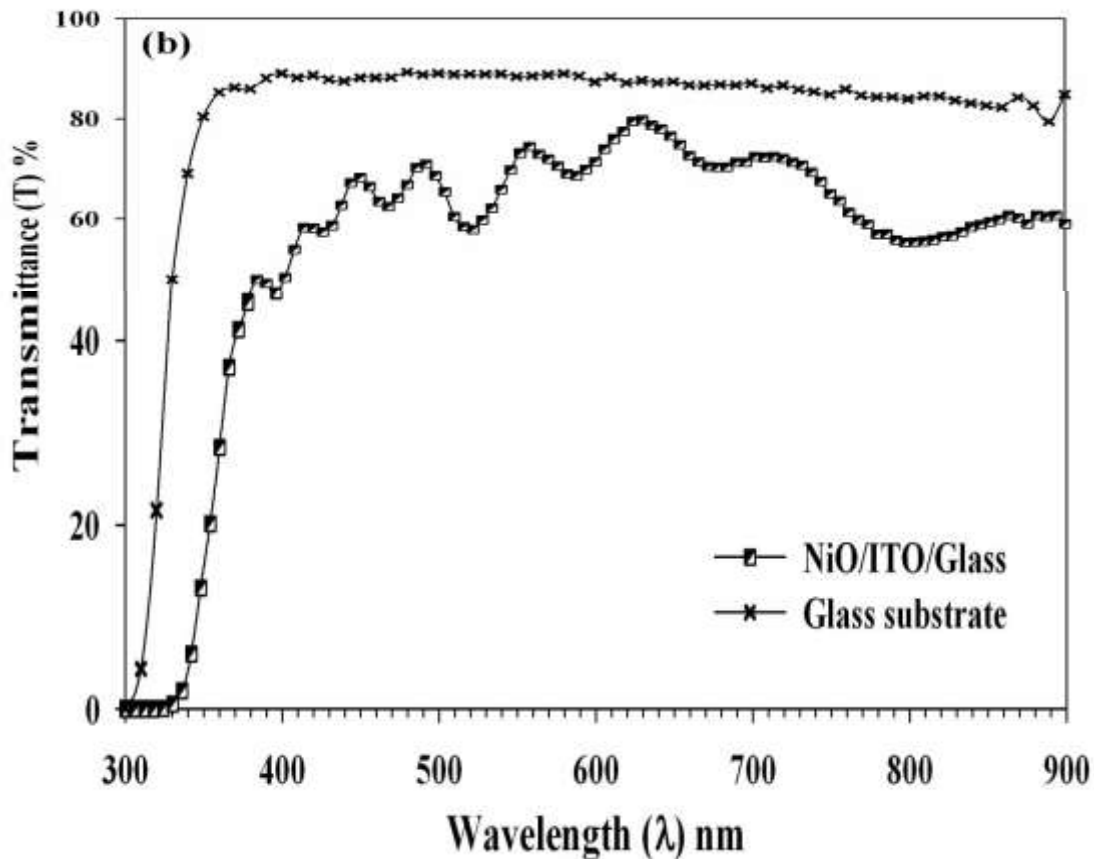


Figure 2.9: transmittance spectra of the p-NiO/n-ITO junction (Patel *et al.*, 2011).

Figure 2.9 shows that p-n junction has an average transmittance 60-65 % in the visible region of light. This p-n-junction diode is suitable for many applications as a transparent p-n Junction (Patel *et al.*, 2011).

2.16.8 p-Type semiconducting nickel oxide as an efficiency-enhancing anode interfacial layer in polymer bulk-heterojunction solar cells

Thin films of *p*-NiO were deposited by pulsed laser deposition (PLD) on patterned ITO anodes, and the presence of crystalline NiO was confirmed by glancing-angle x-ray

diffraction (GA-XRD) . The characteristic NiO (111) and (200) reflections were clearly visible along with the ITO background . The morphology of the present NiO surfaces was surveyed by SEM and AFM . The AFM and SEM images revealed distinct grains remarkably similar to those of the ITO surface, as expected. The NiO deposition process significantly planarized the anode surface from an RMS roughness of 4–5 nm for bare glass/ITO. To minimize interfacial power losses, thin (5–80 nm) layers of NiO, a *p*-type oxide semiconductor, were inserted between the active organic layer, poly(3-hexylthiophene) (P3HT) + [6,6]-phenyl-C₆₁ butyric acid methyl ester (PCBM), and the ITO (tin-doped indium oxide) anode of bulk-heterojunction ITO/P3HT:PCBM/LiF/Al solar cells. The interfacial NiO layer was deposited by pulsed laser deposition directly onto cleaned ITO, and the active layer was subsequently deposited by spin-coating. Insertion of the NiO layer afforded cell power conversion efficiencies as high as 5.2% and enhanced the fill factor to 69% and the open-circuit voltage (V_{oc}) to 638 mV versus an ITO/P3HT:PCBM/LiF/Al control device. The value of such hole-transporting/electron-blocking interfacial layers was clearly demonstrated and applicable to other organic photovoltaics. The reported optical band-gap of NiO ranged from 3.4 eV to 4.3 eV depending exactly on how the location of the band edge was defined: location of the first absorption feature, midpoint of the first rise, or where the maximum slope of absorption extrapolated to zero . In this contribution, the optical band-gap was determined from a standard plot of $(\alpha h\nu)^2$ versus $h\nu$, where α is the absorption coefficient and $h\nu$ is energy in eV; the x axis intercept of the linear portion of the plot

was then taken as the optical band-gap. This yielded a slightly lower value for the band-gap (3.6 eV) (Irwin *et al.*, 2008).

2.16.9 Electronic, Optical and Electrical Properties of Nickel Oxide Thin Films Grown by RF Magnetron Sputtering

Nickel oxide (NiO) thin films were grown on soda-lime glass substrates by RF magnetron sputtering method at room temperature (RT), and they were post-annealed at the temperatures of 100°C, 200 °C, 300 °C and 400 °C for 30 minutes in vacuum. The electronic structure, optical and electrical properties of NiO thin films were investigated. The results demonstrate that the post-annealing played a crucial role in enhancing the electrical and optical properties of NiO thin films. The measured bandgaps of the NiO thin films were 3.69, 3.69, 3.67 and 3.67 eV for RT, 100°C, 200°C, and 300°C, respectively, within an uncertainty of ± 0.1 eV, (Park *et al.*, 2015).

2.16.10 Synthesis and characterization of nickel oxide thin films deposited on glass substrates using spray pyrolysis

A simple and inexpensive spray pyrolysis technique was employed to deposit nickel oxide (NiO) thin films from hydrated nickel chloride salt solution onto amorphous glass substrate. The as-deposited films were transparent, uniform and well adherent to the glass substrate. The structural analysis showed that all the samples had cubic structure. It was found that increase in volume of sprayed solution led to an increment in the crystallite size of NiO film and improved the homogeneity of the film. Optical analysis showed that increase in thickness of the layer resulted to a decrease in the optical transmission, but remained higher than 70% even above 600 nm thickness. The optical

bandgap decreased from 3.7eV to 3.55 eV as the thickness increased from 133nm to 620 nm,(Jlassi *et al.*, 2014).

2.16.11 Preparation and characterization of spray pyrolyzed nickel oxide (NiO) thin films

A simple and inexpensive spray pyrolysis technique (SPT) was used to deposit nickel oxide (NiO) thin films from hydrated nickel chloride salt solution on to glass substrates. The thermogravimetric analysis (TGA) and differential thermal analysis (DTA) techniques were used to study the thermal characteristics of the precursor salt. The effect of the volume of sprayed solution on structural, optical and electrical properties was studied using X-ray diffraction (XRD), infrared (IR), optical absorption, electrical resistivity and thermoelectric power (TEP) techniques. It was found that increase in the volume of sprayed solution led to the increment in film thickness and amelioration of crystallinity of the film, consequently the band-gap energy waned from 3.58 to 3.4 eV. It also affected resistivity and TEP of the film (Patil *et al.*, 2002),

2.16.12 Spray pyrolysis deposition and characterization of highly (100) oriented magnesium oxide thin films

Transparent dielectric thin films of MgO were deposited on quartz substrates at different temperatures between 400 and 600°C by a pneumatic spray pyrolysis technique using $\text{Mg}(\text{CH}_3\text{COO})_2 \cdot 4\text{H}_2\text{O}$ as a single molecular precursor. The prepared films were reproducible, adherent to the substrate, pinhole free and uniform. Amongst the different spray process parameters, the substrate temperature effect was optimized for obtaining single crystalline and transparent MgO thin films. The films crystallized in a cubic

structure. X-ray diffraction measurements showed that the polycrystalline MgO films prepared at 500°C with (100) and (110) orientations were changed to (100) preferred orientation at 600°C. The MgO phase formation was also confirmed with the recorded Fourier Transform Infrared (FTIR) results. The films deposited at 600°C exhibited highest optical transmittivity (>80%) and the direct band gap energy was found to vary from 4.50 to 5.25 eV with a rise in substrate temperature from 500 to 600°C. The measured sheet resistance and the resistivity of the film prepared at 600°C were respectively $10^{13}\Omega/\square$ and $2.06 \times 10^7 \Omega\text{-cm}$. The surface morphology of the prepared MgO thin films was examined by atomic force microscopy (Ezhil *et al.*, 2007).

2.16.13 Tailoring optical and electrical properties of MgO thin films by 1.5 MeV H⁺ implantation to fluencies

Thin films of magnesia (MgO) with (1 0 0) dominant orientations were implanted with 1.5 MeV H⁺ ions at room temperature to various fluences of 10^{13} , 10^{14} and 10^{15} ions/cm². X-ray analysis unambiguously showed crystallinity even after a peak damage fluence of 10^{15} ions/cm². Rutherford backscattering spectrometry combined with ion channeling (RBS/C) was used to analyze radiation damages and defect distributions. Optical absorption band observed at 5.7 eV in implanted films was assigned to the anion vacancies and the defect completely disappeared on annealing at 450 °C. Number of F-type defects estimated was $9.42 \times 10^{15} \text{ cm}^{-2}$ for the film implanted with 10^{15} ions/cm². DC electrical conductivity of $4.02 \times 10^{-4} \text{ S cm}^{-1}$ was observed in the implanted region which was three orders higher than the as-deposited films. In unison, film surface was

modified as a result of the formation of aggregates caused by the atomic mixing of native matrix atoms (Mg and O) and precipitated hydrogen (Ezhil, 2008).

2.16.14 Sputter Deposition of MgO Thin Films: The Effect of Cation Substitution

The MgO structure could be seen as a stable stacking of MgO octahedra. Addition of another metal M with a higher valence electron number than the Mg^{2+} ion will substitute the Mg^{2+} in the octahedral positions. This substitution at low concentration will be compensated by vacancies on the Mg sublattice, (Vyas *et al.*, 1997; In Saraiva, 2012). Based on chemical rules, i.e. the Pauling rules, it could be reasoned as follows: The addition of the metal M will destabilize the MgO structure. First, the third Pauling rule states that the presence of shared edges in a coordinated structure decreases its stability. This effect is especially large for cations with a high valence. Secondly, as indicated by the Vegard's law behavior, the size of the octahedron is changed, hence decreasing the stability of the octahedral stacking in the MgO structure even more.

Another quantity that could be determined from the spectrophotometry measurements is the absorption coefficient α . The spectral dependence of α can be used to calculate the magnitude of the fundamental band gap. The relation between the absorption coefficient and the incident photon energy ($h\nu$) can be written as

$$(\alpha h\nu)^{\frac{1}{2}} = A(h\nu - E_g) \quad (2.18).$$

where A is a constant, E_g denotes the band gap of the material and the exponent n depends on the type of transition. For a direct allowed transition, n is equal to 1/2.

For the pure MgO film, plotting of $(\alpha h\nu)$ versus $h\nu$ and extrapolating the linear part of the graph to the $h\nu$ axis, the direct band gap was obtained from the interception on the $h\nu$ axis, resulting in a band gap of approximately 6.7 eV for the MgO film (Saraiva, 2012).

2.16.15 Layer-by-layer growth of polar MgO (111) ultrathin films

By alternate deposition of Mg and exposure to O₂, layer-by-layer growth, polar MgO(111) ultrathin films with Mg-terminated or O-terminated surfaces have been successfully fabricated on Mo(110) substrate. The surface geometric structure and electronic structures of the polar MgO(111) films were investigated using surface analysis techniques including low-energy electron diffraction and photoelectron emission and electron energy loss spectroscopies. The results indicated that the O-terminated surface is of an insulating character, while for Mg-terminated surface, a prominent new surface state at 2–3 eV and appreciable density of states near Fermi level have been observed. The polar oxide films provide ideal model surfaces for further investigation of support-particle. MgO was quoted as having a bulk bandgap of 7.8eV (Xue and Guo, 2007).

2.16.16 Surface Morphology, Structural and Optical Properties of MgO Films Obtained by Spray Pyrolysis Technique

Magnesium oxide films deposited by the spray pyrolysis technique were studied. 0.2M Magnesium chloride hexahydrate (MgCl₂·6H₂O) solution was used as precursor and the substrate temperature was varied from T_s= 643 K to 693 K. Analysis of optical

properties of the films showed that the bandgap energy of the films increased with increasing substrate temperature, varying from 3.64 eV to 3.70 eV. It was established that the single phase films crystallized into a cubic structure with very fine crystallite size (about 2 nm). The films had high transmittance of 90%,(Diachenko *et al.*, 2016).

2.16.17 Highly conformal Magnesium Oxide thin films by low temperature chemical vapour deposition from $\text{Mg}(\text{H}_3\text{BNMe}_2\text{BH}_3)_2$ and water

Pure, dense, and stoichiometric MgO thin films have been deposited at temperatures as low as 225⁰C by chemical vapor deposition using a recently reported magnesium precursor, magnesium N,N-dimethylaminodiboranate, which has the highest room-temperature vapor pressure among known Mg-containing compounds, with water as a co-reactant. The films were characterized by X-ray photoelectron spectroscopy, atomic force microscopy, scanning electron microscopy, and spectroscopic ellipsometry. Conformal coating on a trench with 35:1 aspect ratio was achieved at a film growth rate of 2 nm/min. The growth rate could be tuned between 2–20 nm/min according to the requirement of the structure to be coated. Magnesium oxide is a technologically important material that has been studied as a high-k dielectric, a barrier for Josephson tunnel junctions, a substrate for the heteroepitaxial overgrowth of high T_c superconductor films, a protective coating on the walls of plasma devices, and in many other applications. The utility of MgO stems from its properties: it has a wide band gap of 7.3 eV, a bulk static dielectric constant of 9.8, a high melting temperature of 2800⁰C,

and a stable, large yield of secondary electrons when its surface is bombarded with ions (Wang *et al.*, 2013).

2.16.18 Synthesis of MgO nanoparticles by solvent mixed spray pyrolysis technique for optical investigation

MgO nanoparticles were synthesized using a solvent mixed spray pyrolysis. The X-ray diffraction pattern confirmed the formation of MgO phase with an excellent crystalline structure. Debye-Scherrer equation was used for the determination of particle size, which was found to be 9.2 nm. Tunneling electron microscope analysis indicated that the as-synthesized particles were nanoparticles with an average particle size of 9 nm. Meanwhile, the ultraviolet-visible spectroscopy of the resulting product was evaluated to study its optical property via measurement of the bandgap energy value obtained as 4.2eV (Nemade and Waghuley, 2014).

2.16.19 Electrochemical deposition and characterization of elongated CdO nanostructures

CdO nanostructures were synthesized by electrodeposition on the indium doped tin oxide conducting glass substrate at low temperatures (70, 80 and 90 °C) from aqueous solution. Scanning electron microscopy (SEM), X-ray diffraction (XRD), UV-vis spectroscopy and X-ray photoelectron spectroscopy (XPS) were employed to characterize the CdO nanostructures. The results demonstrated that the CdO nanostructures synthesized by electrodeposition grew preferably along the [1 1 1] and have face-centered cubic CdO structures and possessed good crystallinity. XPS measurements showed that the nanostructures had Cd and O elements present in the

oxide state and no traces of metallic Cd were observed. The nanostructures were highly transparent in the visible region of spectrum and their energy gap was about 2.45 eV (Singh *et al.*, 2011).

2.16.20 Structural and optical properties of CdO nanostructures prepared by atmospheric-pressure CVD

Cadmium oxide (CdO) nanostructures of various shapes were grown on gold (Au) nanocolloid coated *c*-plane sapphire substrates by atmospheric-pressure CVD using Cd powder and H₂O as source materials. CdO nanorods (NRs) exhibited tapered shapes and the degree of the tapering became larger with increasing substrate temperature. One of the possible reasons for the tapering behavior was the competition between the axial growth due to the vapor–liquid–solid (VLS) mechanism and the radial growth due to the vapor–solid (VS) mechanism. The influence of the competition between the two different growth mechanisms was also confirmed by the appearance of “seaweed-like” NRs. The influence of the shrinkage of catalyst particles during the growth process on the tapering behavior could not be neglected. In addition, there was a possibility that the temporal evolution of catalyst particles, such as diffusion, splitting, migration and coalescence, contributed not only to the disappearance of catalyst particles on the tips of the NRs, resulting in the enhancement of the radial growth relative to the axial growth, but also to the formation of nanobelts (NBs) and nanotrees (NTs). Photoacoustic measurements revealed that the absorption edge shifted towards lower energies and the absorption band below the absorption edge became larger with increasing T_S . This tendency might be due to the increase of intrinsic defects and/or the decrease in residual

impurities. Cadmium oxide (CdO) with a rocksalt structure has a wide direct bandgap of ~ 2.6 eV and exhibits an n-type conduction. Technological applications of CdO are many, such as photodetectors, in solar cells, gas sensors and nonlinear optics (Terasako *et al.*, 2013).

2.16.21 Synthesis, structural and optical characterizations of cadmium oxide (CdO) thin films by chemical bath deposition (CBD) technique

Chemical bath deposition technique was used in the deposition of cadmium oxide (CdO) thin films. Characterization and analysis of the films were carried out. The XRD studies showed amorphous CdO thin films which upon annealing at 623K transformed to polycrystalline structure. The optical studies revealed that the CdO films have high average transmittance over 60% in the visible region and direct optical bandgaps of 2.02 ± 0.05 eV, 2.03 ± 0.05 eV and 2.05 ± 0.05 eV for samples X, Y, Z respectively. These characteristics make them good materials for applications in photodiodes, phototransistors, photovoltaics, transparent electrodes, liquid crystal displays, IR detectors and anti-reflection coatings (Ezeokoye *et al.*, 2013).

2.16.22 Growth of CdO films from CdO films by chemical bath deposition: Influence of the concentration of cadmium precursor

Cadmium oxide films were grown by chemical bath deposition on glass slides at 50°C using solutions of CdCl₂, ammonium hydroxide, and hydrogen peroxide (H₂O₂) as precursors. The films were deposited at different nominal cadmium concentrations. As-grown films were annealed in air at 300°C for obtaining cadmium oxide thin films.

Results of the work showed that the film had maximum transmittance of $>70\%$ in the visible region and bandgap range of 2.38-2.50eV,(Campos-Gonzalez *et al.*,2015)

2.16.23 Structural and optical properties of nanocrystalline CdO thin film growth by solid-vapor deposition

Nanocrystalline cadmium oxide (CdO) thin films were synthesized by a vapor transport process (solid-vapor deposition) without catalyst. Cadmium powder was heated to 1235 K in a tube furnace, and the resultant vapor was carried to the silicon substrate zone by a flow argon gas with oxygen. Scanning electron microscopy revealed that the product was of nanocrystalline cadmium oxide. X-ray diffraction and energy dispersive X-ray techniques were used to characterize structural properties. The grown nanocrystalline thin film had a grain size of 35 nm. Photoluminescence spectroscopy was conducted to investigate the optical properties of the CdO. The red-shift direct band gap energy of the nanocrystalline CdO was at 511 nm (2.43 eV), whereas that of CdO bulk was at 491 nm (2.5 eV) (Zaien *et al.*, 2012).

2.16.24 Characterization of CdO thin films prepared by SILAR deposition technique

Cadmium oxide thin films were deposited by Successive Ionic Layer Adsorption and Reaction (SILAR) method using as a source material of cadmium acetate and ammonium hydroxide solution on glass substrate. The effect of molarity is one of the important factors, which determines the quality of films. The effect of molarity of solution on the structural, optical and morphological properties of as deposited films was studied. XRD and SEM revealed that the crystallite size increased with increase in molarity of

precursor solution. UV-VIS spectrum of the films showed that the optical band gap energy increased with concentration of cadmium acetate in the precursor solution. It was observed that increase in molarities of CdO precursor solution yielded a slight increase in optical band gap from 2.54eV to 2.58eV (Beevi *et al.*, 2010).

2.16.25 Structural, optical and electrical properties of chemically sprayed CdO thin films

Cadmium oxide (CdO) thin films were deposited onto amorphous and fluorine doped tin oxide (FTO) glass substrates using spray pyrolysis technique. The aqueous solution containing precursor of Cd was used to obtain good quality deposits at optimized preparative parameters. The films were characterized by techniques such as X-ray diffraction (XRD), optical absorption, electrical resistivity and thermoelectric power (TEP) measurements. The XRD study revealed that the films were polycrystalline with cubic structure. Optical absorption studies revealed that the value of absorption coefficient was in the order of 10^4 cm^{-1} , indicating direct band to band transition with band gap energy 2.26 eV, close to its value of intrinsic band gap energy. The electrical characterization showed that the electrical resistivity (ρ) was of the order $10^{-3} \Omega \text{ cm}$ and decreased with increase in temperature, indicating that the samples were semiconducting in nature. The value of activation energy was found to be 0.077 eV. TEP measurement showed that the thermoelectric voltage for CdO films was positive towards the hot end, indicating n-type behavior of sample. The value of TEP increased with increase in temperature. The Hall effect measurement study revealed that the carrier concentration

(n), Hall coefficients (R_H) and carrier mobility (μ_H) were of the order of 10^{23} cm^{-3} , $10^{-8} \text{ cm}^3/\text{C}$ and $10^{-4} \text{ cm}^2/\text{V s}$, respectively (Bhosale *et al.*, 2005).

2.16.26 Recent developments in the emerging field of crystalline p-type transparent conducting oxide thin films

Ag-based delafossite thin film with p-type conductivity was reported as silver cobalt oxide (Ag_xCoO_2 ; $x < 1$) (Tate *et al.*, 2002; In Banerjee *et al.*, 2005). The film showed reasonable conductivity ($2 \times 10^{-1} \text{ S cm}^{-1}$) and almost 50% transparency in the visible region with a direct bandgap value of 4.15 eV. p-TCO films, which may open up an extremely important and interesting field of research for the fabrication of all-transparent nanoactive devices and give a new dimension in the field of transparent electronics (Banerjee *et al.*, 2005). Ag_2O is a p-type semiconductor with a smaller bandgap of approximately of 1.2 eV (Fortiu and Weichman, 1964; In Banerjee *et al.*, 2005).

2.16.27 Substrate temperature influenced structural and optical properties of RF magnetron sputtered pure and copper doped silver oxide thin films

Pure and copper doped silver oxide films were deposited on glass and silicon substrates held at temperatures in the range 303 – 473 K and at oxygen partial pressure of 2×10^{-2} Pa by reactive RF magnetron sputtering technique. Analysis of effect of substrate temperature on optical properties showed that the optical bandgap of pure Ag_2O films increased from 2.05 to 2.13 eV with increase of substrate temperature from 303 to 373 K. Optical bandgap of Cu-Ag-O films increased from 1.60 to 1.95 eV with increase of substrate temperature from 303 to 473 K. Transmittance of the films increased as the substrate temperature increased. Result of structural analysis showed that the grain size

of the Cu-Ag-O films increased from 95 to 225 nm with the increase of substrate temperature from 303 to 523 K, (Reddy and Uthanna, 2015)

2.16.28 Synthesis of silver oxide nano-scale thin films and photoactivated dynamic luminescence from their nanoparticles

Well spatial-dispersed and high purity silver oxide nanoparticles, whose size can be controlled from 5 nm to 30 nm, were prepared by vacuum thermal evaporation and glow discharge oxidation. To form island and keep samples in darkness were two key points of synthesis. Based on Ag 3d and O 1s binding energy and the ratio of silver atoms to oxide atoms given by XPS, the sample was confirmed to be Ag₂O. X-ray diffraction of Ag₂O nano-scale thin films was acquired and the strongest diffraction peaks referred to face (111), (110), (200) and (211) of Ag₂O. Absorption spectra of the samples were also studied. The absorption spectrum indicated that band gap of silver oxide is 2.8 eV. After being photo-activated by blue light for a few minutes, intermittent green and yellow photoluminescence from silver oxide nanoparticles were observed with blue excitation. Luminescence from the same region excited by green light was red and also dynamic. This phenomenon was explained by electron transitions to the impurities energy levels induced by photolytic centers (Ag³⁺O, Ag²⁺O and Ag³⁺O) in silver oxide (Xi-Yao, 2003).

2.16.29 Optical studies of Ag₂O thin film prepared by electron beam evaporation method

Silver oxide (Ag₂O) thin films were deposited on glass substrates using electron beam gun evaporation techniques without oxygen atmosphere. The deposited films were post

annealed at 100°C, 150°C, and 200°C, respectively. The surface morphologies, structural and optical properties at different annealing temperatures were studied using scanning electron microscopy (SEM), X-ray diffraction (XRD), and ultra-violet-visible spectroscopy. The XRD results showed that the intensity of (200) plane intensified as the annealing temperature increased from 100°C to 200°C. The XRD spectra revealed that the films were polycrystalline, having cubic structure irrespective of post annealing temperatures. The optical band gap of Ag₂O thin films decreased from 1.716 eV to 1.559 eV as the annealing temperature increased from 100°C to 200°C (Saroja *et al.*, 2013).

2.16.30 Structural and Optical Properties of Chemical Bath Deposited Silver Oxide Thin Films: Role of Deposition Time

Silver oxide thin films were deposited on glass substrates at a temperature of 50°C by chemical bath deposition technique under different deposition times using pure AgNO₃ precursor and triethanolamine as the complexing agent. The films were annealed at temperature of 200°C. Analysis of the work showed that the films had high transmittance in the NIR and direct bandgaps of 1.95eV, 1.64eV, 1.66eV and 1.70eV for dip times of 50mins, 70mins, 80mins and 90mins. Bandgap range of 1.01-0.93 was also obtained for the film (Raju *et al.*, 2009 ; In Nwanya *et al.*, 2013),. The film is a good material for photovoltaic application, (Nwanya *et al.*, 2013).

2.16.31 Study on the crystalline structure and the thermal stability of silver-oxide films deposited by using direct-current reactive magnetron sputtering method

Silver-oxide (Ag_xO) films were deposited on glass substrates by direct-current reactive magnetron sputtering at different oxygen flux ratios (OFR = [O₂]/[Ar]) and substrate

temperatures (T_s). An X-ray diffraction analysis indicated that the Ag_xO films were biphased ($\text{Ag} + \text{Ag}_2\text{O}$) when deposited at low OFR values and that Ag_2O -dominated Ag_xO films could only be synthesized at higher OFR values, as confirmed by X-ray photoelectron spectroscopy. This result might be due to the Ag_2O phase being preferably produced at high OFR value. The AgO phase is thermodynamically unstable compared with the Ag_2O phase. In order to further offer deep insight into the film's thermal stability, Ag_2O -dominated Ag_xO films were thermally treated by using a rapid thermal processing technique at different annealing temperatures for different annealing times. The Ag_2O phase was thermodynamically stable at temperatures below the threshold of the thermal decomposition temperature which approached 175°C . The domination of the Ag_2O phase in the Ag_xO film might be attributed to the chain reaction $\text{AgO} \rightarrow \text{Ag}_2\text{O} \leftrightarrow \text{Ag} + \text{O}$, $\text{AgO} + \text{Ag} \rightarrow \text{Ag}_2\text{O}$. A Ag_xO film with a wide energy band gap range from 1.2 to 3.4 eV could be deposited using magnetron sputtering, chemical bath deposition, electron cyclotron resonance oxygen plasma assisted e-beam evaporation of Ag , *etc.* The wide energy band gap range was due to the different stoichiometries, crystalline phases and properties arising from different deposition techniques (Hong-liang *et al.*, 2010).

2.17 Effect of annealing on crystalline and magnetic properties of semiconductor thin films

The effects of rapid thermal annealing on structural, magnetic and optical properties of Ni doped ZnO thin films was studied. A significant improvement in saturation

magnetization in the films was observed after annealing in air at 600⁰C compared to that in as-deposited film. A stronger magnetic saturation was observed after annealing in argon at 800⁰C compared to that at 600⁰C (Xing *et al.*,2012).

Annealing effects on structural and magnetic properties of Tb and Cr co-implanted AlGa_N was studied and superconducting quantum interference device (SQUID) measurements showed clear room temperature ferromagnetism behavior and an increase in the saturation magnetization as a result of annealing. The saturation magnetization of the 900⁰C annealed sample was about 15 times higher than that of 800⁰C annealed sample (Chun-Hai *et al.*,2012).

Studies on Transport and magnetic properties of LT. annealed Ga_{1-x}Mn_xAs showed that low temperature annealing introduced a rearrangement of Mn sites in Ga_{1-x}Mn_xAs . In particular, the large increase in curie temperature (T_C) accompanied by the increase of saturation magnetization and free carrier concentration could be attributed to the relocation of Mn atoms from interstitial Mn to substitutional sites or to random position. The removal of significant fraction of interstitial Mn provides explanation of the three effects observed after annealing ie, the increase of hole concentration, the increase of the curie temperature and the increase in the saturation magnetization observed at low temperature. As well known, the increase in hole concentration will automatically result in increase of curie temperature. Saturation magnetization increased after heat treatment at the optimal conditions indicating that annealing increased the concentration of magnetically active Mn ions. Conclusively, a large enhancement of ferromagnetism

for the samples annealed at optimal temperature typically about 280⁰C was observed. The increase of the Curie temperature was accompanied by an increase of conductivity and saturation magnetization (Kuryliszyn *et al.*,2002), also increase in the hole concentration(Yu *et al.*, 2002; In Kuryliszyn *et al.*,2002).

To improve ZnO thin film quality, the ZnO thin films grown on silicon (100) by plasma enhanced chemical vapour deposition from Zn(C₂H₅)₂ and CO₂ gas mixtures at a low temperature of 120°C were annealed in an oxygen ambient at temperature ranging from 600°C to 1000°C. The increase in peak intensities indicated an improvement in the crystallinity of films because it is generally noted that the crystallinity can be enhanced while increasing the annealing temperature (Zhi *et al.*,2003).

Thermal annealing effects on the magnetic properties of (Ga_{1-x}Mn_x)As with various Mn mole fractions grown on GaAs (1 0 0) substrates by using molecular beam epitaxy were investigated. When thermal annealing was performed, the ferromagnetic transition temperature (T_C) of the (Ga_{1-x}Mn_x)As thin films increased. The increase in the T_C originated from a decrease in the concentration of the Mn interstitial atoms or from an increase in the uncompensated Mn spin which contributed to the magnitude of the ferromagnetism,(Lee *et al.*, 2004).

The effect of Co incorporation into ZnO nanoparticles synthesized Co-doped ZnO nanoparticles by co-precipitation method using zinc sulfate heptahydrate (ZnSO₄·7H₂O,) , cobalt chloride hexahydrate (CoCl₂·6H₂O,) and NaOH solution was studied. The setup was maintained at pH of 12. The films were annealed at 200⁰C. Magnetic measurements showed a ferromagnetic behavior for all samples. The optical band gap was found to decrease with increasing doping concentrations, indicating a clear

red shift. All samples were found to exhibit room-temperature ferromagnetism (Djaja *et al.*, 2013).

Weak ferromagnetism in Co-doped ZnO films can be activated by post-growth vacuum annealing, changing the films from insulating to semiconducting behavior (Tuan *et al.*, 2004; In Ivill *et al.*, 2008). The role of Zn interstitials was investigated. It was found that the magnetization in Co-doped ZnO was enhanced by introducing Zn interstitials into the lattice during annealing (Khare *et al.*, 2006; In Ivill *et al.*, 2008). Annealing can be used to improve the crystal quality and confirm the stability of the crystal at a given temperature which is important for device purposes (Kuzuya *et al.*, 2005; In Nadana *et al.*, 2013). A well known procedure to improve the quality of an alloy is to subject it to a post growth heat treatment or annealing (DeBoeck *et al.*, 1996; In Mathieu, 2005). From the work, Structure and properties of Co-doped ZnO films prepared by thermal oxidization under a high magnetic field, by molecular beam vapour deposition and subsequent oxidation at 500⁰C for 30minutes, the films obtained exhibited well-defined magnetization hysteresis, implying that they are ferromagnetic at RT (Guojian *et al.*, 2015). In the work, structural, optical, and magnetic properties of Co doped CdTe alloy powders prepared by single step solid-state reaction method , sintered at 500⁰C for 6 hours under a pressure of 10⁻³ Torr, it was observed that the magnetic properties of pure and Co doped CdTe for 5% and 8 % alloy powders were investigated by magnetization measurements carried out at room temperature. Ferromagnetism in pure CdTe was not expected as it is diamagnetic in nature, whereas all the Co doped samples exhibited a

well defined magnetization hysteresis confirming ferromagnetic behaviour at room temperature. It was observed from that the saturation magnetization increased with increase in Co concentrations. The obtained magnetization for 5% and 8% of Co were 0.00086 emu/g and 0.0054 emu/g (Begam Rigana *et al.*, 2013). In the work , Effect of thickness on structural, optical, and magnetic properties of Co doped ZnO thin film by pulsed laser deposition, samples of the films at different thicknesses and annealed at 550⁰C for 1hour were grown. Result of the work showed that the films with 3% Co doping showed a superparamagnetic behaviour while a weak ferromagnetic behavior (magnetic saturation about 0.006emu/g) was obtained by increasing the concentration . The bandgap of the films decreased from 3.32eV to 3.27eV as the thickness increased. This variation of band gap values could be related to increase in crystalline size of thin films because , crystalline size rises with increase of the film thickness (quantum size effect). This change can also be attributed to the improvement in the crystals, changes of structural defects, atomic distances and grain size in the films (Kamalianfar *et al.*,2013). In their work, Structural and optical properties of CdS thin film obtained by chemical bath deposition and effect of annealing, CdS films annealed at 300⁰C for 1hr were grown. Structural characterization of the work revealed good degree of crystallization in the mixed-phase (hexagonal and cubic) which transformed to pure hexagonal phase on annealing with improved crystallinity (Pushpalatha *et al.*, 2014).

2.18 The effect of dopant concentration on bandgap of semiconductor thin films

Structural and optical properties of cobalt-doped zinc oxide thin films prepared by spray pyrolysis technique was studied. It was observed that the optical band gap decreased with increasing Co concentration (Erhaima *et al.*, 2010). The decrease in optical band gap is mainly due to the sp–d exchange interaction between the localized d-electrons of Co^{2+} ions and band electrons of ZnO (Kumar *et al.*, 2009; In Erhaima *et al.*, 2010).

Result of studies on the structural and optical properties of undoped and co doped ZnO nanostructured thin films, showed that due to the exchange interaction between the localized d shell electrons of the magnetic ions and the delocalized band states, the optical band gap E_g decreased from 3.20eV to 3.0 eV for the increasing doping concentration (Nirmala and Anukaliani, 2010).

Based on the research on Effect of Co doping on structural, morphological, electrical and optical properties of nanocrystalline zinc oxide films, it was observed that as the cobalt doping increased, the values of band gap decreased (Girjesh *et al.*,2013) .This may be attributed to the sp-d exchange interactions between the band electrons and the localized electrons of the Co^{2+} ions (Diouri *et al.*, 1985; In Girjesh *et al.*,2013).

2.19 Effect of thickness on bandgap

The study on the Effect of thickness on the optical band gap of silver telluride thin films, showed that the band gap of silver telluride thin films was thickness dependent. It decreased with the increase in film thickness. Silver telluride thin films were

polycrystalline. In thin films, the particle size of crystallites is of the order of film thickness and proportional to thickness of films. Since grain size influences the energy level of electrons, the band gap will be dependent on thickness of films (Pandiaraman *et al.*,2011).

Result of the work on the Effect of film thickness on optical properties of tin selenide thin films prepared by thermal evaporation for photovoltaic applications showed that optical energy bandgap decreased from 1.74eV to 1.24eV as the film thickness increased from 150nm to 500nm which showed its capability to be used as absorber layer in photovoltaic application. It was observed that crystalline size increased from 15nm to 23nm with the increase in film thickness from 150nm to 500nm. The film showed decrease in resistance with increasing temperature showing semiconductor behavior (Kumar *et al.*, 2012).

In the research, Optical properties of ZnS thin films, different thicknesses of the film were deposited on corning glass substrate at room temperature using resistive heating technique. Result of the work showed that bandgap of the films decreased with increasing thickness of the films (Nadeem and Ahmed, 2000).

2.20 Effect of Cobalt doping on thickness of thin film

In the work, Co doping induced structural and optical properties of sol–gel prepared ZnO thin films, obtained results showed increase of film thickness with increasing cobalt dopant concentration (Ebru *et al.*,2014).

Result of the work on Effect of manganese percentage doping on thickness and conductivity of zinc sulphide nanofilms prepared by electrodeposition method, using $ZnCl_2$, $MnCl_2 \cdot 2H_2O$, triethanolamine to prepare the nanofilms, with Mn percentage doping of 3%, 8%, 13%, 18% and 23% showed that the thickness of ZnMnS films increased from 14.67nm to 92.48nm as Mn percentage doping increased from 3% to 8% and then decreased to 31.80nm as percentage increased to 23% (Okafor *et al.*, 2015)

2.21 Bandgap bowing parameter

The bandgap of an alloy is a continuous function of composition. In ternary alloy, the variation with composition is linear if the two constituents that are varied have nearly the same atomic radii and the same bonding strength to the third constituent. When the characteristic parameters of the two constituents are significantly different, bowing of the bandgap occurs (Balkanski and Wallis, 2000).

For many semiconductor alloys, bowing parameter is positive (Boer, 1990; In Balkanski and Wallis, 2000). A positive value of bowing parameter represents a downward bowing and negative value represents an upward bowing, (Yun *et al.*, 2002). The bowing parameter is significant for investigating the bandgap energy of ternary alloys (Gulebagian *et al.*, 2014)

The bandgap energy of the $Al_xIn_{1-x}N$ can be approximated by the following formula:

$$E_g(x) = x \cdot E_{g,AlN} + (1-x) \cdot E_{g,InN} - b \cdot x \cdot (1-x) \quad (2.19)$$

where $E_g(x)$ is the bandgap energy of the $Al_xIn_{1-x}N$, E_g,AlN is the bandgap energy of the AlN, E_g,InN is the bandgap energy of the InN, and b is the bandgap bowing parameter (Wen-Wei and Yen-Kuang, 2002).

The energy-gap bowing parameter is calculated by the following definition,

$$E_g(A_xB_{1-x}) = x \cdot E_g(A) + (1 - x) \cdot E_g(B) - b(x) \cdot x \cdot (1 - x) \quad (2.20)$$

where $E_g(A)$ and $E_g(B)$ are the calculated pure constituent energy-gaps, and $E_g(A_xB_{1-x})$ is the calculated alloy energy-gap at boron content x (Xiong *et al.*, 2008). The bowing parameter is strongly composition dependent. For composition, $x = 0.0625, 0.125$ and 0.25 , bowing parameters obtained were $4.8\text{eV}, 3.5\text{eV}$, and 3.0eV respectively (Van de walley *et al.*, 1999). Composition $x = 6.125\%$ and 12.5% , had bowing parameters of 2.29eV and 1.79eV respectively (Moses and Van de Walle, 2010).

2.22 Magnetic susceptibility

Magnetic susceptibility (χ) of a specimen measures the ease with which the specimen can be magnetized and can be defined as the ratio of intensity of magnetization introduced in it and the magnetizing field, i.e.,

$$\chi = \frac{I}{H} \quad (2.21)$$

Where I is intensity of magnetization and H is the magnetizing field (Gaur and Gupta, 2007). Susceptibility $\chi = \frac{dM}{dH}$ is slope of $M(H)$ curve (Youssif *et al.*, 2000)

For materials whose magnetization, M , depends linearly on applied field, H , the susceptibility χ is defined by the formular

$$M = \chi H. \quad (2.22)$$

Magnetic susceptibility of diamagnetic materials ranges from -1 to -10^{-5} , Paramagnetic ranges from 10^{-5} to 10^{-2} , ferromagnetic ranges from 10^{-2} to 10^6 (John, 1996).

Magnetic susceptibility (χ), is a parameter that demonstrates the type of magnetic material and the strength of that type of magnetic effect.

$$\chi = \frac{M}{H} \quad (2.23)$$

Where M is the magnetization and H is the applied field.

Magnetic susceptibility measures the magnetisability of a material. Classification of materials according to magnetic susceptibility is as shown in Tables 2.1 and 2.2

Table 2.1: Classification of materials

Material	Magnetic susceptibility
Diamagnetic	Small and negative, eg, -2.74×10^{-6} for gold,
Paramagnetic	Small and positive, eg, 21.04×10^{-6} for platinum
Antiferromagnetic	Small and positive,
Ferrimagnetic	Large and positive. Function of applied field and microstructure eg Ba ferrite up to 3
Ferromagnetic	Large and positive, function of applied field and microstructure dependant,

(Harris and Williams, 2009).

In diamagnetic materials, the susceptibility is negative, usually its magnitude of the order -10^{-6} to -10^{-5}

. The negative value of the susceptibility means that in an applied magnetic field, diamagnetic materials acquire the magnetization which is pointed opposite to the applied field. In paramagnetic materials, magnetic susceptibility is positive and very small, 10^{-5} to 10^{-4} . Antiferromagnetic materials have small positive susceptibilities at all temperatures.(Tsymbal, 2015)

Table 2.2: Classification of materials according to magnetic susceptibility

Material	Magnetic susceptibility	Class of material
H ₂ O	-8×10^{-6}	Diamagnetic
Cu	-10^{-5}	Diamagnetic
Al	2×10^{-5}	Paramagnetic
Iron (depends on purity)	$\approx 100 - 1000$	Ferromagnetic

(Scheffler *et al.*, 2012)

CHAPTER THREE

MATERIALS AND METHOD

3.1 Over-view

This research employed electrodeposition technique to deposit nanofilms of some magnetic oxide semiconductors namely nickel cobalt oxides, magnesium cobalt oxides , cadmium cobalt oxides and silver cobalt oxides. This was achieved by doping the appropriate precursors with hydrated cobalt chloride salt in the presence of citric acid as oxidizing agent , sodium hydroxide as pH adjuster and ITO as deposition substrate. In each case three parameters were varied namely, percentage doping, deposition voltage and deposition time. The films were characterized for their optical, magnetic and structural properties and their possible applications deduced. The undoped nanofilms namely nickel oxide, magnesium oxide, cadmium oxide and silver oxides were also deposited and their optical properties also determined. The deposition apparatus is as shown in fig. 3.1.

3.2 Slide Preparation: ITO used as deposition substrates were washed with detergent and rinsed three times with distilled water. They were soaked in acetone for fifteen minutes to degrease them, and then rinsed in distilled water three times. The substrates were immersed in a beaker almost half-full of distilled water and put inside ultrasonic bath for ten minutes. After this step, clean forceps were used to bring them out, and put in another clean dry beaker and then put inside the oven for ten minutes for drying. The slides ready for use were handled with clean forceps to avoid contamination.

3.3 Electrodeposition apparatus



Figure 3.1: Electrodeposition apparatus

This apparatus consists of three electrodes viz; cathode, carbon anode and saturated calomel electrode serving as reference electrode. The ITO substrate was mounted as the cathode. These electrodes were contained in the small beaker serving as reaction container which also contained the precursors. Other components are two multimeters and the voltage supply unit for the electrical connection.

3.4 Deposition of NiO nanofilm

The precursors for deposition of nanofilm of NiO were heptahydrated nickel tetraoxosulphate (VI) salt as source of nickel ion, citric acid as oxidizing agent and sodium hydroxide as pH adjuster. The deposition was carried out at room temperature of 30°C (303K), pH of 8.6, deposition time of 10min, deposition voltage of 10V, particular concentration and volume of citric acid, sodium hydroxide, $\text{NiSO}_4 \cdot 7\text{H}_2\text{O}$ as shown in Table 3.1. The deposited films were annealed at 200°C for 30 min.

Table 3.1: Deposition of NiO nanofilm

Reaction Bath	$\text{NiSO}_4 \cdot 7\text{H}_2\text{O}$		Citric acid		NaOH		Deposition voltage(V)	pH	Time (mins)
	Conc.(M)	Vol.(ml)	Conc.(M)	Vol.(ml)	Conc.(M)	Vol.(ml)			
N_{53}	0.046	15	0.05	30	1	6	10	8.6	10

3.5 Deposition of MgO nanofilm

The precursors for deposition of nanofilm of MgO were heptahydrated magnesium tetraoxosulphate (VI) salt as source of magnesium ion, citric acid as oxidizing agent and sodium hydroxide as pH adjuster. The deposition was carried out at room temperature of 30⁰C (303K) , pH of 8.6, deposition time of 10min, deposition voltage of 10V, particular concentration and volume of citric acid, sodium hydroxide and MgSO₄.7H₂O as shown in Table 3.2. The deposited films were annealed at 200⁰C for 30 min.

Table 3.2: Deposition of MgO nanofilm

Reaction Bath	MgSO ₄ .7H ₂ O		Citric acid		NaOH		Deposition voltage(V)	pH	Time (mins)
	Conc.(M)	Vol.(ml)	Conc.(M)	Vol.(ml)	Conc.(M)	Vol.(ml)			
N ₅₄	0.046	15	0.05	30	1	6	10	8.6	10

3.6 Deposition of CdO nanofilm

The precursors for deposition of nanofilm of CdO were hydrated cadmium chloride salt as source of cadmium ion, citric acid as oxidizing agent and sodium hydroxide as pH adjuster. The deposition was carried out at room temperature of 30⁰C (303K) , pH of 8.6, deposition time of 10min, deposition voltage of 10V, particular concentration and volume of citric acid, sodium hydroxide and CdCl₂.2H₂O as shown in Table 3.3. The deposited films were annealed at 200⁰C for 30 min.

Table 3.3: Deposition of CdO nanofilm

Reaction bath	CdCl ₂ .2H ₂ O		Citric acid		NaOH		Deposition voltage(V)	pH	Time (mins)
	Conc.(M)	Vol.(ml)	Conc.(M)	Vol.(ml)	Conc.(M)	Vol.(ml)			
N ₅₅	0.046	15	0.05	30	1	6	10	8.6	10

3.7 Deposition of AgO nanofilm

The precursors for deposition of nanofilm of AgO were silver trioxonitrate (V) salt as source of silver ion, citric acid as oxidizing agent and sodium hydroxide as pH adjuster. The deposition was carried out at room temperature of 30⁰C (303K) , pH of 8.6, deposition time of 45s, deposition voltage of 0.5V, particular

concentration and volume of citric acid, sodium hydroxide and AgNO_3 as shown in Table 3.4. The deposited films were annealed at 200°C for 30 min.

Table 3.4: Deposition of AgO nanofilm

Reaction bath	AgNO_3		Citric acid		NaOH		Deposition voltage(V)	pH	Time (secs)
	Conc.(M)	Vol.(ml)	Conc.(M)	Vol.(ml)	Conc.(M)	Vol.(ml)			
N ₅₆	0.046	15	0.05	30	1	6	0.5	8.6	45

3.8 Deposition of nickel cobalt oxide nanofilms

Various nanofilms of cobalt doped nickel oxide are to be deposited by variation of percentage doping, deposition voltage and deposition time by varying the appropriate parameters in each case.

3.8.1 Variation of percentage doping for nickel cobalt oxide nanofilms

The precursors for deposition of nanofilms of NiCo_2O_4 with various percentages of cobalt dopant were heptahydrated nickel tetraoxosulphate (VI) salt as source of nickel ion, citric acid as oxidizing agent, hexahydrated cobalt chloride salt as source of cobalt ion and sodium hydroxide as pH adjuster. The deposition was carried out at room temperature of 30°C (303K) using laboratory thermometer for temperature measurement, pH of 8.6 using pH meter, deposition time of 10min using stop watch, deposition voltage of 10V, constant concentrations and volumes of citric acid, sodium hydroxide and various concentrations of $\text{NiSO}_4 \cdot 7\text{H}_2\text{O}$ and $\text{CoCl}_2 \cdot 6\text{H}_2\text{O}$ in accordance with their percentage doping as shown in Table 3.5. The percentage doping was chosen to run from 3% to 23% in intervals of 5% while the concentration of dopant and host precursor was determined using the relation; $\text{Ni}_{1-x}\text{Co}_x\text{O}_4$

Concentration of dopant = x , Concentration of host precursor = 1-x , As x is in percentage,

$1-x \Rightarrow 100 - x\%$. The volumes were measured with measuring cylinder. The deposited films were annealed at 200°C for 30 min in the oven.

Table 3.5: Variation of percentage doping for NiCo₂O₄ nanofilms

Reaction bath	NiSO ₄ .7H ₂ O		Citric acid		CoCl ₂ .6H ₂ O		NaOH		Deposition voltage(V)	pH	Doping (%)	Time (mins)
	Conc.(M)	Vol.(ml)	Conc.(M)	Vol.(ml)	Conc.(M)	Vol.(ml)	Conc.(M)	Vol.(ml)				
N ₁₀	0.0485	15	0.05	30	0.0015	15	1	6	10	8.6	3	10
N ₁	0.0460	15	0.05	30	0.0040	15	1	6	10	8.6	8	10
N ₁₁	0.0435	15	0.05	30	0.0065	15	1	6	10	8.6	13	10
N ₁₂	0.0410	15	0.05	30	0.0090	15	1	6	10	8.6	18	10
N ₁₃	0.0385	15	0.05	30	0.0115	15	1	6	10	8.6	23	10

3.8.2 Variation of deposition voltage for nickel cobalt oxide nanofilms

The precursors for deposition of nanofilms of NiCo₂O₄ at various deposition voltages were heptahydrated nickel tetraoxosulphate (VI) salt as source of nickel ion, citric acid as oxidizing agent, hexahydrated cobalt chloride salt as source of cobalt ion and sodium hydroxide as pH adjuster. The deposition was carried out at room temperature of 30⁰C (303K) , pH of 8.6, deposition time of 10min, percentage doping of 8%, constant concentrations and volumes of citric acid, sodium hydroxide, NiSO₄.7H₂O and CoCl₂.6H₂O and varying deposition voltage as shown in Table 3.6. The deposited films were annealed at 200⁰C for 30 min.

Table 3.6: Variation of deposition voltage for NiCo₂O₄ nanofilms

Reaction bath	NiSO ₄ .7H ₂ O		Citric acid		CoCl ₂ .6H ₂ O		NaOH		Deposition voltage(V)	pH	Doping (%)	Time (mins)
	Conc.(M)	Vol.(ml)	Conc.(M)	Vol.(ml)	Conc.(M)	Vol.(ml)	Conc.(M)	Vol.(ml)				
N ₆	0.046	15	0.05	30	0.004	15	1	6	8.5	8.6	8	10
N ₁	0.046	15	0.05	30	0.004	15	1	6	10.0	8.6	8	10
N ₇	0.046	15	0.05	30	0.004	15	1	6	11.5	8.6	8	10
N ₈	0.046	15	0.05	30	0.004	15	1	6	13.0	8.6	8	10
N ₉	0.046	15	0.05	30	0.004	15	1	6	14.5	8.6	8	10

3.8.3 Variation of deposition time for nickel cobalt oxide nanofilms

The precursors for deposition of nanofilms of NiCo₂O₄ at various deposition times were heptahydrated nickel tetraoxosulphate (VI) salt as source of nickel ion, citric acid as oxidizing agent, hexahydrated cobalt chloride salt as source of cobalt ion and sodium hydroxide as pH adjuster. The deposition was carried out at room temperature of 30⁰C (303K) , pH of 8.6, deposition voltage of 10V, percentage doping of 8%,

constant concentrations and volumes of citric acid, Sodium hydroxide, NiSO₄.7H₂O and CoCl₂.6H₂O and varying deposition time as shown in Table 3.7. The deposited films were annealed at 200⁰C for 30 min.

Table 3.7: Variation of deposition time for NiCo₂O₄ nanofilms

Reaction bath	NiSO ₄ .7H ₂ O		Citric acid		CoCl ₂ .6H ₂ O		NaOH		Deposition voltage(V)	pH	Doping (%)	Time (mins)
	Conc.(M)	Vol.(ml)	Conc.(M)	Vol.(ml)	Conc.(M)	Vol.(ml)	Conc.(M)	Vol.(ml)				
N ₅	0.046	15	0.05	30	0.004	15	1	6	10.0	8.6	8	5.0
N ₁	0.046	15	0.05	30	0.004	15	1	6	10.0	8.6	8	10
N ₂	0.046	15	0.05	30	0.004	15	1	6	10.0	8.6	8	15
N ₃	0.046	15	0.05	30	0.004	15	1	6	10.0	8.6	8	20
N ₄	0.046	15	0.05	30	0.004	15	1	6	10.0	8.6	8	25

3.9 Deposition of magnesium cobalt oxide nanofilms

Various nanofilms of cobalt doped magnesium cobalt oxide are to be deposited by variation of percentage doping, deposition voltage and deposition time by varying the appropriate parameters in each case.

3.9.1 Variation of percentage doping for magnesium cobalt oxide nanofilms

The precursors for deposition of nanofilms of MgCo₂O₄ with various percentages of cobalt dopant were heptahydrated magnesium tetraoxosulphate (VI) salt as source of magnesium ion, citric acid as oxidizing agent, hexahydrated cobalt chloride salt as source of cobalt ion and sodium hydroxide as pH adjuster. The deposition was carried out at room temperature of 30⁰C (303K) using laboratory thermometer for temperature measurement, pH of 8.6 using pH meter, deposition time of 10min using stop watch, deposition voltage of 10V, constant concentrations and volumes of citric acid, sodium hydroxide and various concentrations of MgSO₄.7H₂O and CoCl₂.6H₂O in accordance with their percentage doping as shown in Table 3.8. The percentage doping was chosen to run from 3% to 23% in intervals of 5% while the concentration of dopant and host precursor was determined using the relation; Mg_{1-x}Co_xO₄

Concentration of dopant = x , concentration of host precursor = $1-x$, as x is in percentage, $1-x = 100- x\%$,
 The volumes were measured with measuring cylinder. The deposited films were annealed at 200°C for 30 min..

Table 3.8: Variation of percentage doping for MgCo_2O_4 nanofilms

Reaction bath	$\text{MgSO}_4 \cdot 7\text{H}_2\text{O}$		Citric acid		$\text{CoCl}_2 \cdot 6\text{H}_2\text{O}$		NaOH		Deposition voltage(V)	pH	Doping (%)	Time (mins)
	Conc.(M)	Vol.(ml)	Conc.(M)	Vol.(ml)	Conc.(M)	Vol.(ml)	Conc.(M)	Vol.(ml)				
N ₂₃	0.0485	15	0.05	30	0.0015	15	1	6	10	8.6	3	10
N ₁₄	0.0460	15	0.05	30	0.0040	15	1	6	10	8.6	8	10
N ₂₄	0.0435	15	0.05	30	0.0065	15	1	6	10	8.6	13	10
N ₂₅	0.0410	15	0.05	30	0.0090	15	1	6	10	8.6	18	10
N ₂₆	0.0385	15	0.05	30	0.0115	15	1	6	10	8.6	23	10

3.9.2 Variation of deposition voltage for magnesium cobalt oxide nanofilms

The precursors for deposition of nanofilms of MgCo_2O_4 at various deposition voltages were heptahydrated magnesium tetraoxosulphate (VI) salt as source of magnesium ion, citric acid as oxidizing agent, hexahydrated cobalt chloride salt as source of cobalt ion and sodium hydroxide as pH adjuster. The deposition was carried out at room temperature of 30°C (303K) , pH of 8.6, deposition time of 10 min, percentage doping of 8%, constant concentrations and volumes of citric acid, sodium hydroxide, $\text{MgSO}_4 \cdot 7\text{H}_2\text{O}$ and $\text{CoCl}_2 \cdot 6\text{H}_2\text{O}$ and varying deposition voltage as shown in Table 3.9. The deposited films were annealed at 200°C for 30 min.

Table 3.9: Variation of deposition voltage for MgCo_2O_4 nanofilms

Reaction bath	$\text{MgSO}_4 \cdot 7\text{H}_2\text{O}$		Citric acid		$\text{CoCl}_2 \cdot 6\text{H}_2\text{O}$		NaOH		Deposition voltage(V)	pH	Doping (%)	Time (mins)
	Conc.(M)	Vol.(ml)	Conc.(M)	Vol.(ml)	Conc.(M)	Vol.(ml)	Conc.(M)	Vol.(ml)				
N ₂₂	0.046	15	0.05	30	0.004	15	1	6	7.0	8.6	8	10
N ₁₉	0.046	15	0.05	30	0.004	15	1	6	8.5	8.6	8	10
N ₁₄	0.046	15	0.05	30	0.004	15	1	6	10.0	8.6	8	10
N ₂₀	0.046	15	0.05	30	0.004	15	1	6	11.5	8.6	8	10
N ₂₁	0.046	15	0.05	30	0.004	15	1	6	13.0	8.6	8	10

3.9.3 Variation of deposition time for magnesium cobalt oxide nanofilms

The precursors for deposition of nanofilms of MgCo_2O_4 at various deposition times were heptahydrated magnesium tetraoxosulphate (VI) salt as source of magnesium ion, citric acid as oxidizing agent, hexahydrated cobalt chloride salt as source of cobalt ion and sodium hydroxide as pH adjuster. The deposition was carried out at room temperature of 30°C (303K), pH of 8.6, deposition voltage of 10V, percentage doping of 8%, constant concentrations and volumes of citric acid, sodium hydroxide, $\text{MgSO}_4 \cdot 7\text{H}_2\text{O}$ and $\text{CoCl}_2 \cdot 6\text{H}_2\text{O}$ and varying deposition time as shown in Table 3.10. The deposited films were annealed at 200°C for 30 min.

Table 3.10: Variation of deposition time for MgCo_2O_4 nanofilms

Reaction bath	$\text{MgSO}_4 \cdot 7\text{H}_2\text{O}$		Citric acid		$\text{CoCl}_2 \cdot 6\text{H}_2\text{O}$		NaOH		Deposition voltage(V)	pH	Doping (%)	Time (mins)
	Conc.(M)	Vol.(ml)	Conc.(M)	Vol.(ml)	Conc.(M)	Vol.(ml)	Conc.(M)	Vol.(ml)				
N ₁₈	0.046	15	0.05	30	0.004	15	1	6	10	8.6	8	5
N ₁₄	0.046	15	0.05	30	0.004	15	1	6	10	8.6	8	10
N ₁₅	0.046	15	0.05	30	0.004	15	1	6	10	8.6	8	15
N ₁₆	0.046	15	0.05	30	0.004	15	1	6	10	8.6	8	20
N ₁₇	0.046	15	0.05	30	0.004	15	1	6	10	8.6	8	25

3.10 Deposition of cadmium cobalt oxide nanofilms

Various nanofilms of cobalt doped cadmium cobalt oxide are to be deposited by variation of percentage doping, deposition voltage and deposition time by varying the appropriate parameters in each case.

3.10.1 Variation of percentage doping for cadmium cobalt oxide nanofilms

The precursors for deposition of nanofilms of CdCo_2O_4 with various percentages of cobalt dopant were hydrated cadmium chloride salt as source of cadmium ion, citric acid as oxidizing agent, hexahydrated cobalt chloride salt as source of cobalt ion and sodium hydroxide as pH adjuster. The deposition was carried out at room temperature of 30°C (303K) using laboratory thermometer for temperature measurement, pH of 8.6 using pH meter, deposition time of 10min using stop watch, deposition voltage of

10V, constant concentrations and volumes of citric acid, sodium hydroxide and various concentrations of $\text{CdCl}_2 \cdot 2\text{H}_2\text{O}$ and $\text{CoCl}_2 \cdot 6\text{H}_2\text{O}$ in accordance with their percentage doping as shown in Table 3.11. The percentage doping was chosen to run from 3% to 23% in intervals of 5% while the concentration of dopant and host precursor was determined using the relation; $\text{Cd}_{1-x}\text{Co}_x\text{O}_4$

Concentration of dopant = x , concentration of host precursor = 1-x , as x is in percentage, 1-x = 100- x%.

The volumes were measured with measuring cylinder. The deposited films were annealed at 200°C for 30 min.

Table 3.11: Variation of percentage doping for CdCo_2O_4 nanofilms

Reaction bath	$\text{CdCl}_2 \cdot 2\text{H}_2\text{O}$		Citric acid		$\text{CoCl}_2 \cdot 6\text{H}_2\text{O}$		NaOH		Deposition voltage(V)	pH	Doping (%)	Time (mins)
	Conc.(M)	Vol.(ml)	Conc.(M)	Vol.(ml)	Conc.(M)	Vol.(ml)	Conc.(M)	Vol.(ml)				
N ₂₇	0.0485	15	0.05	30	0.0015	15	1	6	10	8.6	3	10
N ₂₈	0.0460	15	0.05	30	0.0040	15	1	6	10	8.6	8	10
N ₂₉	0.0435	15	0.05	30	0.0065	15	1	6	10	8.6	13	10
N ₃₀	0.0410	15	0.05	30	0.0090	15	1	6	10	8.6	18	10
N ₃₁	0.0385	15	0.05	30	0.0115	15	1	6	10	8.6	23	10

3.10.2 Variation of deposition voltage for cadmium cobalt oxide nanofilms

The precursors for deposition of nanofilms of CdCo_2O_4 at various deposition voltages are hydrated cadmium chloride salt as source of cadmium ion, citric acid as oxidizing agent, hexahydrated cobalt chloride salt as source of cobalt ion and sodium hydroxide as pH adjuster. The deposition was carried out at room temperature of 30°C (303K) , pH of 8.6, deposition time of 10min, percentage doping of 8%, constant concentrations and volumes of citric acid, sodium hydroxide, $\text{CdCl}_2 \cdot 2\text{H}_2\text{O}$ and $\text{CoCl}_2 \cdot 6\text{H}_2\text{O}$ and varying deposition voltage as shown in Table 3.12. The deposited films were annealed at 200°C for 30 min.

Table 3.12: Variation of deposition voltage for CdCo_2O_4 nanofilms

Reaction bath	$\text{CdCl}_2 \cdot 2\text{H}_2\text{O}$		Citric acid		$\text{CoCl}_2 \cdot 6\text{H}_2\text{O}$		NaOH		Deposition voltage(V)	pH	Doping (%)	Time (mins)
	Conc.(M)	Vol.(ml)	Conc.(M)	Vol.(ml)	Conc.(M)	Vol.(ml)	Conc.(M)	Vol.(ml)				
N ₃₅	0.046	15	0.05	30	0.004	15	1	6	7.0	8.6	8	10
N ₃₂	0.046	15	0.05	30	0.004	15	1	6	8.5	8.6	8	10
N ₂₈	0.046	15	0.05	30	0.004	15	1	6	10.0	8.6	8	10
N ₃₃	0.046	15	0.05	30	0.004	15	1	6	11.5	8.6	8	10
N ₃₄	0.046	15	0.05	30	0.004	15	1	6	13.0	8.6	8	10

3.10.3 Variation of deposition time for cadmium cobalt oxide nanofilms

The precursors for deposition of nanofilms of CdCo_2O_4 at various deposition times are hydrated cadmium chloride salt as source of chloride ion, citric acid as oxidizing agent, hexahydrated cobalt chloride salt as source of cobalt ion and sodium hydroxide as pH adjuster. The deposition was carried out at room temperature of 30°C (303K), pH of 8.6, deposition voltage of 10V, percentage doping of 8%, constant concentrations and volumes of citric acid, sodium hydroxide, $\text{CdCl}_2 \cdot 2\text{H}_2\text{O}$ and $\text{CoCl}_2 \cdot 6\text{H}_2\text{O}$ and varying deposition time as shown in Table 3.13. The deposited films were annealed at 200°C for 30 min.

Table 3.13: Variation of deposition time for CdCo_2O_4 nanofilms

Reaction bath	$\text{CdCl}_2 \cdot 2\text{H}_2\text{O}$		Citric acid		$\text{CoCl}_2 \cdot 6\text{H}_2\text{O}$		NaOH		Deposition voltage(V)	pH	Doping (%)	Time (mins)
	Conc.(M)	Vol.(ml)	Conc.(M)	Vol.(ml)	Conc.(M)	Vol.(ml)	Conc.(M)	Vol.(ml)				
N ₃₉	0.046	15	0.05	30	0.004	15	1	6	10	8.6	8	5
N ₂₈	0.046	15	0.05	30	0.004	15	1	6	10	8.6	8	10
N ₃₆	0.046	15	0.05	30	0.004	15	1	6	10	8.6	8	15
N ₃₇	0.046	15	0.05	30	0.004	15	1	6	10	8.6	8	20
N ₃₈	0.046	15	0.05	30	0.004	15	1	6	10	8.6	8	25

3.11 Deposition of silver cobalt oxide nanofilms

Various nanofilms of cobalt doped silver cobalt oxide were to be deposited by variation of percentage doping, deposition voltage and deposition time by varying the appropriate parameters in each case.

3.11.1 Variation of percentage doping for silver cobalt oxide nanofilms

The precursors for deposition of nanofilms of AgCoO_2 with various percentages of cobalt dopant were silver trioxonitrate (V) salt as source of silver ion, citric acid as oxidizing agent, hexahydrated cobalt chloride salt as source of cobalt ion and sodium hydroxide as pH adjuster. The deposition was carried out at room temperature of 30°C (303K) using laboratory thermometer for temperature measurement, pH of 8.6 using pH meter, deposition time of 45s using stop watch, deposition voltage of 0.5V, constant concentrations and volumes of citric acid, sodium hydroxide and various concentrations of AgNO_3 and $\text{CoCl}_2 \cdot 6\text{H}_2\text{O}$ in accordance with their percentage doping as shown in Table 3.14. The percentage doping

was chosen to run from 3% to 23% in intervals of 5% while the concentration of dopant and host precursor was determined using the relation; $Ag_{1-x}Co_xO_2$

Concentration of dopant = x , concentration of host precursor = $1-x$, as x is in percentage, $1-x = 100- x\%$. The volumes were measured with measuring cylinder. The deposited films were annealed at $200^{\circ}C$ for 30 min.

Table 3.14: Variation of percentage doping for $AgCoO_2$ nanofilms

Reaction Bath	AgNO ₃		Citric acid		CoCl ₂ .6H ₂ O		NaOH		Deposition voltage(V)	pH	Doping (%)	Time (secs)
	Conc.(M)	Vol.(ml)	Conc.(M)	Vol.(ml)	Conc.(M)	Vol.(ml)	Conc.(M)	Vol.(ml)				
N ₄₀	0.0485	15	0.05	30	0.0015	15	1	6	0.5	8.6	3	45
N ₄₁	0.0460	15	0.05	30	0.0040	15	1	6	0.5	8.6	8	45
N ₄₂	0.0435	15	0.05	30	0.0065	15	1	6	0.5	8.6	13	45
N ₄₃	0.0410	15	0.05	30	0.0090	15	1	6	0.5	8.6	18	45
N ₄₄	0.0385	15	0.05	30	0.0115	15	1	6	0.5	8.6	23	45

3.11.2 Variation of deposition voltage for silver cobalt oxide nanofilms

The precursors for deposition of nanofilms of $AgCoO_2$ at various deposition voltages are silver trioxonitrate (V) salt as source of silver ion, citric acid as oxidizing agent, hexahydrated cobalt chloride salt as source of cobalt ion and sodium hydroxide as pH adjuster. The deposition was carried out at, room temperature of 303K , pH of 8.6, deposition time of 45s, percentage doping of 8%, constant concentrations and volumes of citric acid, sodium hydroxide, AgNO₃ and CoCl₂.6H₂O and varying deposition voltage as shown in Table 3.15. The deposited films were annealed at $200^{\circ}C$ for 30 min..

Table 3.15: Variation of deposition voltage for $AgCoO_2$ nanofilms

Reaction bath	AgNO ₃		Citric acid		CoCl ₂ .6H ₂ O		NaOH		Deposition voltage(V)	pH	Doping (%)	Time (secs)
	Conc.(M)	Vol.(ml)	Conc.(M)	Vol.(ml)	Conc.(M)	Vol.(ml)	Conc.(M)	Vol.(ml)				
N ₄₈	0.046	15	0.05	30	0.004	15	1	6	0.1	8.6	8	45
N ₄₁	0.046	15	0.05	30	0.004	15	1	6	0.5	8.6	8	45
N ₄₅	0.046	15	0.05	30	0.004	15	1	6	1.0	8.6	8	45
N ₄₆	0.046	15	0.05	30	0.004	15	1	6	1.5	8.6	8	45
N ₄₇	0.046	15	0.05	30	0.004	15	1	6	2.0	8.6	8	45

3.11.3 Variation of deposition time for silver cobalt oxide nanofilms

The precursors for deposition of nanofilms of AgCoO_2 at various deposition times are hydrated silver trioxonitrate (V) salt as source of silver ion, citric acid as oxidizing agent, hexahydrated cobalt chloride salt as source of cobalt ion and sodium hydroxide as pH adjuster. The deposition was carried out at room temperature of 30°C (303K), pH of 8.6, deposition voltage of 0.5V, percentage doping of 8%, constant concentrations and volumes of citric acid, sodium hydroxide, AgNO_3 and $\text{CoCl}_2 \cdot 6\text{H}_2\text{O}$ and varying deposition time as shown in Table 3.16. The deposited films were annealed at 200°C for 30 min.

Table 3.16: Variation of deposition time for AgCoO_2 nanofilms

Reaction bath	AgNO_3		Citric acid		$\text{CoCl}_2 \cdot 6\text{H}_2\text{O}$		NaOH		Deposition voltage(V)	pH	Doping (%)	Time (secs)
	Conc.(M)	Vol.(ml)	Conc.(M)	Vol.(ml)	Conc.(M)	Vol.(ml)	Conc.(M)	Vol.(ml)				
N ₄₉	0.046	15	0.05	30	0.004	15	1	6	0.5	8.6	8	15
N ₅₀	0.046	15	0.05	30	0.004	15	1	6	0.5	8.6	8	30
N ₄₁	0.046	15	0.05	30	0.004	15	1	6	0.5	8.6	8	45
N ₅₁	0.046	15	0.05	30	0.004	15	1	6	0.5	8.6	8	60
N ₅₂	0.046	15	0.05	30	0.004	15	1	6	0.5	8.6	8	75

3.12 Optical characterization of the nanofilms.

The films were characterized for absorbance and transmittance with UV/Visible spectrophotometer; JENWAY 6405 UV-Visible. Other optical properties like reflectance, extinction coefficient, refractive index, complex dielectric constant and optical conductivity were analyzed using appropriate mathematical tool as stated on 3.16

3.13 Compositional characterization

This was done on the doped samples with X-ray fluorescence spectrometer.

3.14 Thickness characterization

This was carried out with profilometer, Model; Veeco Dektak 150

3.15 Magnetic property characterization

This was carried out on the doped samples with microsense VSM system, EZ7

3.16 Mathematical tools for analysis of optical properties

The following mathematical tools were employed in the analysis of the following optical properties

3.16.1 Reflectance

The Reflectance of the films was calculated using the relation:

$$R = 1 - (A + T) \quad 3.1$$

Where A is absorbance, T is transmittance (Rubby and Suman, 2011), however, the absorbance and transmittance were obtained by the spectrophotometer measurement.

3.16.2 Refractive index (n)

The refractive index of the films was calculated using the relation:

$$n = \frac{1+\sqrt{R}}{1-\sqrt{R}} \quad 3.2$$

where R is reflectance (Rubby and Suman, 2011).

3.16.3 Absorption coefficient (α)

The absorption coefficient of the films was calculated using the relation given by:

$$\alpha = \frac{A}{\lambda} \quad 3.3$$

Where A is absorbance and λ is wavelength

3.16.4 Extinction coefficient (k)

Extinction coefficient of the films was determined using the relation:

$$k = \frac{\alpha\lambda}{4\pi} \quad 3.4$$

Where α is absorption coefficient and λ is wavelength, (Forouhi, and Bloomer, 1988; In Bakr, *et al.*, 2011).

3.16.5 Optical conductivity (σ_o)

By the mathematical relation below the optical conductivity of the films was calculated;

$$\sigma_o = \frac{\alpha n c}{4\pi} \quad 3.5$$

Where α is absorption coefficient, n is refractive index and c is velocity of light, (Sharma and Katyal, 2007).

3.16.6 Complex dielectric constant (ϵ_c)

This parameter was calculated by the relation :

$$\epsilon_c = \epsilon_r + \epsilon_i \quad 3.6$$

Where $\epsilon_r = n^2 - k^2$ and is the real dielectric constant and $\epsilon_i = 2nk$ which is the imaginary dielectric constant. (Chopra,1969; In Nadeem and Ahmed, 2000, Goswami, 2005; In Bakr *et al.*, 2011)

3.16.7 Photon energy ($h\nu$)

Photon energy is given by:

$$E = h\nu \quad 3.7$$

Where h is Planck's constant, $h = 6.63 \times 10^{-34} \text{Js}$, ν is frequency of photon, (Nadeem and Waqas, 2000).

However,

$$\nu = \frac{c}{\lambda} \quad 3.8$$

Where c is velocity of light, $c = 3 \times 10^8 \text{m/s}$, λ is wavelength, therefore photon energy can be calculated by the relation:

$$E = \frac{hc}{\lambda} \quad 3.9$$

In terms of electron volt, $1eV = 1.602 \times 10^{-19} \text{J}$,

$$\text{Planck's constant } h = \frac{6.63 \times 10^{-34} \text{Js}}{1.602 \times 10^{-19} \text{J}} \approx 4.14 \times 10^{-15} \text{eV}$$

$$\therefore \text{ Photon energy } E = \frac{4.14 \times 10^{-15} \text{eV} \times 3 \times 10^8 \text{m/s}}{\lambda(m)} = \frac{1.242 \times 10^{-6}}{\lambda(m)} \text{eV}$$

3.16.8 Bandgap (E_g)

To obtain the bandgaps of the films, square of absorption coefficient was plotted against the photon energy, the straight part of the graph was extrapolated to the photon energy axis (horizontal axis) and the energy corresponding to zero value of absorption coefficient squared (zero value of vertical axis) is noted as the bandgap.

3.16.9 Bandgap bowing parameter

To obtain the bandgap bowing parameter of the ternary compounds, the equation below was adapted for each of the compounds accordingly.

The bandgap energy of the $Al_xIn_{1-x}N$ can be approximated by the following formula:

$$E_g(x) = x \cdot E_{g,AlN} + (1-x) \cdot E_{g,InN} - b \cdot x \cdot (1-x) \quad 3.10$$

Where $E_g(x)$ is the bandgap energy of the $Al_xIn_{1-x}N$, $E_{g,AlN}$ is the bandgap energy of the AlN, $E_{g,InN}$ is the bandgap energy of the InN, and b is the bandgap bowing parameter (Wen-Wei and Yen-Kuang, 2002).

3.17 Pictures of deposited samples

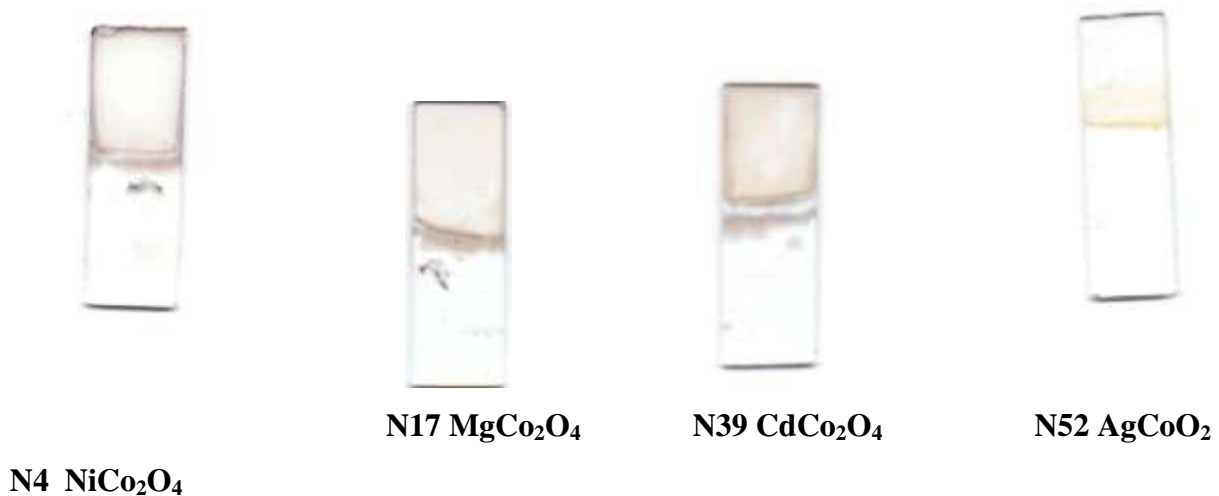


Figure 3.2: Pictures of deposited nanofilms

CHAPTER FOUR

RESULTS AND DISCUSSIONS

4.1 Analysis of nickel cobalt oxide nanofilms

The nanofilms were analyzed for their optical and magnetic properties.

4.1.1 Bandgaps of NiCo₂O₄ nanofilms at various percentages doping

The bandgaps of the cobalt doped nickel oxides and undoped nickel oxide as shown in figures fig 4.1 to 4.6 are depicted in Table 4.1. As shown in Table 4.1, the bandgap for 23% cobalt doping tends to deviate from the trend due to peeling off effect on the slide which occurs as a result of the deposits being thicker hence the film peels off and starts building up again. The bandgap values compares well with the works of other researchers, viz; Nano particles of NiCo₂O₄ has bandgaps of 1.748eV at 700⁰C, 1.79eV at 500⁰C, 1.827eV and 1.81eV at 900⁰C (Nisha *et al.*, 2008). Nickel oxide thin films have bandgaps of 3.95eV, 3.97eV, 3.63eV (Valyukh *et al.*, 2010). Nickel oxide thin film has bandgap of 3.11eV (Hakim *et al.*, 2009). Bandgap range of 2.1eV to 3.9eV was obtained for NiO thin film (Ezema *et al.*, 2008). NiO thin film has bandgap of 3.61eV (Desai *et al.*, 2006). Optical bandgap for the post deposition heat treated film of NiO nanofilm is 3.6eV (Biljana *et al.*, 2000). NiO has allowed direct transition, and the energy bandgap that varies from 3.76eV to 3.79eV as the substrate temperature increases from room temperature to 400⁰C. The change in the optical bandgap is due to the change in the stiochiometry and crystallinity in the film (Patel *et al.*, 2011). NiO thin film has a bandgap of 3.6eV (Irwin *et al.*, 2008). Bandgap of 3.4eV for NiO thin film was obtained (Patil *et al.*, 2002), and 4.3eV for NiO thin film (Hufner 1994). Result in figure 4.7 shows that the bandgap is inversely proportional to the percentage doping. The result compares well with the works of other researchers, viz; (Erhaima *et al.*, 2010), (Nirmala *et al.*, 2010), (Girjesh *et al.*, 2013). However the trend tends to reverse due to peeling off effect of the film on the slide beyond 18% doping. The film becomes thicker, peels off and starts building up again within the available time. However the peeling off could be as a result of weight of the film overwhelming the electrical force attaching it on the slide. This could be avoided by lower percentage doping or increasing the deposition

voltage. The graph has the minimum value at bandgap of 1eV. The minimum value corresponds to condition of maximum magnetic property, hence magnetic application is maximized. The bandgap decreased with percentage doping with cobalt. From figure 4.8, bandgap of nickel cobalt oxide nanofilm decreases as the thickness of the film increases. This compares well with the work of (Kumar *et al.*, 2012). However formation of impurity level within the bandgap could also lead to decrease in bandgap,

From Figure 4.10, the bowing parameter decreases as percentage cobalt dopant increases. As the bowing is downwards, it is positive. This compares well with the works of (Van de walley *et al.*, 1999), (Moses and Van de Walle, 2010). Bowing parameter is significant for investigating the bandgap energies of ternary alloys (Gulebagian *et al.*, 2014).

Figure 4.9, shows that thickness of nickel cobalt oxide nanofilm increases with percentage doping with cobalt, attained maximum value of 29nm at 13% doping then decreases. The decrease corresponds to peeling off effect as thickness increases. Since thickness of the films increased with percentage doping, this compares well with the works of (Ebru *et al.*, 2014) and (Okafor *et al.*, 2015), and since crystallite size (grain size) is directly proportional to film thickness (Pandiaraman *et al.*, 2011) and (Kumar *et al.*, 2012), this decrease in bandgap could be attributed to increase in crystallite size as thickness increases. Increase in grain size has a decreasing effect on bandgap (Ramana *et al.*, 2003).

However, as wide bandgap semiconductor, electronics made of it have the advantage of being smaller, faster, more reliable and more efficient than the Si based counterparts. Devices made of the material can operate at higher temperatures, voltages and higher frequencies.

Table 4.1: Variation of bandgap with percentage doping with cobalt, for nickel cobalt oxide nanofilm.

Doping (%)	0 (undoped)	3	8	13	18	23
Bandgap (eV)	4.5	3.8	2.0	1.8	1.0	3.0

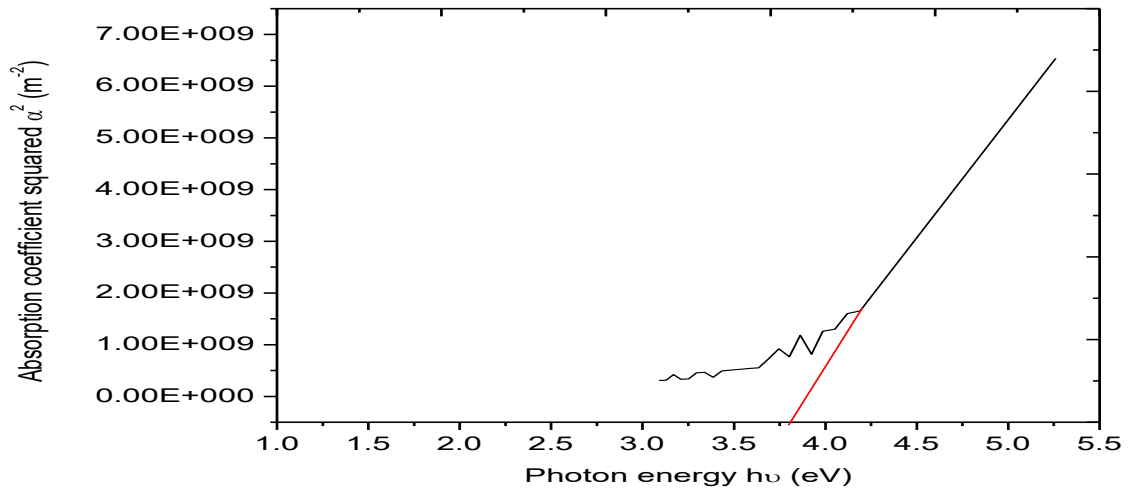


Figure 4.1: Absorption coefficient squared versus photon energy for NiCo₂O₄ nanofilm.(3% doped with cobalt).

From figure 4.1, 3% cobalt doped nickel oxide nanofilm has a direct allowed bandgap of 3.8eV.

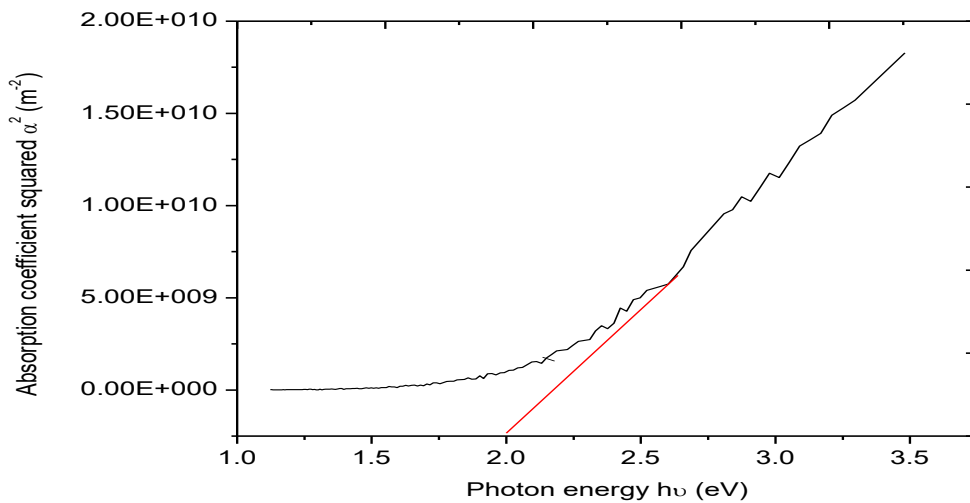


Figure 4.2: Absorption coefficient squared versus photon energy for NiCo₂O₄ nanofilm .(8% doped with cobalt).

From figure 4.2, 8% cobalt doped nickel oxide nanofilm has direct allowed bandgap of 2eV.

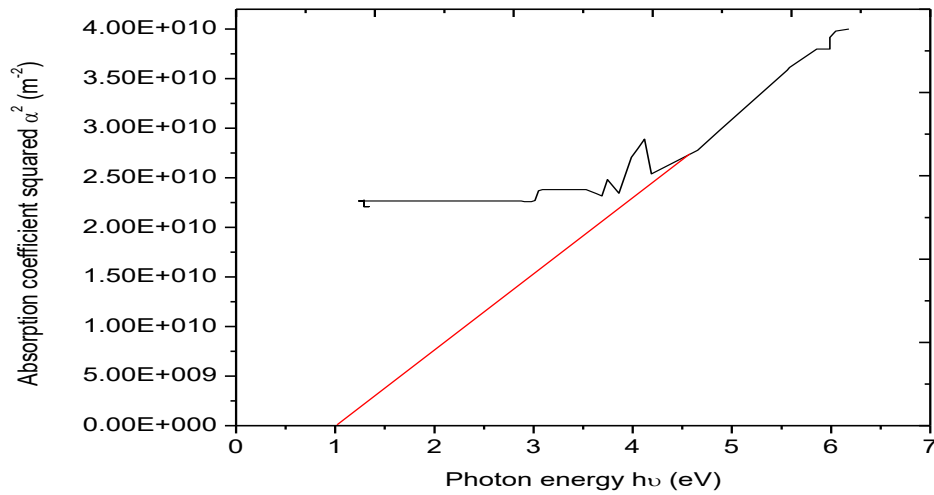


Figure 4.3: Absorption coefficient squared versus photon energy for NiCo₂O₄ nanofilm .(13% doped with cobalt).

From figure 4.3, 13% cobalt doped nickel oxide nanofilm has direct allowed bandgap of 1.8eV.

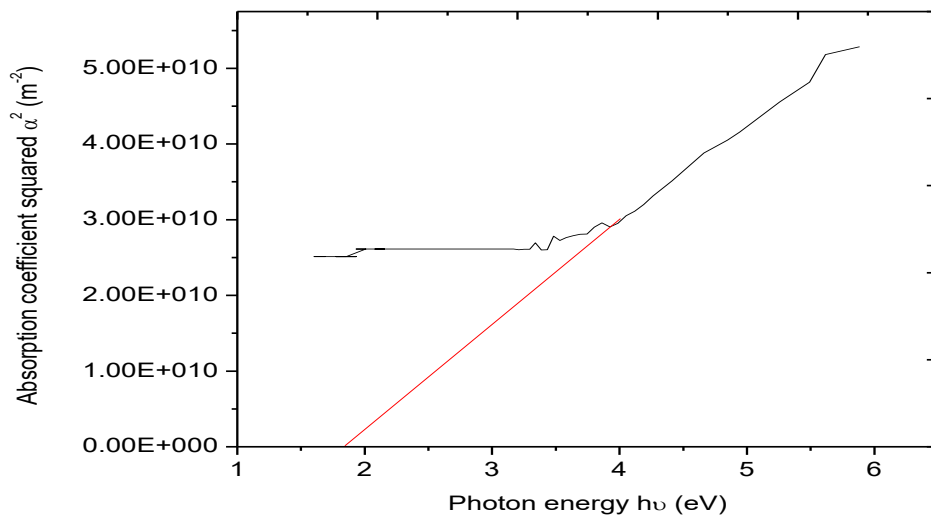


Figure 4.4: Absorption coefficient squared versus photon energy for NiCo₂O₄ nanofilm .(18% doped with cobalt).

From figure 4.4, 18% cobalt doped nickel oxide nanofilm has a direct allowed bandgap of 1eV.

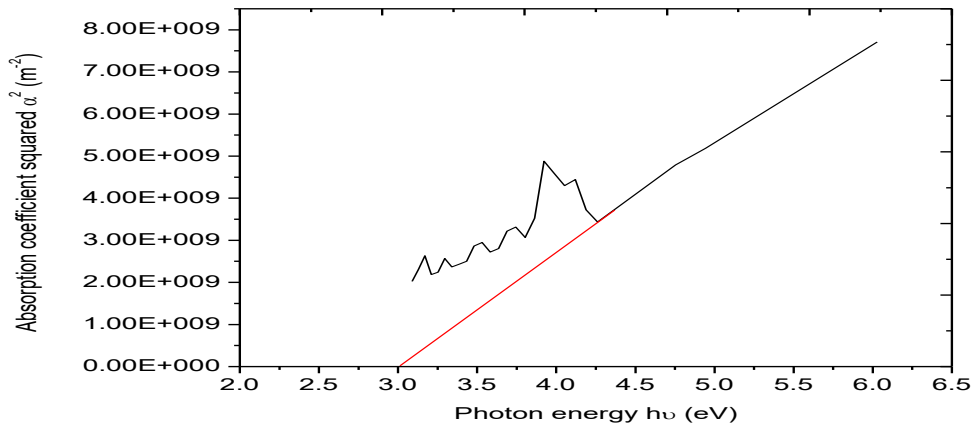


Figure 4.5: Absorption coefficient squared versus photon energy for NiCo₂O₄ nanofilm .(23% doped with cobalt).

From figure 4.5, 23% cobalt doped nickel oxide nanofilm has a direct allowed bandgap of 3eV.

4.1.2 Bandgap of undoped NiO nanofilm

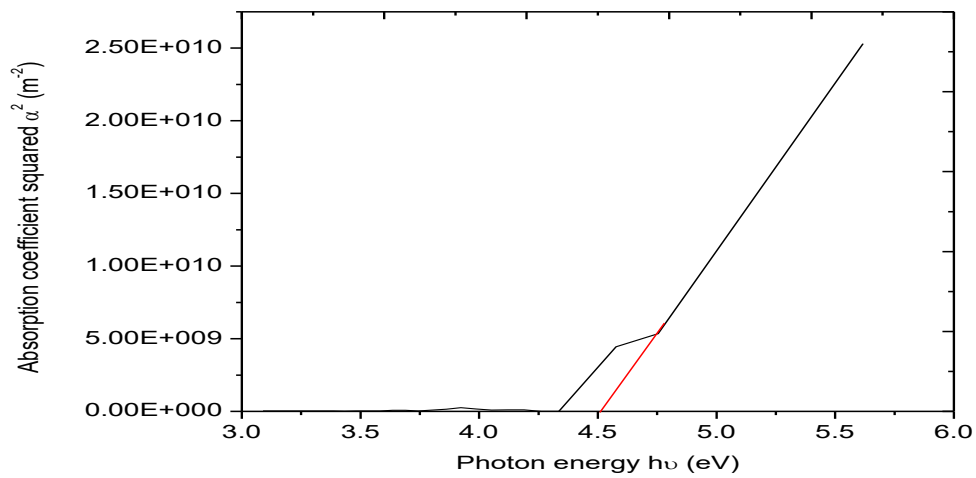


Figure 4.6: Absorption coefficient squared versus photon energy for undoped nickel oxide nanofilm.

From figure 4.6, nickel oxide nanofilm has allowed direct bandgap of 4.5eV.

4.1.3 Bandgap variations and thickness variation

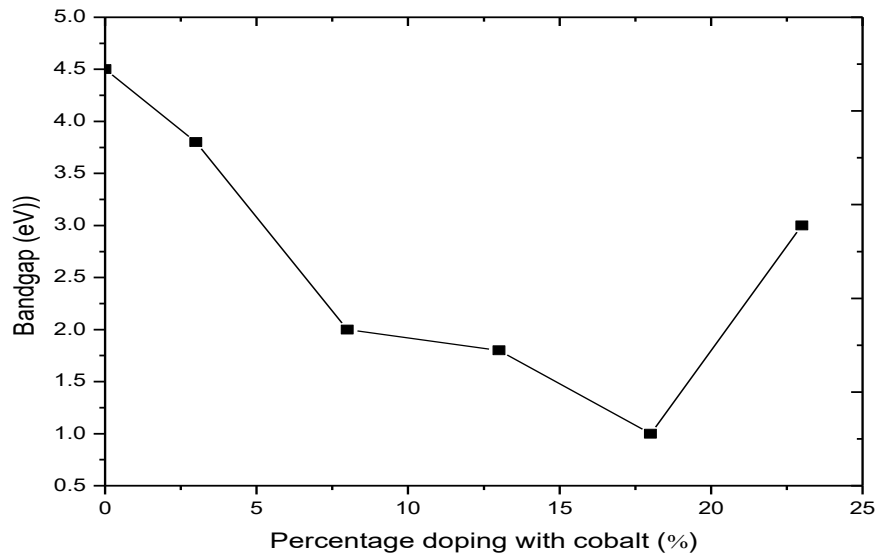


Figure 4.7: Variation of bandgap with percentage doping with cobalt for NiCo_2O_4 nanofilm

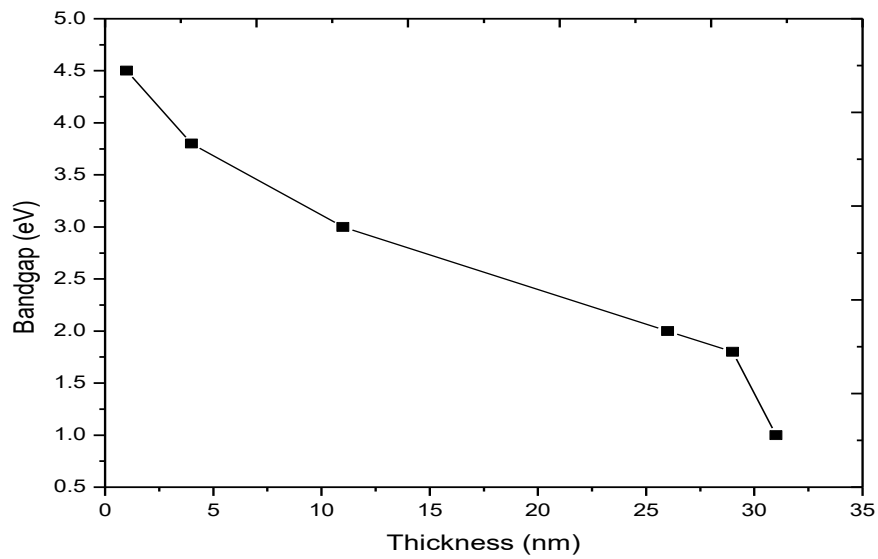


Figure 4.8: Variation of bandgap with thickness for NiCo_2O_4 nanofilm.

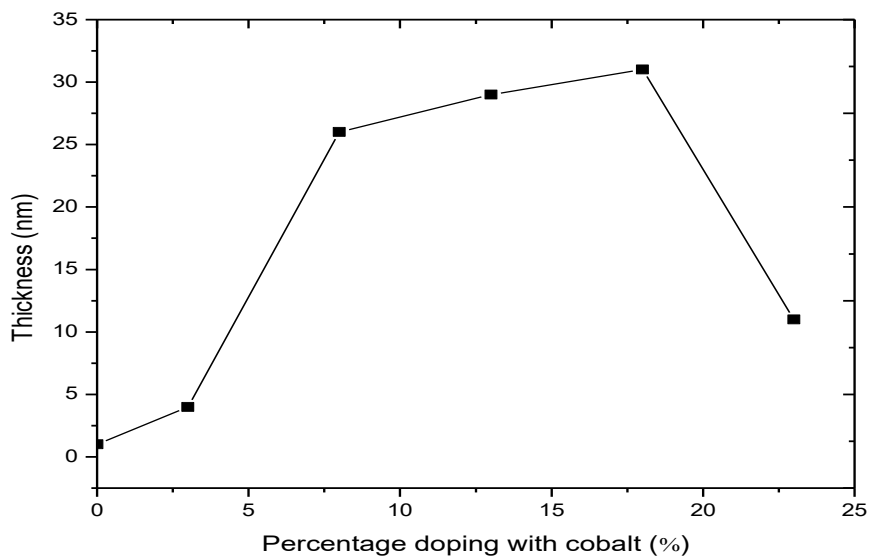


Figure 4.9 : Variation of thickness with percentage doping with cobalt for NiCo₂O₄ nanofilm

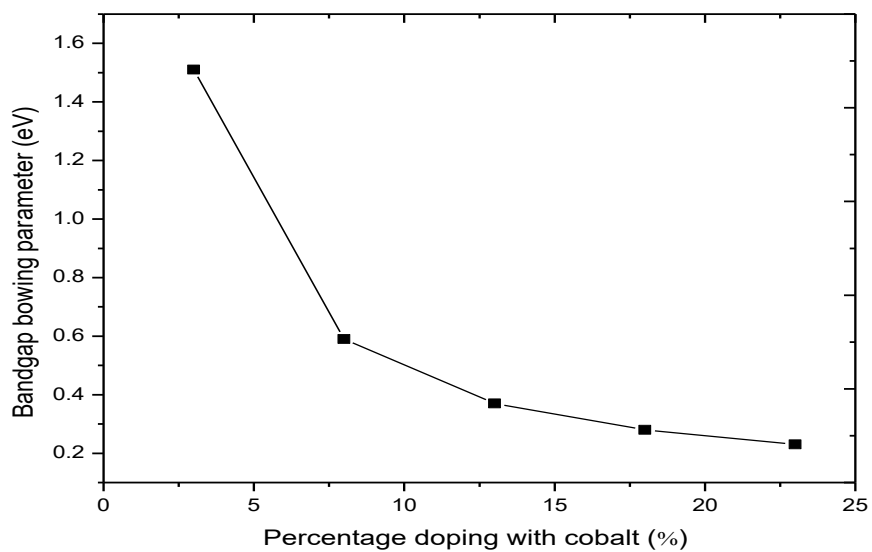


Figure 4.10: Variation of bandgap bowing parameter with percentage doping for nickel cobalt oxide nanofilms.

4.1.4 Effect of percentage doping on optical properties of nickel cobalt oxide nanofilms

Figure 4.11, shows that the absorbance of cobalt doped nickel oxide nanofilm is very low. The films have highest absorbance ($0.053=5.3\%$) in the UV region and tends to zero in the near infra red region of the electromagnetic spectrum. However the absorbance increases with increasing percentage doping, not minding the case of 23% doping which deviates from the trend due to peeling off effect from the slide as it becomes thicker, peels off and starts depositing afresh. The absorbance of the undoped film is very low in all the regions, maximum of $0.005=0.5\%$

Figure 4.12, shows that the transmittance of the films is generally high in the UV-VIS-NIR regions ($<89.3\%$), with the lightly doped (3%) having maximum transmittance (99.4%) in the visible region and decreasing to minimum (98.76%) in the NIR region. Higher doping 8%, 13% and 18% have minimum transmittance of 89.51%, 89.86% and 90.54% respectively in the UV region and increases to maximum 98.72 and 100% respectively in the NIR region. This property makes the films useful in any application requiring high doses of UV, VIS and NIR radiations such as photothermal application, Phosphors, Solar cell. The transmittance of the films decreases as the percentage cobalt dopant increases. However, the undoped film has maximum transmittance of 99.44% in UV region and decreases to 98.98% in NIR region.

From the figure 4.13, the films have maximum reflectance ($0.052=5.2\%$) in the UV region which decreases to zero in the near infra red region of the electromagnetic spectrum. However, the reflectance increases with increasing percentage doping, not minding 23% which deviated due to peeling off effect. Low reflectance in the Infra red region makes it a good material for cold mirror. The undoped film has the lowest reflectance, maximum of $0.007=0.7\%$ in UV-VIS-NIR region. As shown in figure 4.14, the films exhibited maximum refractive index (1.58) in the UV and decreased to minimum in the NIR (1.04). The low refractive indices of some of the films in the visible region 1.08, 1.13, 1.17 for 23% doped, undoped and 3% doped respectively makes them good materials for multilayer antireflection coating in the visible region and in film stalk for colour selective coatings.

However, the refractive index increases with increasing percentage doping, not minding 23% which deviated from the trend due to peeling off effect. The undoped film has the minimum refractive index of 1.10 in UV region.

Figure 4.15, shows that the film has maximum extinction coefficient in the UV region which tends to zero in the NIR region. The extinction coefficient increases with increasing percentage doping not minding 23% which deviated from the trend due to peeling off effect of the film as it gets thicker. The undoped film has the lowest extinction coefficient, maximum of $3.98E-04$ in UV-VIS regions.

As shown in figure 4.16, the complex dielectric constant of the film is maximum (2.54) in the UV region . It increases with increasing percentage doping regardless of 23% which deviated from the trend due to peeling off effect as the film gets thicker. The undoped film has the lowest complex dielectric constant, maximum of 1.41 in UV-VIS regions.

From figure 4.17, the optical conductivity of the film is maximum in the UV region and decreases to zero in the NIR region. It increases with increasing percentage doping, however 23% deviated as the films became thicker and peeled off from the substrate. The undoped film has the lowest optical conductivity, maximum of $3.492E+11$ in UV region and as such has lower response to optical stimulations than the doped films.

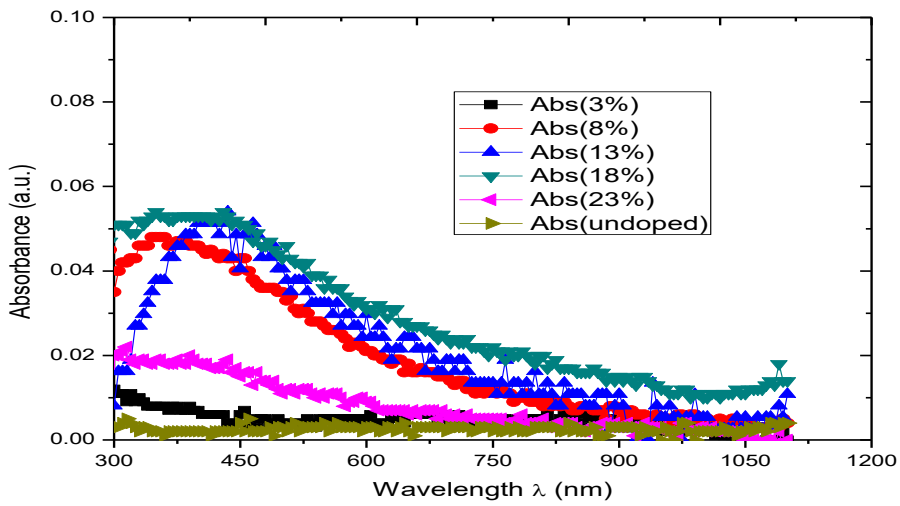


Figure 4.11: Variation of absorbance with wavelength for NiCo_2O_4 nanofilms for different percentages doping with cobalt.

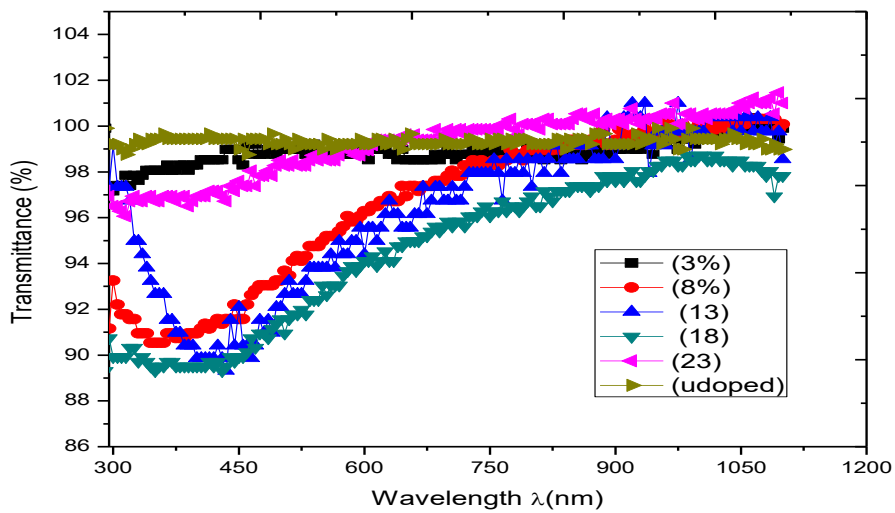


Figure 4.12: Variation of percentage transmittance with wavelength for NiCo_2O_4 nanofilms for different percentages doping with cobalt.

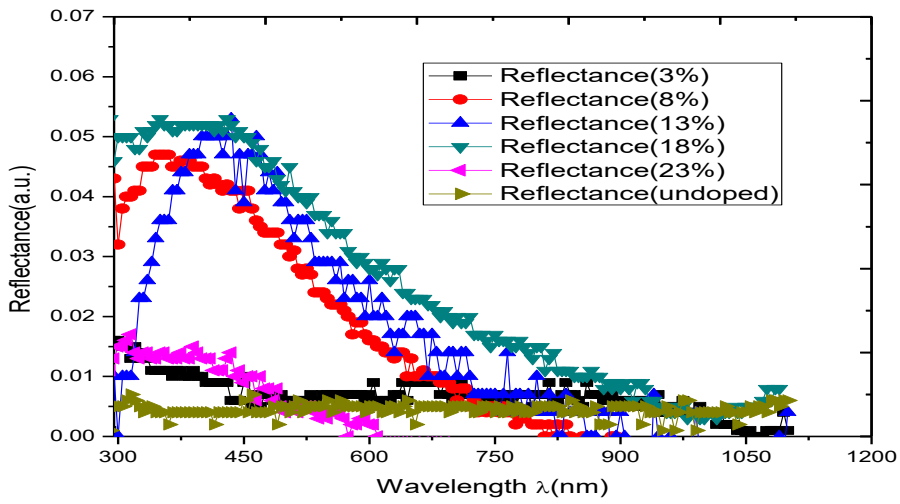


Figure 4.13: Variation of reflectance with wavelength for NiCo₂O₄ nanofilms for different percentages doping with cobalt.

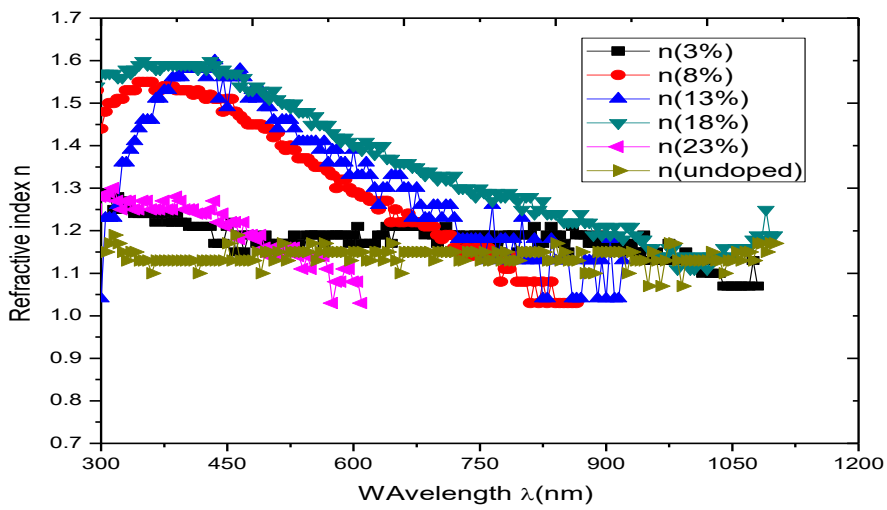


Figure 4.14: Variation of refractive index with wavelength for NiCo₂O₄ nanofilms for different percentages doping with cobalt.

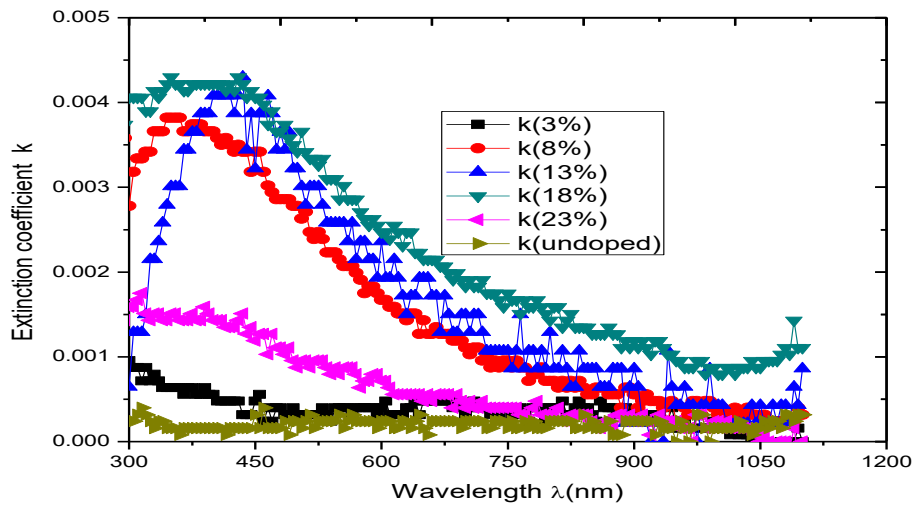


Figure 4.15: Variation of extinction coefficient with wavelength for NiCo_2O_4 nanofilms for different percentages doping with cobalt.

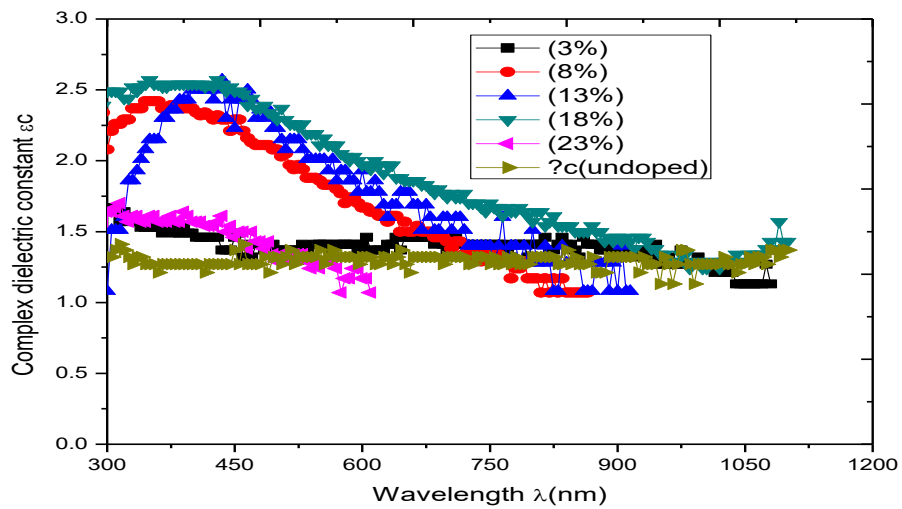


Figure 4.16: Variation of complex dielectric constant with wavelength for NiCo_2O_4 nanofilms for different percentages doping with cobalt.

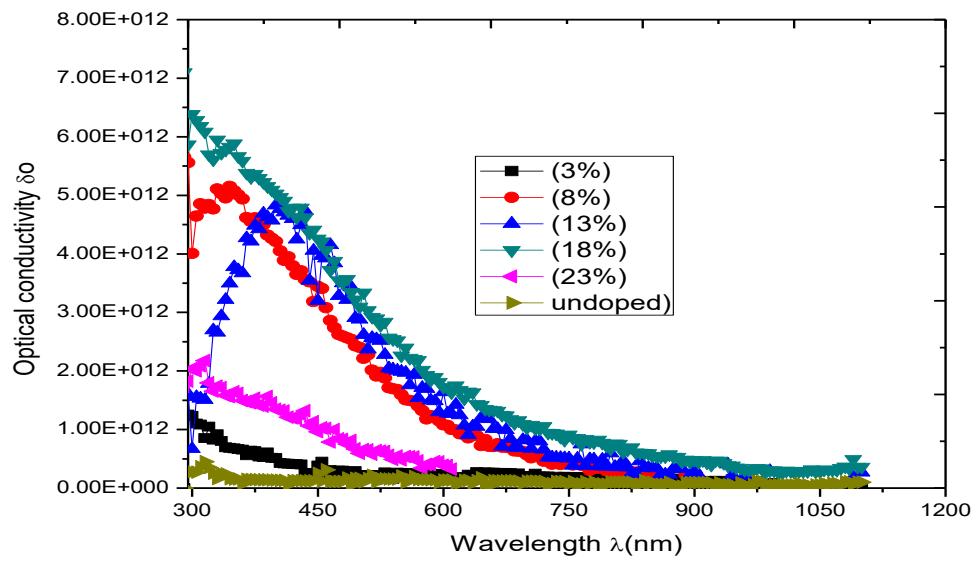


Figure 4.17: Variation of optical conductivity with wavelength for NiCo₂O₄ nanofilms for different percentages doping with cobalt.

4.1.5 Effect of thickness on optical properties of nickel cobalt oxide nanofilms

Figure 4.18, shows that the absorbance of the film increases with increasing thickness of the films.

Maximum value of 0.053= 5.3% in the UV region and decreases to zero in NIR. However, the undoped film with thickness of 1nm has very low absorbance maximum of 0.005=0.5% in UV region

Figure 4.19 shows that the transmittance of the films decreases with increasing thickness of the films.

Minimum of 89.31% for 31nm, in the UV region and increases to maximum (98.5% to 100%) in NIR.

As shown in figure 4.20, the reflectance of the films increases with increasing thickness of the films.

Maximum of 0.053 = 5.3% for 31nm in UV region and decreases to zero in NIR. The undoped film with thickness of 1nm has very low reflectance, maximum of 0.007=0.7% in UV region. Figure 4.21

shows that the refractive index of the films increases with increasing thickness of the films. Maximum of 1.59 for 31nm in UV region and decreases to minimum in NIR. The undoped film with thickness of 1nm has very low refractive index, maximum of 1.17 in UV-VIS-NIR region

As shown in figure 4.22, extinction coefficient of the films increases with increasing thickness of the films. Maximum of 4.22E-03 for 31nm in UV region and tends to zero in NIR. The undoped film with thickness of 1nm has the lowest extinction coefficient, maximum of 3.98E-04 in UV-VIS region.

From figure 4.23, complex dielectric constant of the films increases with increasing thickness of the films. Maximum of 2.54 for 31nm in UV region and decreases to minimum in NIR. The undoped film with thickness of 1nm has the lowest complex dielectric constant, maximum of 1.41 in UV-VIS region.

As shown in figure 4.24, optical conductivity of the films increases with increasing thickness of the films. Maximum of 6.38929E+12 for 31 nm in UV region and decreases to zero in NIR. The undoped film with thickness of 1nm has the lowest optical conductivity, maximum of 3.492E+11 in UV region and as such has lower response to optical stimulations than the doped films.

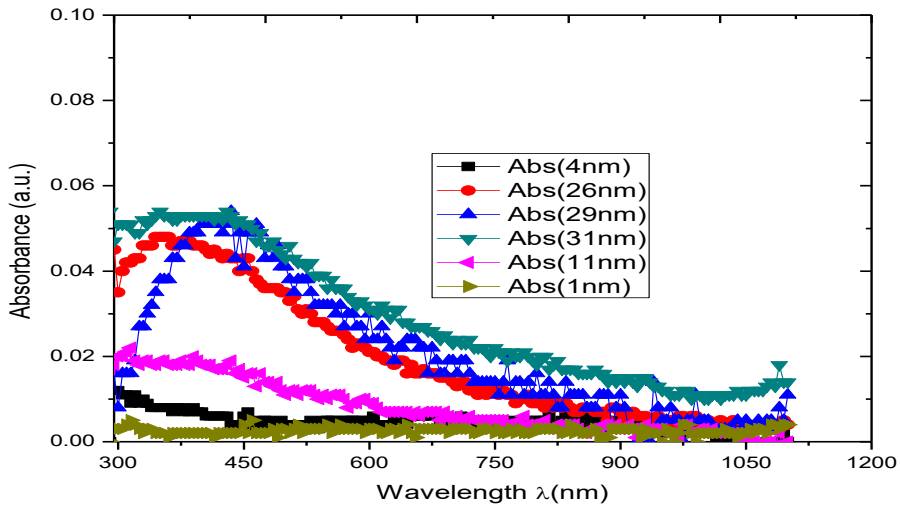


Figure 4. 18: Variation of absorbance with wavelength for NiCo₂O₄ nanofilms for different thicknesses

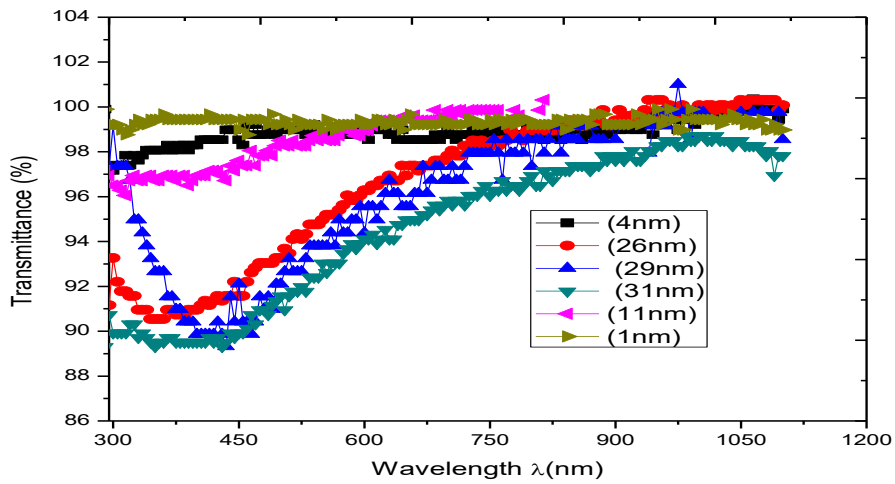


Figure 4.19: Variation of transmittance with wavelength for NiCo₂O₄ nanofilms for different thicknesses

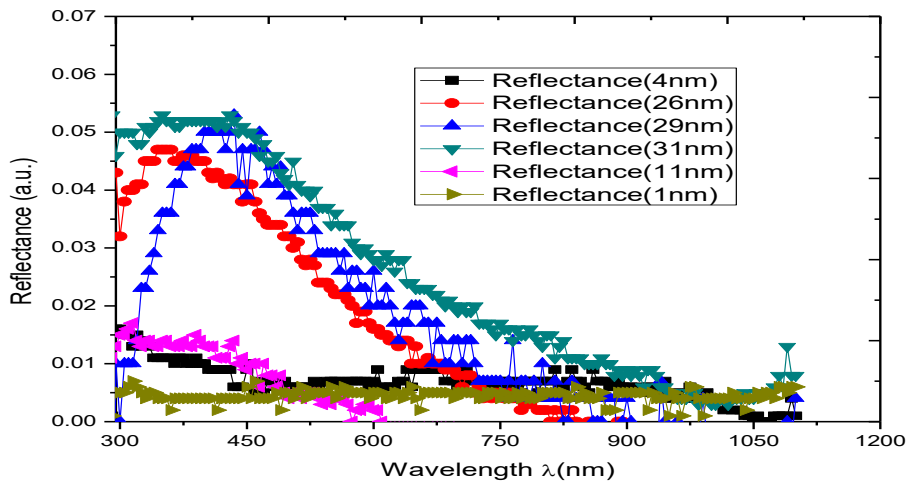


Figure 4.20: Variation of reflectance with wavelength for NiCo₂O₄ nanofilms for different thicknesses

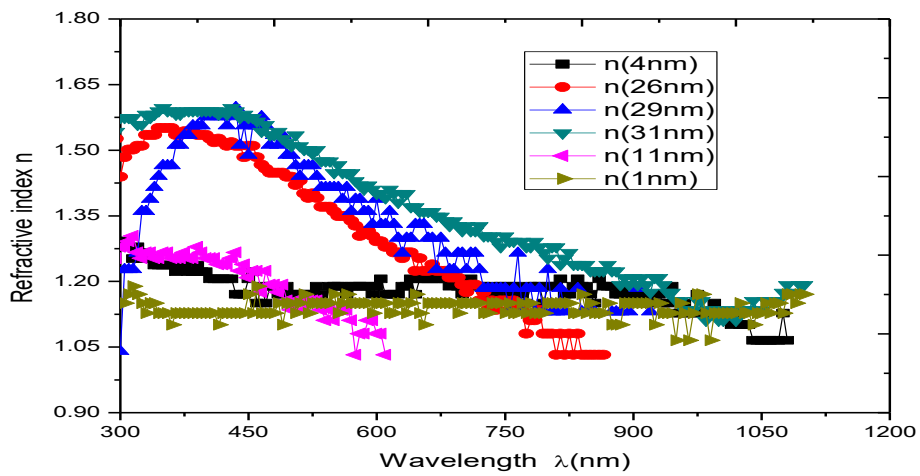


Figure 4.21: Variation of refractive index with wavelength for NiCo₂O₄ nanofilms for different thicknesses

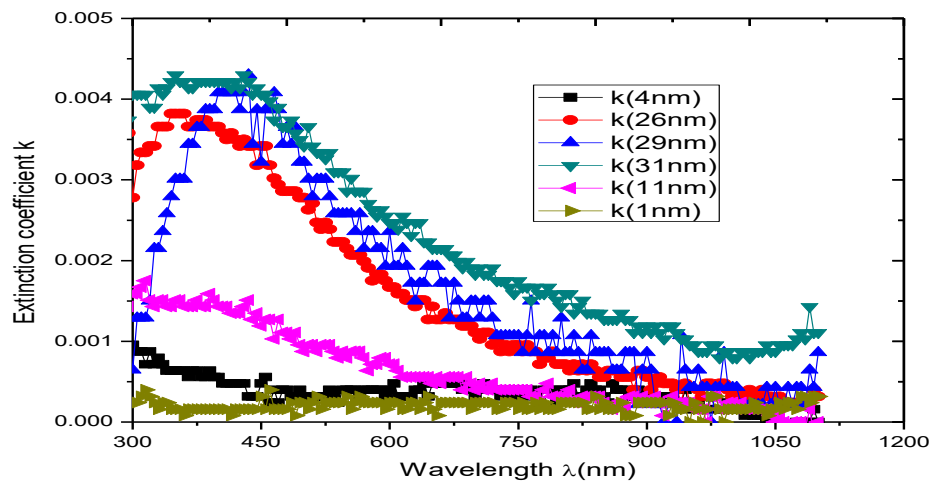


Figure 4.22: Variation of extinction coefficient with wavelength for NiCo_2O_4 nanofilms for different thicknesses

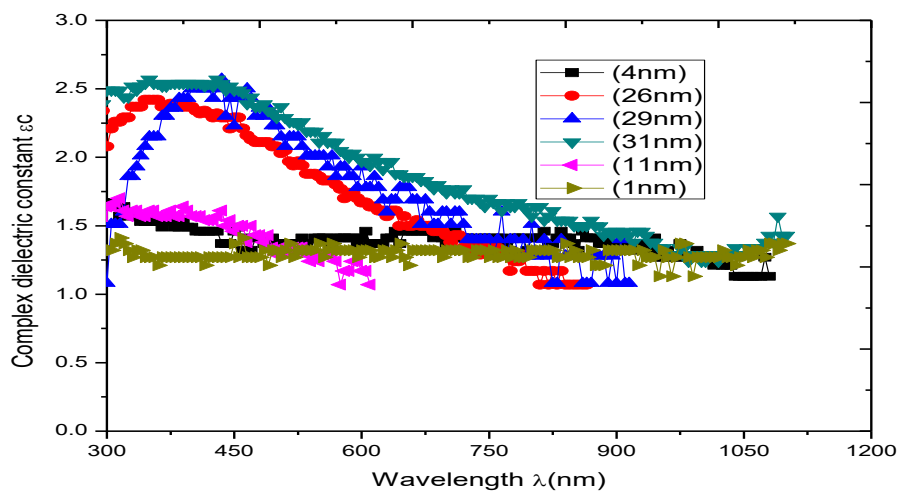


Figure 4.23: Variation of complex dielectric constant with wavelength for NiCo_2O_4 nanofilms for different thicknesses

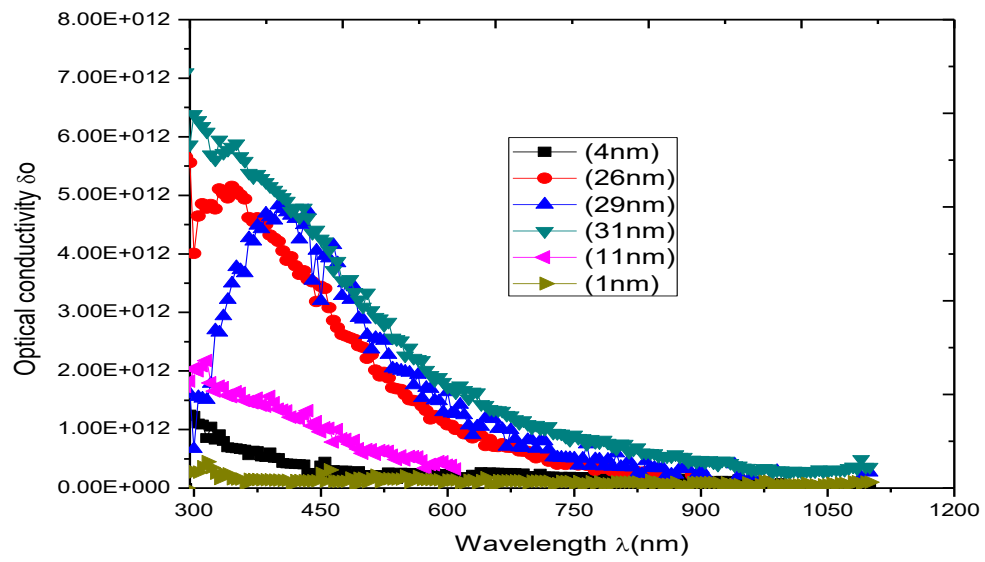


Figure 4.24: Variation of optical conductivity with wavelength for NiCo₂O₄ nanofilms for different thicknesses.

4.1.6 Effect of deposition time on optical properties of nickel cobalt oxide nanofilms

Figure 4.25 shows that the absorbance of the film increases with deposition time. However, absorbance of the film attained peak value at 10 mins deposition time beyond which it peels off from substrate due to heavy thickness and new deposit starts building up.

Figure 4.26 shows that the transmittance of the film decreases with deposition time. However, beyond 10 mins, the film peels off from the substrate due to heavy thickness and starts building up again.

From figure 4.27, reflectance of the film increases with time of deposition . However, peeling off effect which occurred beyond 10 mins caused the film to start building up afresh.

Figure 4.28 shows that refractive index of the film increases with time of deposition . However, beyond 10 mins deposition time the film peeled off from the substrate and started depositing afresh.

As shown in figure 4.29, extinction coefficient of the film increases with deposition time . However, peeling off effect which occurred beyond 10 mins caused the film to start building up afresh.

Result shown in figure 4.30 indicates that complex dielectric constant of the film increases with time of deposition . However, peeling off effect which occurred beyond 10 mins caused the film to start building up afresh. From figure 4.31, optical conductivity of the film increases with time of deposition . However, the optical conductivity reached the peak value at deposition time of 10mins, peeled off from the substrate and started depositing afresh.

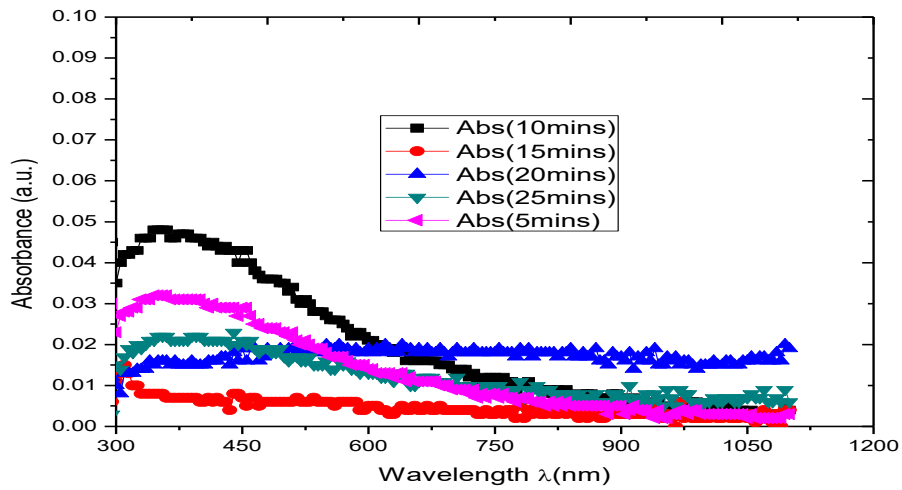


Figure 4.25: Variation of absorbance with wavelength for NiCo₂O₄ nanofilms for different deposition times.

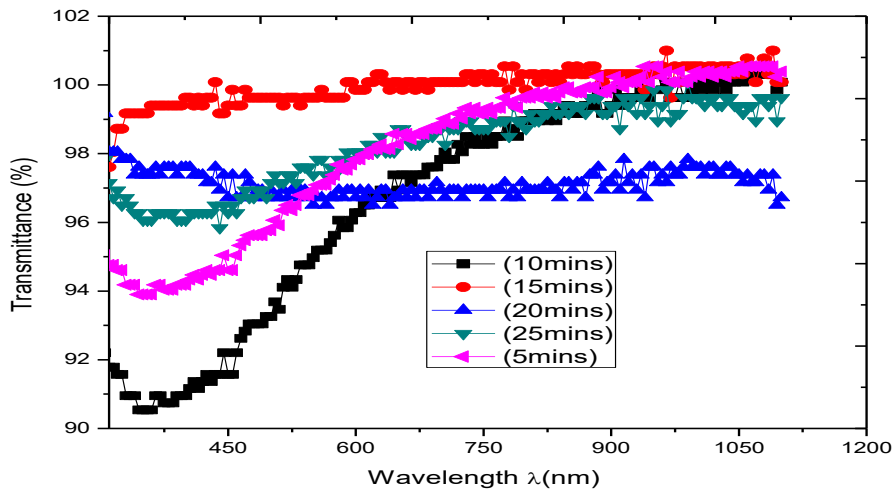


Figure 4.26: Variation of transmittance with wavelength for NiCo₂O₄ nanofilms for different deposition times.

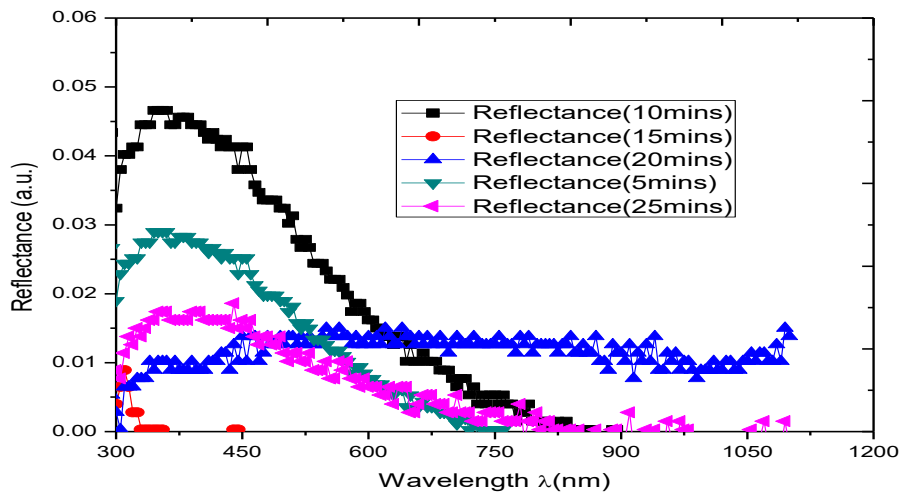


Figure 4.27: Variation of reflectance with wavelength for NiCo_2O_4 nanofilms for different deposition times.

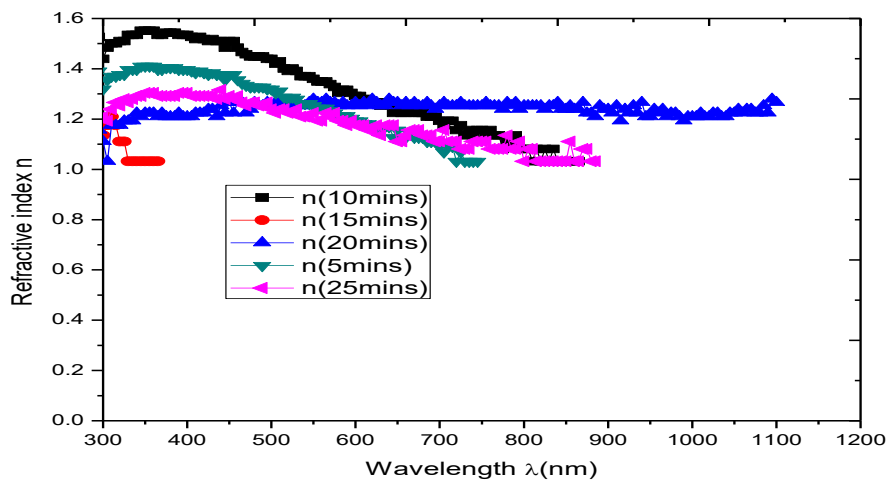


Figure 4.28: Variation of refractive index with wavelength for NiCo_2O_4 nanofilms for different deposition times.

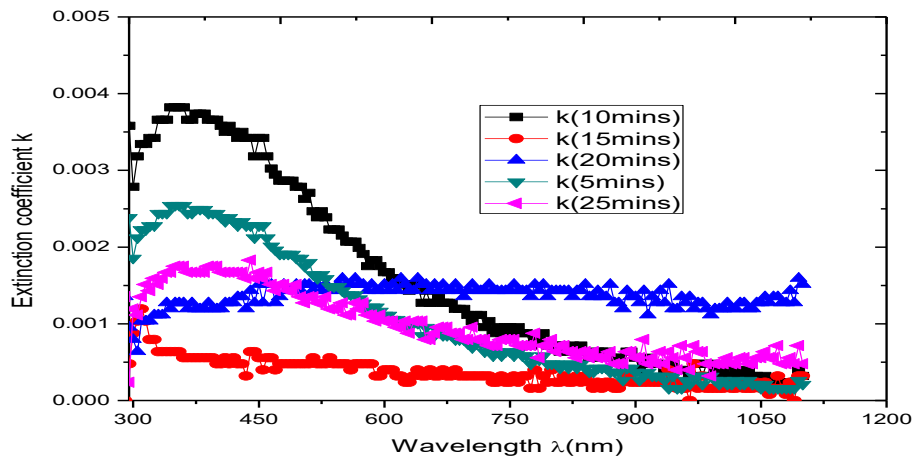


Figure 4.29: Variation of extinction coefficient with wavelength for NiCo₂O₄ nanofilms for different deposition times.

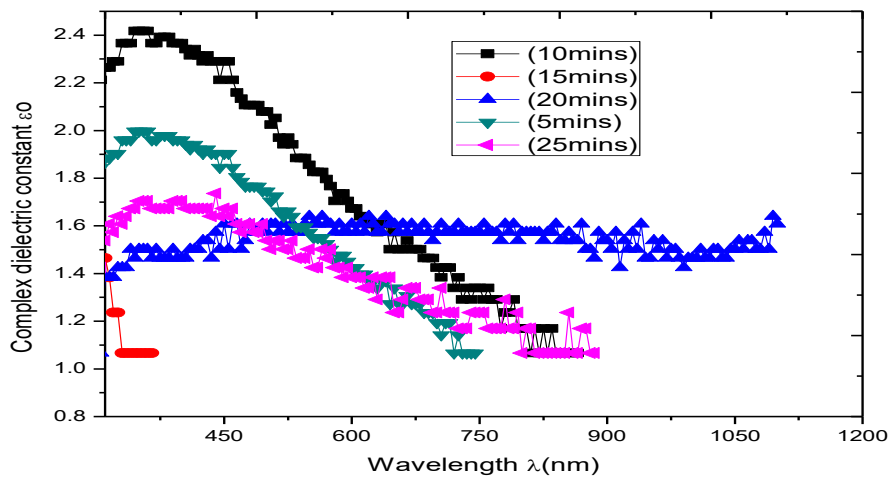


Figure 4.30: Variation of complex dielectric constant with wavelength for NiCo₂O₄ nanofilms for different deposition times.

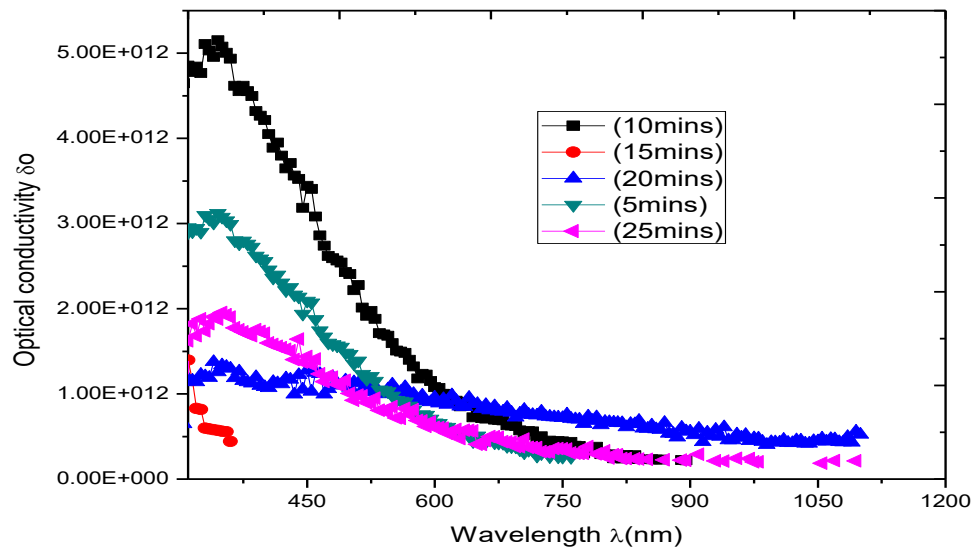


Figure 4.31: Variation of optical conductivity with wavelength for NiCo_2O_4 nanofilms for different deposition times.

4.1.7 Effect of deposition voltage on optical properties of nickel cobalt oxide nanofilms

As shown in figure 4.32, the ultrathin nature of the films generally reduces the absorptive capacity and increases the transmittance of the films throughout the UV, VIS and NIR regions. However, the absorbance of the films is maximum in the second half of UV region (0.048=4.8%) and decreases to zero in the NIR region of electromagnetic spectrum. 8.5V and 11.5V have the lowest absorbance (0.002=0.2% and 0.003=0.3% respectively) in the visible region. However, the absorbance of the films increases as the deposition voltage increases.

From figure 4.33, transmittance of the film decreases with increasing deposition voltage. However, peeling off effect creates another trend of the decrease for voltages beyond 10V.

Figure 4.34 shows that, reflectance of the film increases with increasing deposition voltage. However, due to peeling off effect at voltages beyond 10V, the film starts afresh to deposit. Figure 4.35 shows that, refractive index of the film increases with increasing deposition voltage. However, due to peeling off effect at voltages beyond 10V, the film starts afresh to build up. From figure 4.36, extinction coefficient of the film increases with increasing deposition voltage.

The extinction coefficient of the film attained peak value at 10V deposition voltage beyond which it peels off from substrate due to heavy thickness and new deposit starts building up

Figure 4.37 shows that complex dielectric constant of the film increases with increasing deposition voltage. The film peeled off beyond 10V deposition voltage and starts building up again.

Result from figure 4.38 shows that optical conductivity of the film increases with increasing deposition voltage. However, optical conductivity of the film attained peak value at 10V deposition voltage beyond which it peeled off from substrate due to heavy thickness and new deposit started building up.

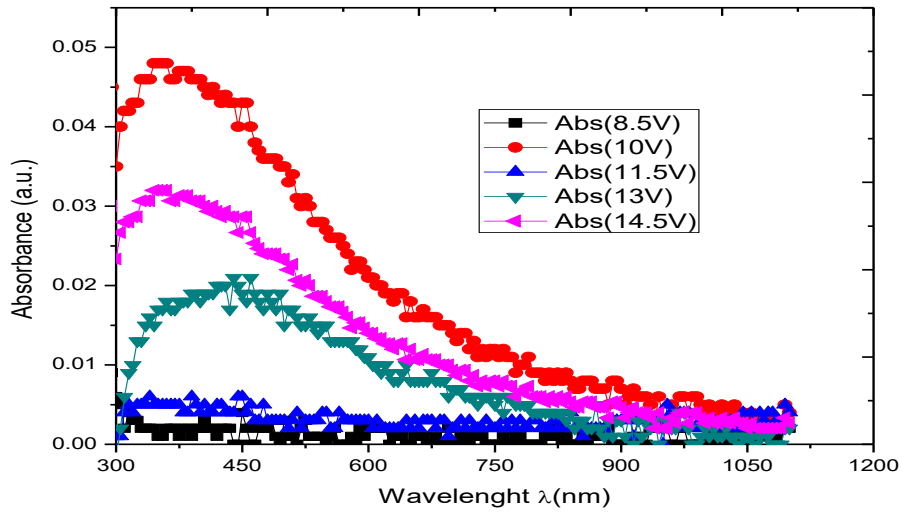


Figure 4.32: Variation of absorbance with wavelength for NiCo_2O_4 nanofilms for different deposition voltages.

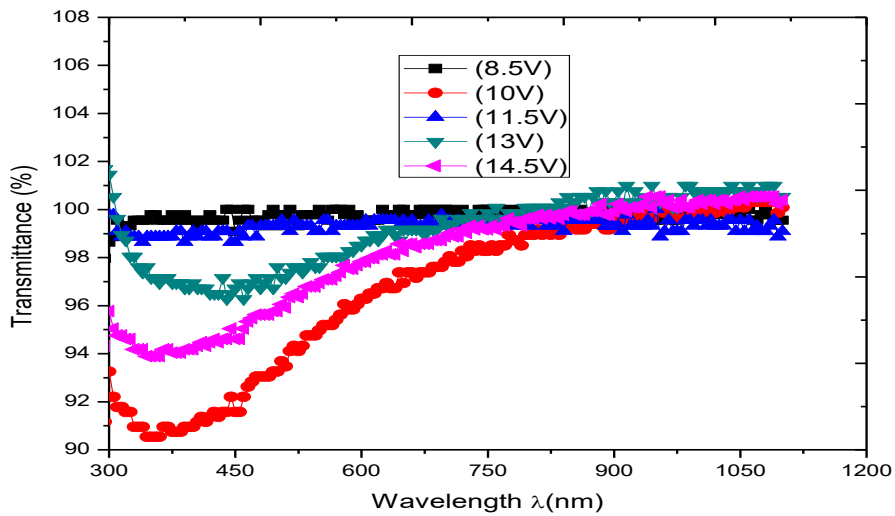


Figure 4.33: Variation of transmittance with wavelength for NiCo_2O_4 nanofilms for different deposition voltages.

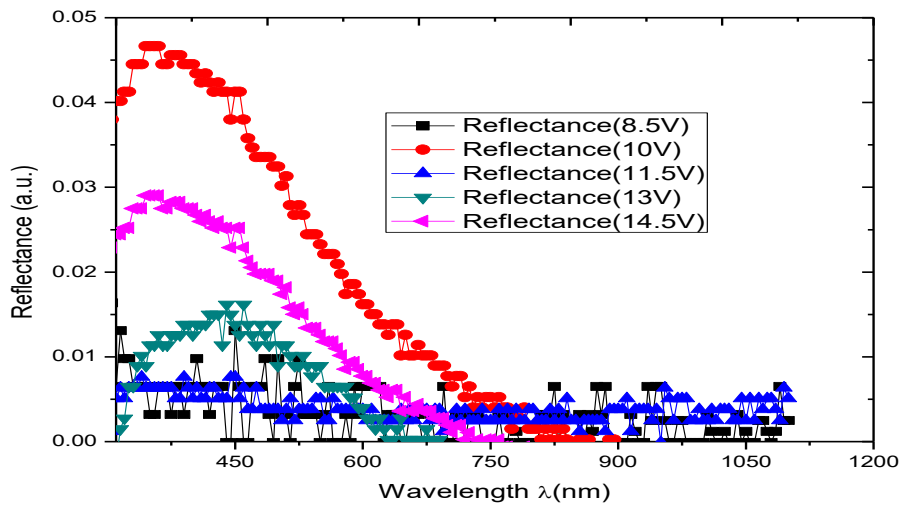


Figure 4.34: Variation of reflectance with wavelength for NiCo_2O_4 nanofilms for different deposition voltages.

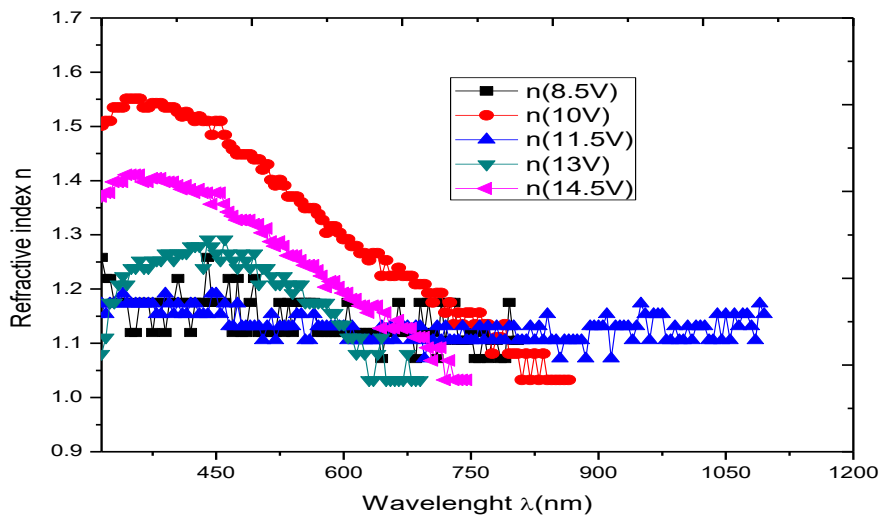


Figure 4.35: Variation of refractive index with wavelength for NiCo_2O_4 nanofilms for different deposition voltages.

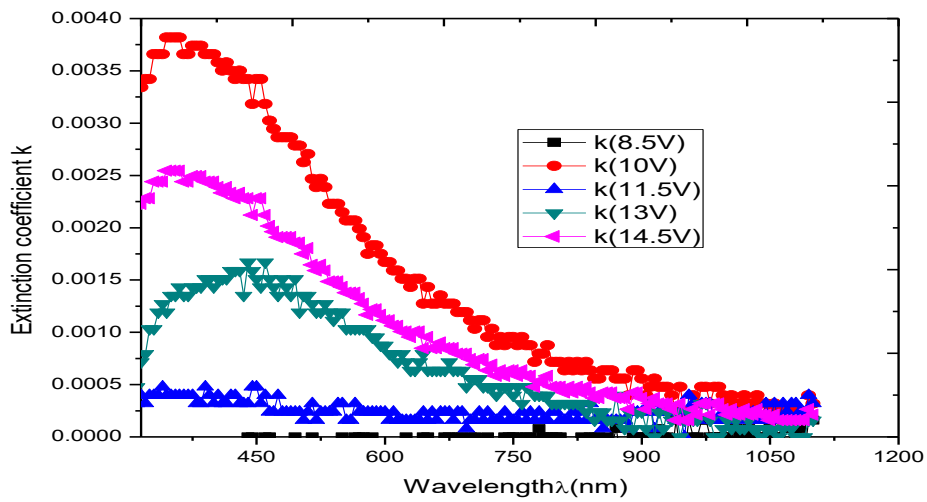


Figure 4.36: Variation of extinction coefficient with wavelength for NiCo₂O₄ nanofilms for different deposition voltages.

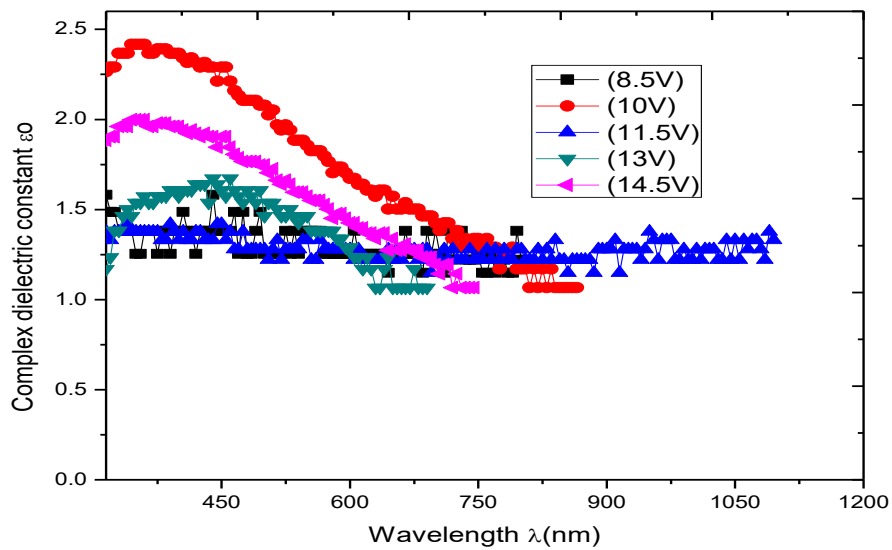


Figure 4.37: Variation of complex dielectric constant with Wavelength for NiCo₂O₄ nanofilms for different deposition voltages.

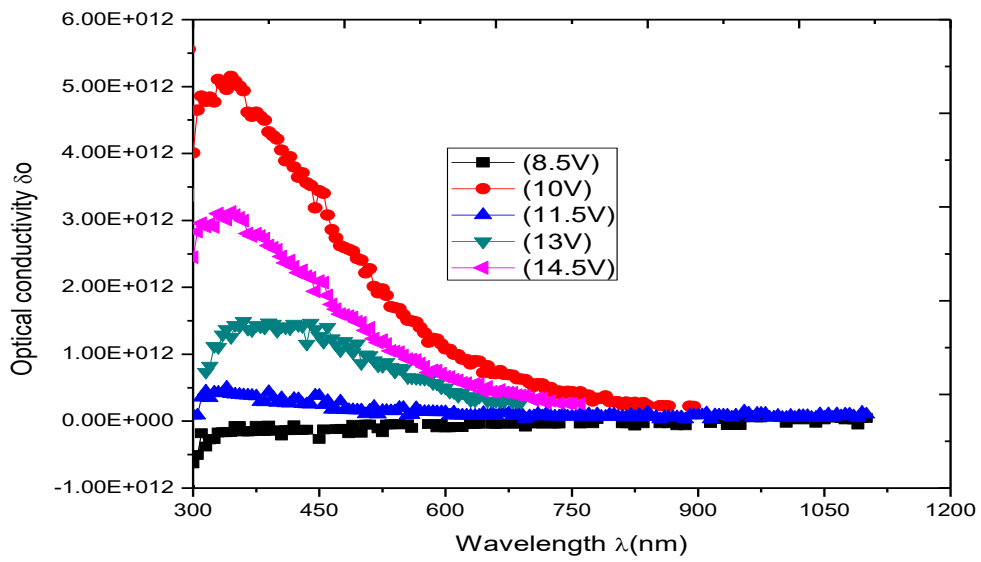


Figure 4.38: Variation of optical conductivity with wavelength for NiCo₂O₄ nanofilms for different deposition voltages.

4.1.8 Variation of magnetic saturation with percentage doping with cobalt

Figure 4.39 shows that magnetic saturation of pinned layer for NiCo₂O₄ nanofilm fluctuates with percentage doping with cobalt, it rises to a peak value of 3.63E-04 in the lower percentage range, decreases to zero at subsequent percentage dopings and rises to a lower peak of 2.50E-04 in the higher percentage range. Result in figure 4.40 shows that magnetic saturation of free layer for NiCo₂O₄ nanofilm is inversely proportional to the percentage doping with cobalt.

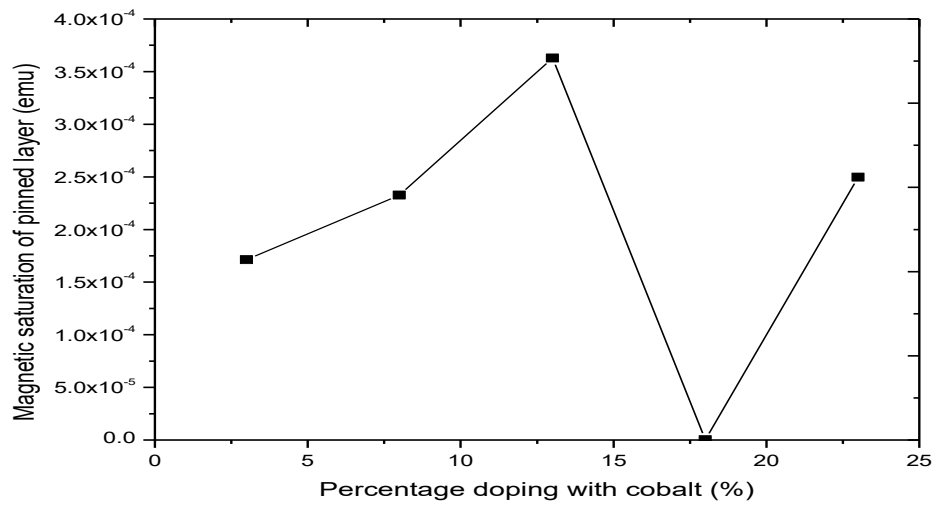


Figure 4.39: Variation of magnetic saturation of pinned layer with percentage doping with cobalt.

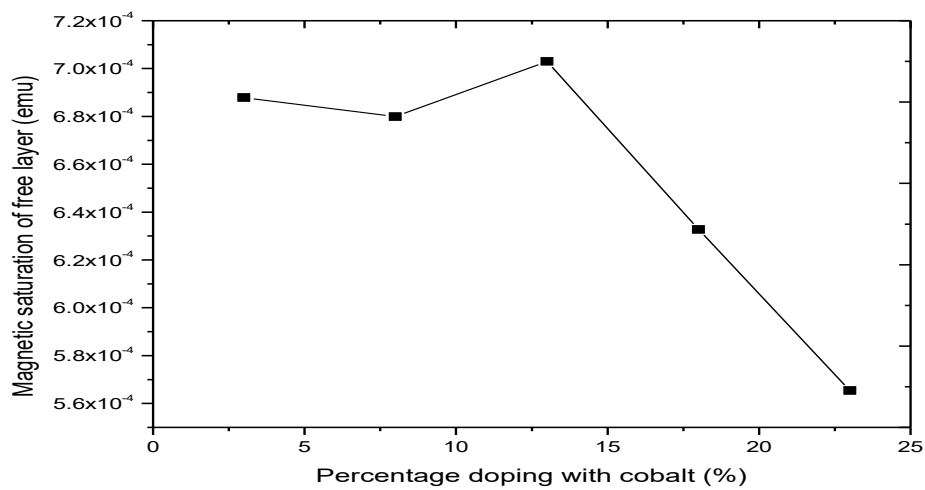


Figure 4.40: Variation of magnetic saturation of free layer with percentage doping with cobalt.

4.1.9 Variation of magnetization with applied field for different percentages of cobalt dopant, for NiCo₂O₄ nanofilm

From figure 4.41, slope of the graph is 176.67 , therefore magnetic susceptibility of 3% doped film is 176.67. Figure 4.42 shows that the slope of the graph is 180.00 , therefore magnetic susceptibility of 8% doped film is 180.00. As shown in figure 4.43, Slope of the graph is 184.00 , therefore magnetic susceptibility of 13% doped film is 184.00. Figure 4.44 shows that the slope of the graph is 186.00 , therefore magnetic susceptibility of 18% doped film is 186.00. Figure 4.45 shows that the slope of the graph is 189.00 , therefore magnetic susceptibility of 23% doped film is 189.00. Magnetic saturation of the films are 687.902E-6emu for 3% doped, 679.871E-6emu for 8% doped, 703.017E-6emu for 13% doped , 632.750E-6emu for 18% doped and 565.390E-6emu for 23% doped. Since the film has no Fe³⁺ ion, it is not ferrimagnetic and by virtue of positive high magnetic susceptibility and magnetic saturation, the material is ferromagnetic. Figure 4.46 shows that the magnetic susceptibility increases as percentage cobalt dopant increases.

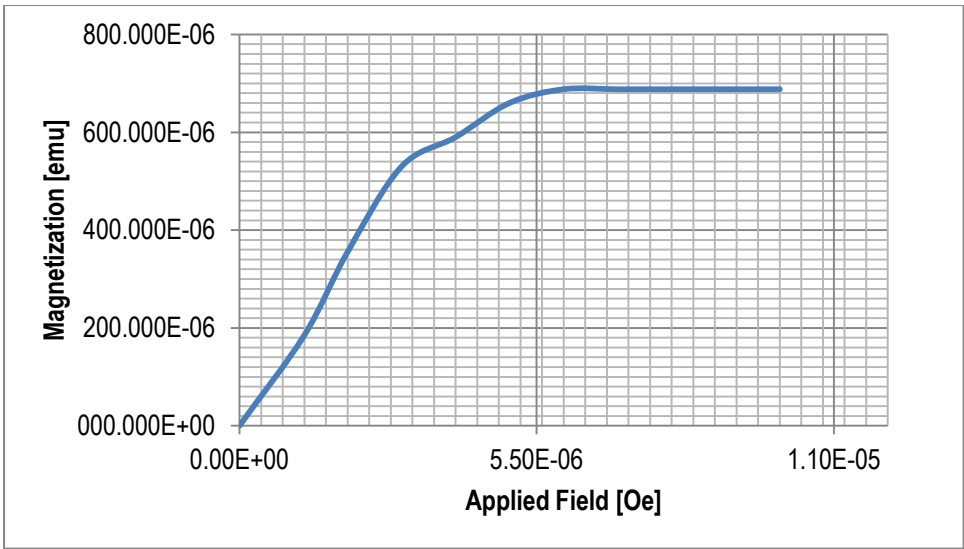


Figure. 4.41: Variation of magnetization with applied voltage (3% doping)
 slope of the graph is 176.67

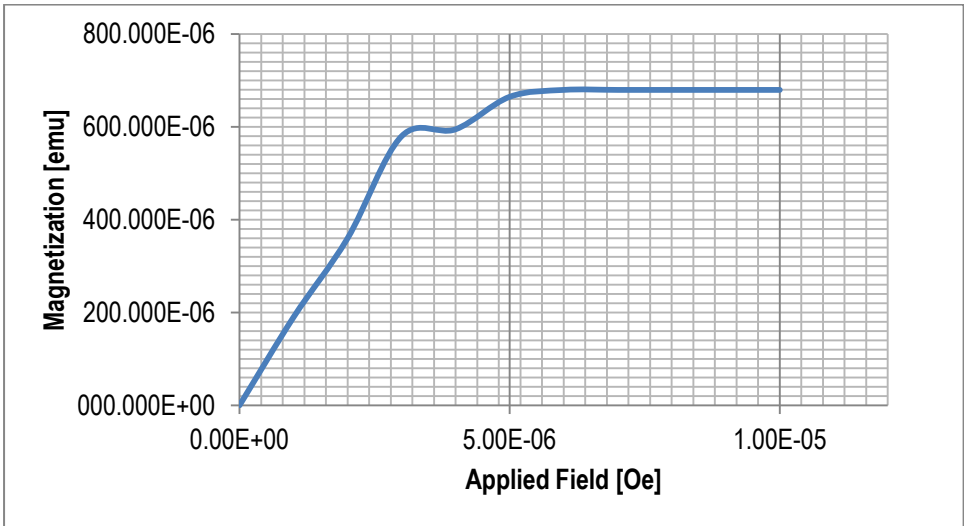


Figure. 4.42: Variation of magnetization with applied voltage (8% doping)
 slope of the graph is 180.00

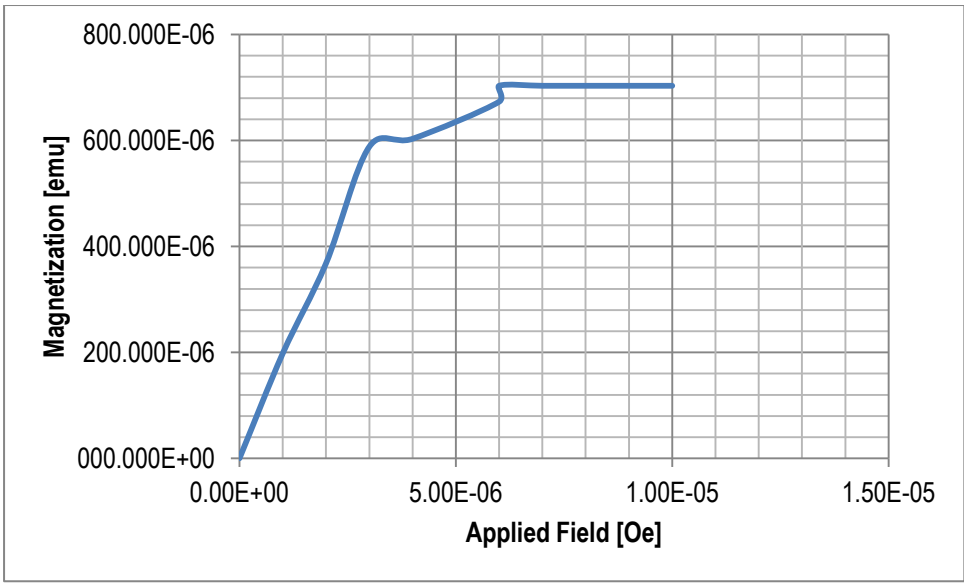


Figure. 4.43: Variation of magnetization with applied voltage (13% doping)

Slope of the graph is 184.00

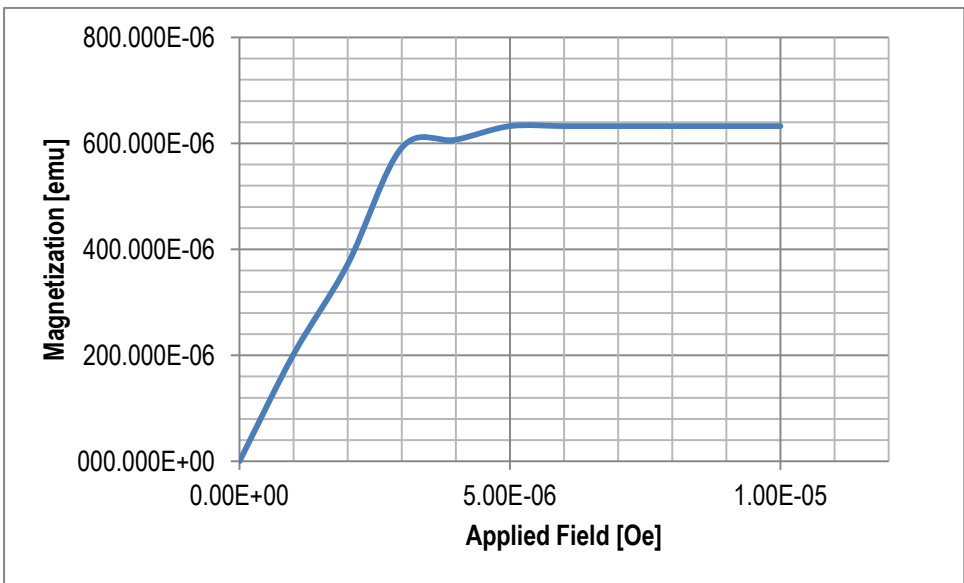


Figure. 4.44: Variation of magnetization with applied voltage (18% doping)

slope of the graph is 186.00

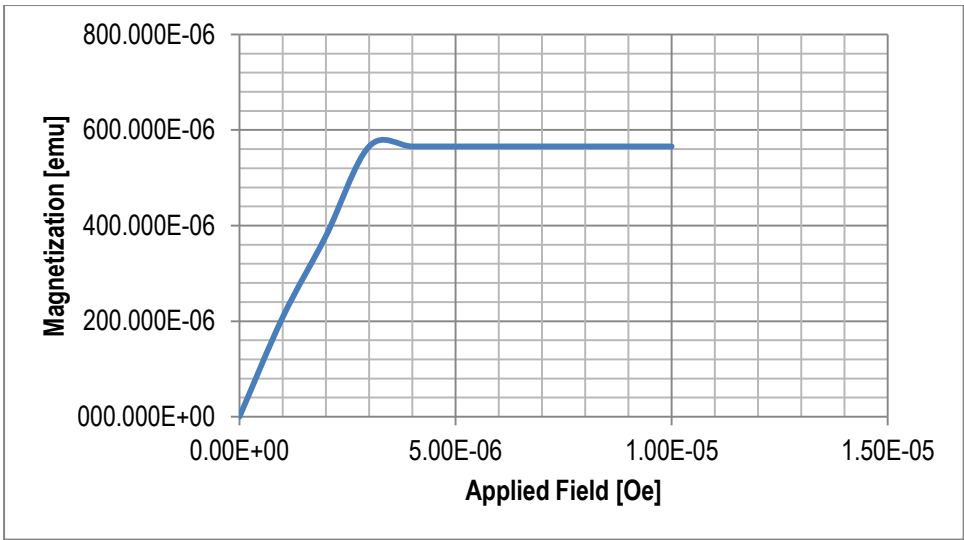


Figure. 4.45: Variation of magnetization with applied voltage (23% doping)

Slope of the graph is 189.00

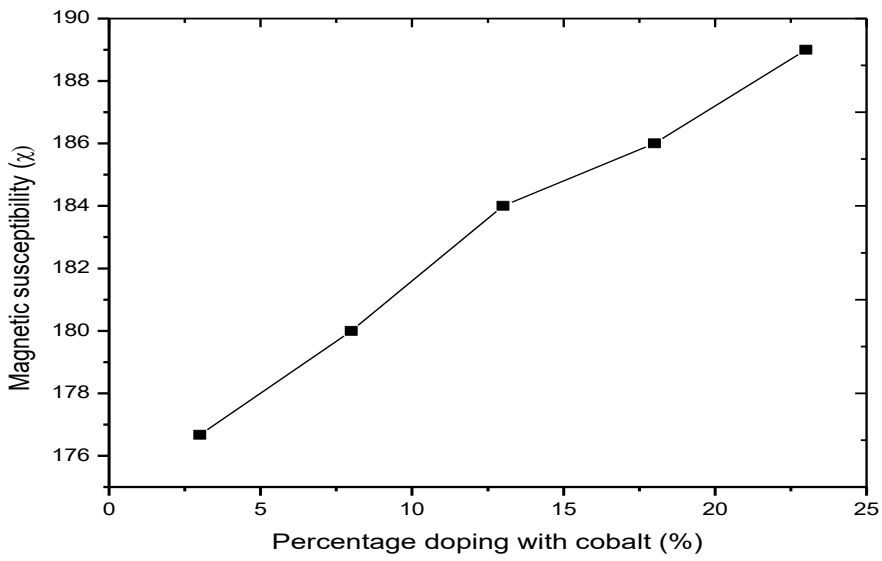


Figure. 4.46: Variation of magnetic susceptibility with percentage cobalt dopant.

4.1.10 Applications of ferromagnetic semiconductors

As the metal oxides are doped with small percentage of cobalt, they have attained the status of dilute magnetic semiconductor (DMS) and as such could have the following applications.

It is widely believed that DMS are ideal material for spintronics. Spintronics involves Giant magnetoresistance (GMR) used in making more sensitive hard disk drive read heads .It is also used in making Giant tunneling magnetoresistance for a more efficient hard disk drive read head. Spintronics, the development of high speed, non-volatile Magnetic random access memory (MRAM) which is expected to revolutionize the memory market and contribute to the development of advanced and versatile computing and personal devices. It is also applied in the development of racetrack memory which uses currents of spin oriented electrons to move magnetic regions along magnetic race tracks, nanoscopic magnetic wires. Racetrack memory is a new technology that could offer higher storage density than flash memory and eventually replace disk drives with a solid state memory device. Spintronics may also enable a leap to quantum computing where units of quantum information known as qubits can occupy spin up and spin down states simultaneously and so allow massive increase in computational power (Zheng, 2008).

4.1.11 Compositional analysis for nickel cobalt oxide nanofilm

Table 4.2 shows that as the mass of cobalt dopant increases, mass of host metal (nickel) decreases.

Table 4.2: Compositional analysis for NiCo₂O₄ at various percentage doping with cobalt

Sample	Percentage doping	Ni	O	Co
N10	3	76.3067	21.3333	2.3600
N1	8	72.3046	21.3321	6.2933
N11	13	68.4399	21.3334	10.2267
N12	18	64.5099	21.3301	14.1600
N13	23	60.5745	21.3322	18.0933

4.2 Analysis of magnesium cobalt oxide (MgCo₂O₄) nanofilms

The nanofilms were analyzed for their optical, structural, and magnetic properties.

4.2.1 Bandgaps of magnesium cobalt oxide nanofilms at various percentage doping

Results of figs. 4.47 to 4.52 are summarized in Table 4.3 and this depicts the bandgaps for doped and undoped magnesium oxide nanofilms as direct wide bandgap. Result of some researchers are in agreement with this result. viz: MgO thin films has a direct bandgap ranging from 4.5eV to 5.25eV (Ezhil-Raj *et al.*, 2007). A bandgap of 4.2eV was obtained for MgO thin film (Nemade *et al.*, 2014) . Optical absorption band of 5.7eV was obtained for MgO thin film (Ezhil-Raj *et al.*, 2008). Direct bandgap of 6.7eV was obtained for MgO thin film (Saraiva, 2012). However, pure MgO has a bulk bandgap of 7.8eV (Xue *et al.*, 2007). MgO thin film as has a bandgap of 7.3eV (Wang *et al.*, 2013).

However, as wide bandgap semiconductor, electronics made of it have the advantage of being smaller, faster, more reliable and more efficient than the Si based counterparts. Devices made of the material can operate at higher temperatures, voltages and higher frequencies.

From figure 4.53, it is observed that bandgap of MgCo_2O_4 decreases as percentage cobalt dopant increases. The result compares well with the works of other researchers, viz; (Erhaima *et al.*,2010), (Nirmala *et al.*,2010), (Girjesh *et al.*,2013) confirming decrease of bandgap with increasing dopant concentration. Result from figure 4.55, shows that the thickness of MgCo_2O_4 nanofilm increases as the percentage cobalt dopant increases. Since thickness of the films increased with percentage doping, this compares well with the works of (Ebru *et al.*,2014) and (Okafor *et al.*, 2015), and since crystallite size(grain size) increases as film thickness increases (Pandiaraman *et al.*,2011) and (Kumar *et al.*, 2012), this decrease in bandgap could be attributed to increase in crystallite size as thickness increases. Increase in grain size has a decreasing effect on bandgap (Ramana *et al.*, 2003). From figure 4.54, bandgap of magnesium cobalt oxide nanofilm decreases as the thickness of the film increases. This compares well with the work of (Kumar *et al.*, 2012). However formation of impurity level within the bandgap could also lead to decrease in bandgap,

From figure 4.56, the bowing parameter decreases as percentage cobalt dopant increases. Bowing downwards shows that it is positive. This compares well with the works of (Van de walley *et al.*, 1999), (Moses and Van de Walle, 2010) confirming decrease of bowing parameter with increasing percentage dopant.. Bowing parameter is significant for investigating the bandgap energies of ternary alloys, (Gulebagian *et al.*, 2014).

Table 4.3: Variation of bandgap with percentage doping for cobalt doped magnesium oxide

Doping (%)	0 (undoped)	3	8	13	18	23
Bandgap (eV)	5.5	4.4	3.9	3.4	2.8	2.6

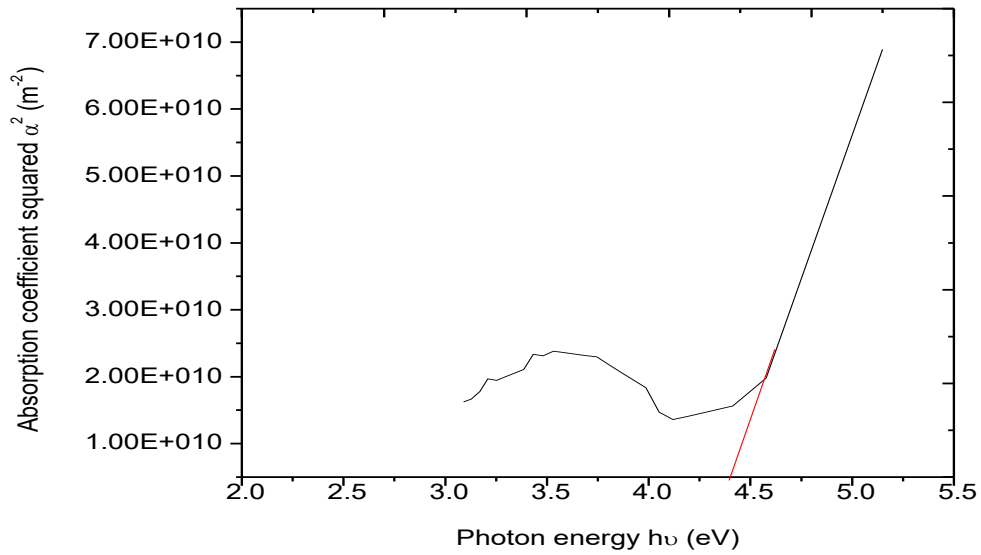


Figure 4.47: Absorption coefficient squared versus photon energy for MgCo₂O₄ nanofilm.(3% doped with cobalt)

MgCo₂O₄ (3% cobalt doped) nanofilm has a direct allowed bandgap of 4.4eV

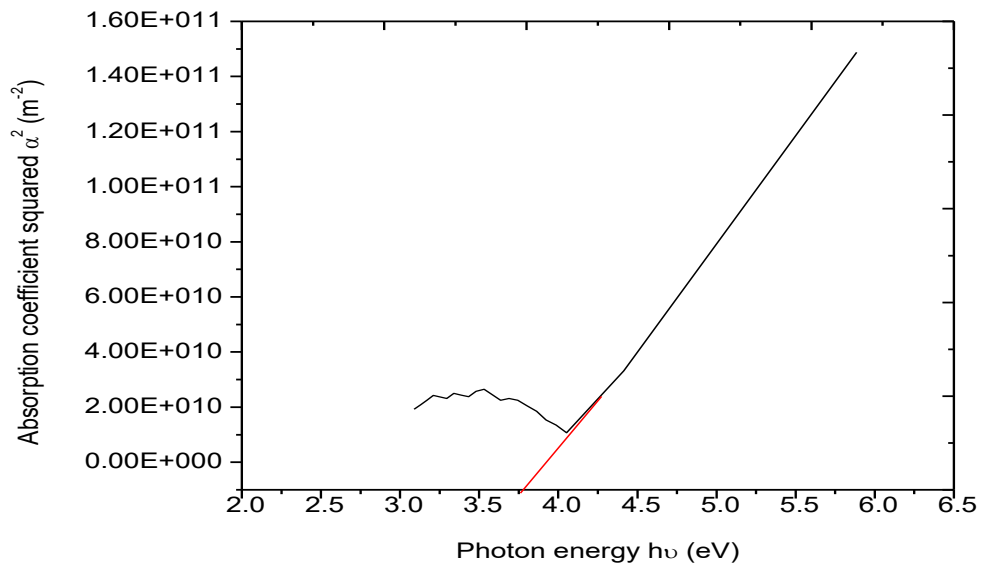


Figure 4.48: Absorption coefficient squared versus photon energy for MgCo₂O₄ nanofilm (8% doped with cobalt)

MgCo₂O₄ nanofilm (8% cobalt doped) has a direct allowed bandgap of 3.8eV

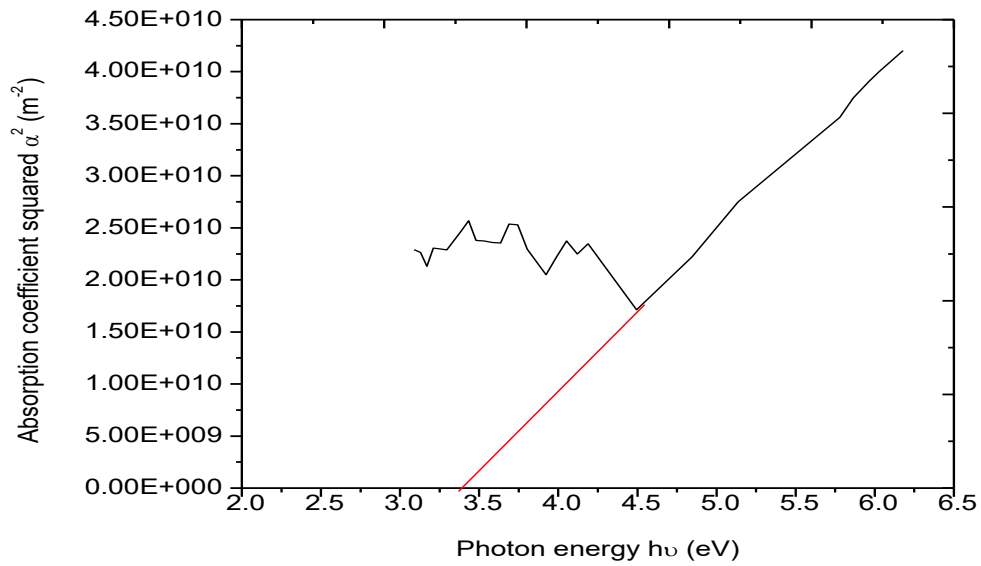


Figure 4.49: Absorption coefficient squared versus photon energy for MgCo₂O₄ nanofilm(13% doped with cobalt)

Figure 4.48 shows that, MgCo₂O₄ nanofilm(13% cobalt doped) has a direct allowed bandgap of 3.4eV

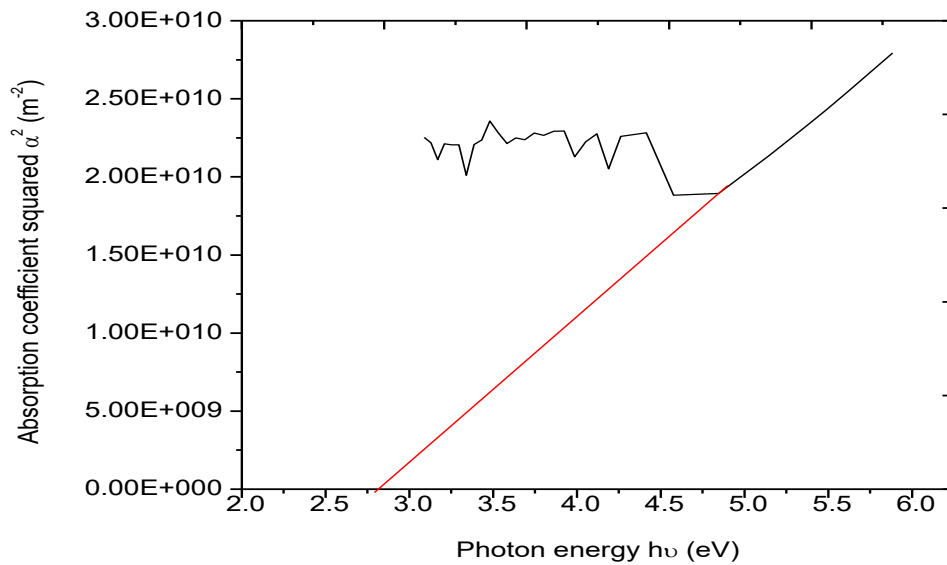


Figure 4.50: Absorption coefficient squared versus photon energy for MgCo₂O₄ nanofilm (18% doped with cobalt).

MgCo₂O₄ nanofilm (18% cobalt doped) has a direct allowed bandgap of 2.8eV

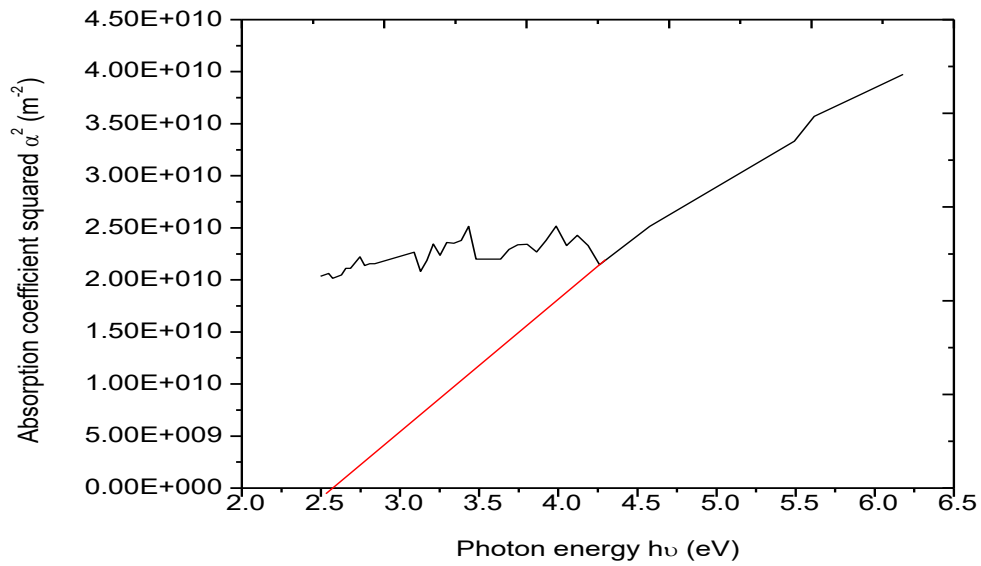


Figure 4.51: Absorption coefficient squared versus photon energy for MgCo₂O₄ nanofilm(23 % doped with cobalt).

MgCo₂O₄ nanofilm (23% cobalt doped) has a direct allowed bandgap of 2.6eV

4.2.2 Bandgap of MgO nanofilm (undoped)

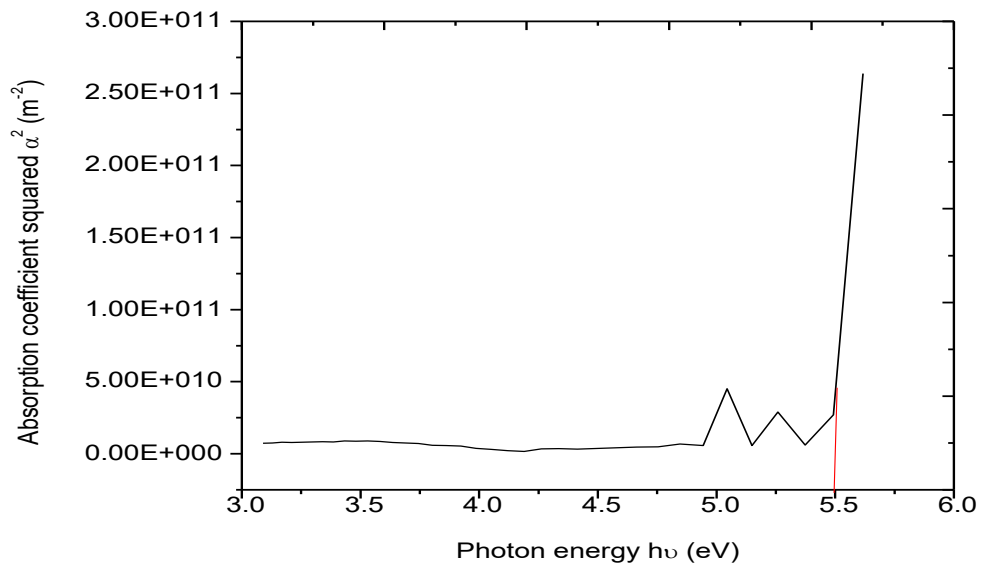


Figure 4. 52: Absorption coefficient squared versus photon energy for MgO nanofilm .

Figure 4.52 shows that, magnesium oxide nanofilm has a direct allowed bandgap of 5.5eV

4.2.3 Bandgap variations and thickness variation

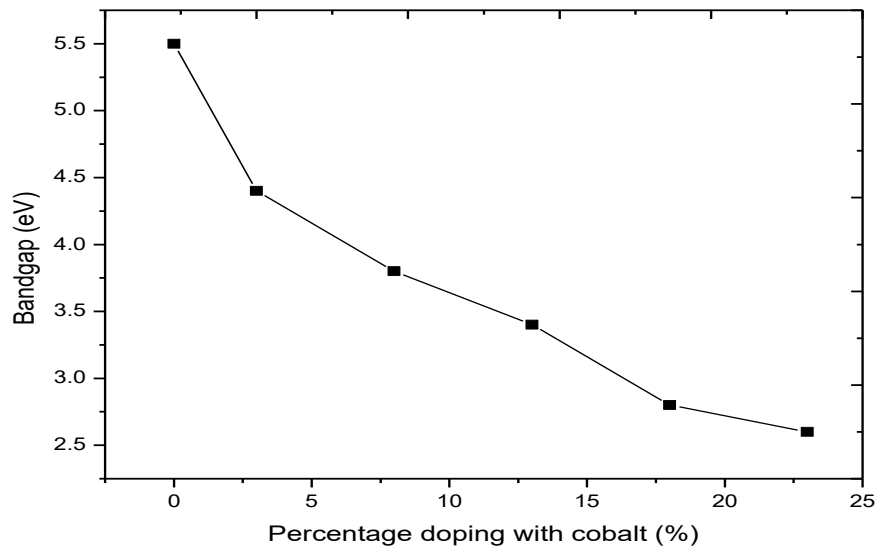


Figure 4. 53: Variation of bandgap with percentage doping with cobalt, for MgCo_2O_4 nanofilm.

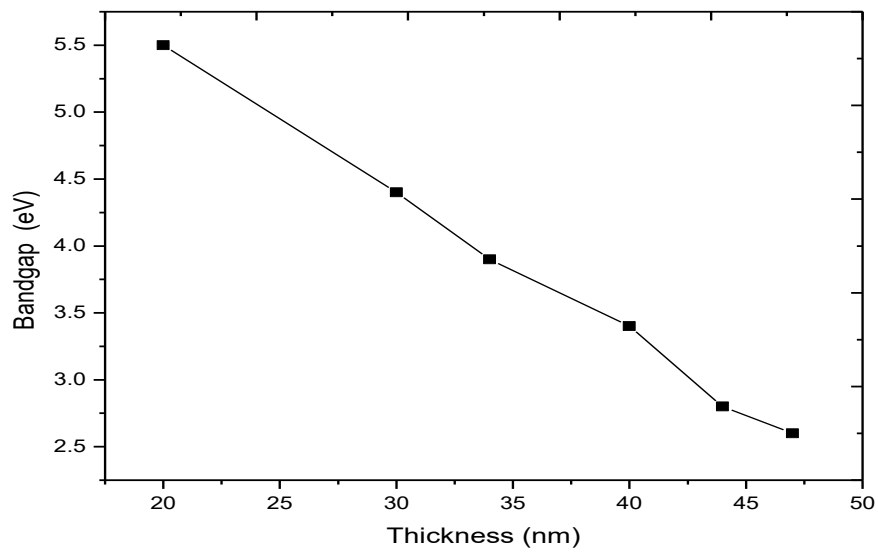


Figure 4. 54: Variation of bandgap with thickness for MgCo_2O_4 nanofilms.

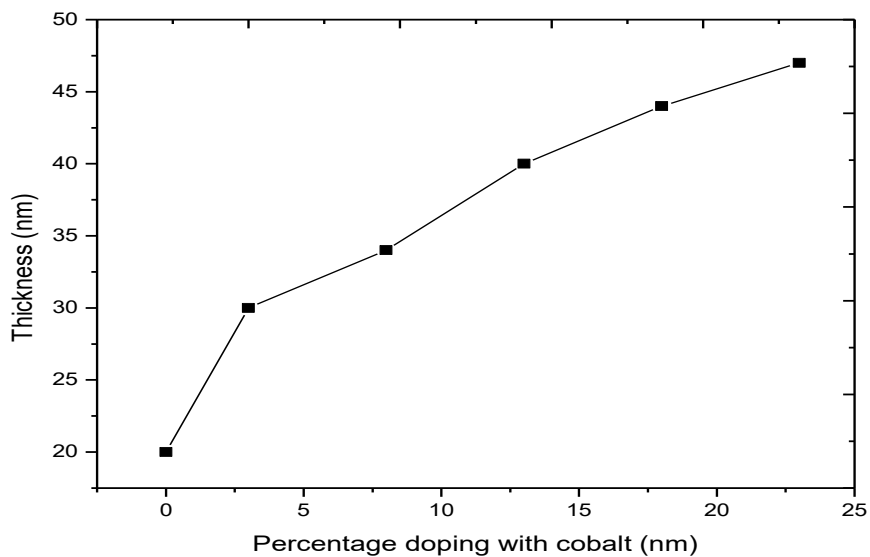


Figure 4.55: Variation of thickness with percentage doping for MgCo₂O₄ nanofilm

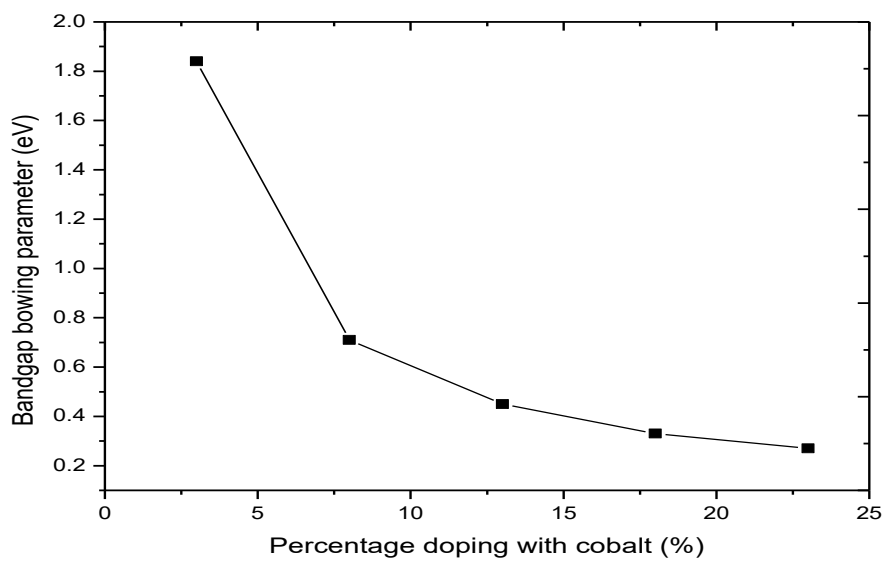


Figure 4.56: Variation of bandgap bowing parameter with percentage doping for magnesium cobalt oxide nanofilms.

4.2.4 Effect of percentage doping on optical properties of magnesium cobalt oxide nanofilms

From figure 4.57, the films generally have low absorbance due to their ultrathin nature. The absorbance is maximum in the UV region,(23% : 0.08=8%) and decreases to zero in the NIR region. The undoped film has the lowest absorbance, maximum of 0.035=3.5% in UV region and decreases to zero in NIR region. Absorbance of the film increases as the percentage cobalt dopant increases.

Figure 4.58 shows that transmittance of the films is generally high in all the regions (UV-Vis-NIR) with minimum in the UV region(23%: 84%) and increases to maximum in NIR(\approx 100%). The undoped film has minimum transmittance of 93.47% in UV region and tends to 100% in NIR region. This property makes the films good material for phosphors, solar cell and photothermal application. The transmittance decreases with increasing percentage doping. As shown in figure 4.59, reflectance of the films is generally low, with maximum value of 0.0781 \approx 7.8%(23% doping) and decreases to zero in the NIR. The undoped film has lowest reflectance, maximum of 0.031=3.1% in UV region and tends to zero in visible region. This property makes it a good material for antireflection coating. Reflectance increases as the percentage cobalt dopant increases.

From figure 4.60, refractive index of the doped films is generally high in the UV region with 23% doping having maximum (1.78) and 3% (1.6) and decreases to minimum in VIS-NIR region. The undoped film has the lowest, maximum of 1.44 in UV region and tends to zero in VIS region. This low refractive index makes it a good material for antireflection stack. The refractive index increases as the percentage cobalt dopant increases. Figure 4.61 shows that extinction coefficient of the film is maximum in the UV region(0.007 for 23%) and decreases to zero in the NIR region of electromagnetic spectrum. The undoped film has the lowest value 0.003 in UV region and tends to zero in NIR region. The extinction coefficient increases with increasing percentage doping with cobalt. Figure 4.60 shows that complex dielectric constant of the film is maximum in the UV region(3.2 for 23%) and decreases to minimum in the VIS -NIR regions of electromagnetic spectrum. The undoped film has lowest complex dielectric constant, maximum of 2.078 in UV region and tends to zero in NIR region. The complex dielectric constant increases with increasing percentage doping with cobalt.

From figure 4.63, optical conductivity of the film is maximum in the UV region ($9.7014\text{E}+12$ for 23%) and decreases to zero in the NIR region of electromagnetic spectrum. The undoped film has the lowest optical conductivity, maximum of $3.22\text{E}+12$ in UV region and decreases to zero in visible region. The optical conductivity increases with increasing percentage doping with cobalt.

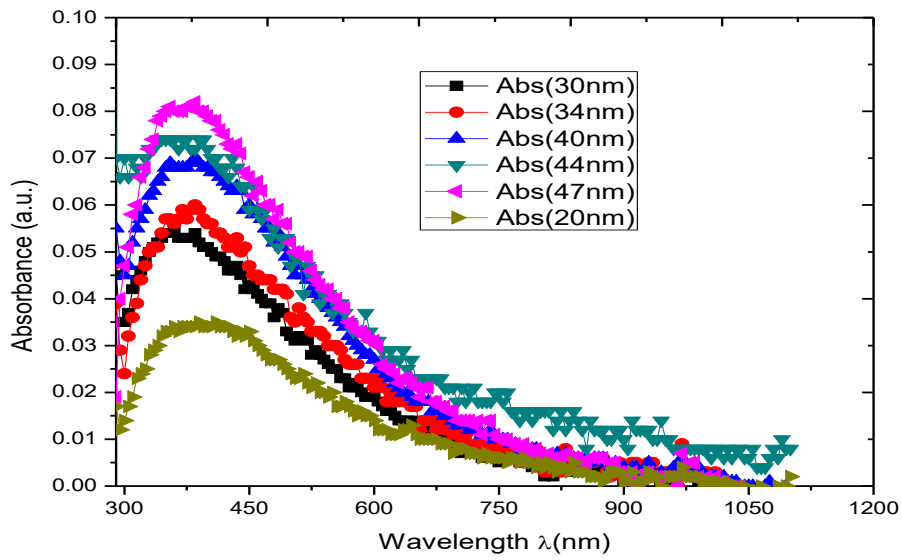


Figure 4.57: Variation of absorbance with wavelength for MgCo_2O_4 nanofilms for different percentages doping with cobalt.

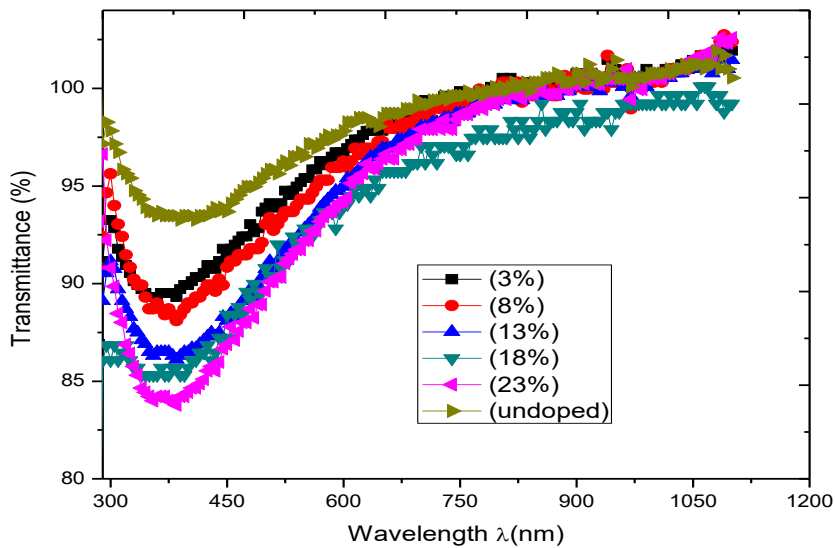


Figure 4.58: Variation of transmittance with wavelength for MgCo_2O_4 nanofilms for different percentages doping with cobalt.

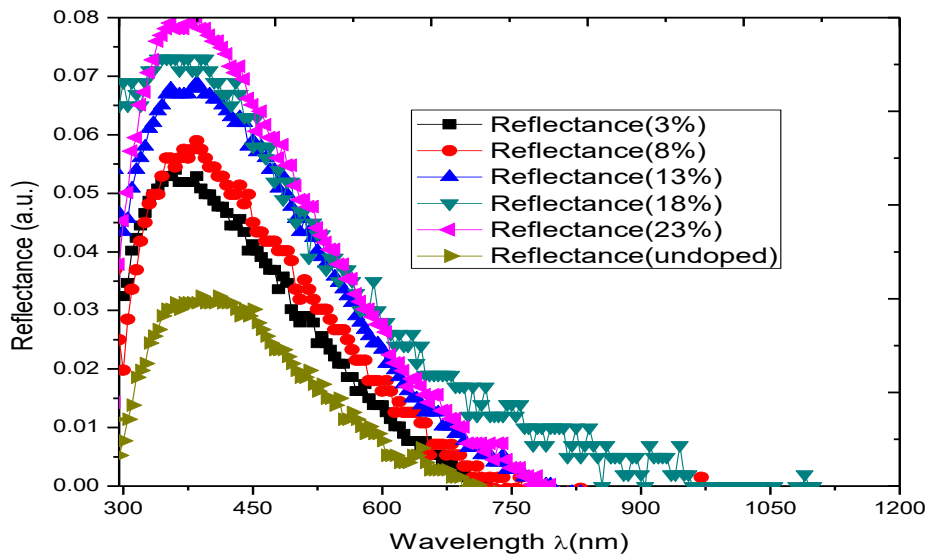


Figure 4.59: Variation of reflectance with wavelength for cobalt doped MgCo_2O_4 nanofilms for different percentages doping with cobalt.

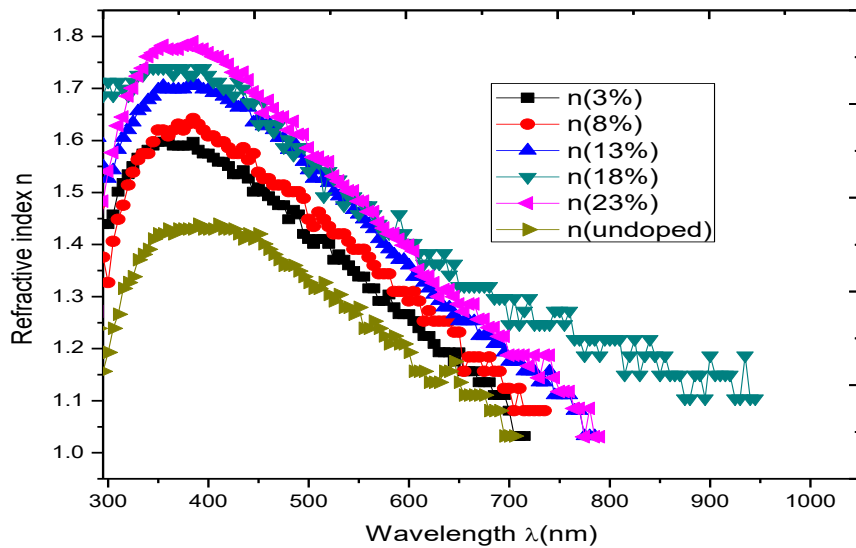


Figure 4.60: Variation of refractive index with wavelength for MgCo_2O_4 nanofilms for different percentages doping with cobalt.

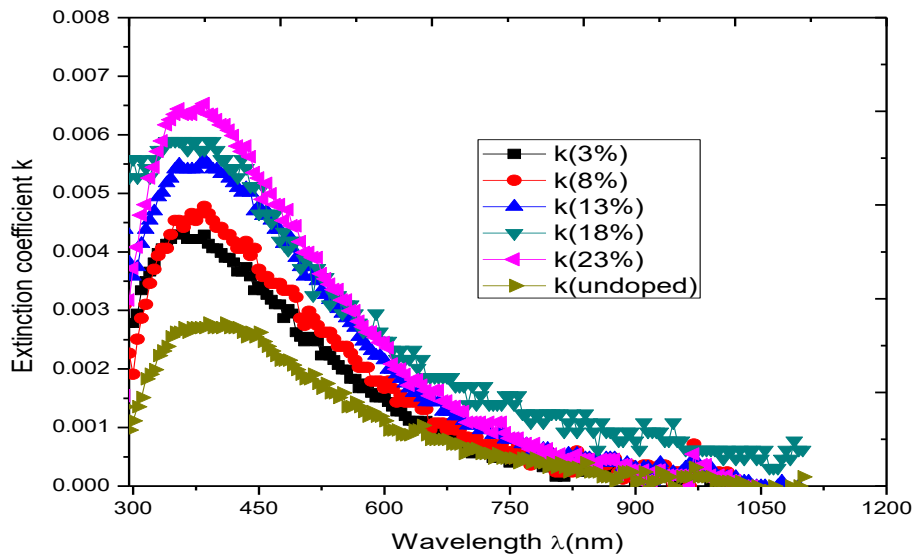


Figure 4.61 Variation of extinction coefficient with wavelength for MgCo_2O_4 nanofilms for different percentages doping with cobalt.

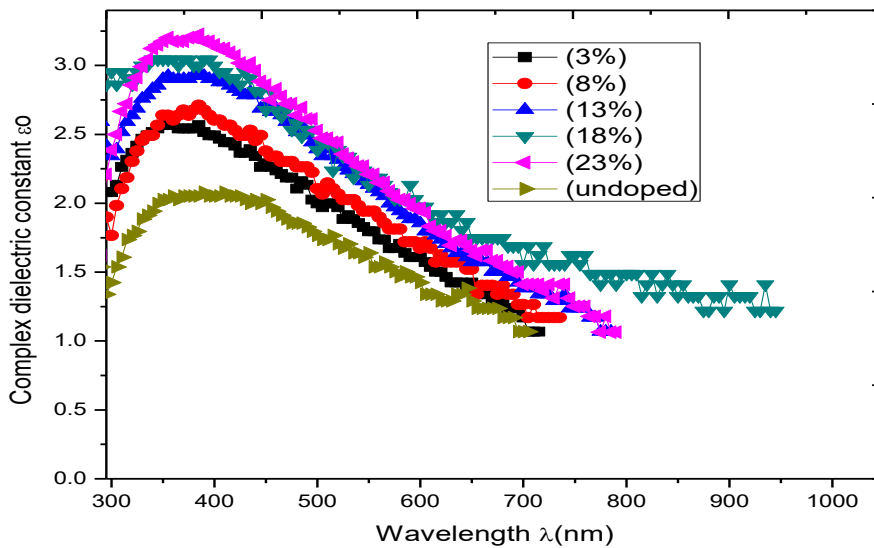


Figure 4.62: Variation of complex dielectric constant with wavelength for MgCo_2O_4 nanofilms for different percentages doping with cobalt.

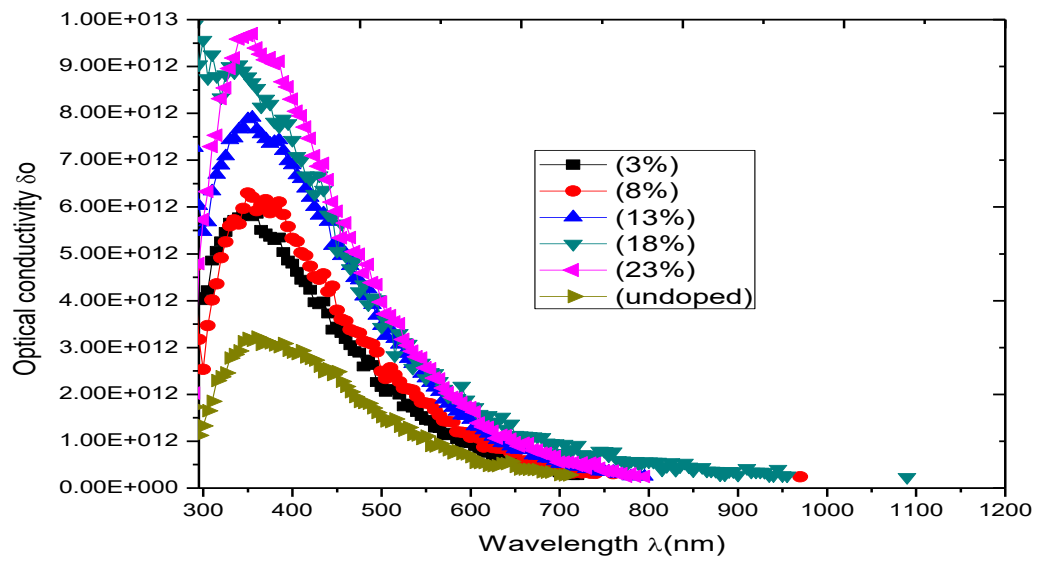


Figure 4.63: Variation of optical conductivity with wavelength for MgCo₂O₄ nanofilms for different percentages doping with cobalt.

4.2.5 Effect of thickness on optical properties of magnesium cobalt oxide nanofilms

From figure 4.64 , absorbance of the films increases with increasing thickness of the films. Maximum of 0.082 in UV region for 47nm. The undoped (thickness of 20nm) has the lowest absorbance, maximum of 0.035=3.5% in UV region . The absorbance decreases to zero in NIR region.

The result in figure 4.65 shows that transmittance of the films decreases with increasing thickness of the films. Minimum of 83.78% for 47nm in UV region . The undoped film (thickness of 20nm) has minimum transmittance of 93.25% in UV region. However, transmittance of the films tends to 100% in NIR region.

From figure 4.66, reflectance of the films increases with increasing thickness of the films. Maximum of 0.079= 7.9% for 47nm in UV region.

Figure 4.67 shows that the refractive index of the films increases with increasing thickness of the films. Maximum of 1.78 for 47nm in UV region and tends to zero in NIR region. The undoped film (thickness of 20nm) has the lowest refractive index, maximum of 1.43 in UV region and tends to zero in visible region.

As shown in figure 4.68, extinction coefficient of the films increases with increasing thickness of the films. Maximum of 6.53E-03 for 47nm in UV region.

As shown in figure 4.69, complex dielectric constant of the films increases with increasing thickness of the films. Maximum of 3.23 for 47nm in UV region. The undoped film (thickness of 20nm) has the lowest extinction coefficient, maximum of 0.00278 in UV region. Extinction coefficient of the films decreases to zero in NIR region.

From figure 4.70, optical conductivity of the films increases with increasing thickness of the films. Maximum of 9.70E+12 for 47nm in UV region. The undoped film (thickness of 20nm) has the lowest optical conductivity, maximum of 3.15E+12 in UV region. Optical conductivity of the films decreases to zero in NIR region.

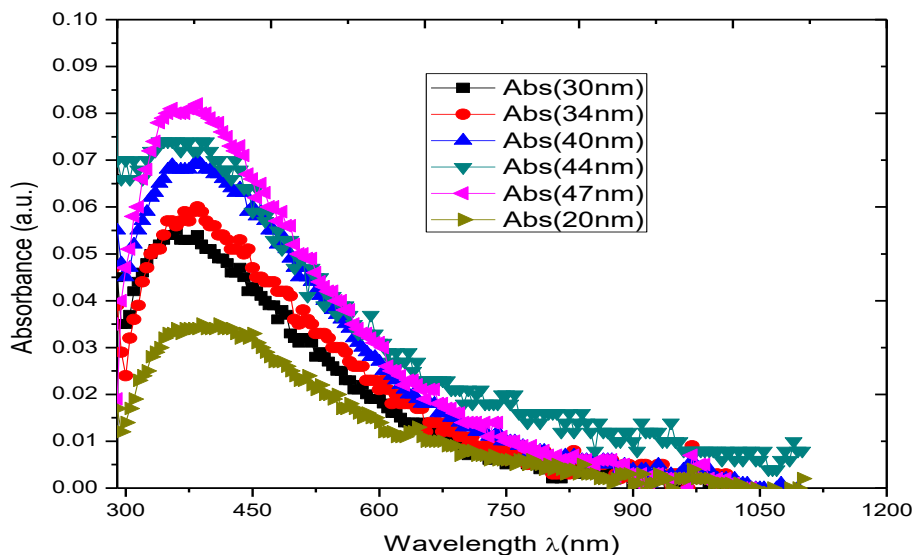


Figure 4.64: Variation of absorbance with wavelength for MgCo_2O_4 nanofilms for different thicknesses.

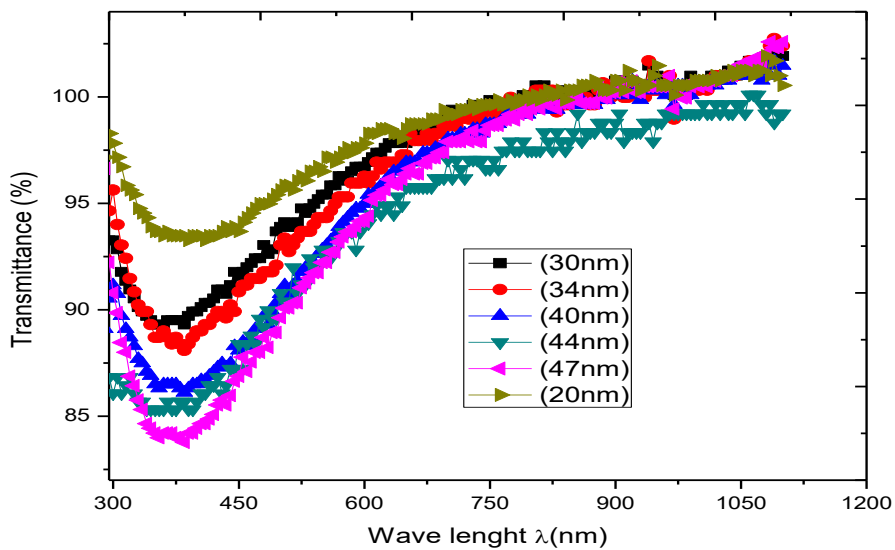


Figure 4.65: Variation of transmittance with wavelength for MgCo_2O_4 nanofilms for different thicknesses.

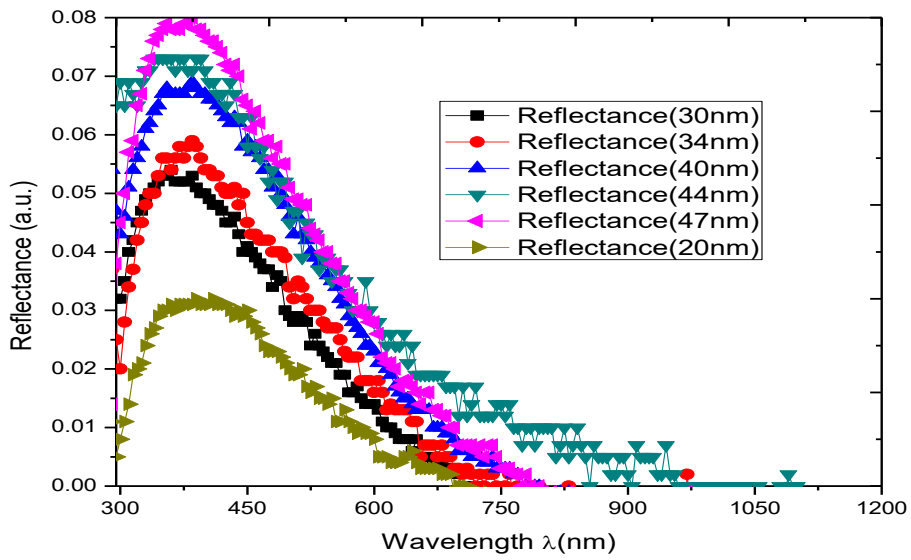


Figure 4.66: Variation of reflectance with wavelength for MgCo_2O_4 nanofilms for different thicknesses.

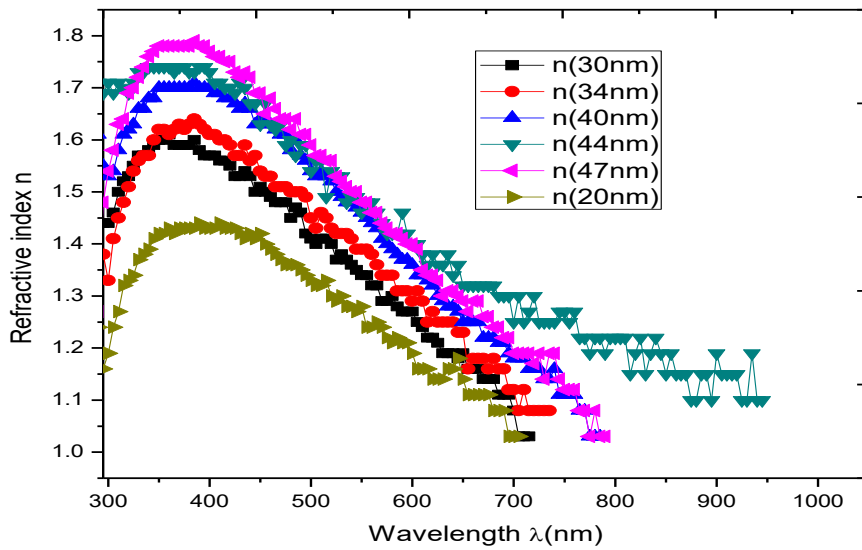


Figure 4.67: Variation of refractive index with wavelength for MgCo_2O_4 nanofilms for different thicknesses.

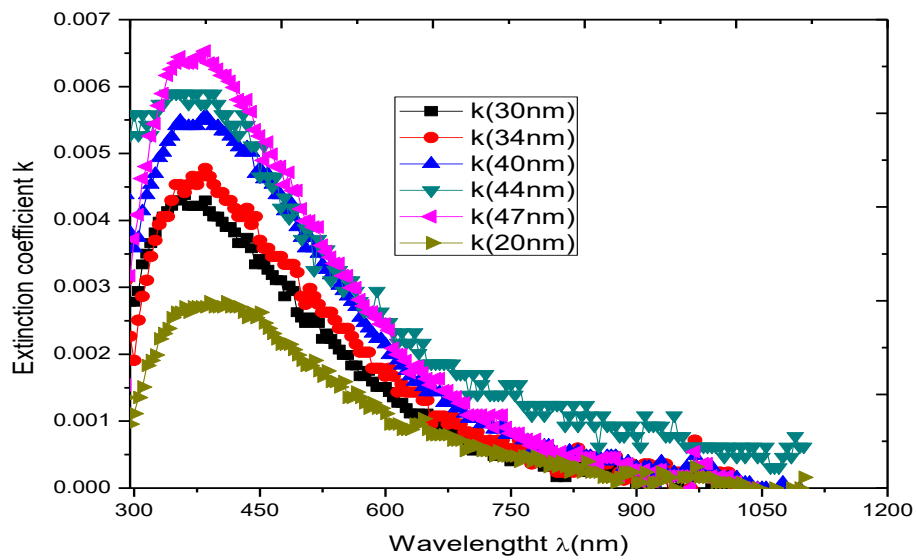


Figure 4.68: Variation of extinction coefficient with wavelength for MgCo_2O_4 nanofilms for different thicknesses.

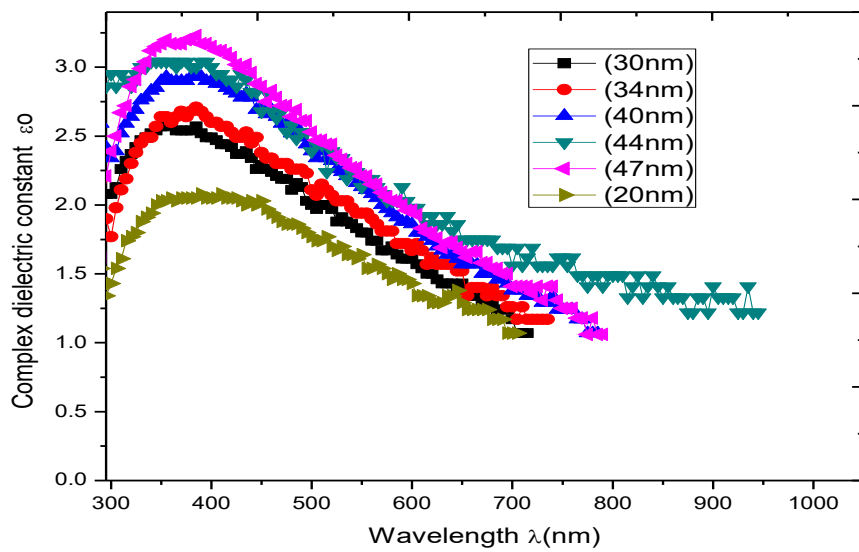


Figure 4.69: Variation of complex dielectric constant with wavelength for MgCo_2O_4 nanofilms for different thicknesses.

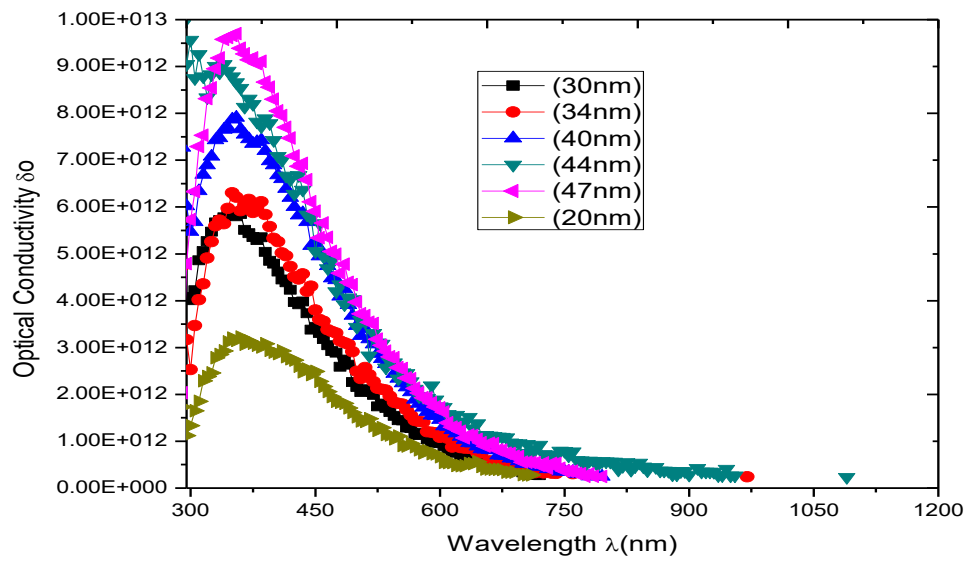


Figure 4.70: Variation of optical conductivity with wavelength for MgCo_2O_4 nanofilms for different thicknesses.

4.2.6 Effect of deposition time on optical properties of magnesium cobalt oxide nanofilms

Figure 4.71 shows that absorbance of the film increases as the deposition time increases. Maximum of 0.064=6.4% in UV region.

From figure 4.72, transmittance of the film decreases as time of deposition increases. Minimum of 87.3 in UV region

Figure 4.73 shows that, reflectance of the film increases as the deposition time increases, maximum of 0.063=6.3% in UV region

As shown in figure 4.74, refractive index of the film increases as the deposition time increases, maximum of 1.65 in UV region

As shown in figure 4.75, extinction coefficient of the film increases as the deposition time increases. Maximum of 0.005 in UV region

Figure 4.76 shows that, complex dielectric constant of the film increases as the deposition time increases, maximum of 2.81 in UV region.

As shown in figure 4.77, optical conductivity of the film increases as the deposition time increases, maximum of $7.1E+12$ in UV region.

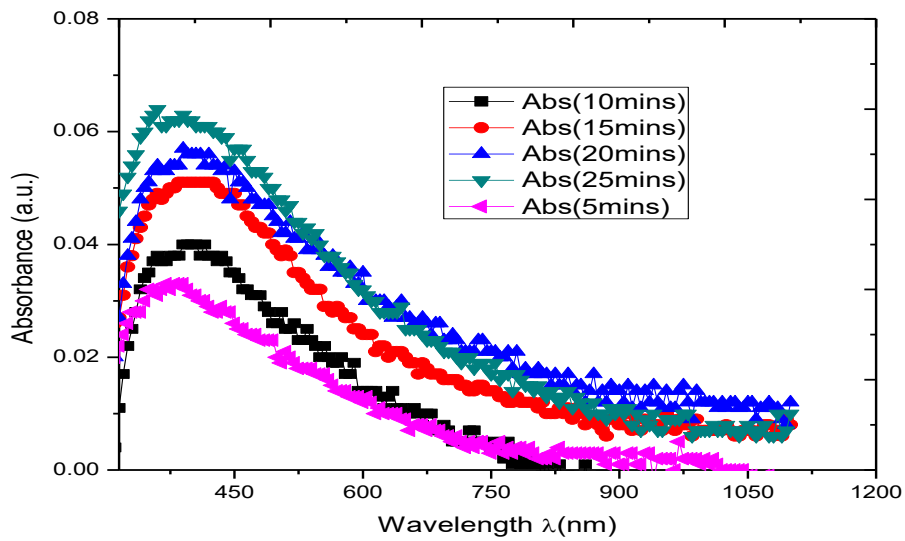


Figure 4.71: Variation of absorbance with wavelength for $MgCo_2O_4$ nanofilms for different deposition times.

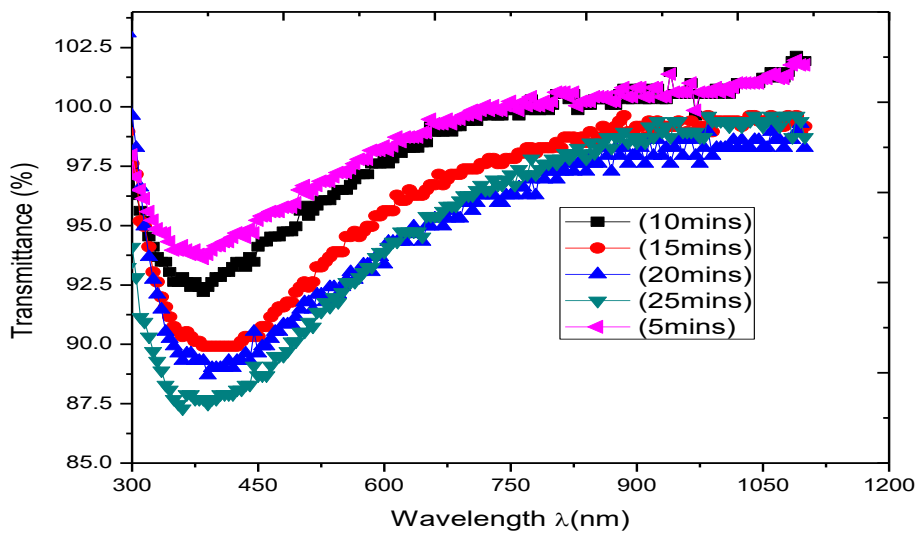


Figure 4.72: Variation of percentage transmittance with wavelength for $MgCo_2O_4$ nanofilms for different deposition times.

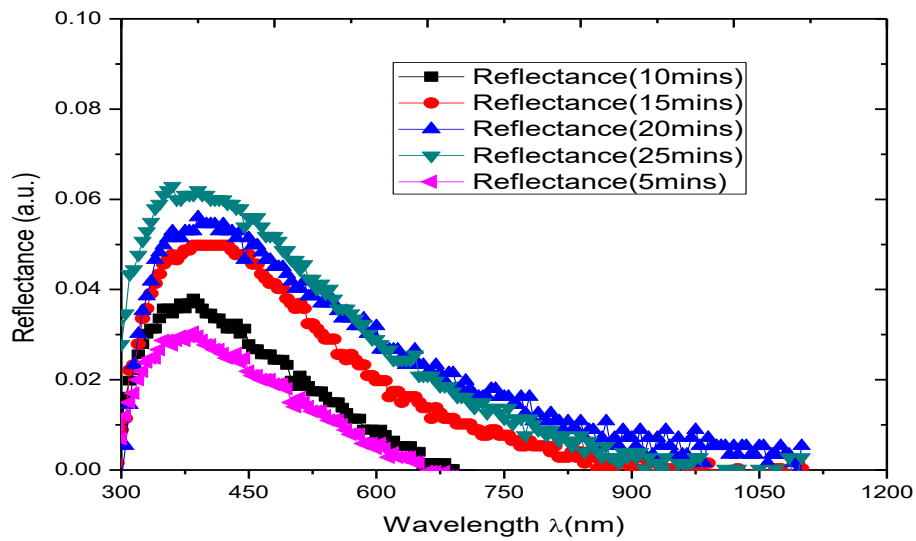


Figure 4.73: Variation of reflectance with wavelength for MgCo_2O_4 nanofilms for different deposition times.

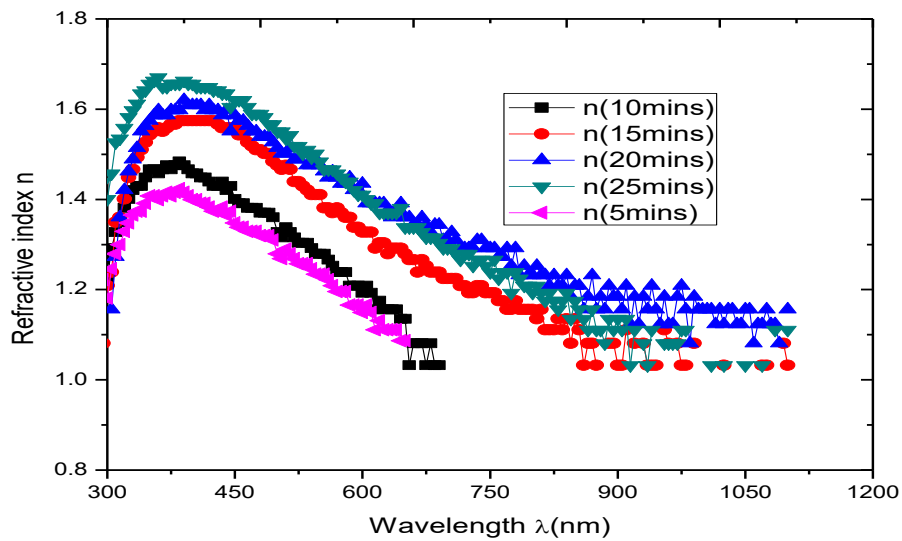


Figure 4.74: Variation of refractive index with wavelength for MgCo_2O_4 nanofilms for different deposition times.

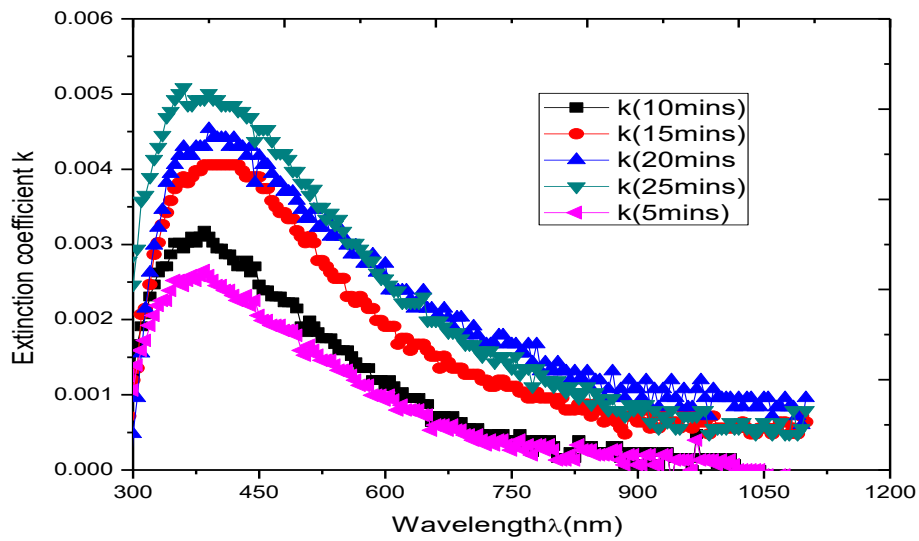


Figure 4.75: Variation of extinction coefficient with wavelength for MgCo_2O_4 nanofilms for different deposition times.

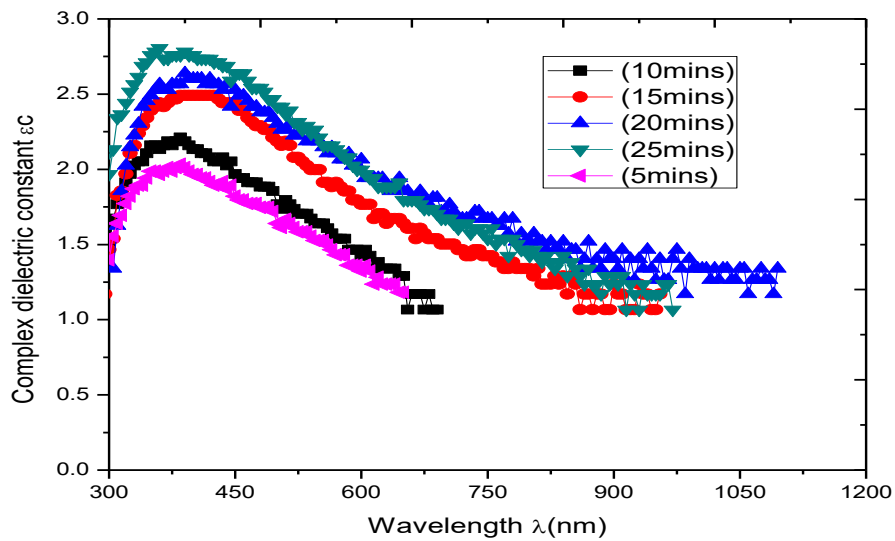


Figure 4.76: Variation of complex dielectric constant with wavelength for MgCo_2O_4 nanofilms for different deposition times.

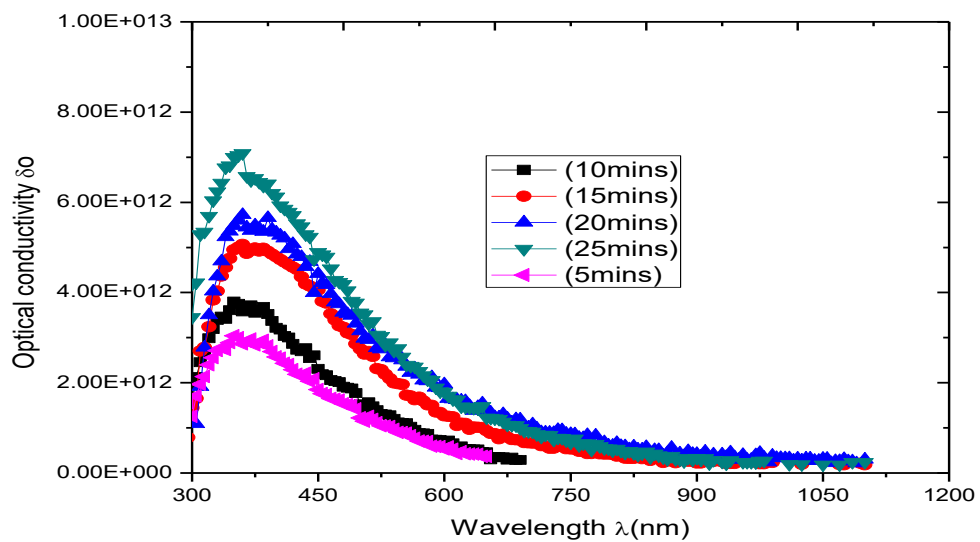


Figure 4.77: Variation of optical conductivity with wavelength for MgCo_2O_4 nanofilms for different deposition times.

4.2.7 Effect of deposition voltage on optical properties of magnesium cobalt oxide nanofilms

Figure 4.78 shows that absorbance of the film increases as deposition voltage increases. Maximum of 0.071=7.1% for 13V in UV region.

Figure 4.79 shows that transmittance of the film decreases as deposition voltage increases, minimum of 85.14 for 13V in UV region.

As shown in figure 4.80, reflectance of the film increases as deposition voltage increases. Maximum of 0.0755= 7.55% for 13V in UV region.

From figure 4.81, refractive index of the film increases as deposition voltage increases. Maximum of 1.74 for 13V in UV region

Figure 4.82 shows that extinction coefficient of the film increases as deposition voltage increases. Maximum of 0.006 for 13V in UV region.

From figure 4.83, complex dielectric constant of the film increases as deposition voltage increases. Maximum of 3.1 for 13V in UV region.

As shown in figure 4.84, optical conductivity of the film increases as deposition voltage increases. Maximum of 9.1E+12 for 13V in UV region.

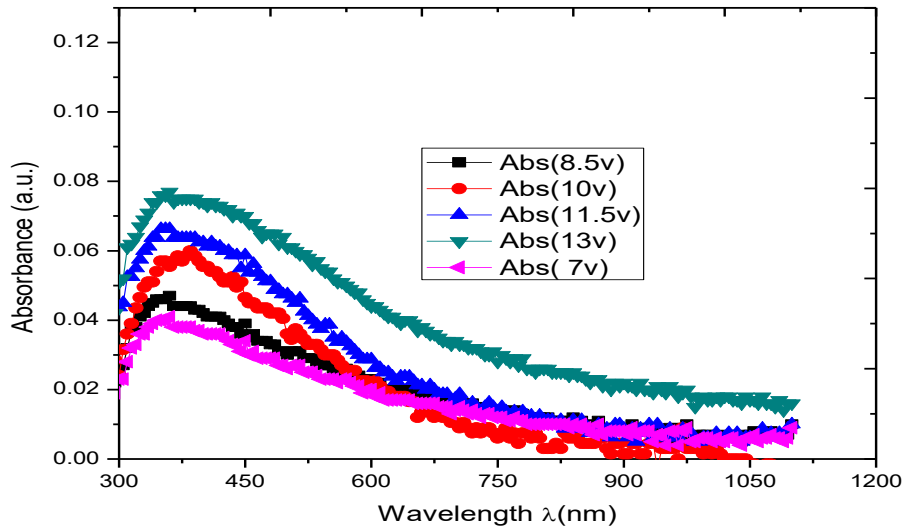


Figure 4.78: Variation of absorbance with wavelength for MgCo_2O_4 nanofilms for different deposition voltages.

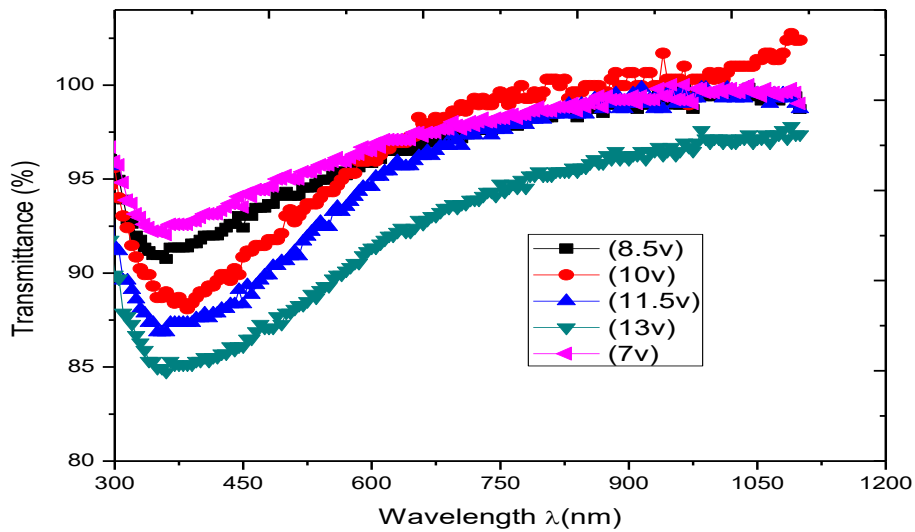


Figure 4.79: Variation of transmittance with wavelength for MgCo_2O_4 nanofilms for different deposition voltages.

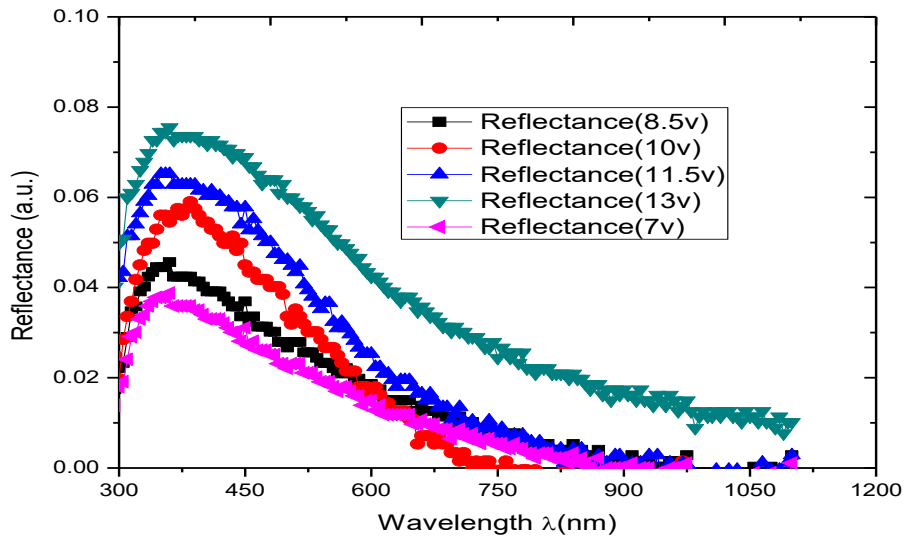


Figure 4.80: Variation of reflectance with wavelength for MgCo_2O_4 nanofilms for different deposition voltages.

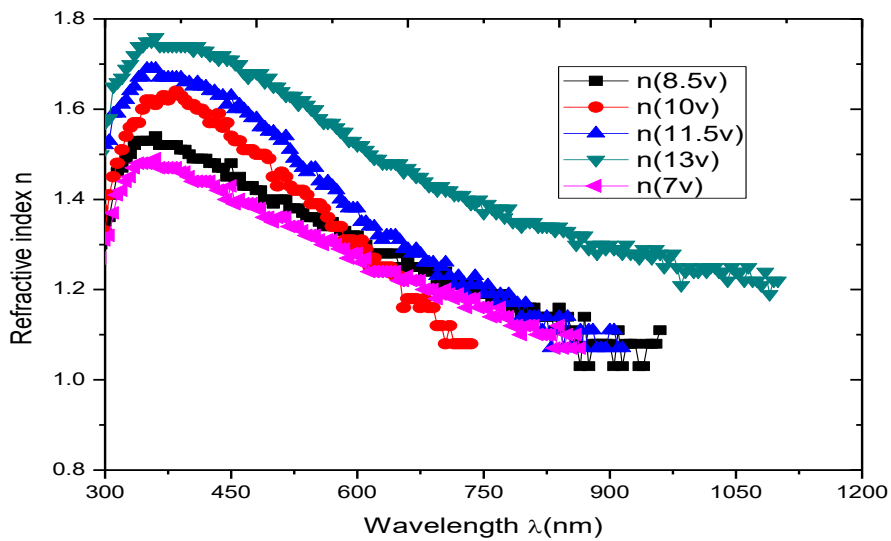


Figure 4.81: Variation of refractive index with wavelength for MgCo_2O_4 nanofilms for different deposition voltages.

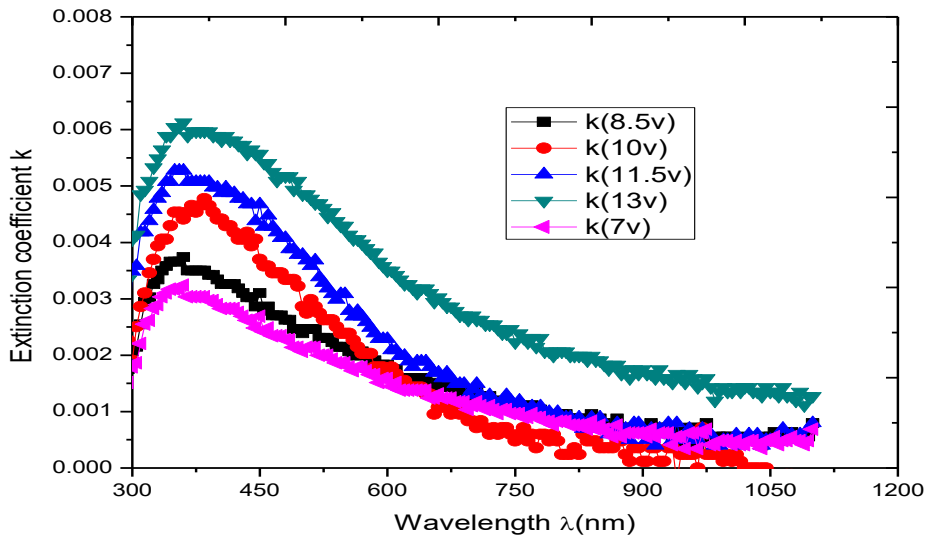


Figure 4.82: Variation of extinction coefficient with wavelength for MgCo_2O_4 nanofilms for different deposition voltages.

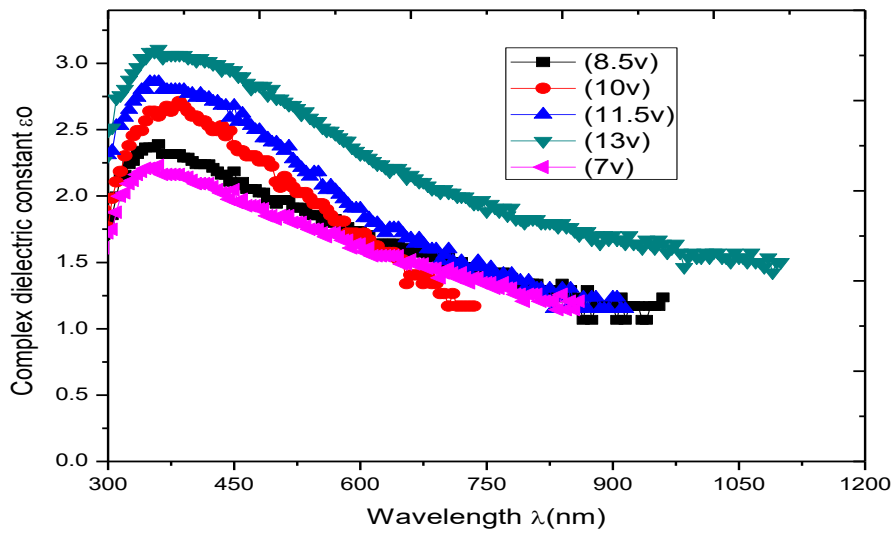


Figure 4.83: Variation of complex dielectric constant with wavelength for MgCo_2O_4 nanofilms for different deposition voltages.

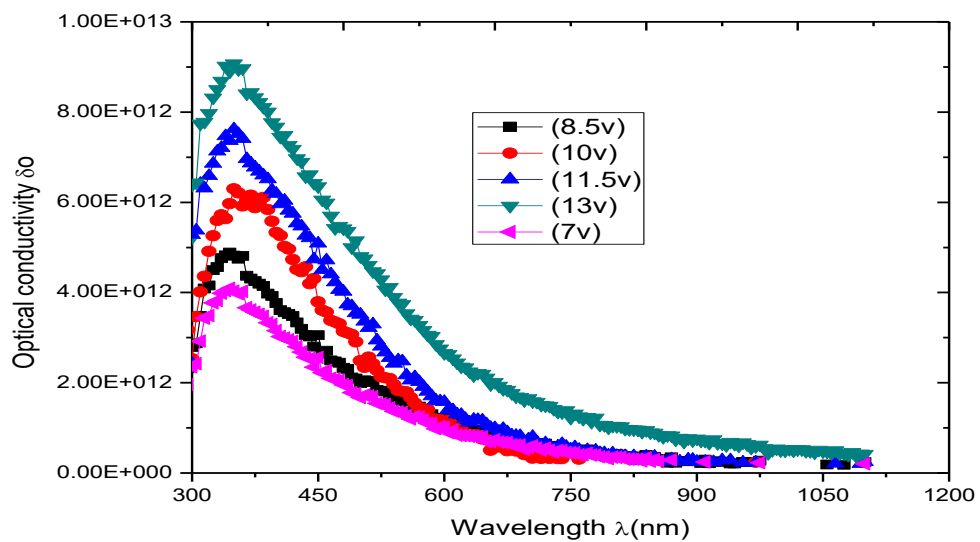


Figure 4.84: Variation of optical conductivity with wavelength for MgCo_2O_4 nanofilms for different deposition voltages.

4.2.8 Variation of magnetic saturation with percentage doping with cobalt for MgCo₂O₄ nanofilms

Figure 4.85 shows that magnetic saturation of pinned layer for MgCo₂O₄ nanofilm rises to a peak value of 3.20E-04 (emu) within the lower percentage range and decreases to minimum value of 1.57E-04 (emu) in the higher percentage doping range. From figure 4.86, magnetic saturation of free layer for MgCo₂O₄ nanofilm fluctuates with percentage doping with cobalt. It rises to a peak value of 7.45E-04 (emu) in the low percentage region and tends to minimum in the subsequent percentage dopings, then rises to a lower peak value of 6.85E-04 (emu) in the higher percentage range. The peak values are the points where it experiences maximum magnetic saturation.

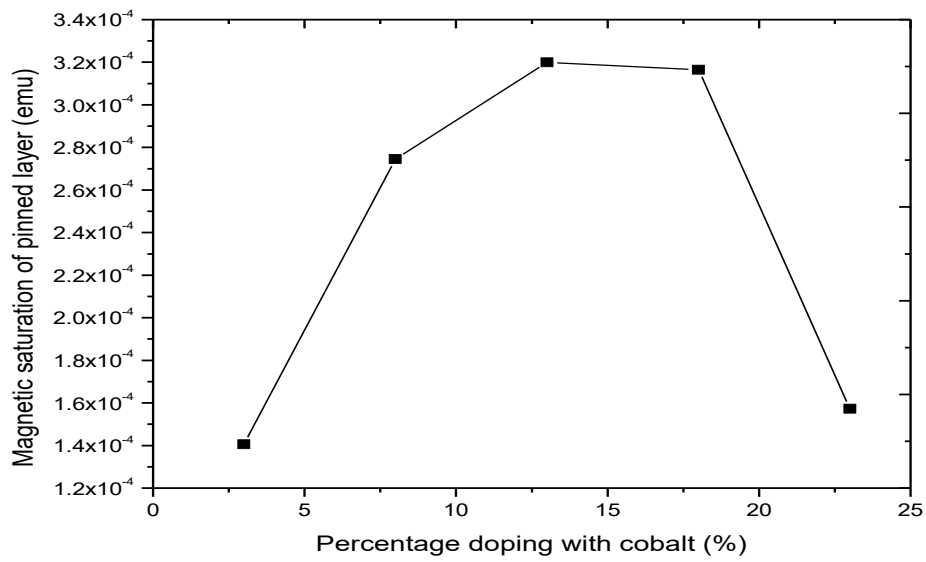


Figure 4.85: Variation of magnetic saturation of pinned layer with percentage doping with cobalt.

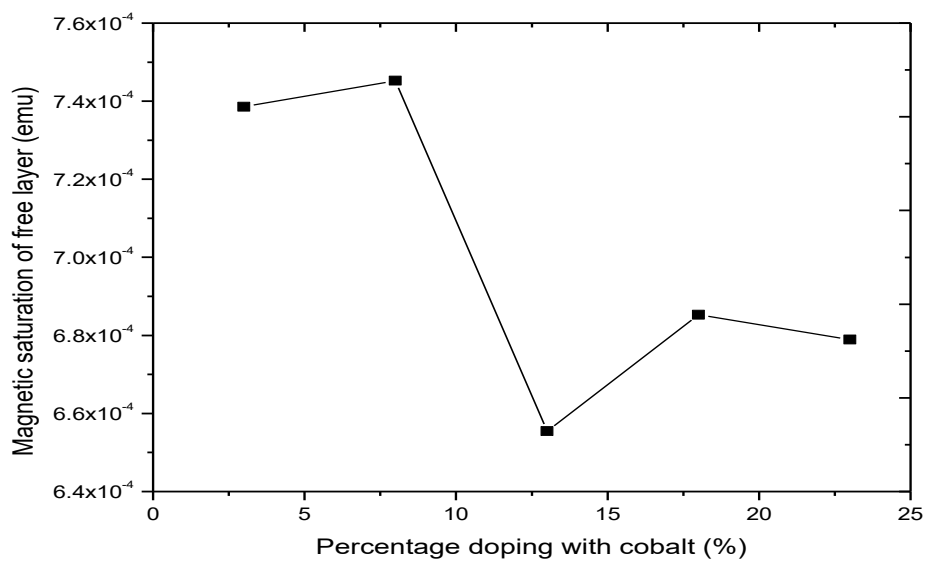


Figure 4.86: Variation of magnetic saturation of free layer with percentage doping with cobalt for MgCo_2O_4

4.2.9 Variation of magnetization with applied voltage at various percentages of cobalt dopant for MgCo₂O₄ nanofilms

From figure 4.87, slope of the graph is 118.00 , therefore magnetic susceptibility for 3% doped film is 118.00. Figure 4.88 shows that slope of the graph is 119.00 , therefore magnetic susceptibility of 8% doped film is 119.00. As shown in figure 4.89, slope of the graph is 120.50 , therefore magnetic susceptibility of 13% doped film is 120.50. As shown in figure 4.90, slope of the graph is 122.00 , therefore magnetic susceptibility of 18% doped film is 122.00. From figure 4.91, slope of the graph is 123.75 , therefore magnetic susceptibility of 23% doped film is 123.75. Result in figure 4.92 show that magnetic susceptibility increases as percentage cobalt dopant increases. The magnetic saturation of the films are 739.579E-6emu for 3% doped, 745.234E-6emu for 8% doped , 655.454E-6emu for 13doped, 685.291E-6emu for 18% doped and 678.924E-6emu for 23% doped. Since the film has no Fe³⁺ ion, it is not ferrimagnetic and by virtue of positive high magnetic susceptibility and magnetic saturation, the material is ferromagnetic. Applications as ferromagnetic semiconductor is as stated in 4.1.10.

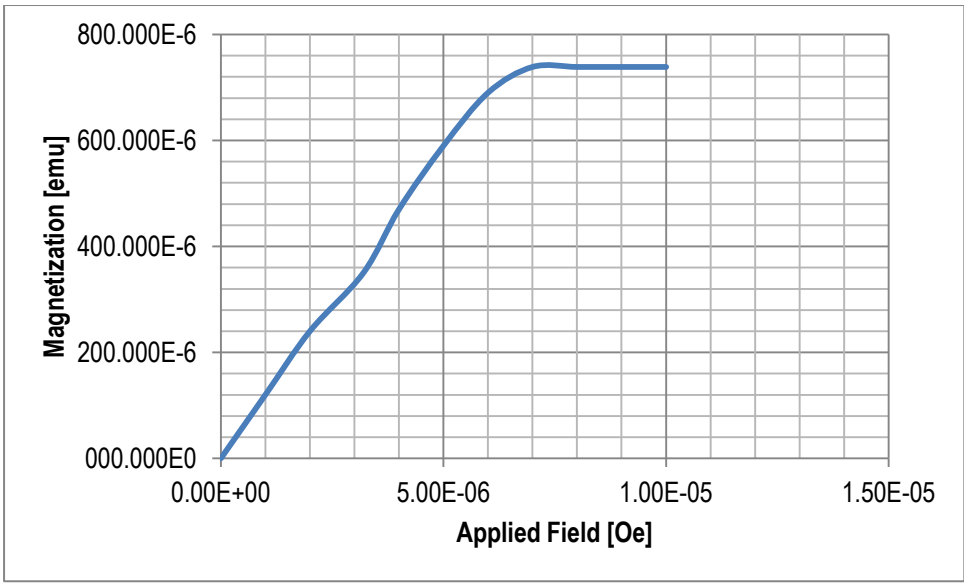


Figure. 4.87: Variation of magnetization with applied voltage (3% doping)

Slope of the graph is 118.00

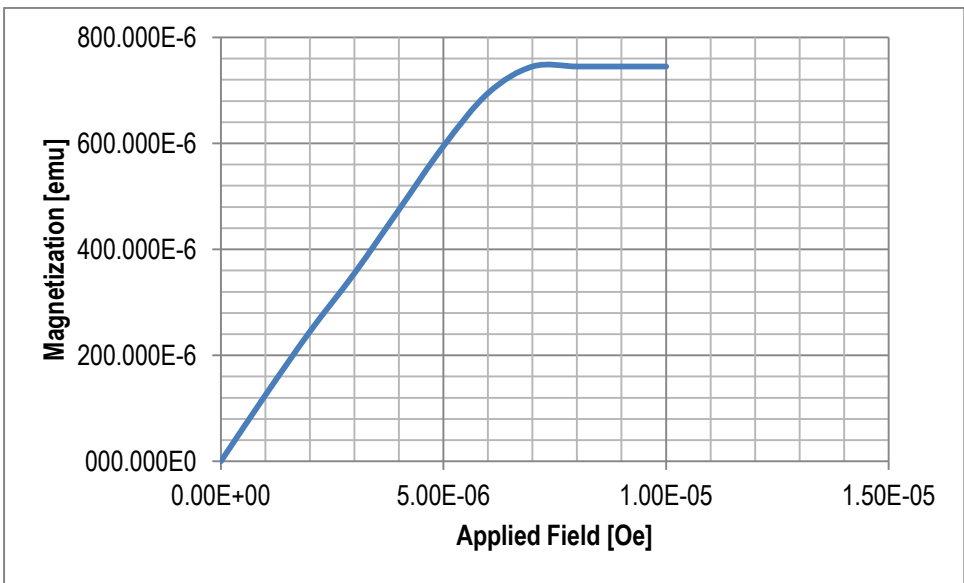


Figure. 4.88: Variation of magnetization with applied voltage (8% doping)

Slope of the graph is 119.00

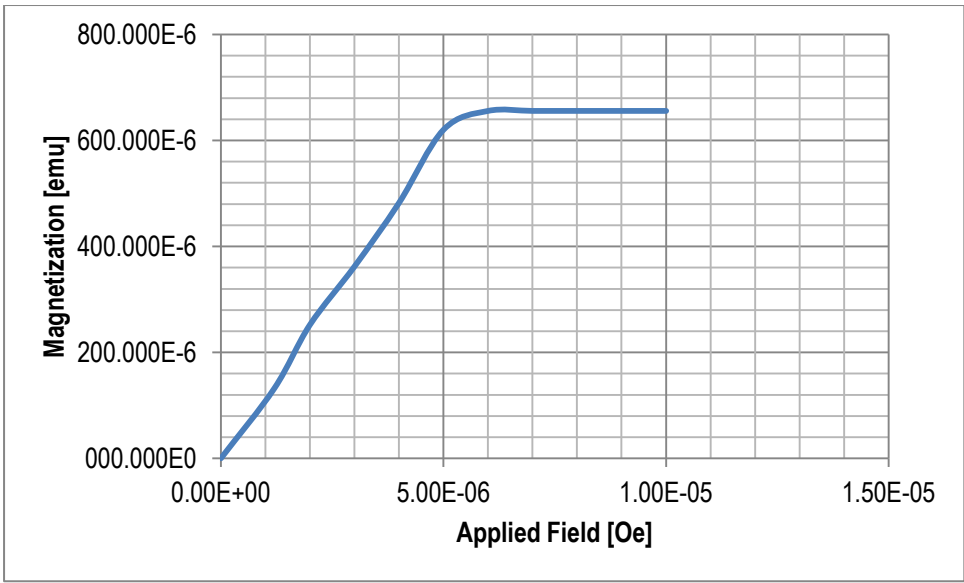


Figure. 4.89: Variation of magnetization with applied voltage (13% doping)

Slope of the graph is 120.50

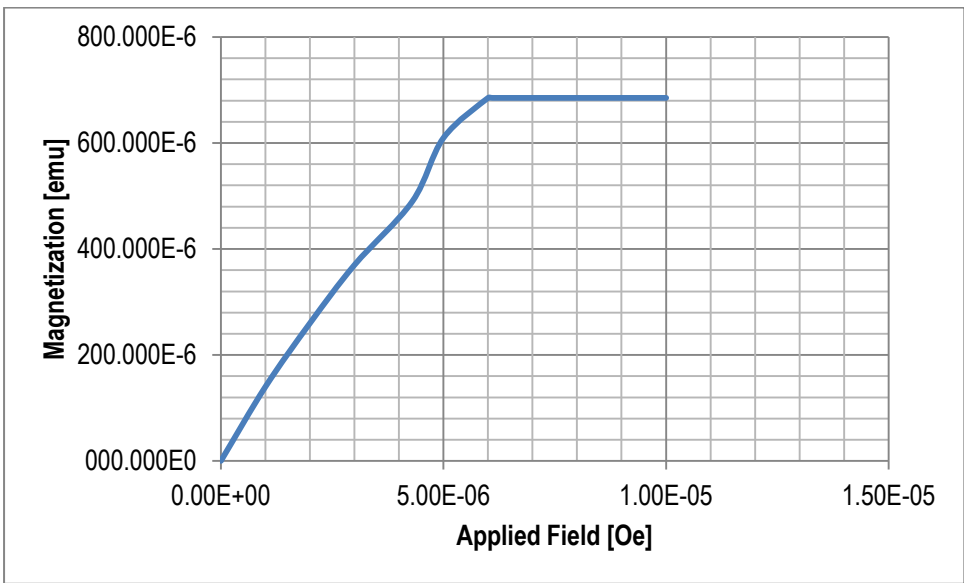


Figure. 4.90: Variation of magnetization with applied voltage (18% doping)

Slope of the graph is 122.00

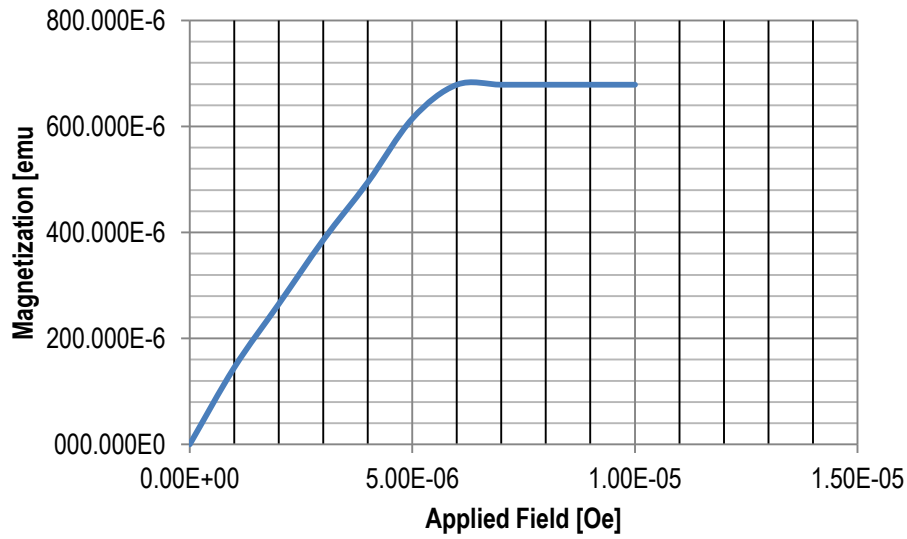


Figure. 4.91: Variation of magnetization with applied voltage (23% doping)

Slope of the graph is 123.75

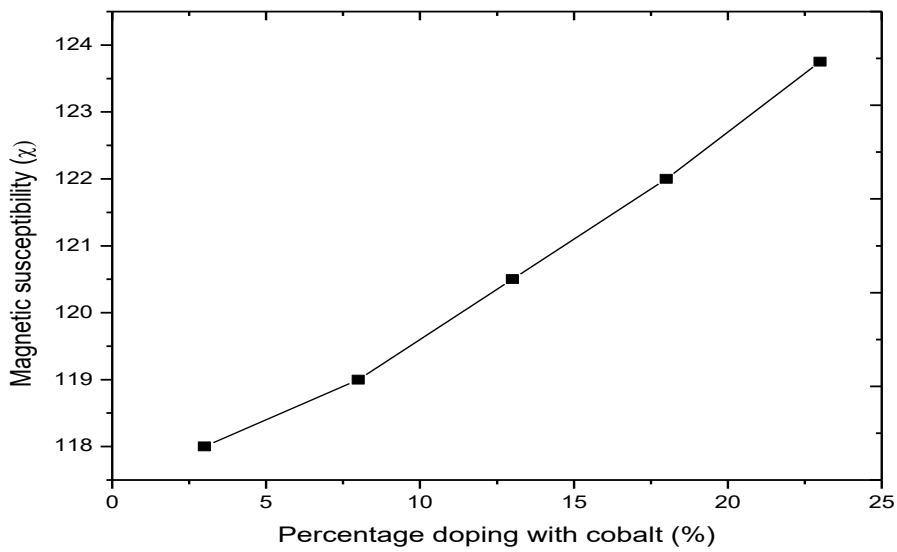


Figure 4.92: Variation of magnetic susceptibility with percentage cobalt dopant for MgCo_2O_4 nanofilms

4.2.10 Compositional analysis

Table 4.4 reveals that the mass of host metal (magnesium) decreases as mass of cobalt dopant increases.

Table 4.4: Compositional analysis for magnesium cobalt oxide nanofilms at various percentage doping with cobalt

Sample	Percentage doping (%)	Mg	O	Co
N23	3	58.4863	39.7022	1.8089
N14	8	55.4744	39.7018	4.8238
N24	13	52.4590	39.7023	7.8387
N25	18	49.4438	39.7026	10.8536
N26	23	46.4306	39.7009	13.8685

4.3 Analysis of cadmium cobalt oxide nanofilms

The nanofilms were analyzed for their optical, structural, and magnetic properties.

4.3.1 Bandgaps of cadmium cobalt oxide nanofilms at various percentages doping

The results as shown in figures 4.93 to 4.98 are summarized in table 4.5.

The bandgaps as depicted in Table 4.5 is in conformity with the results of other researchers, especially the lower percentage doping, since they fall within the same close range .viz: CdO thin film has a direct bandgap of 2.26eV (Bhosale *et al.*, 2005). A bandgap of 2.45eV was obtained for Cdo nanofilm (Singh *et al.*, 2011), CdO nanofilm has a wide direct bandgap of 2.6eV (Terasako *et al.*, 2012), bandgaps of $2.02 \pm 0.05\text{eV}$, $2.03 \pm 0.05\text{eV}$, $2.05 \pm 0.05\text{eV}$ for CdO thin films (Ezeokoye *et al.*, 2013). Direct bandgap of 2.43eV was obtained for CdO thin film (Zaien *et al.*, 2012) . Increase in molarities of CdO precursor solution yields a slight increase in optical bandgap from 2.54eV to 2.58eV (Beevi *et al.*, 2010).

From figure 4.99, it is observed that bandgap of CdCo₂O₄ nanofilm decreases as the percentage doping with cobalt increases. The result compares well with the works of other researchers, viz; (Erhaima *et al.*,2010), (Nirmala *et al.*,2010), (Girjesh *et al.*,2013). Since thickness of the films increased with percentage doping as shown in figure 4.101, this compares well with the works of (Ebru *et al.*,2014) and (Okafor *et al.*, 2015), and since crystallite size(grain size) is directly proportional to film thickness (Pandiaraman *et al.*,2011) and (Kumar *et al.*, 2012), this decrease in bandgap could be attributed to increase in crystallite size as thickness increases. Increase in grain size has a decreasing effect on bandgap (Ramana *et al.*, 2003). From figure 4.100, bandgap of cadmium cobalt oxide nanofilm decreases as the thickness of the film increases.This compares well with the work of (Kumar *et al.*, 2012). However formation of impurity level within the bandgap could also lead to decrease in bandgap,

From Figure 4.102, the bowing parameter decreases as the percentage doping with cobalt increases. As it bows downwards, it is positive. This compares well with the works of (Van de walley *et al.*,

1999), (Moses and Van de Walle, 2010). Bowing parameter is significant for investigating the bandgap energies of ternary alloys (Gulebagian *et al.*, 2014).

However, as wide bandgap semiconductor, electronics made of it have the advantage of being smaller, faster, more reliable and more efficient than the Si based counterparts. Devices made of the material can operate at higher temperatures, voltages and higher frequencies.

Table 4.5: Variation of bandgap of cobalt doped cadmium oxide with percentage doping.

Doping(%)	0 (undoped)	3	8	13	18	23
Bandgap(eV)	2.5	2.2	2.0	1.8	1.6	1.5

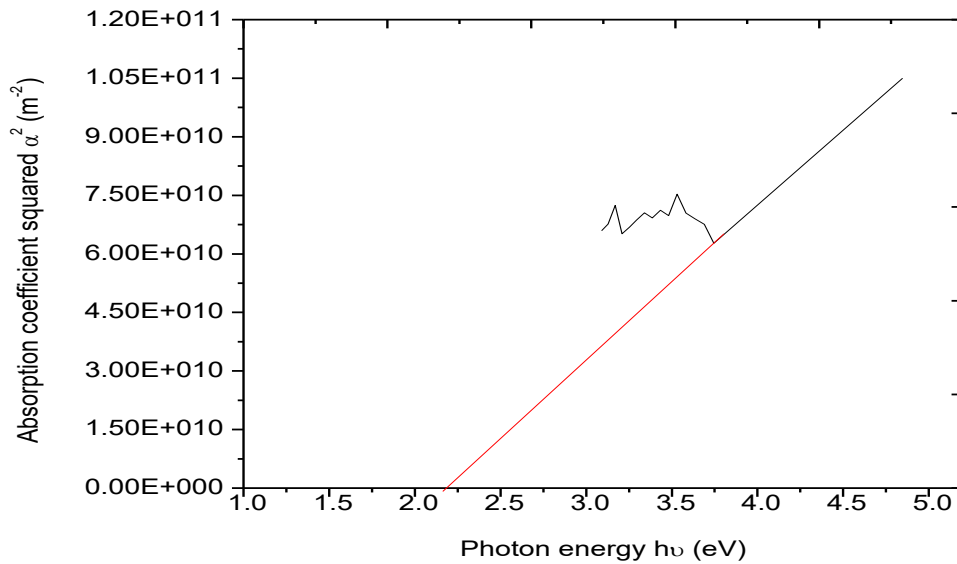


Figure 4.93: Graph of absorption coefficient squared versus photon energy for CdCo₂O₄ nanofilm(3% doped with cobalt).

From 4.93, 3% cobalt doped CdCo₂O₄ nanofilm has a direct allowed bandgap of 2.2ev.

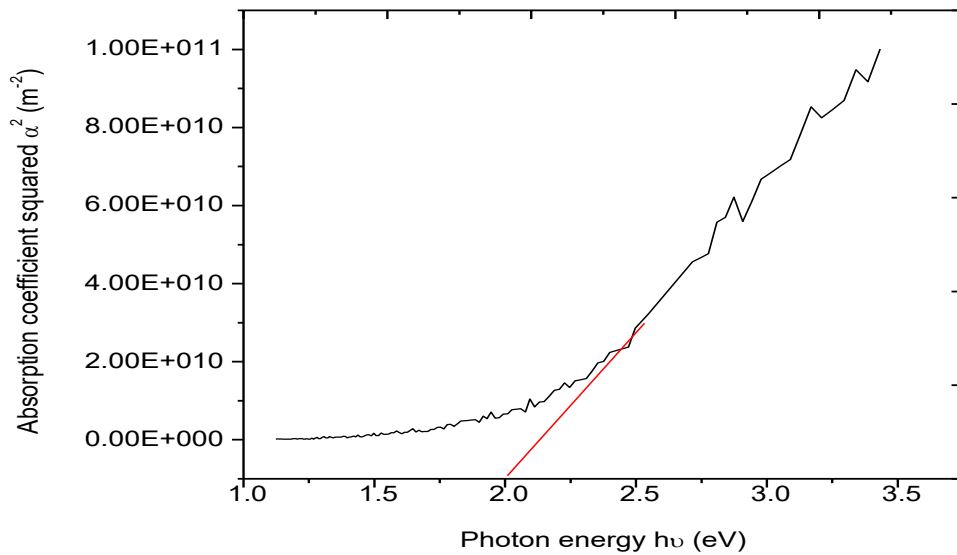


Figure 4.94 .: Graph of absorption coefficient squared versus photon energy for CdCo₂O₄ nanofilm(8% doped with cobalt).

From figure 4.94, 8% cobalt doped CdCo₂O₄ nanofilm has a direct allowed bandgap of 2.0eV.

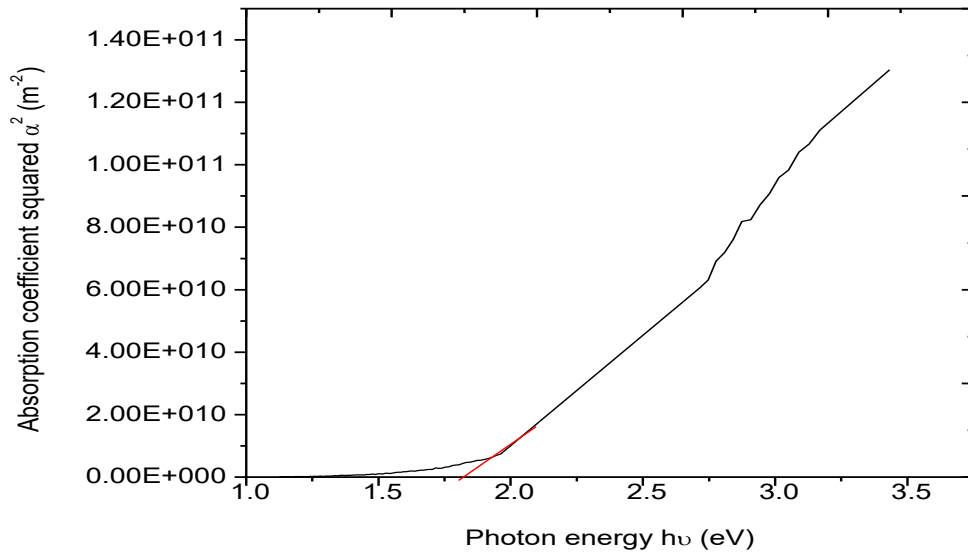


Figure 4.95: Graph of absorption coefficient squared versus photon energy for CdCo₂O₄ nanofilm(13% doped with cobalt).

From figure 4.95, 13% cobalt doped CdCo₂O₄ nanofilm has a direct allowed bandgap of 1.8eV.

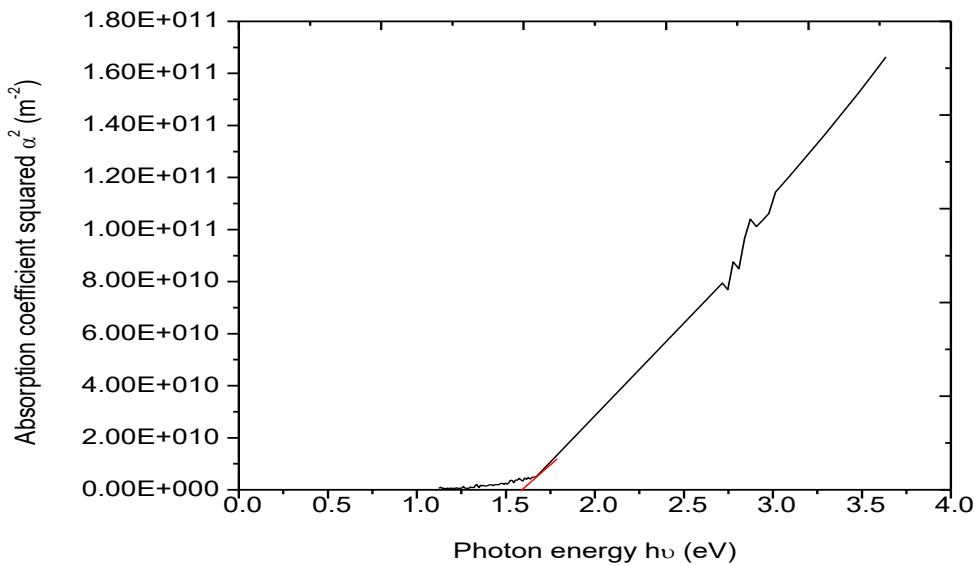


Figure 4.96: Graph of absorption coefficient squared versus photon energy for CdCo₂O₄ nanofilm (18% doped with cobalt).

From figure 4.96, 18% cobalt doped CdCo₂O₄ nanofilm has a direct allowed bandgap of 1.6eV.

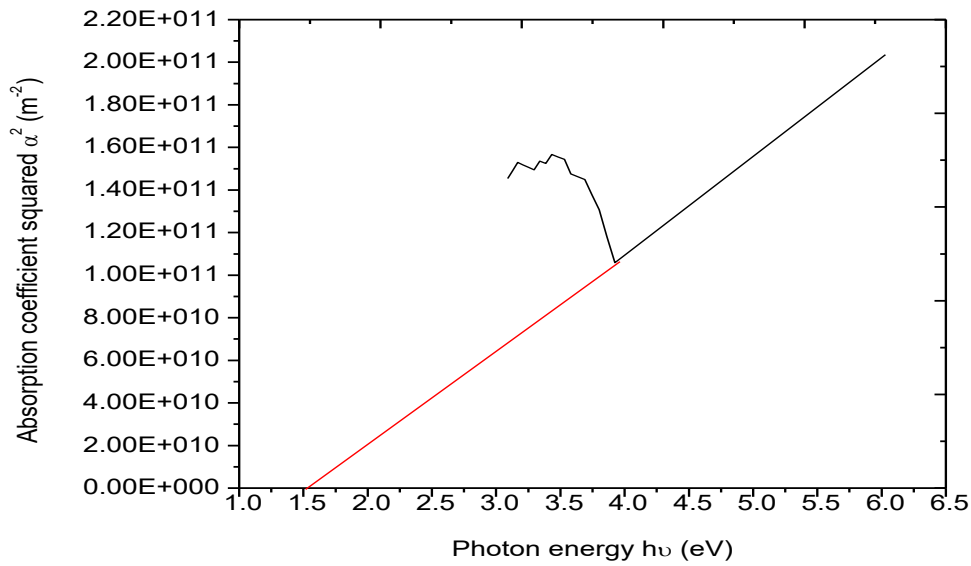


Figure 4. 97: Graph of absorption coefficient squared versus photon energy for CdCo_2O_4 nanofilm(23% doped with cobalt).

From the graph 23% cobalt doped CdCo_2O_4 nanofilm has a direct allowed bandgap of 1.5eV.

4.3.2 Bandgap of CdO nanofilm (undoped)

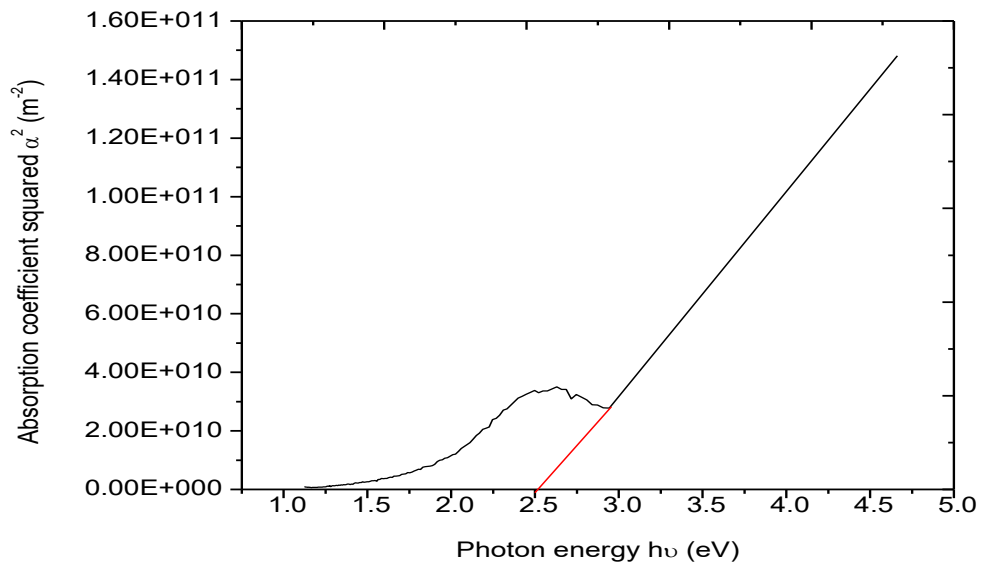


Figure 4.98: Absorption coefficient squared versus photon energy for undoped cadmium oxide nanofilm.

From figure 4.96, undoped cadmium oxide nanofilm has a direct allowed bandgap of 2.5eV.

4.3.3 Bandgap variations and thickness variation

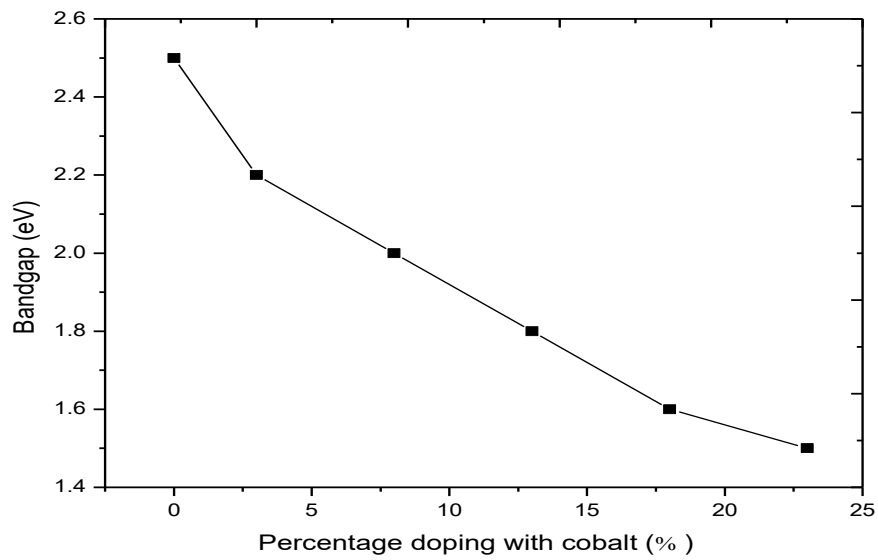


Figure 4. 99: Variation of bandgap with percentage doping with cobalt, for CdCo_2O_4 nanofilm.

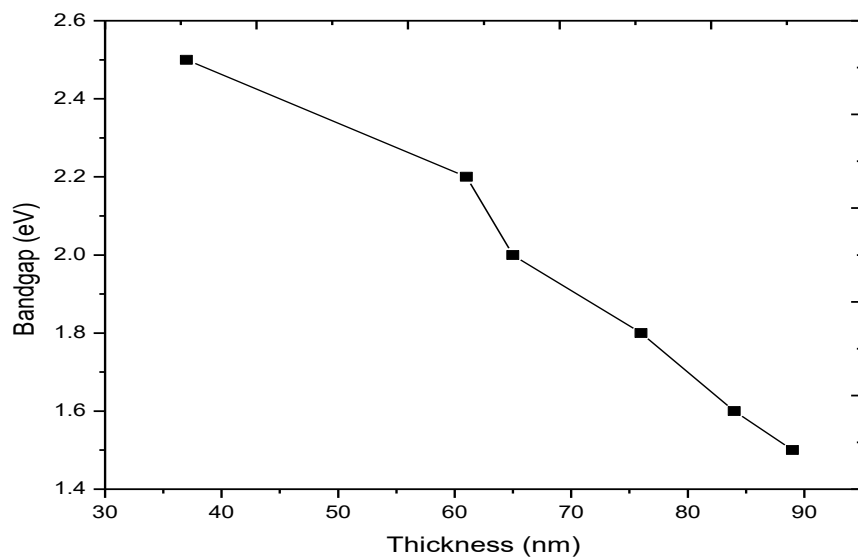


Figure 4.100 : Variation of bandgap with thickness for CdCo_2O_4 nanofilm.

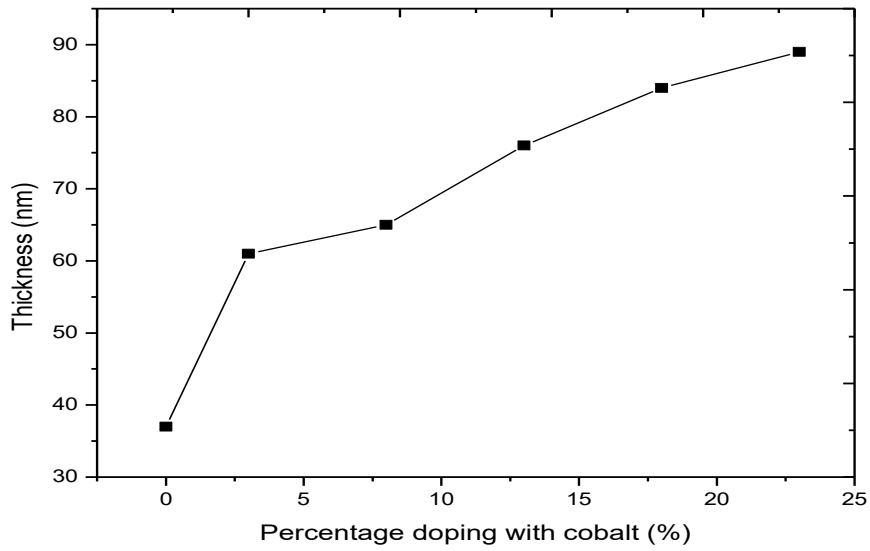


Figure 4.101: Variation of thickness with Percentage doping with cobalt for CdCo₂O₄ nanofilm

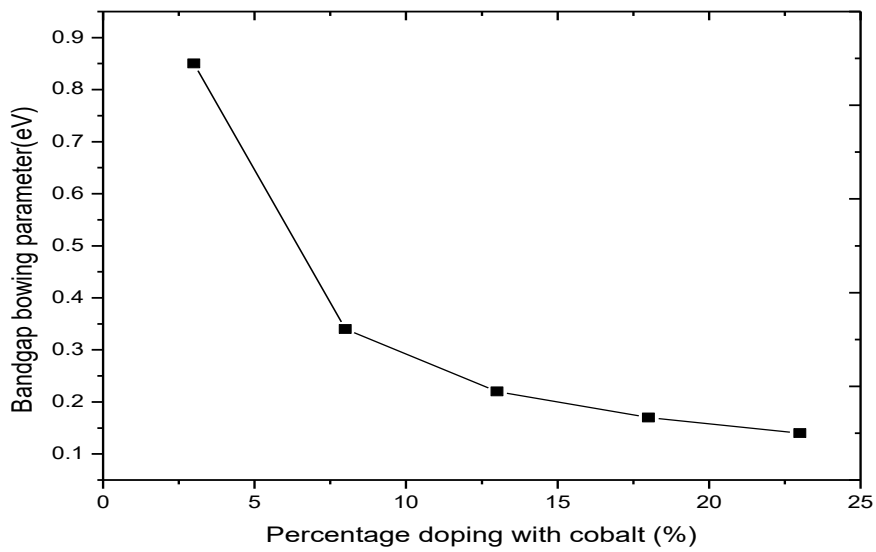


Figure 4.102: Variation of bandgap bowing parameter with percentage doping for cadmium cobalt oxide nanofilm.

4.3.4 Effect of percentage doping on optical properties of cadmium cobalt oxide nanofims

Due to the ultrathin nature of the films, they have general low absorbance in all the regions with maximum in the UV region (0.15=15%) and decreases to minimum in the NIR as shown in figure 4.103. The 23% doped has the maximum absorbance of 0.15 which attenuates down the VIS, NIR regions. The undoped film has the lowest absorbance, maximum of 0.091=9.1% in the visible region and tends to zero in the NIR region. The absorbance of the films increases as the percentage doping with cobalt increases.

From figure 4.104, transmittance of the films is generally high with minimum in the UV region (71.4%, for 23% doping) and increases to maximum in the NIR (<94.7% for undoped, < 98.7% for 13% doping) in the NIR. This makes the film a good material for solar cell, phosphors and photothermal application. Transmittance of the films decreases as the percentage doping with cobalt increases.

As shown in figure 4.105, reflectance of the films is generally very low with the doped films having maximum of 0.13=13% in the UV and the undoped 0.085=8.5% in the visible region and attenuate down to NIR regions. Reflectance of the films increases as the percentage doping with cobalt increases.

Figure 4.106 shows that refractive index of the doped films is generally high in the UV region (2.15 maximum) and undoped maximum of 1.78 in the visible region and decreases to minimum in the NIR. The refractive index increases as the percentage doping with cobalt increases.

Figure 4.107 shows that the doped films exhibited maximum extinction coefficient in the UV (23%: 0.012) while the undoped has maximum (0.007) in the visible region and decreases to minimum in the NIR. Extinction coefficient of the films increases as the percentage doping with cobalt increases.

From figure 4.108, the complex dielectric constant of the doped film is maximum in the UV region (maximum of 4.68 for 24%) while the undoped has maximum complex dielectric constant (3.42) in the visible region. However the complex dielectric constant decreases to minimum in the NIR region of electromagnetic spectrum. Complex dielectric constant of the film increases as the percentage doping with cobalt increases. Result as shown in figure 4.109 shows that optical

conductivity of the doped film is maximum in the UV region (maximum of 1.98×10^{13} for 23%) while the undoped has maximum optical conductivity (8.01×10^{12}) in the visible region. However the optical conductivity tends to zero in the NIR region of electromagnetic spectrum. Optical conductivity of the film increases as the percentage doping with cobalt increases

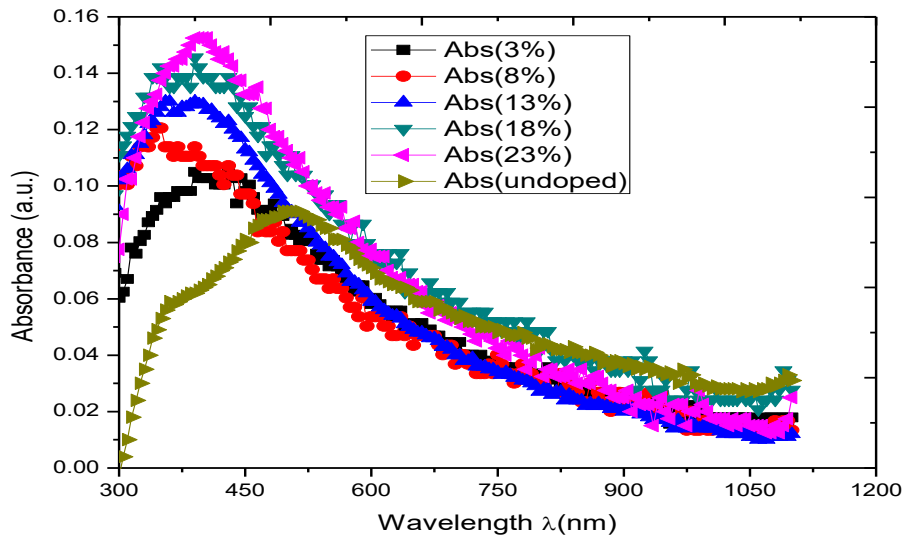


Figure 4. 103: Variation of absorbance with wavelength for CdCo_2O_4 nanofilms for different percentages doping with cobalt.

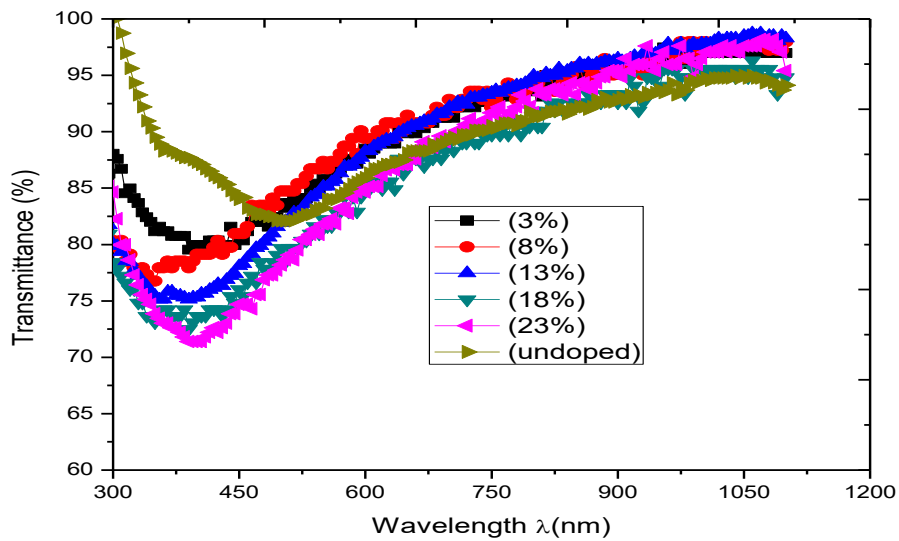


Figure 4. 104: Variation of transmittance with wavelength for CdCo_2O_4 nanofilms for different percentages doping with cobalt.

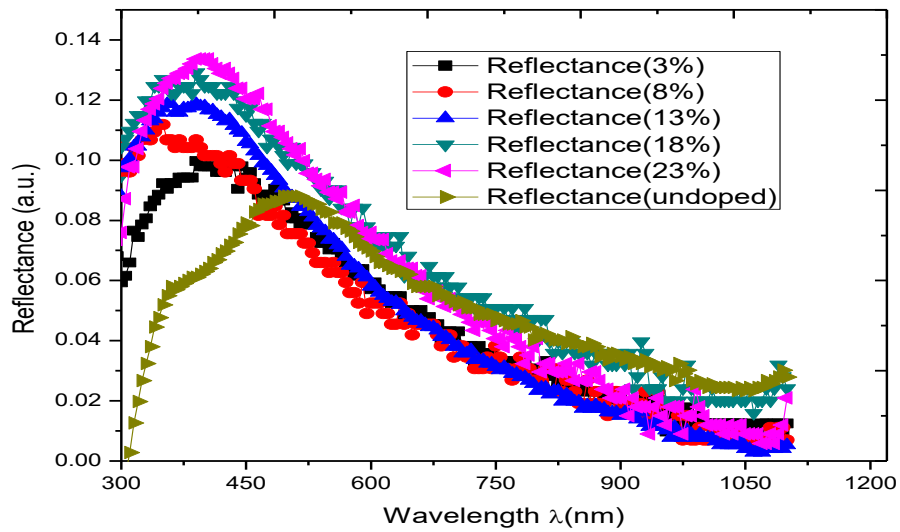


Figure 4.105: Variation of reflectance with wavelength for CdCo_2O_4 nanofilms for different percentages doping with cobalt.

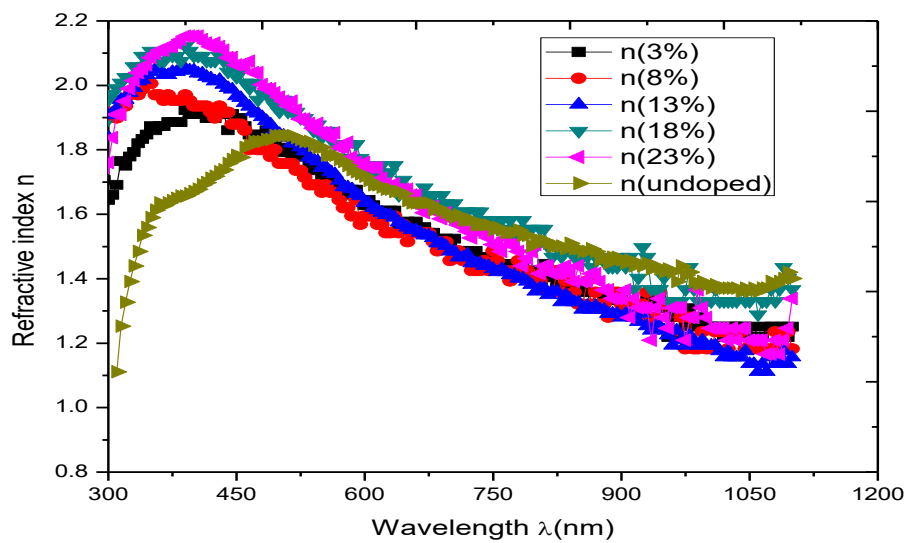


Figure 4. 106: Variation of refractive index with wavelength for CdCo_2O_4 nanofilms for different percentages doping with cobalt.

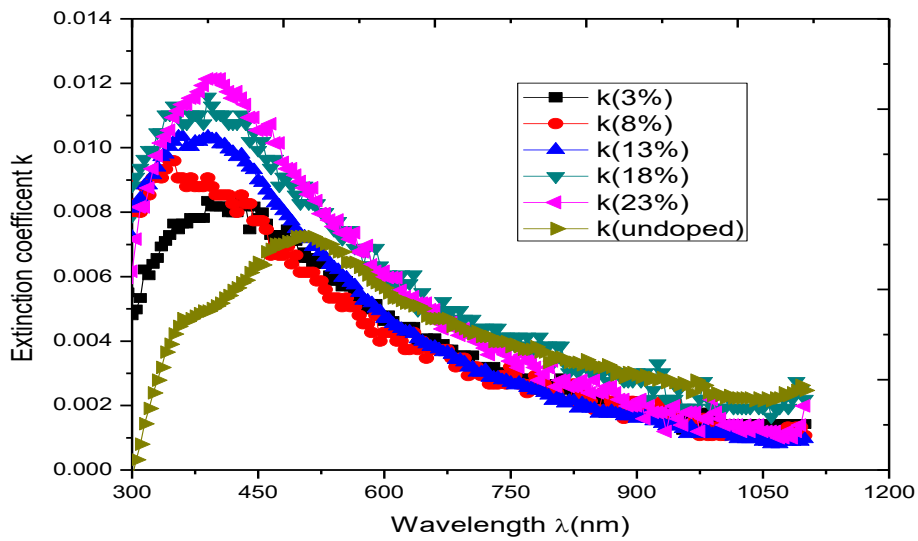


Figure 4. 107: Variation of extinction coefficient with wavelength for CdCo_2O_4 nanofilms for different percentages doping with cobalt.

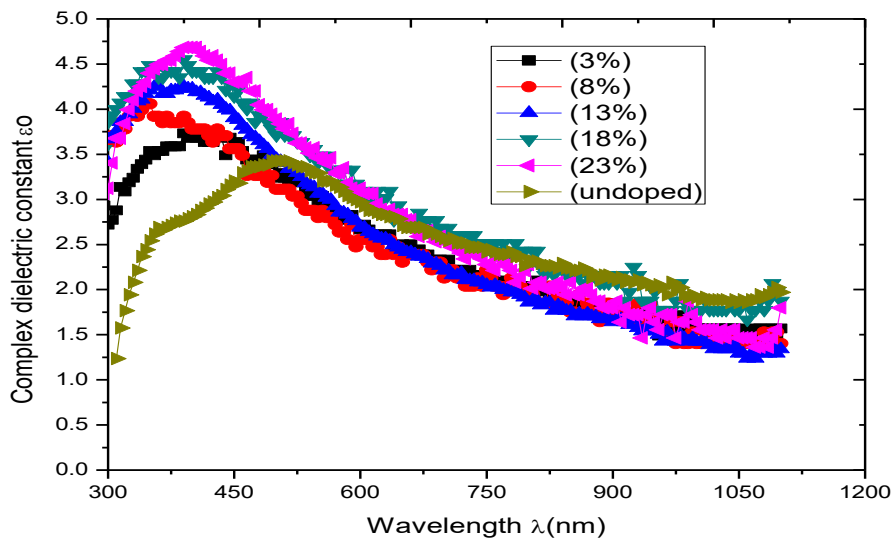


Figure 4. 108: Variation of complex dielectric constant with wavelength for CdCo_2O_4 nanofilms for different percentages doping with cobalt.

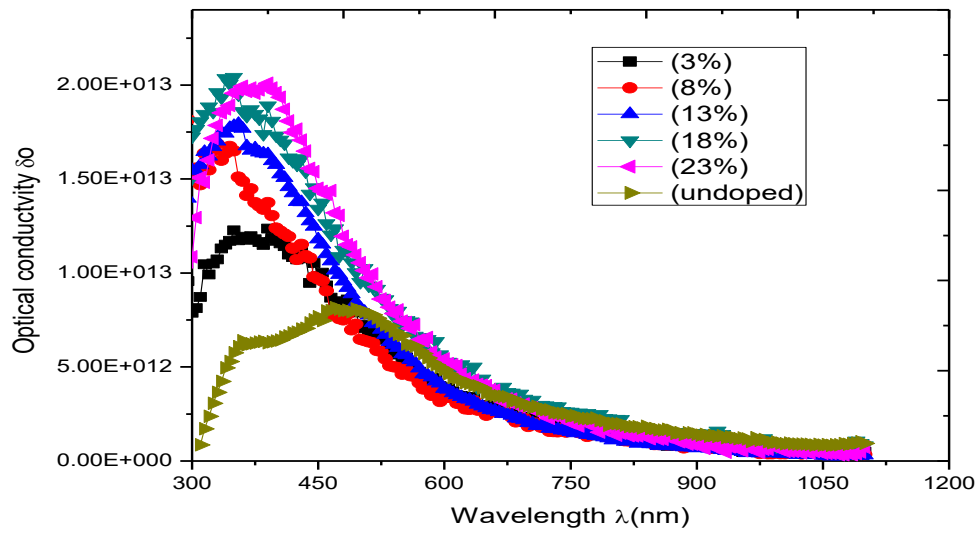


Figure 4. 109: Variation of optical conductivity with wavelength for CdCo₂O₄ nanofilms for different percentages doping with cobalt.

4.3.5 Effect of thickness on optical properties of cadmium cobalt oxide nanofilms

Figure 4.100 shows that absorbance of the film increases as thickness of the film increases. Maximum of 0.1525=15.25 in UV region for 89nm. The undoped film(37nm) has the lowest absorbance, maximum of 0.091=9.1% in the visible region. Absorbance of the films tend to zero in the NIR region. From figure 4.111, the transmittance of the film decreases as the film thickness increases. Minimum of 71.39 in the UV region for 89nm and tend to 100% in NIR region. However, the undoped film(37nm) has minimum transmittance of 82.01% in the visible region and increases to 94.76% in the NIR region.

As shown in figure 4.112, reflectance of the film increases as thickness increases. Maximum of 0.13=13% in UV region for 89nm. The undoped film (37nm) has the lowest reflectance 0.085=8.5% in the visible region. Reflectance of the films attenuate zero in NIR regions

Figure 4.113 shows that refractive index of the film increases as thickness increases, maximum of 2.15 in UV region for 89nm . The undoped film(37nm) has the lowest refractive index, maximum of 1.78 in the visible region. Refractive index of the films decreases to minimum in the NIR. Figure 4.114 shows that extinction coefficient of the film increases as thickness increases. Maximum of 0.012 in UV region for 89nm. The undoped film(37nm) has the lowest extinction coefficient, maximum(0.007) in the visible region. Extinction coefficient of the films decreases to minimum in the NIR. As shown in figure 4.115, complex dielectric constant of the film increases as film thickness increases. Maximum of 4.68 in UV region for 89nm. The undoped(37nm) has the lowest complex dielectric constant, maximum (3.42) in the visible region. Complex dielectric constant of the films tends to zero in NIR region. From figure 4.116, optical conductivity of the film increases as film thickness increases .Maximum of 2.00E+13 in UV region for 89nm. The undoped film(37nm) has the lowest optical conductivity, maximum of 8.01E+12 in the visible region. However the optical conductivity of the films tend to zero in the NIR region of electromagnetic spectrum.

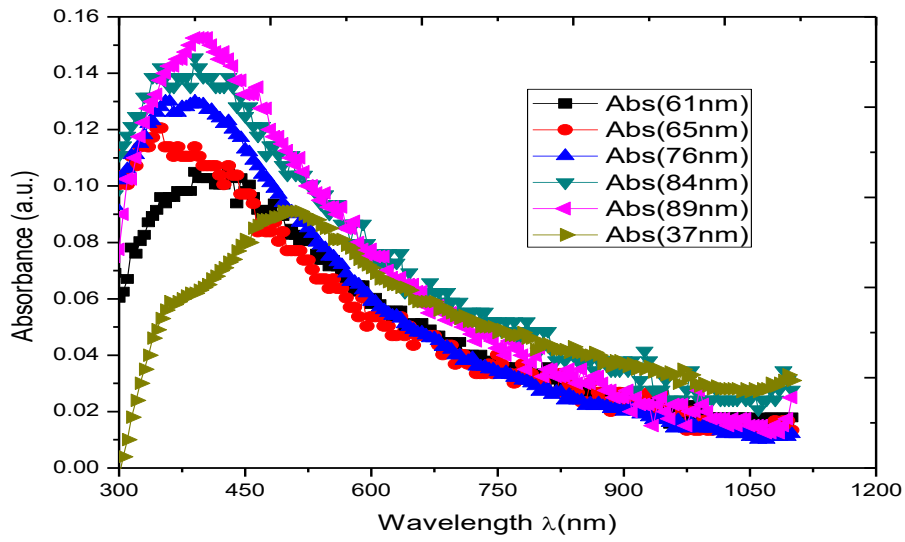


Figure 4.110: Variation of absorbance with wavelength for CdCo_2O_4 nanofilms for different thicknesses.

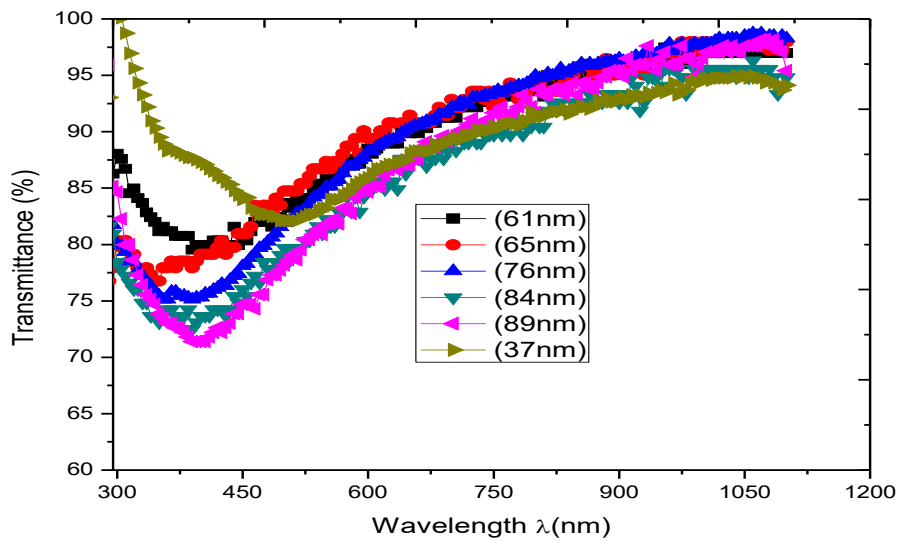


Figure 4. 111: Variation of transmittance with wavelength for CdCo_2O_4 nanofilms for different thicknesses.

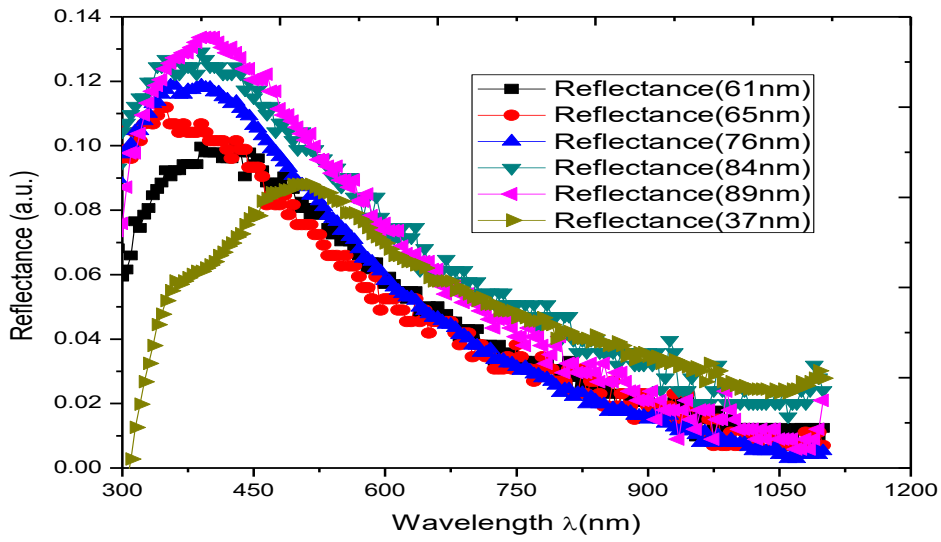


Figure 4. 112: Variation of reflectance with wavelength for CdCo_2O_4 nanofilms for different thicknesses.

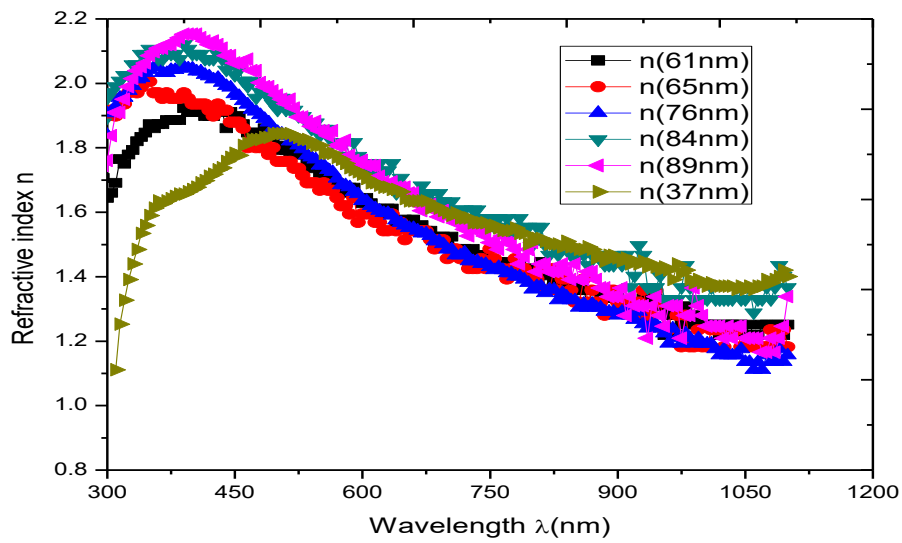


Figure 4. 113: Variation of refractive index with wavelength for CdCo_2O_4 nanofilms for different thicknesses.

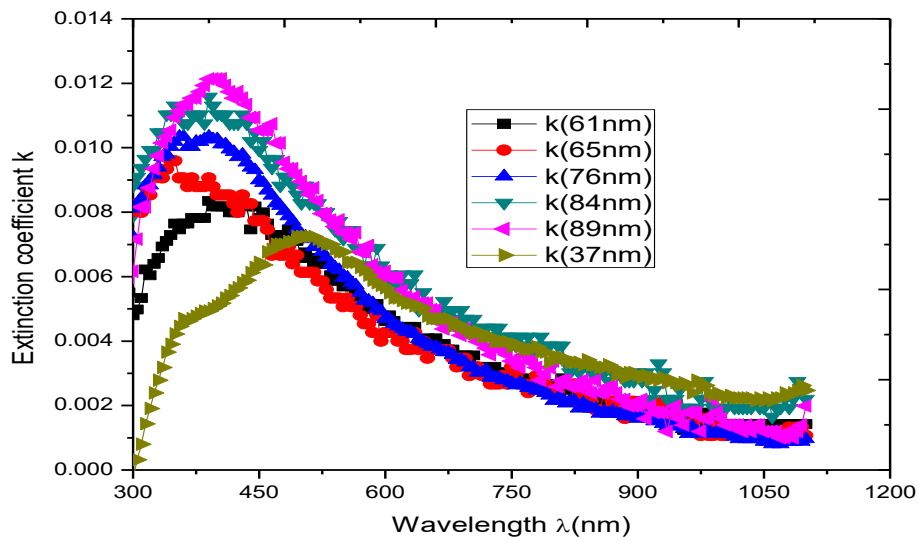


Figure 4. 114: Variation of extinction coefficient with wavelength for CdCo₂O₄ nanofilms for different thicknesses.

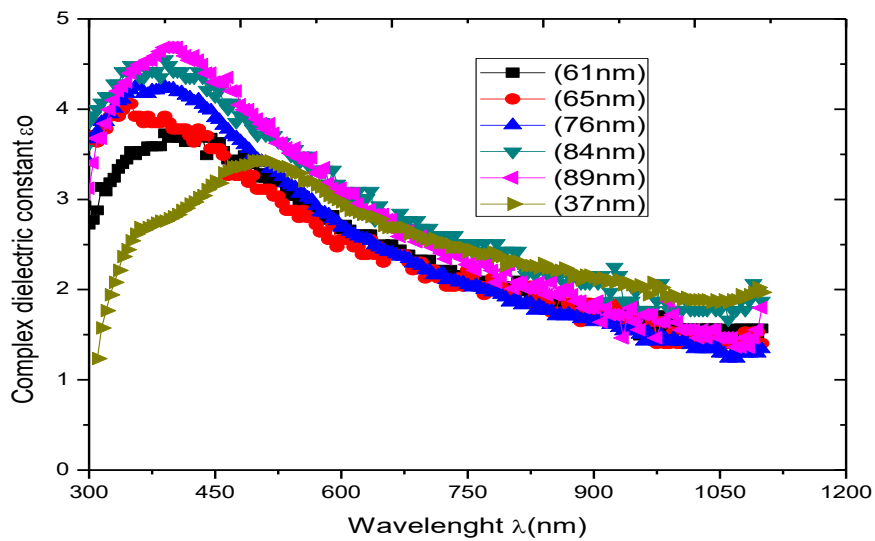


Figure 4. 115: Variation of complex dielectric constant with wavelength for CdCo₂O₄ nanofilms for different thicknesses.

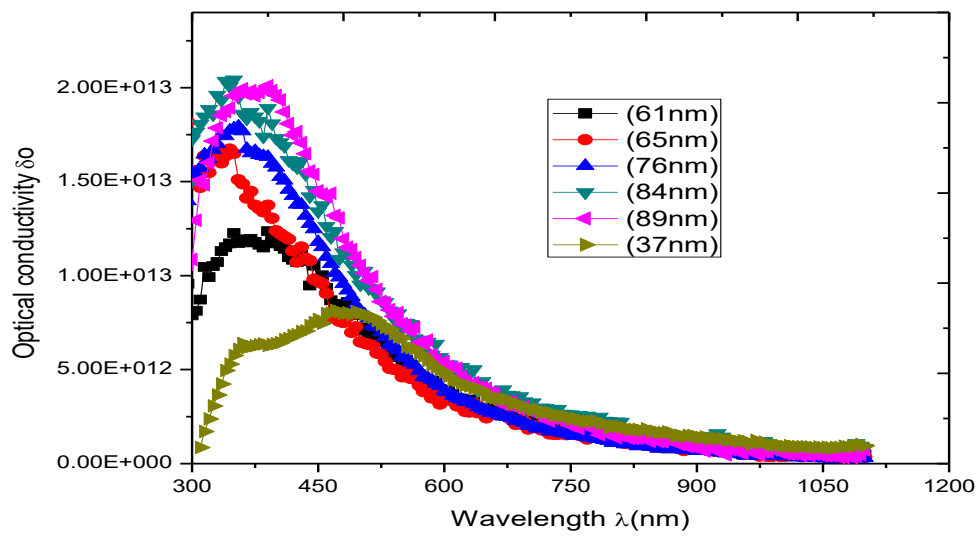


Figure 4. 116: Variation of optical conductivity with wavelength for CdCo₂O₄ nanofilms for different thicknesses.

4.3.6 Effect of deposition voltage on optical properties of CdCo₂O₄ nanofilms

From figure 4.117, absorbance of the film increases as deposition voltage increases. Maximum of 0.276=2.76% in UV region for 13V

As shown in figure 4.118, transmittance of the film decreases as deposition voltage increases. Minimum of 53.84% in UV region for 13V.

Figure 4.119 shows that reflectance of the film increases as deposition voltage increases. Maximum of 0.18 in UV region for 13V.

Figure 4.120 shows that refractive index of the film increases as deposition voltage increases, maximum of 2.51 in UV region for 13V.

As shown in figure 4.121, extinction coefficient of the film increases as deposition voltage increases. Maximum of 0.022 in UV region for 13V.

Figure 4.122 shows that complex dielectric constant of the film increases as deposition voltage increases. Maximum of 6.4 in UV region for 13V.

As shown in figure 4.123, optical conductivity of the film increases as deposition voltage increases. Maximum of 4.7E+13 in UV region for 13V.

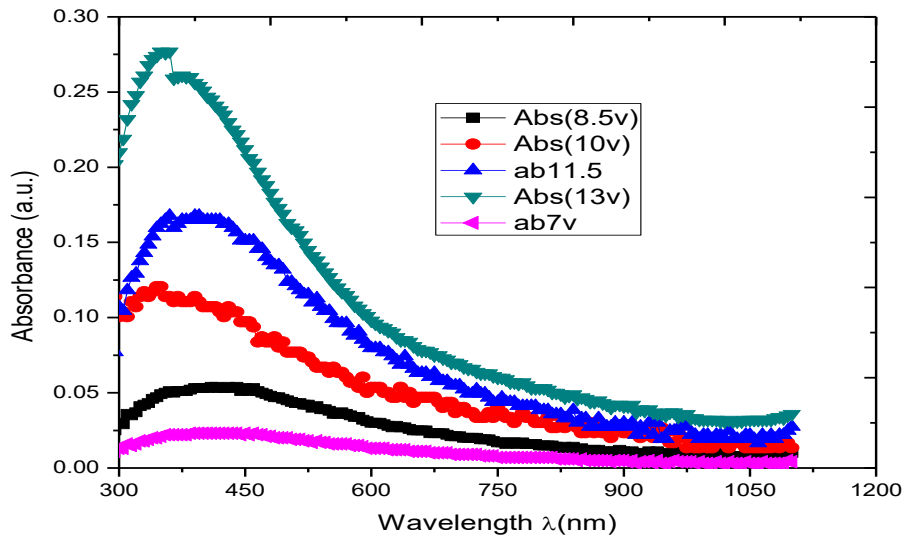


Figure 4. 117: Variation of absorbance with wavelength for CdCo_2O_4 nanofilms for different deposition voltages.

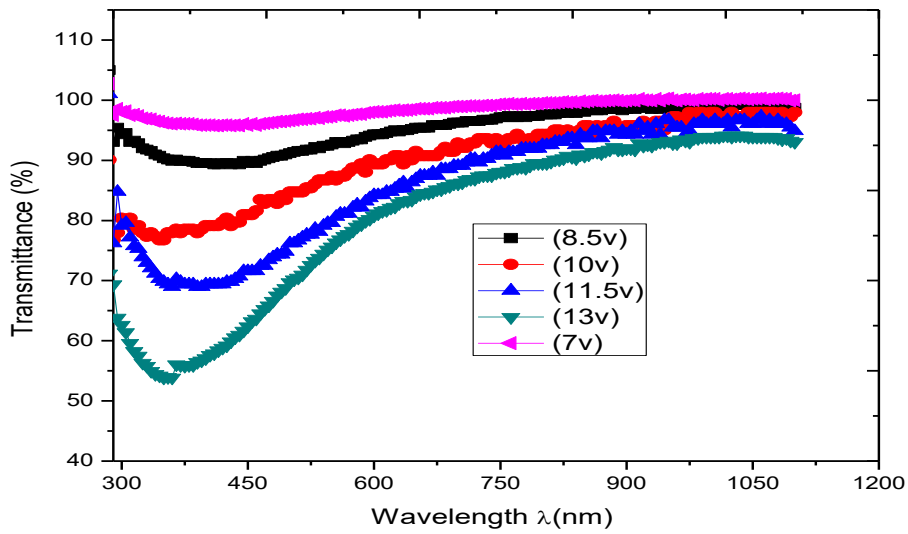


Figure 4. 118: Variation of transmittance with wavelength for CdCo_2O_4 nanofilms for different deposition voltages.

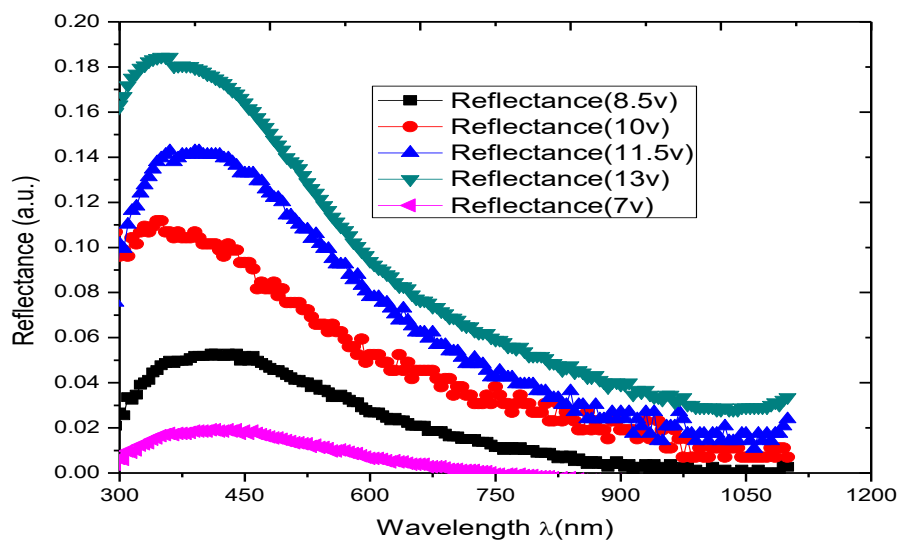


Figure 4. 119: Variation of reflectance with wavelength for CdCo_2O_4 nanofilms for different deposition voltages.

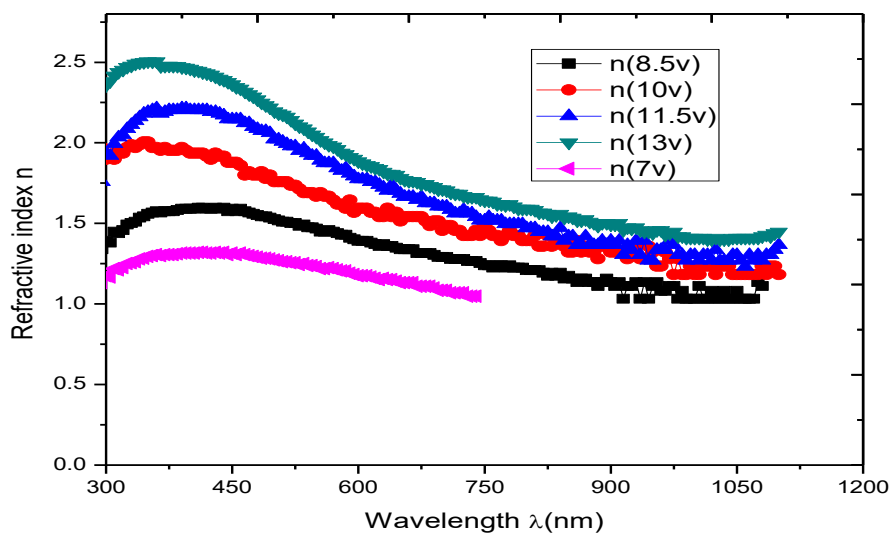


Figure 4. 120: Variation of refractive index with wavelength for CdCo_2O_4 nanofilms for different deposition voltages.

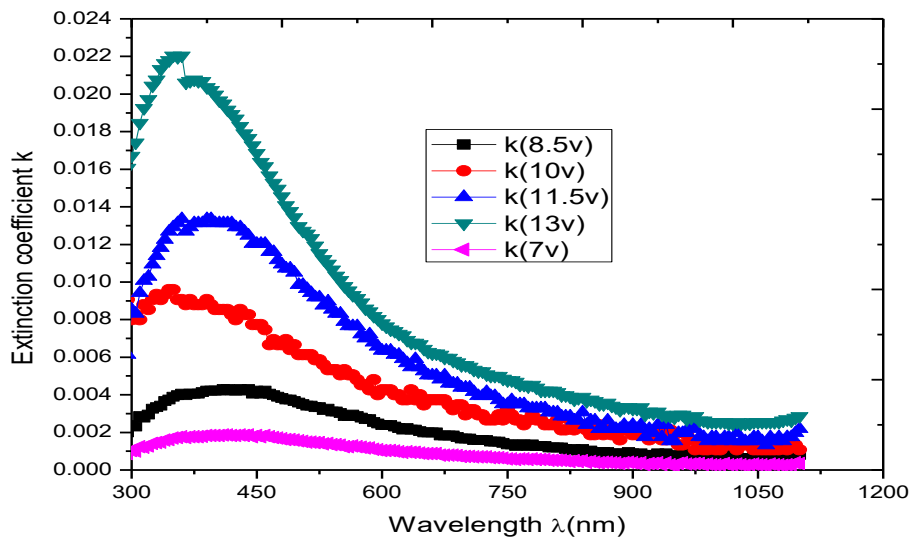


Figure 4. 121: Variation of extinction coefficient with wavelength for CdCo₂O₄ nanofilms for different deposition voltages.

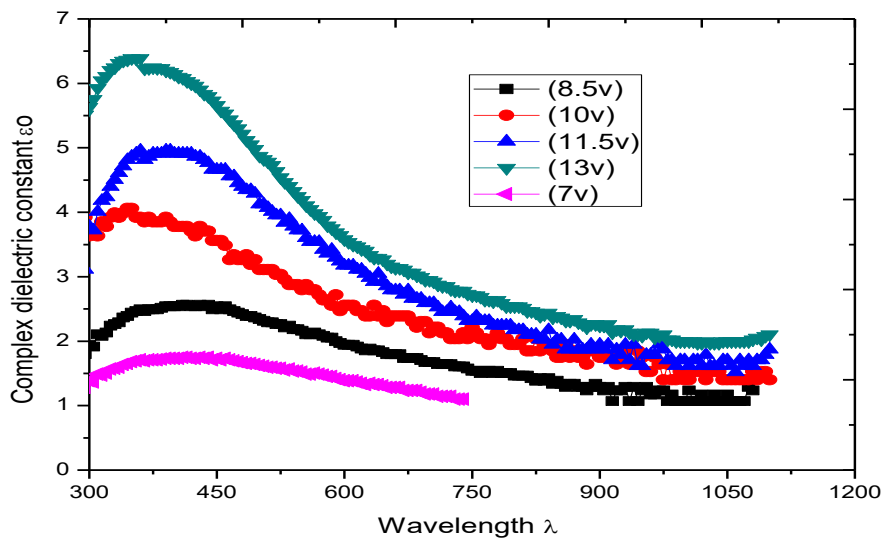


Figure 4. 122: Variation of complex dielectric constant with wavelength for CdCo₂O₄ nanofilms for different deposition voltages.

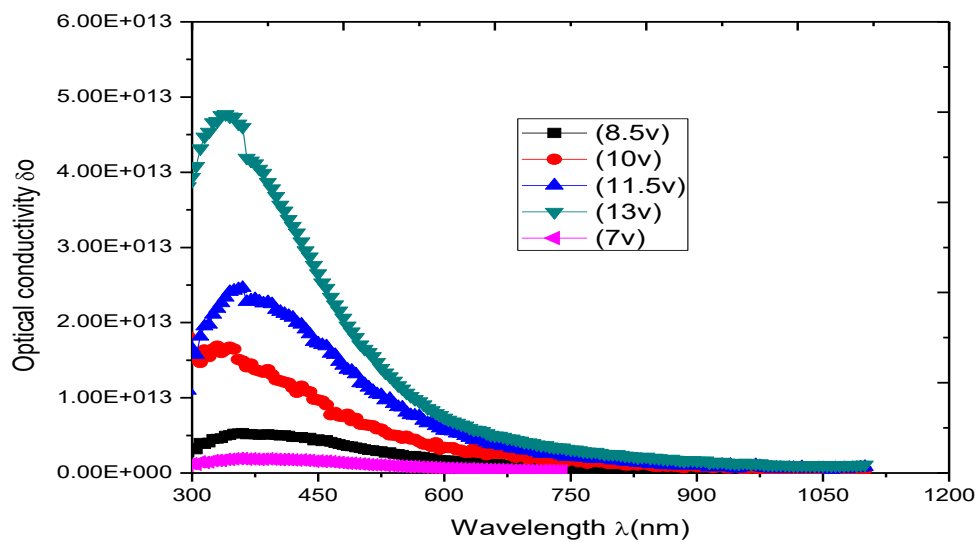


Figure 4. 123: Variation of optical conductivity with wavelength for CdCo₂O₄ nanofilms for different deposition voltages.

4.3.7 Effect of deposition time on optical properties of cadmium cobalt oxide nanofilms

From figure 4.124, absorbance of the film increases as deposition time increases. Maximum of 0.074=7.4% in UV region for 25 mins

Figure 4.125 shows that transmittance of the film decreases as deposition time increases. Minimum of 85.33% in UV region for 25mins

Figure 4.126 shows that reflectance of the film increases as deposition time increases. Maximum of 0.073=7.3% in UV region for 25mins

As shown in figure 4.127, refractive index of the film increases as deposition time increases. Maximum of 1.72 in UV region for 25mins.

From figure 4.128, extinction coefficient of the film increases as deposition time increases. Maximum of 0.0059 in UV region for 25 mins.

As shown in figure 4.129, complex dielectric constant of the film increases as deposition time increases. Maximum of 3.04 in UV region for 25 mins.

From figure 4.130, optical conductivity of the film increases as deposition time increases. Maximum of $8.47E+12$ in UV region for 25 mins.

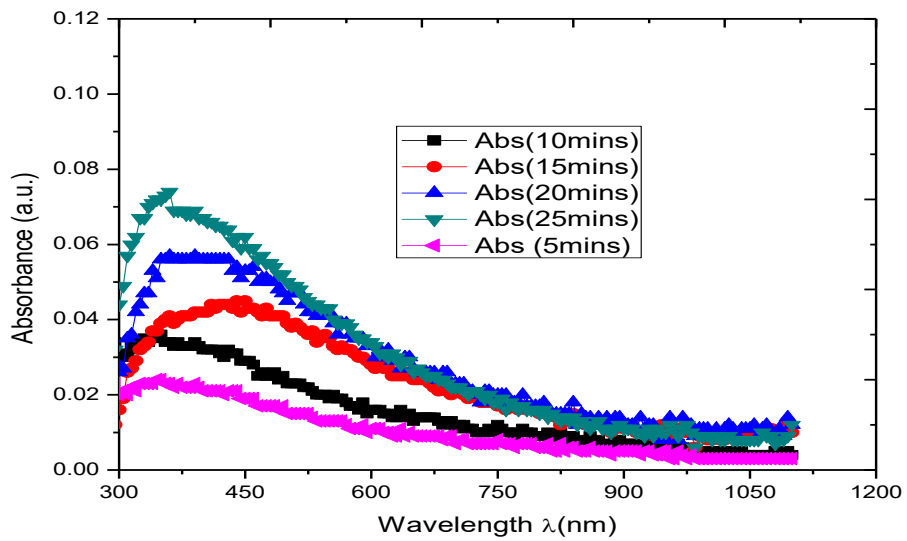


Figure 4.124: Variation of absorbance with wavelength for CdCo_2O_4 nanofilms for different deposition times.

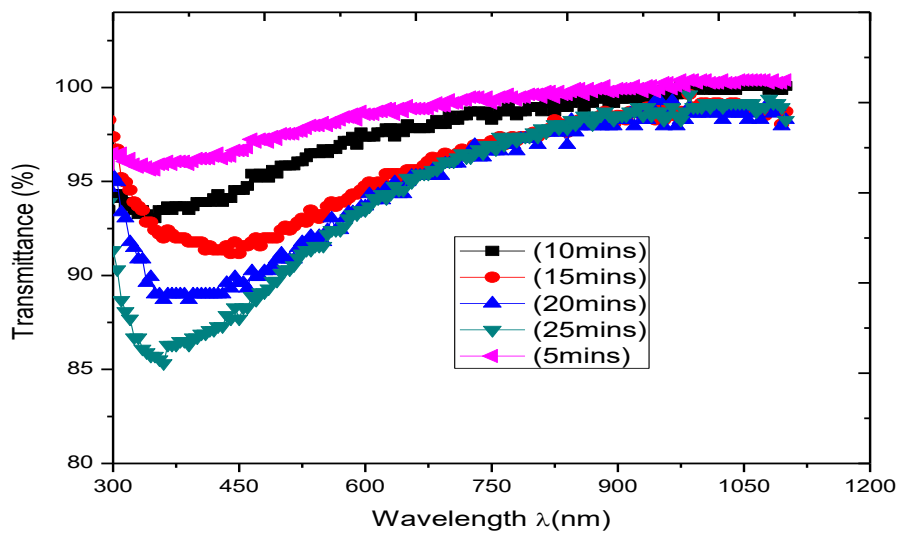


Figure 4. 125: Variation of transmittance with wavelength for CdCo_2O_4 nanofilms for different deposition times.

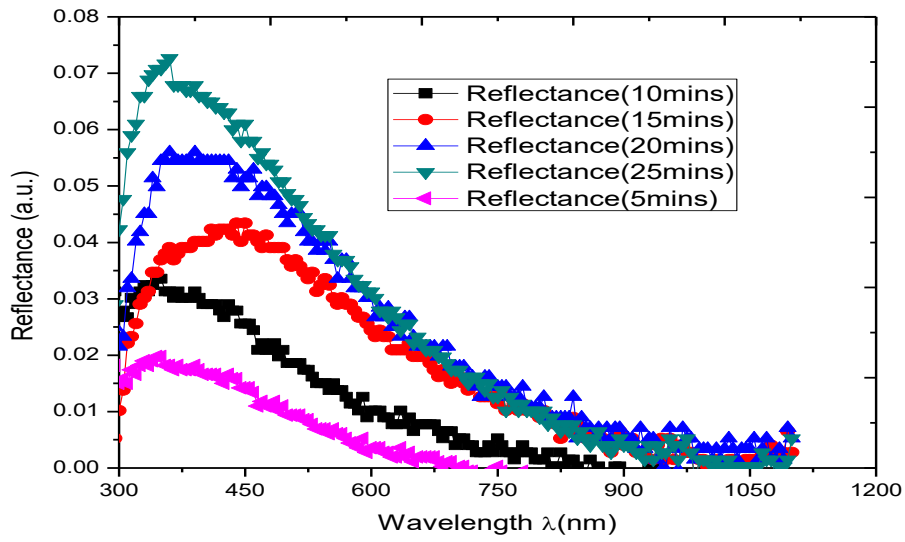


Figure 4. 126: Variation of reflectance with wavelength for CdCo_2O_4 nanofilms for different deposition times.

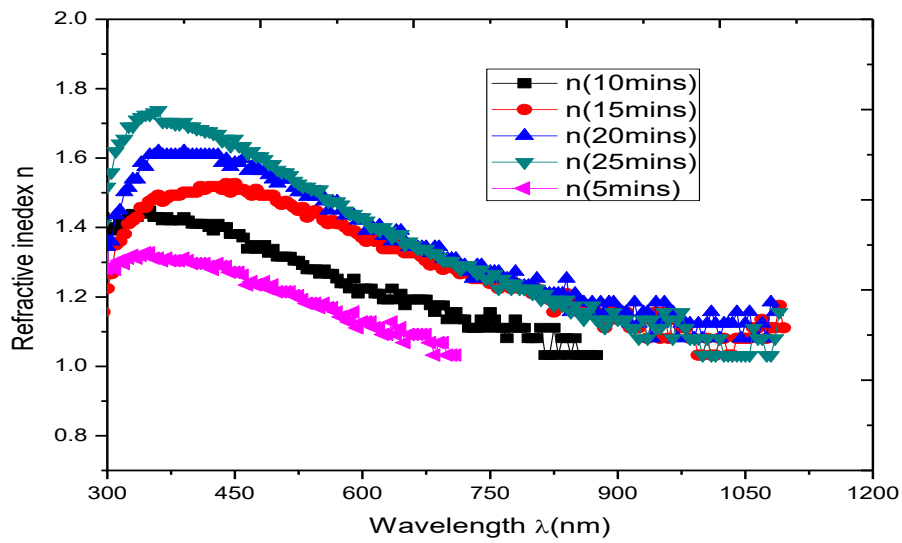


Figure 4. 127: Variation of refractive index with wavelength for CdCo_2O_4 nanofilms for different deposition times.

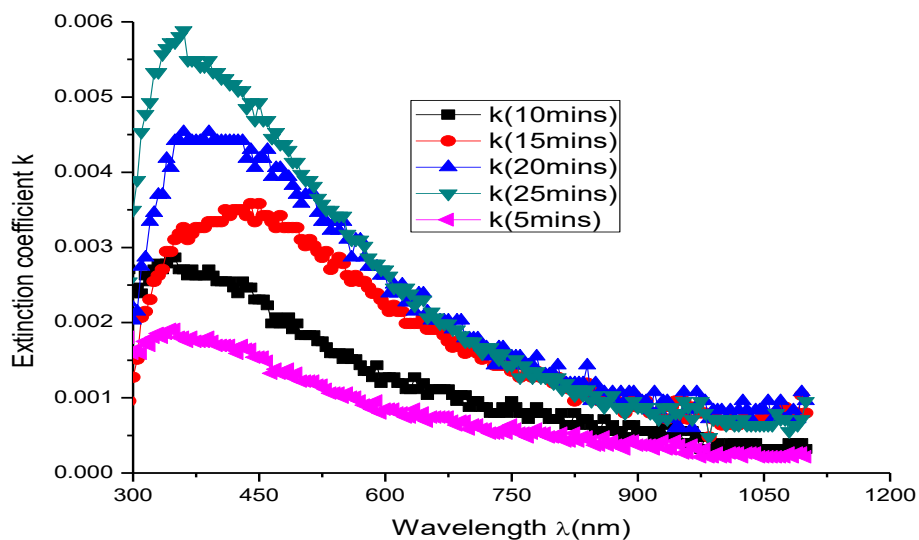


Figure 4.128: Variation of extinction coefficient with wavelength for CdCo_2O_4 nanofilms for different deposition times.

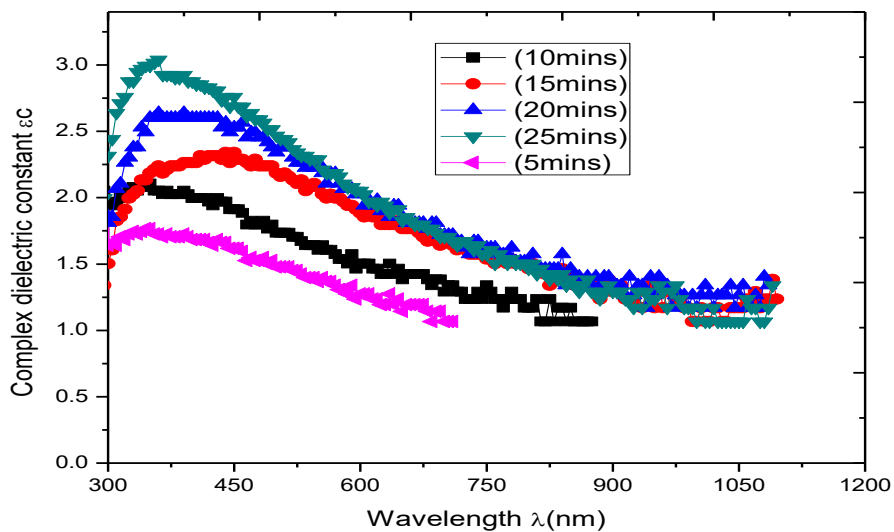


Figure 4. 129: Variation of complex dielectric constant with wavelength for CdCo_2O_4 nanofilms for different deposition times.

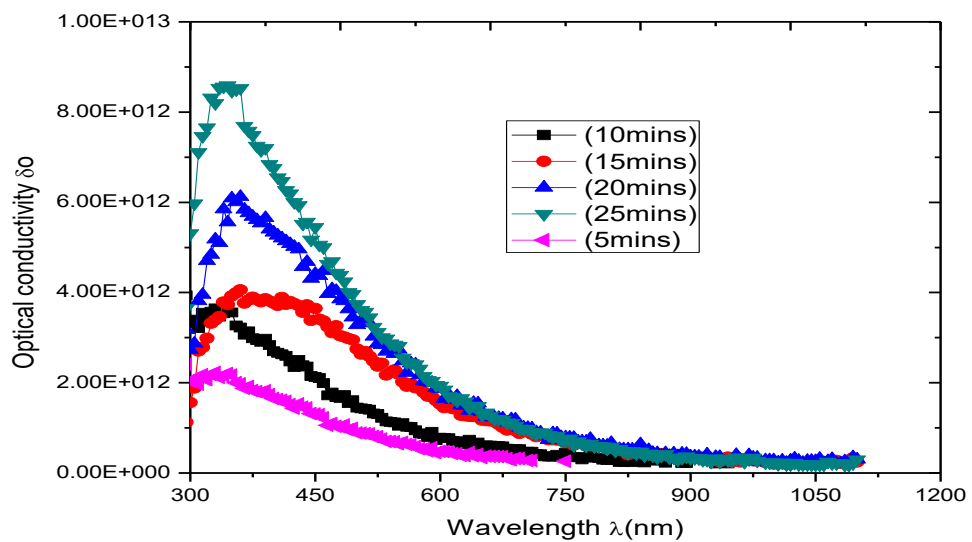


Figure 4. 130: Variation of optical conductivity with wavelength for CdCo₂O₄ nanofilms for different deposition times.

4.3.8 Variation of magnetic properties with percentage doping with cobalt

Figure 4.131 shows that remanent magnetization of cadmium cobalt oxide rises to a peak value of $1.94E-04$ in the low percentage doping range and decreases to zero in the higher percentage range

Figure 4.132 shows that saturation magnetization of cadmium cobalt oxide rises to a peak value of 4.01 in the low percentage doping range and decreases to zero in the higher percentage range. The implication of the result is that maximum magnetic property of the film is obtained in the low percentage doping.

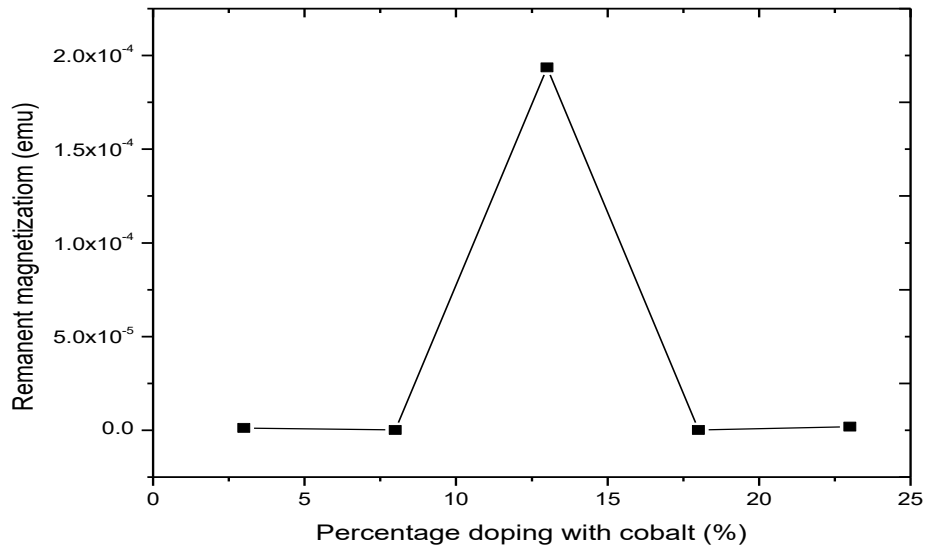


Figure 4.131: Variation of remanent magnetization with percentage doping with cobalt for CdCo₂O₄ nanofilm

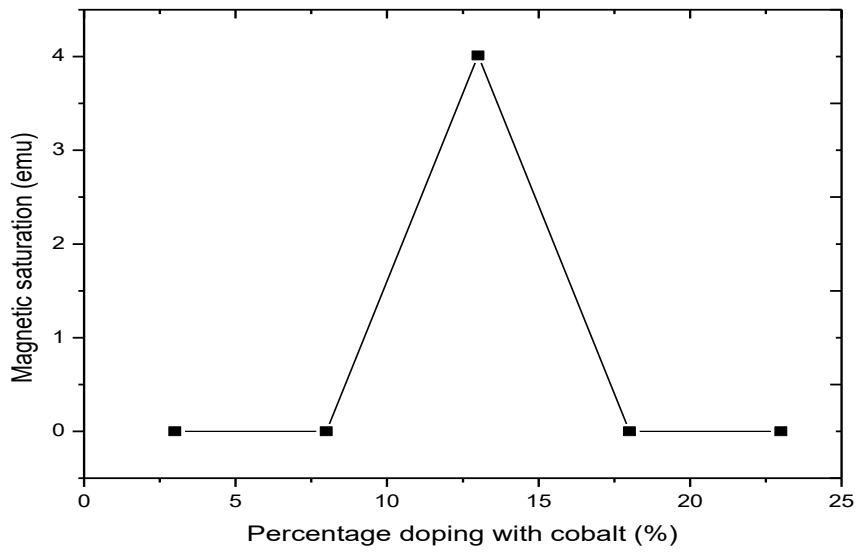


Figure 4.132: Variation of Saturation magnetization with percentage doping with cobalt for CdCo₂O₄ nanofilm

4.3.9 Variation of magnetization with applied voltage at various percentages of cobalt dopant for CdCo₂O₄ nanofilm

From figure 4.133, slope of the graph is 121.25 , therefore magnetic susceptibility of 3% doped film is 121.25. As shown in figure 4.134, slope of the graph is 124.25 , therefore magnetic susceptibility of 8% doped film is 124.25. Result as shown in figure 4.135 shows that the slope of the graph is 117.00, therefore magnetic susceptibility of 13% doped film is 117.00. As shown in figure 4.136, slope of the graph is 127.50, therefore magnetic susceptibility of 18% doped film is 127.50. Figure 4.137 shows that slope of the graph is 128.50, therefore magnetic susceptibility of 23% doped film is 128.50. Result in figure 4.138 shows that magnetic susceptibility increases as percentage cobalt dopant increases not minding the deviation of 13% doping to a lower value which distorted the trend. The magnetic saturation of thr films are 696.879emu for 3% doped,736.945E-6emu for 8% doped, 4.011emu for 13% doped,738.436E-6emu for 18% doped and734.881E-6emu for 23% doped. Since the film has no Fe³⁺ ion, it is not ferrimagnetic and by virtue of positive high magnetic susceptibility and magnetic saturation, the material is ferromagnetic. Applications as ferromagnetic semiconductor is as stated in 4.1.10.

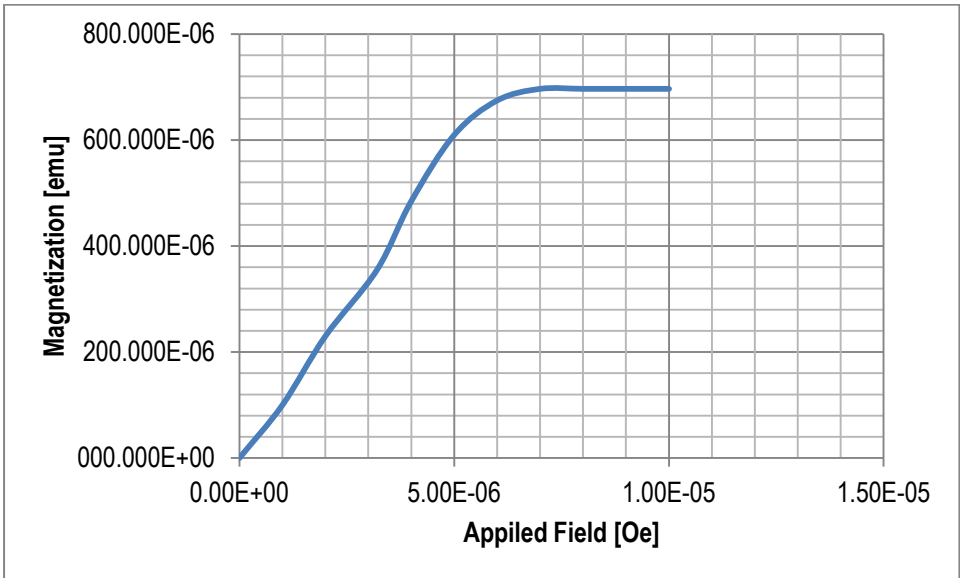


Figure. 4.133: Variation magnetization with applied voltage (3% doping)

Slope of the graph is 121.25

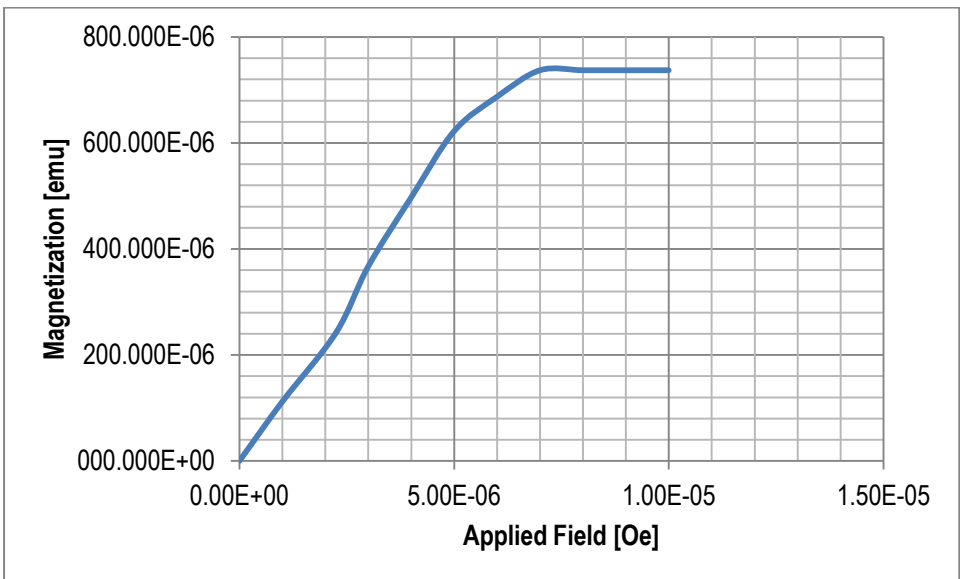


Figure. 4.134: Variation magnetization with applied voltage (8% doping)

Slope of the graph is 124.25

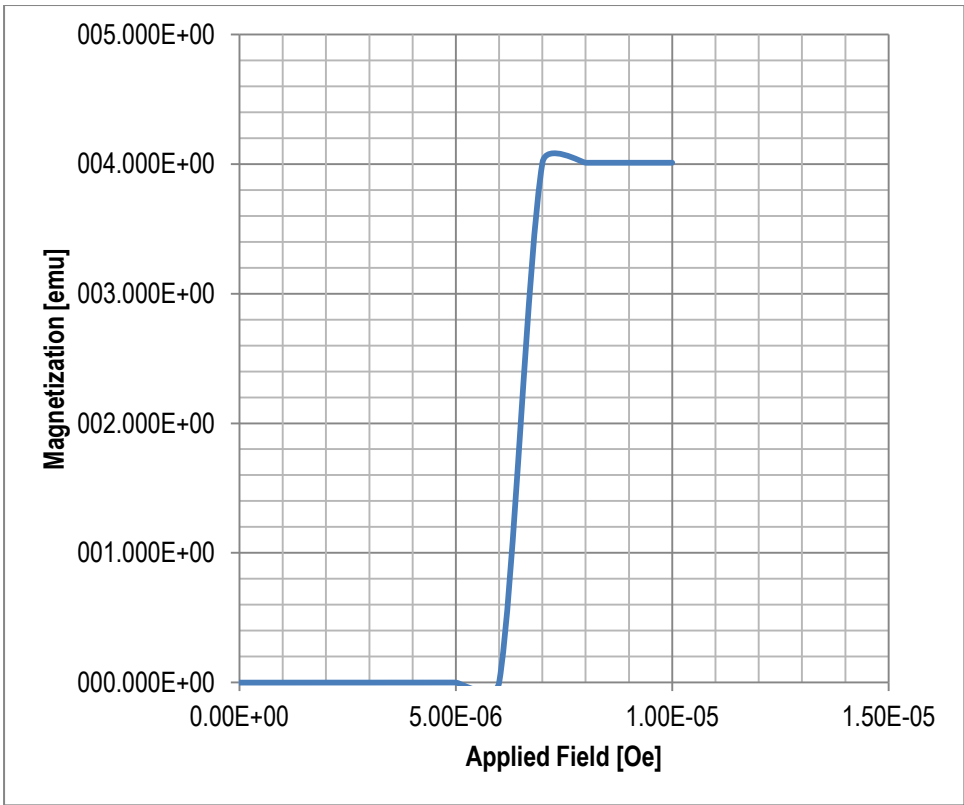


Figure. 4.135: Variation magnetization with applied voltage (13% doping)

Slope of the graph is 117.00

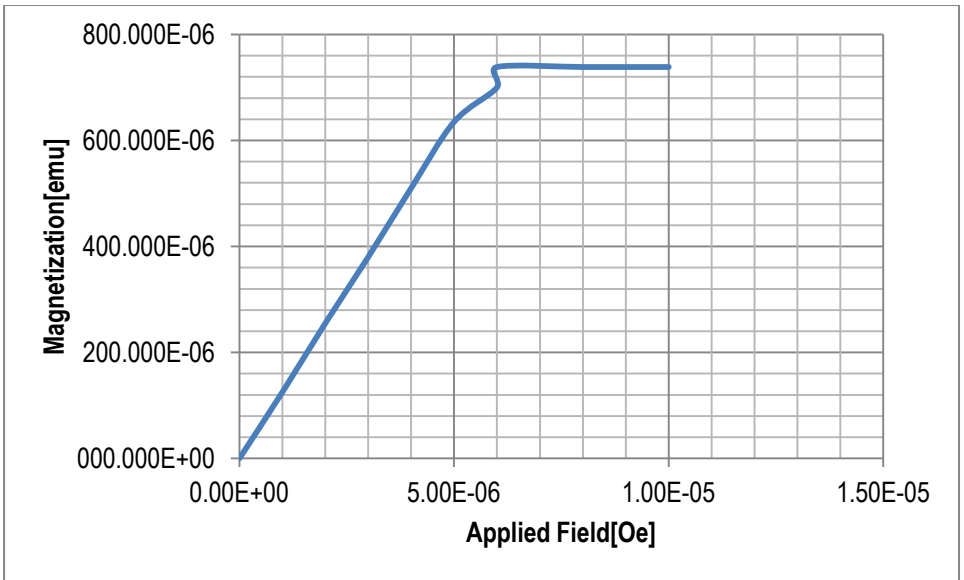


Figure. 4.136: Variation magnetization with applied voltage (18% doping)

Slope of the graph is 127.50

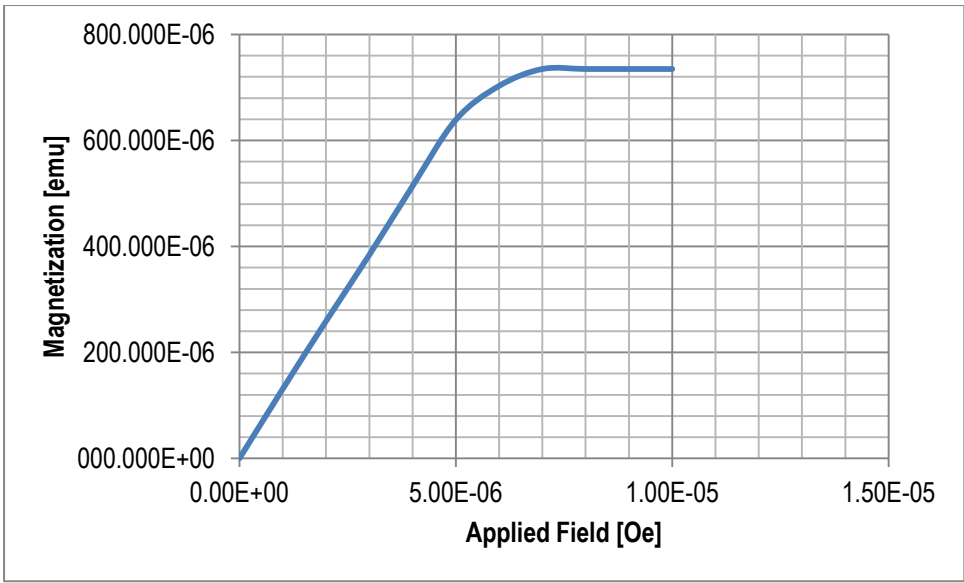


Figure. 4.137: Variation magnetization with applied voltage (23% doping)

Slope of the graph is 128.50

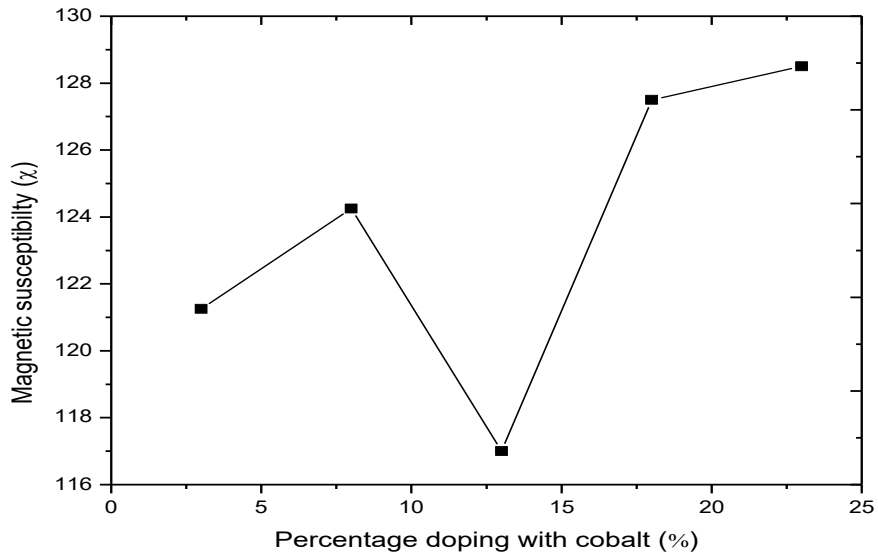


Figure 4.138: Variation of magnetic susceptibility with percentage cobalt dopant for CdCo₂O₄ nanofilm.

4.3.10. Compositional analysis

Table 4.6 shows that as the mass of cobalt dopant increases, mass of host metal (cadmium) decreases.

Table 4.6: Compositional analysis for cadmium cobalt oxide nanofilm at various percentage doping with cobalt

Sample	Percentage doping (%)	Cd	O	Co
N27	3	84.8739	12.5000	2.6250
N28	8	80.4963	12.5019	7.0000
N29	13	76.1217	12.5011	11.3750
N30	18	71.7467	12.5021	15.7500
N31	23	67.3735	12.5007	20.1250

The film contains Germanium as impurity.

4.4 Analysis of silver cobalt oxide (AgCoO₂) nanofilms

The nanofilms were analyzed for their optical, structural, and magnetic properties.

4.4.1 Bandgaps of silver cobalt oxide nanofilms at various percentages doping

The results as shown in figures 4.139 to 4.144 are summarized in table 4.7.

The results of this work as shown in the Table 4.7 and figure 4.142, show that silver cobalt oxide has a wide bandgap which increases as the percentage doping with cobalt increases. The results are in agreement with the results obtained by other researchers since they fall within the same close range, viz; Silver cobalt oxide thin film has a direct bandgap of 4.15eV (Banerjee *et al.*, 2005). A bandgap of 1.2eV was obtained for silver oxide thin film (Fortiu *et al.*, 1964; In Banerjee *et al.*, 2005). Bandgap of 1.64eV -1.95eV was obtained by (Nwanya *et al.*, 2013). Silver oxide nanofilm has a bandgap of 2.8eV (Xi-yao *et al.*, 2003). Ag_xO film with a wide energy bandgap range from 1.2 to 3.4 eV can be deposited using magnetron sputtering, chemical bath deposition, electron cyclotron resonance oxygen plasma assisted e-beam evaporation of Ag, etc (Hong-Liang *et al.*, 2010). The optical band gap of Ag₂O thin films decreases from 1.716 eV to 1.559 eV as the annealing temperature increases from 100°C to 200°C (Saroja *et al.*, 2013). However, as wide bandgap semiconductor, electronics made of it have the advantage of being smaller, faster, more reliable and more efficient than the Si based counterparts. Devices made of the material can operate at higher temperatures, voltages and higher frequencies.

From figure 4.146, bandgap of AgCoO₂ nanofilm is inversely proportional to thickness of the film.

This decrease in bandgap could be attributed to increase in crystallite size as thickness increases. Increase in grain size has a decreasing effect on bandgap (Ramana *et al.*, 2003). However formation of impurity level within the bandgap could also lead to decrease in bandgap.

From figure 4.148, the bowing parameter decreases as the percentage doping with cobalt increases. Bowing downwards implies that it is positive. This compares well with the works of (Van de walley *et al.*, 1999), (Moses and Van de Walle, 2010). Bowing parameter is significant for investigating the bandgap energies of ternary alloys, (Gulebagian *et al.*, 2014).

Figure 4.147 shows that, thickness of AgCoO₂ nanofilm decreases as the percentage doping with cobalt increases. This could be attributed to the fact that silver is the best conductor of electricity, so replacing the atom(s) with another element decreases the conductivity of the electrolyte and so less deposition on the slide. The more it is doped the less conductive it becomes and less deposit obtained hence less thickness.

Table 4.7: Variation of bandgap with percentage doping for cobalt doped silver cobalt oxide nanofilm.

Doping (%)	0 (undoped)	3	8	13	18	23
Bandgap (eV)	1.8	2.6	3.0	3.2	3.9	4.1

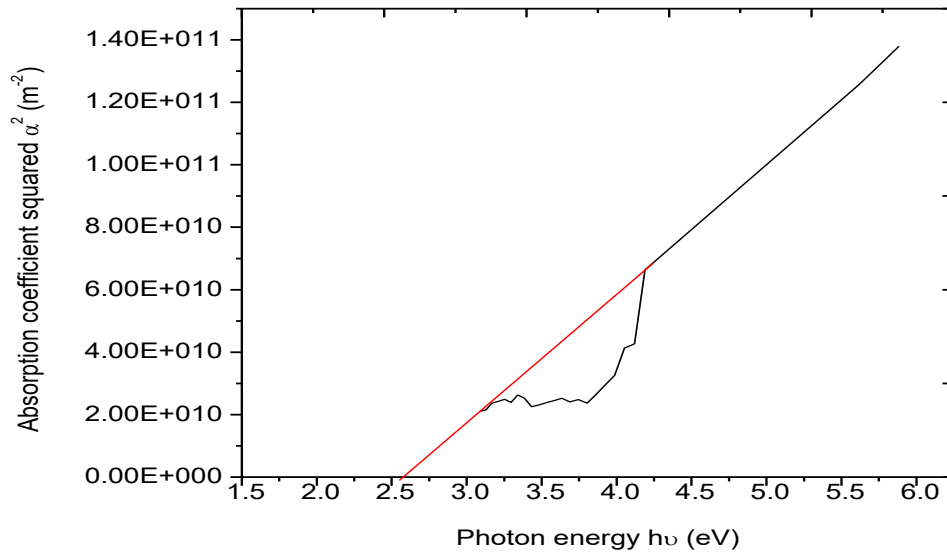


Figure 4.139: Absorption coefficient versus photon energy for AgCoO₂ nanofilm(3% doped with cobalt).

From figure 4.136, 3% cobalt doped AgCoO₂ nanofilm has direct allowed bandgap of 2.6ev.

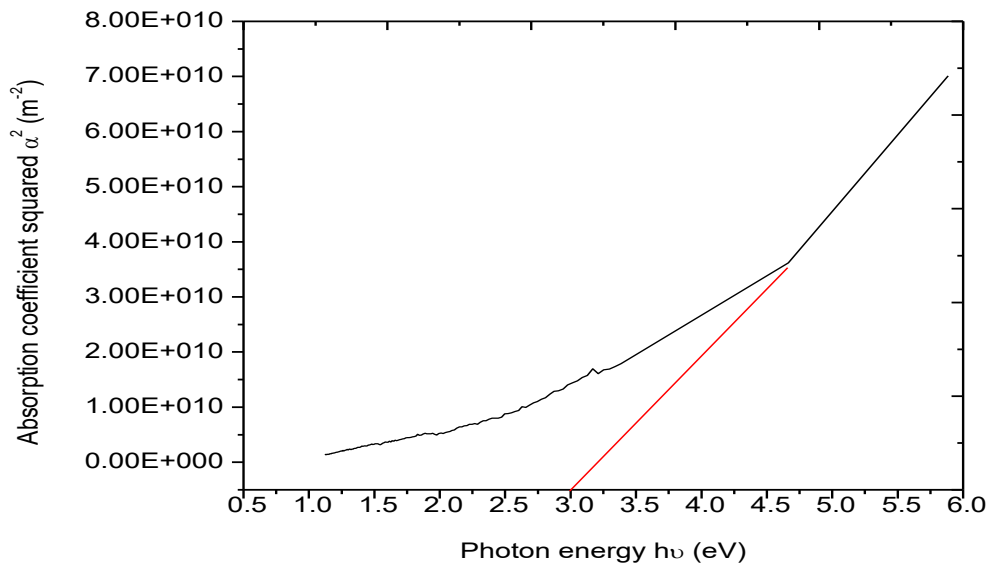


Figure 4.140: Absorption coefficient versus photon energy for AgCoO₂ nanofilm(8% doped with cobalt).

From figure 4.140, 8% cobalt doped AgCoO₂ nanofilm has direct allowed band gap of 3.0ev.

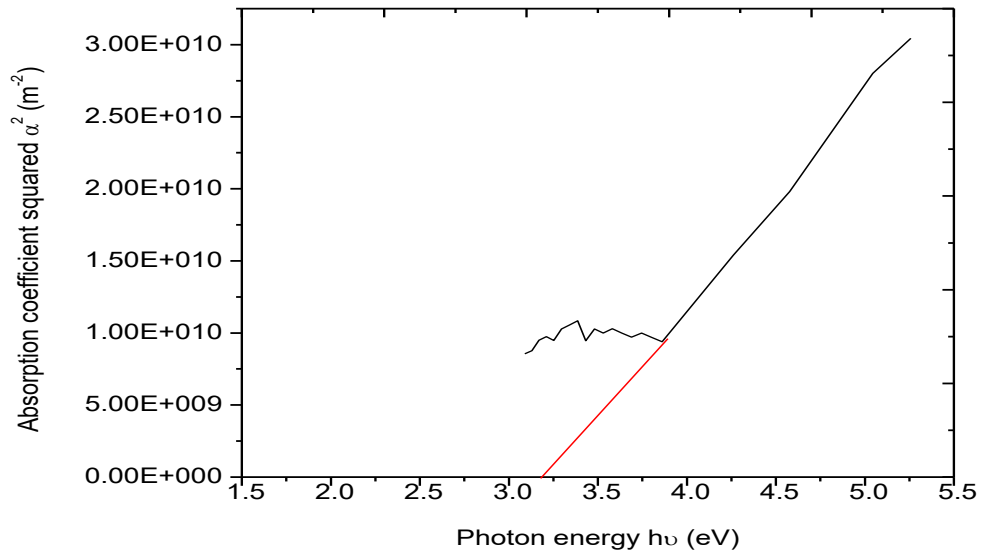


Figure 4.141: Absorption coefficient versus photon energy for AgCoO₂ nanofilm(13% doped with cobalt).

From figure 4.141, 13% cobalt doped AgCoO₂ nanofilm has a direct allowed bandgap of 3.2ev.

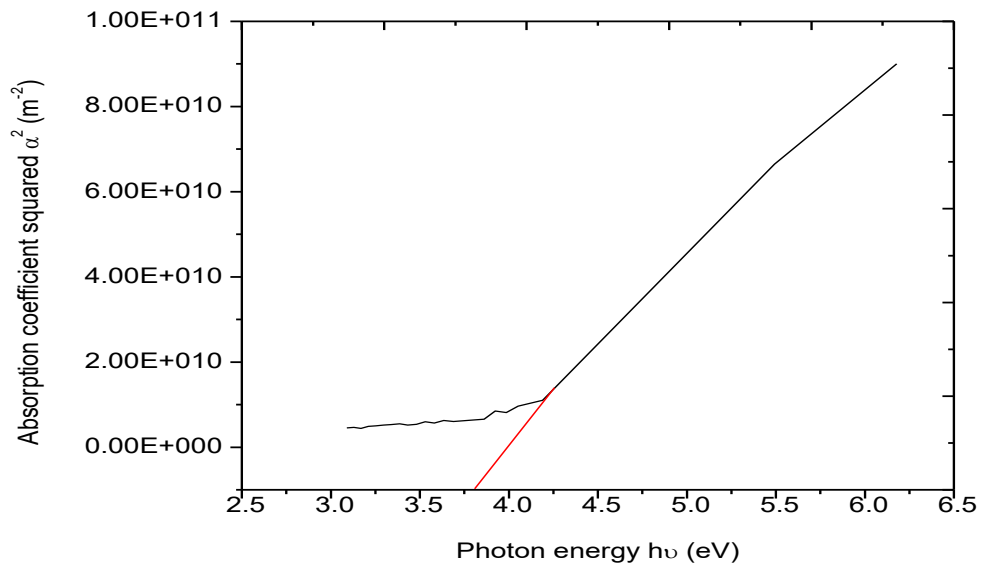


Figure 4.142: Absorption coefficient versus photon energy for AgCoO₂ nanofilm(18% doped with cobalt).

From figure 4.142, 18% cobalt doped AgCoO₂ nanofilm has a direct allowed bandgap of 3.8ev

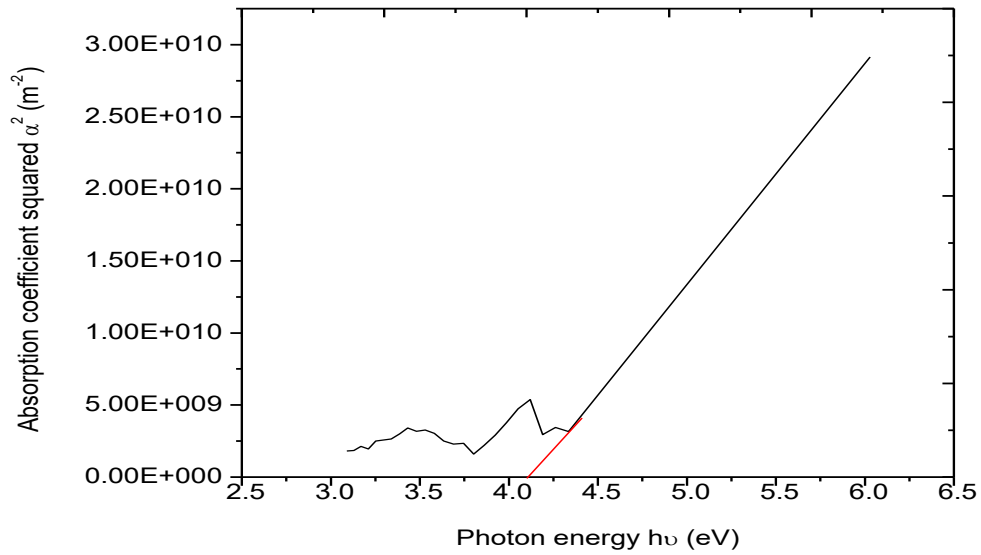


Figure 4.143: Absorption coefficient versus photon energy for AgCoO₂ nanofilm(23% doped with cobalt).

From figure 4.143, 23% cobalt doped AgCoO₂ nanofilm has a direct allowed bandgap of 4.1eV.

4.4.2 Bandgap of Ag₂O nanofilm (undoped)

Figure 4.144: Absorption coefficient versus photon energy for undoped silver oxide (Ag₂O) nanofilm.

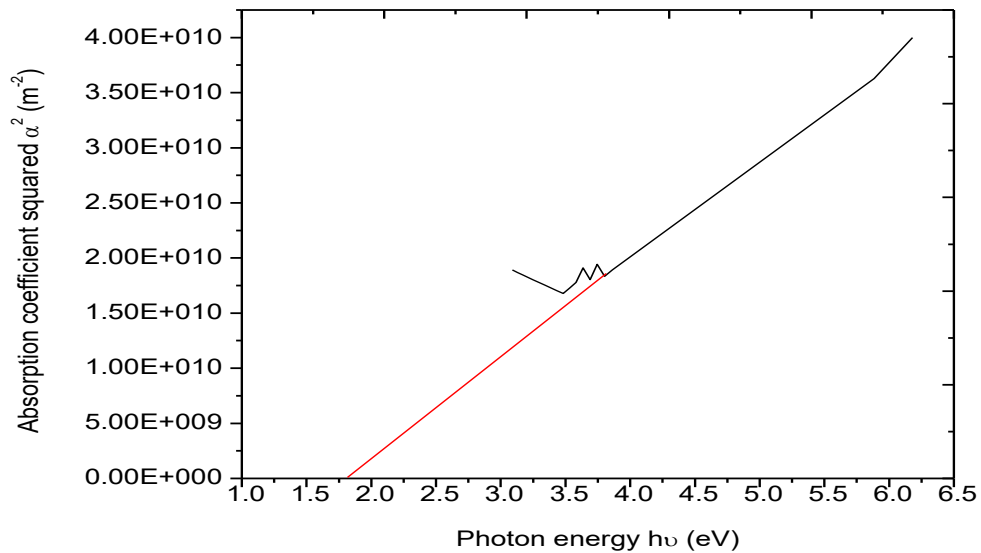


Figure 4.144 shows that, undoped silver oxide nanofilm has direct allowed bandgap of 1.8eV.

4.4.3 Bandgap variations and thickness variation

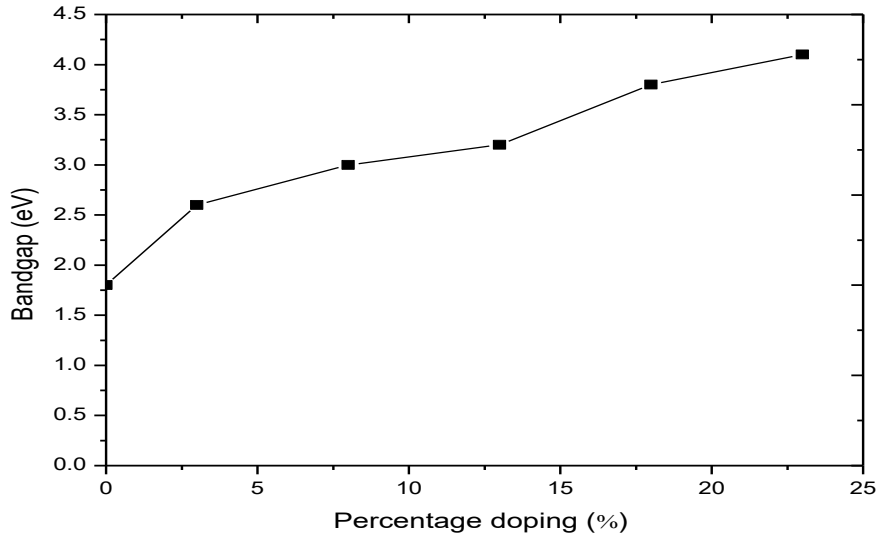


Figure 4.145: Variation of bandgap with percentage doping with cobalt, for cobalt doped AgCoO₂ nanofilm.

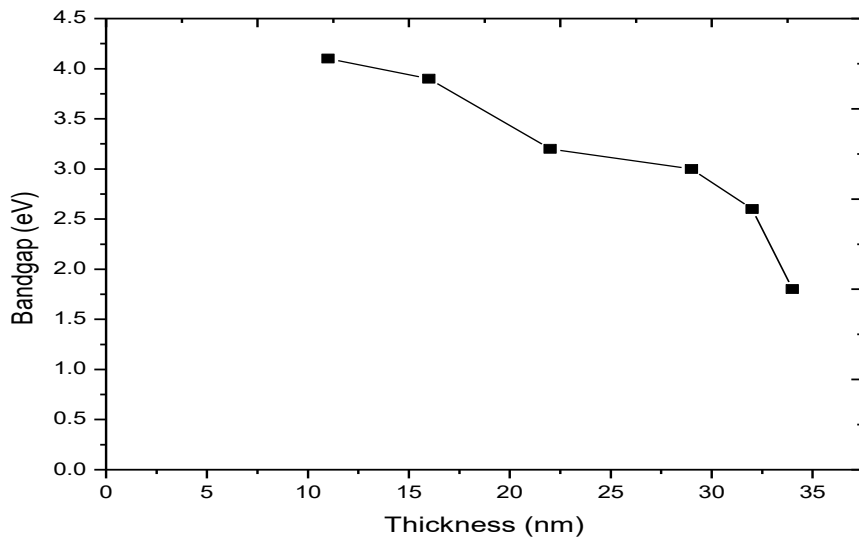


Figure 4.146: Variation of bandgap with thickness for cobalt doped AgCoO₂ nanofilm.

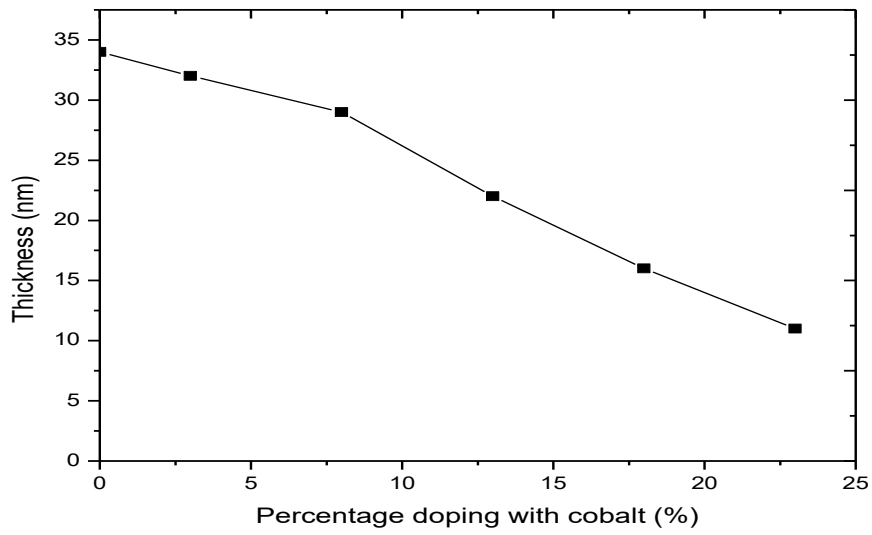


Figure 4.147: Variation of thickness with percentage doping with cobalt for AgCoO₂ nanofilm

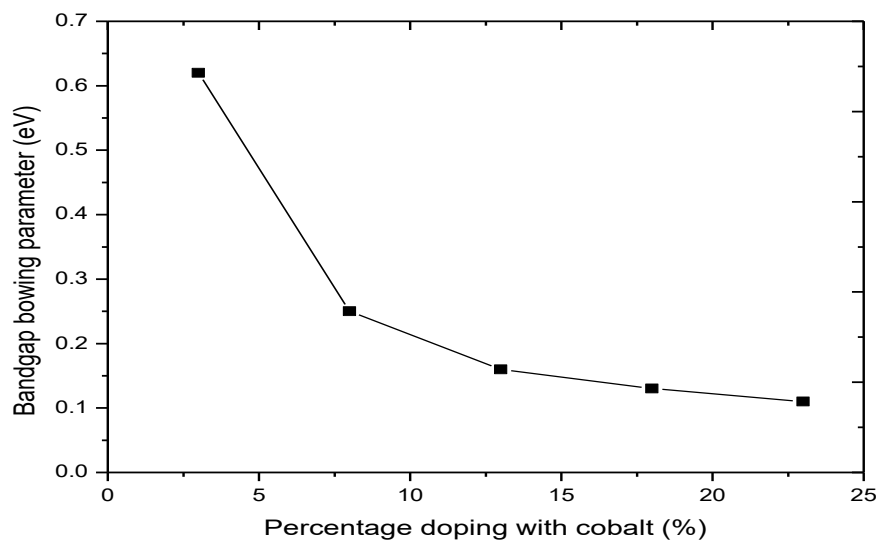


Figure 4.148: Variation of bandgap bowing parameter with percentage doping for silver cobalt oxide nanofilm.

4.4.4 Effect of percentage doping on optical properties of AgCoO₂ nanofilms

As shown in figure 4.149, the ultrathin nature of the film gave it very low absorbance in all the regions(UV-VIS-NIR) . For the doped films, maximum absorbance is 0.06=6% for 3% doped in UV-VIS-NIR regions. The undoped film has maximum absorbance (6.7%) in the UV region and decreases to minimum in the NIR. The absorbance of the films decreases as the percentage doping with cobalt increases. This is attributed to the fact that silver is the best conductor of electricity, so replacing the atom(s) with another element decreases the conductivity and so less deposition on the slide. The more it is doped the less conductive it becomes and less deposit obtained and absorbance is directly proportional to thickness of the film. Absorbance of a film increases with increasing film thickness and decreases with decreasing film thickness (Nadeem *et al.*, 2000).

From figure 4.150, the transmittance of the films is generally high; for the doped, minimum of 87.7%(3%) in UV region and maximum of 98.5%(23%) in NIR region. The undoped film has minimum of 86.7% in visible region and increases to maximum(90.5%) in the NIR. Their excellent light transmission makes the film good material for UV laser application. Transmittance of the films increases as the percentage doping with cobalt increases.

Figure 4.151 shows that the reflectance of the films is generally very low in all the regions; maximum of 0.059=5.9% for the doped. Each doped film exhibited almost same level of reflectance in all the regions. The undoped has maximum reflectance of 0.066=6.6% in the visible region and decreases to minimum in the NIR. Reflectance of the films decreases as the percentage doping with cobalt increases.

Figure 4.152 shows that lower percentage doping have high refractive indices while higher percentage doping have low refractive indices. 3% doping has refractive indices UV(~1.64) ,VIS (~ 1.67), NIR (~1.61), 8% has ~1.57 , 13% has UV (~1.47) ,VIS (~1.48), NIR (~1.46), 18% has UV (~1.39) , VIS (~1.39) ,NIR (~1.40) , 23% has UV (~1.28) , VIS (~1.27), NIR(~1.19). The undoped film has

maximum refractive index(1.69) in the visible region and decreases to minimum(1.51) in the NIR. This makes the films good materials for multilayer antireflection coatings and in film stack for colour selective coating. The refractive index of the films decreases as the percentage doping with cobalt increases. As shown in figure 4.153, each doped film showed almost same level of extinction coefficient from UV to NIR region, maximum of 0.0048 for 3% doped. Extinction coefficient of the undoped film is maximum(0.0053) in the visible region and decreases to minimum in the NIR of the electromagnetic spectrum. However the extinction coefficient of the film decreases as percentage doping increases. Figure 4.154 shows that each percentage of doped film showed almost same level of complex dielectric constant from UV to NIR region, maximum of 2.7 for 3% doped . Complex dielectric constant of the undoped film is maximum(2.9) in the visible region and decreases to minimum in the NIR of the electromagnetic spectrum. However the complex dielectric constant of the film decreases as percentage doping increases. From figure 4.155, the doped films have maximum optical conductivity at the UV region(maximum of $6.36E+12$ for 3% doped) and decreases to minimum in NIR region . Optical conductivity of the undoped film is maximum($5.9E+12$) in the visible region and decreases to minimum in the NIR of the electromagnetic spectrum. However the optical conductivity of the film decreases as percentage doping increases.

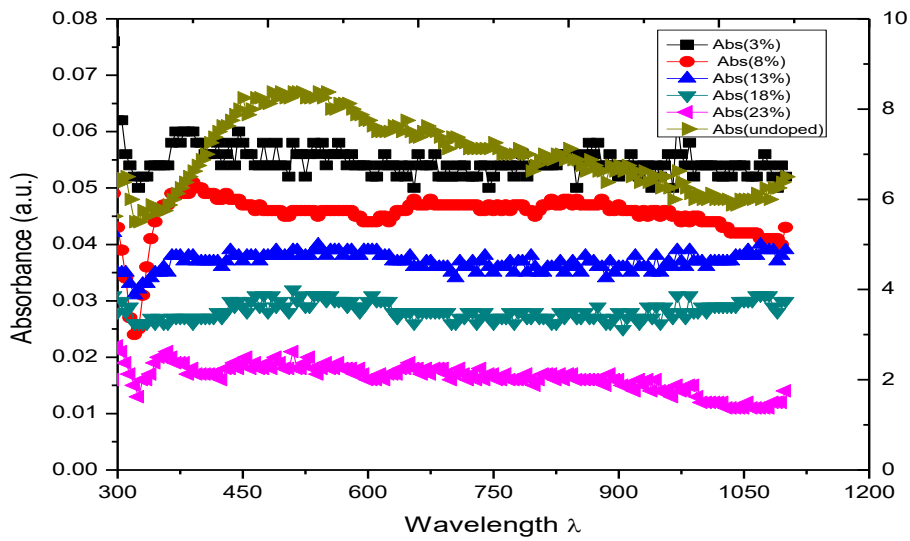


Figure 4.149: Variation of absorbance with percentage doping for AgCoO_2 nanofilms for different percentages doping with cobalt.

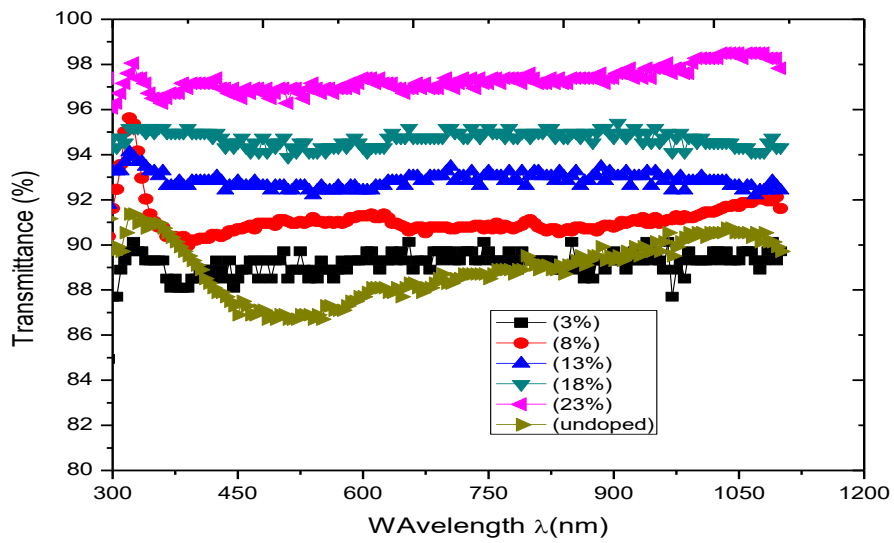


Figure 4.150: Variation of transmittance with wavelength for AgCoO_2 nanofilms for different percentages doping with cobalt.

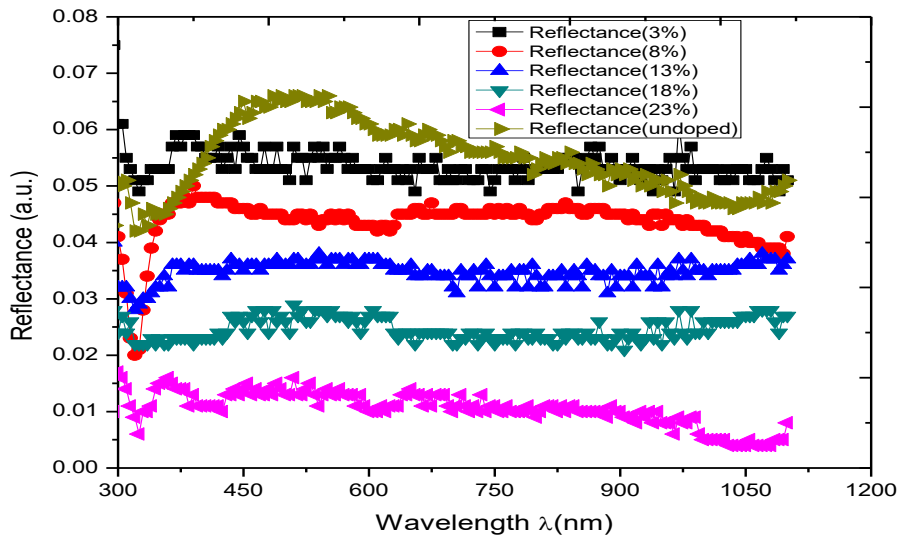


Figure 4.151: Variation of reflectance with wavelength for cobalt doped AgCoO_2 nanofilms for different percentages doping with cobalt.

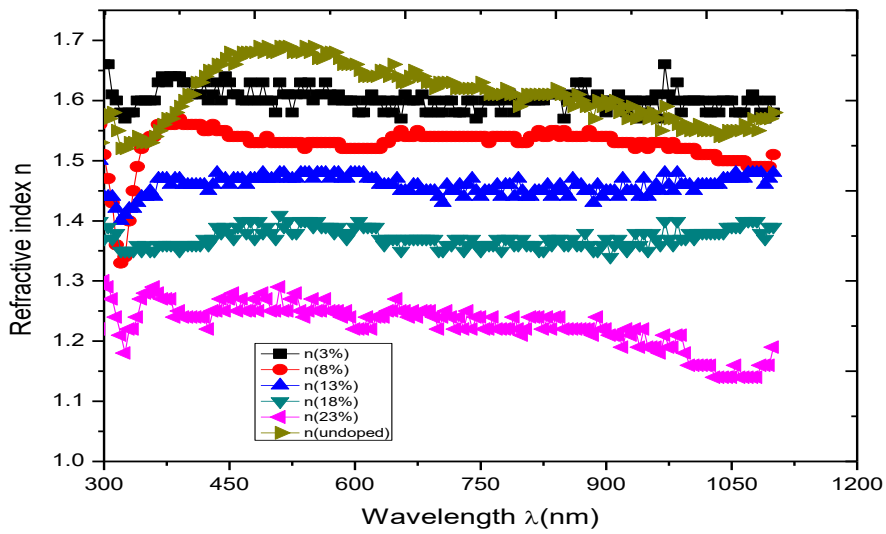


Figure 4.152: Variation of refractive index with wavelength for cobalt doped AgCoO_2 nanofilms for different percentages doping with cobalt..

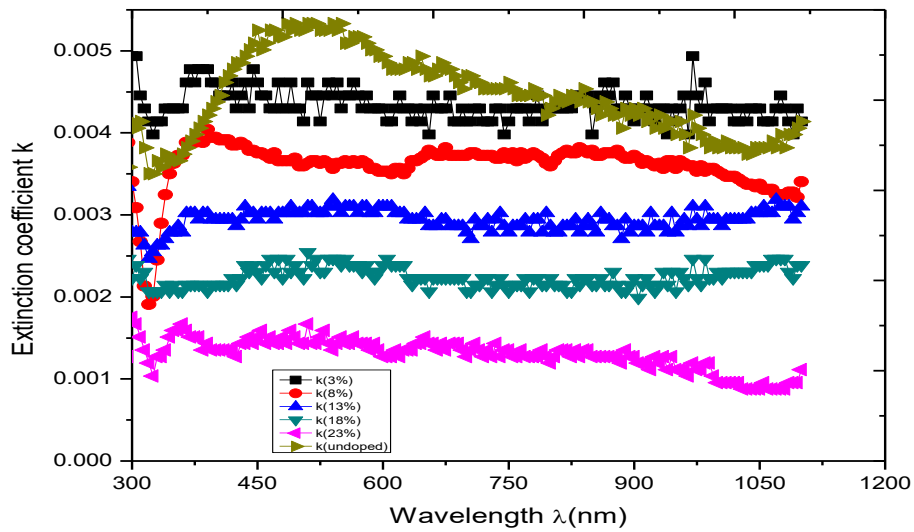


Figure 4.153: Variation of extinction coefficient with wavelength for cobalt doped AgCoO_2 nanofilms for different percentages doping with cobalt.

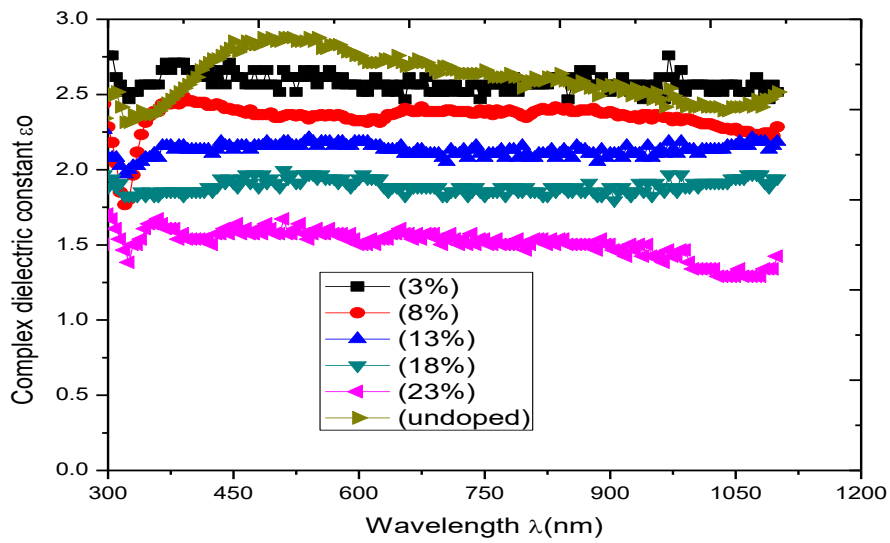


Figure 4.154: Variation of complex dielectric constant with wavelength for cobalt doped AgCoO_2 nanofilms for different percentages doping with cobalt.

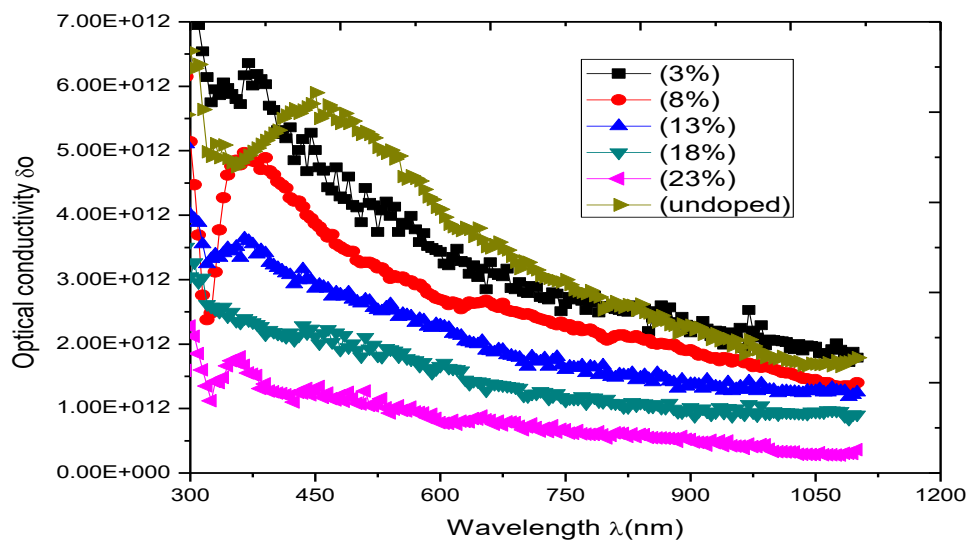


Figure 4.155: Variation of optical conductivity with wavelength for cobalt doped AgCoO_2 nanofilms for different percentages doping with cobalt.

4.4.5 Effect of thickness on optical properties of silver cobalt oxide nanofilms

Figure 4.156 shows that absorbance of the films increases as the thickness of the films increases, maximum of 0.06=6% in UV region for highest thickness, 34nm. The undoped film(34nm) has maximum absorbance (6.7%) in the UV region and decreases to minimum in the NIR

From figure 4.157, transmittance of the films decreases as the thickness increases. Minimum of 86.9% in visible region for highest thickness, 34nm. The undoped film(34nm) has minimum of 86.7% in visible region and increases to maximum(90.5%) in the NIR

Reflectance of the film increases as the thickness increases as shown in figure 4.158. Maximum of 0.061=6.1% for (32nm) in NIR region. The undoped(34nm) has maximum reflectance of 0.066=6.6% in the visible region and decreases to minimum in the NIR

Figure 4.159 shows that refractive index of the film increases as the thickness increases. Maximum of 1.66 in NIR region for 32nm. The undoped film(34nm) has maximum refractive index(1.69) in the visible region and decreases to minimum(1.51) in the NIR

As shown in figure 4.160, extinction coefficient of the film increases as the thickness increases. Maximum of 0.0049 in NIR region for highest thickness, 32nm. Extinction coefficient of the undoped film is maximum(0.0053) in the visible region and decreases to minimum in the NIR of the electromagnetic spectrum. The complex dielectric constant of the film increases as the thickness increases as depicted in figure 4.161, maximum of 2.76 in NIR region for 32nm thickness. Complex dielectric constant of the undoped film is maximum(2.9) in the visible region and decreases to minimum in the NIR of the electromagnetic spectrum. From figure 4.162, optical conductivity of the film increases as the thickness increases. Maximum of $5.70E+12$ in visible region for thickness, 32nm. Optical conductivity of the undoped film(34nm) is maximum($5.9E+12$) in the visible region and decreases to minimum in the NIR of the electromagnetic spectrum.

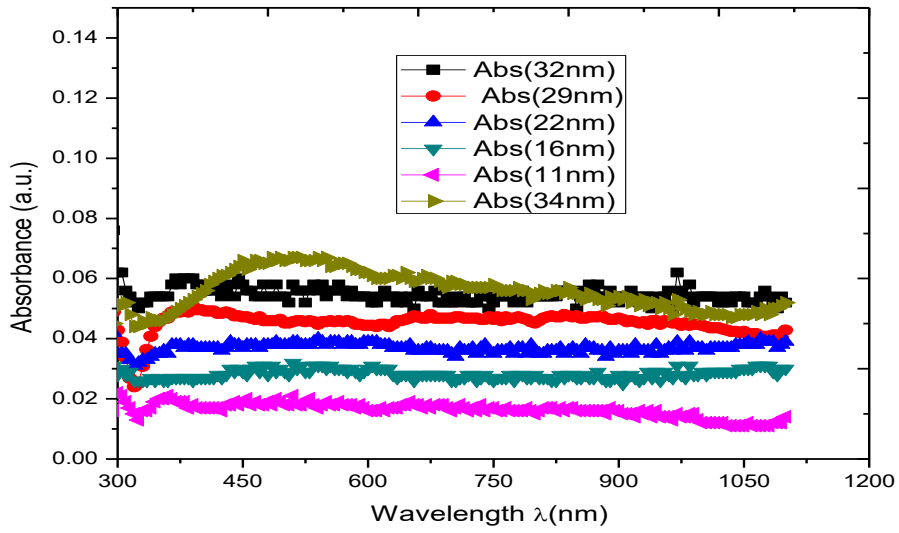


Figure 4.156: Variation of absorbance with wavelength for AgCoO_2 nanofilms for different thicknesses.

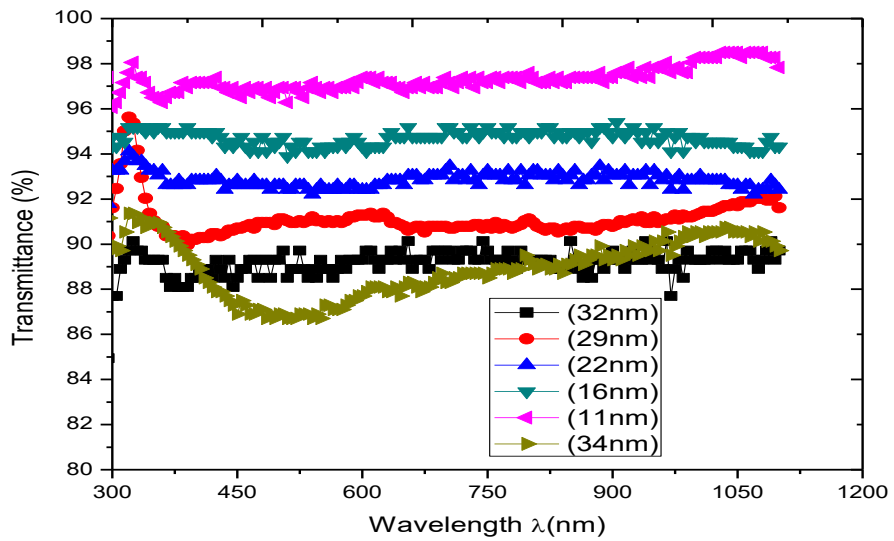


Figure 4.157: Variation of transmittance with wavelength for AgCoO_2 nanofilms for different thicknesses.

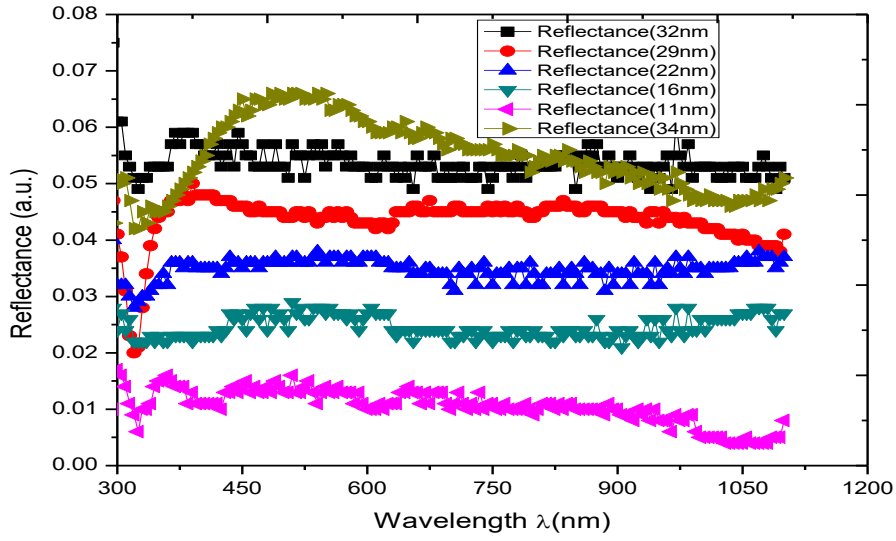


Figure 4.158: Variation of reflectance with wavelength for AgCoO_2 nanofilms for different thicknesses.

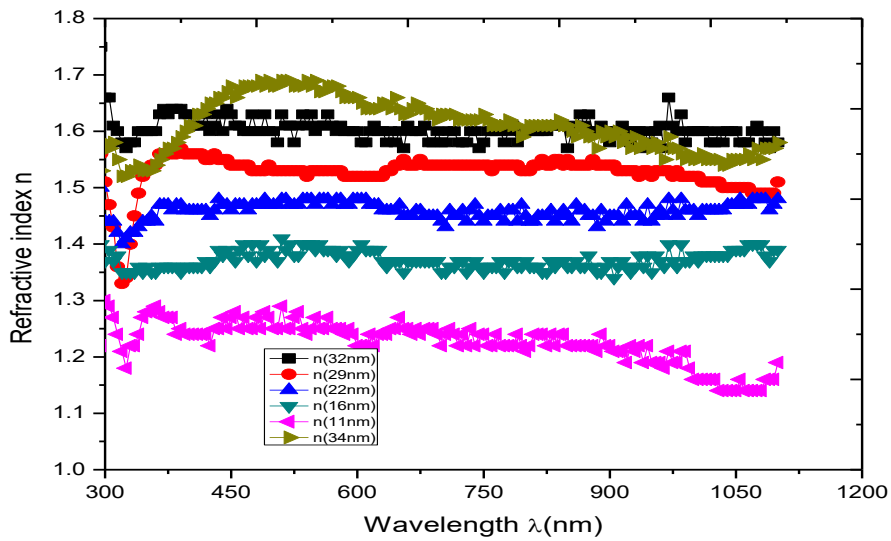


Figure 4.159: Variation of refractive index with wavelength for AgCoO_2 nanofilms for different thicknesses.

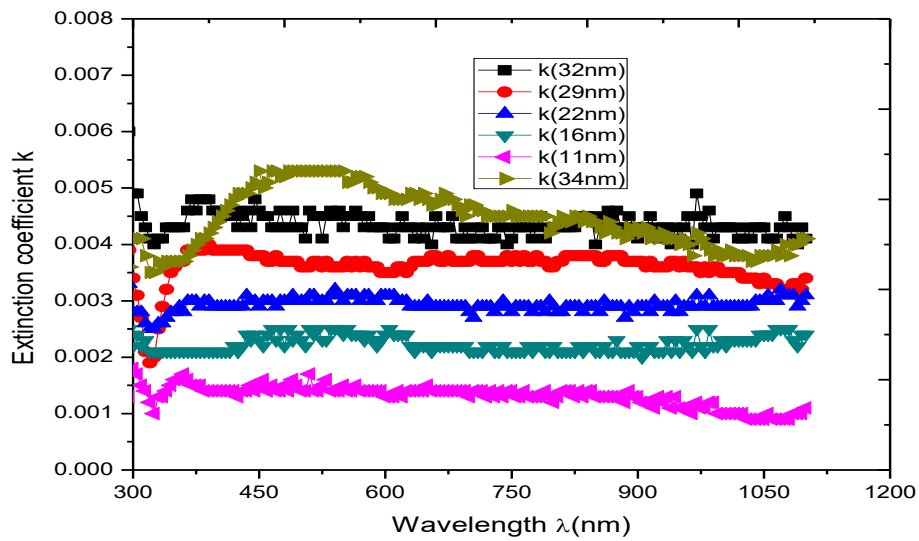


Figure 4.160: Variation of extinction coefficient with wavelength for AgCoO_2 nanofilm for different thicknesses.

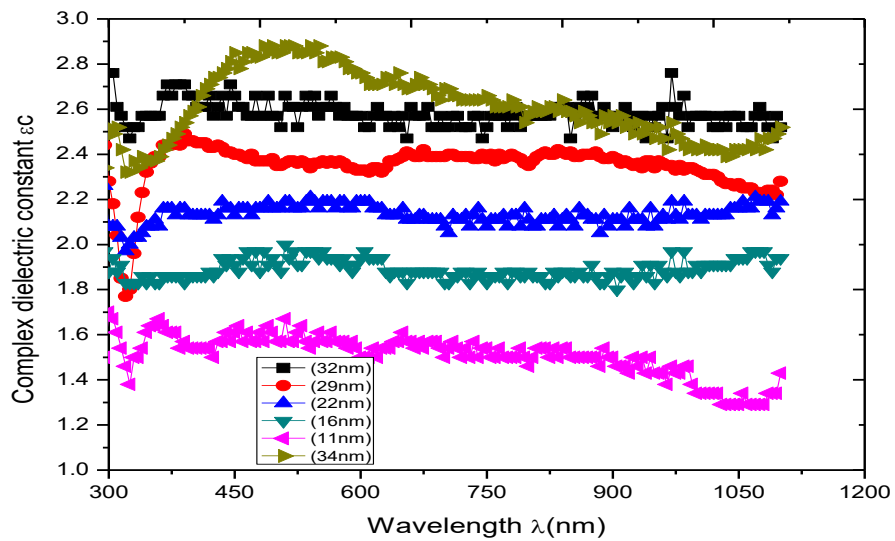


Figure 4.161: Variation of complex dielectric constant with wavelength for AgCoO_2 nanofilms for different thicknesses.

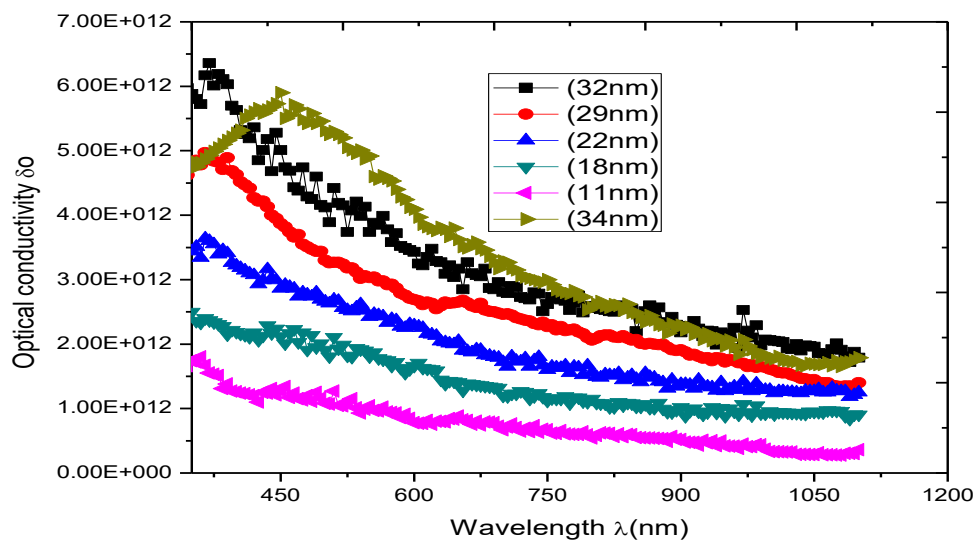


Figure 4.162: Variation of optical conductivity with wavelength for AgCoO₂ nanofilms for different thicknesses.

4.4.6 Effect of deposition time on optical properties of silver cobalt oxide nanofilms

From figure 4.163, absorbance of the film increases with increase in deposition time 0.24=0.24% in NIR for 60s. However, the film with deposition time 75s deviated from the trend due to peeling off effect whereby the film becomes thicker, peels off from the slide and starts building up afresh.

Figure 4.164 shows that transmittance of the film decreases with increase in deposition time minimum of 58.41% in NIR for 60s. However the film with deposition time 75s deviated from the trend due to peeling off effect.

As shown in figure 4.165, reflectance of the film increases with increase in deposition time, 0.17=0.17% in NIR for 60s. However, the film with deposition time 75s deviated from the trend due to peeling off effect whereby the film becomes thicker, peels off from the slide and starts building up afresh.

Figure 4.166 shows that refractive index of the film increases with increase in deposition time, maximum of 2.43 in NIR for 60s. However, the film with deposition time 75s deviated from the trend due to peeling off effect whereby the film over becomes thicker, peels off from the slide and starts building up afresh. Figure 4.167 shows that extinction coefficient of the film increases with increase in deposition time, 0.019 in NIR for 60s. However, the film with deposition time 75s deviated from the trend due to peeling off effect whereby the film becomes thicker, peels off from the slide and starts building up afresh.

As shown in figure 4.168, complex dielectric constant of the film increases with increase in deposition time, maximum of 6.02 in NIR for 60s. However, the film with deposition time 75s deviated from the trend due to peeling off effect whereby the film becomes thicker, peels off from the slide and starts building up afresh.

From figure 4.169, optical conductivity of the film increases with increase in deposition time, maximum of 2.41E+13 in VIS for 60s. However, the film with deposition time 75s deviated from the trend due to peeling off effect whereby the film becomes thicker, peels off from the slide and starts building up afresh.

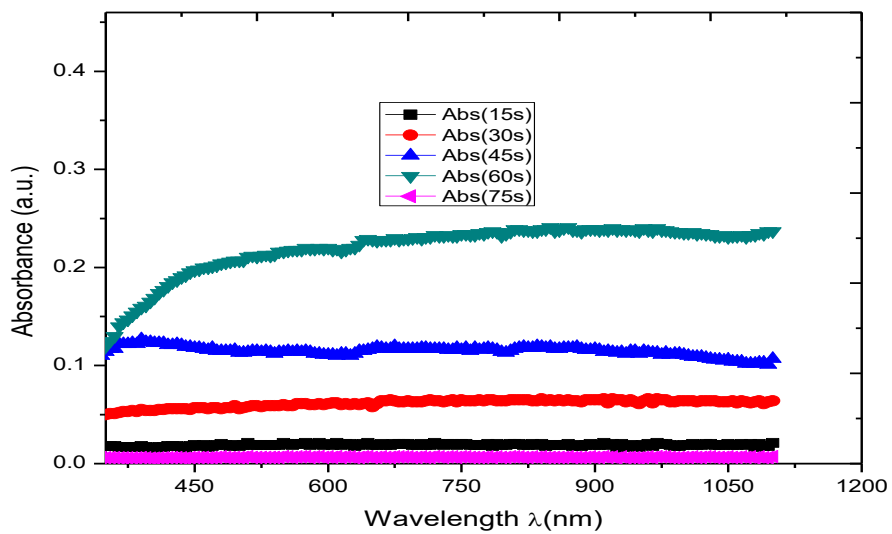


Figure 4.163: Variation of absorbance with wavelength for AgCoO_2 nanofilms for different deposition times.

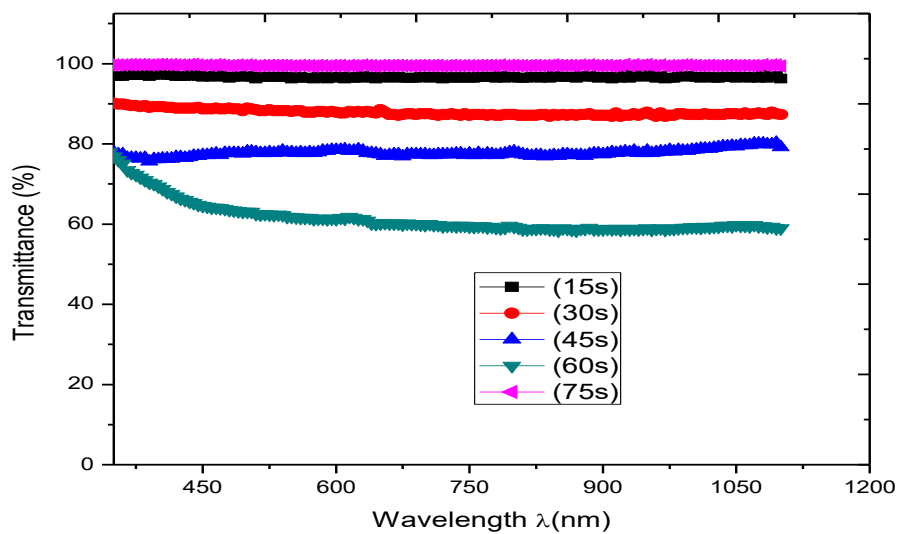


Figure 4.164: Variation of percentage transmittance with wavelength for AgCoO_2 nanofilms for different deposition times.

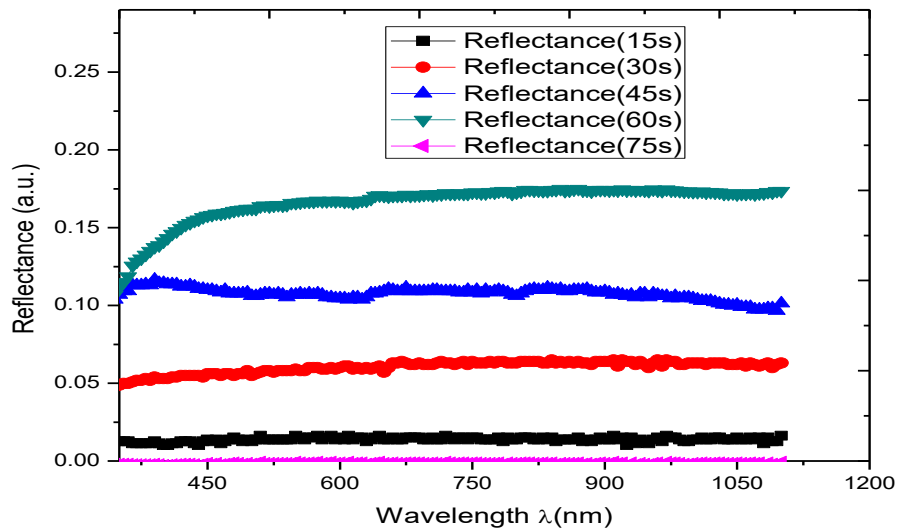


Figure 4.165: Variation of reflectance with wavelength for AgCoO_2 nanofilms for different deposition times.

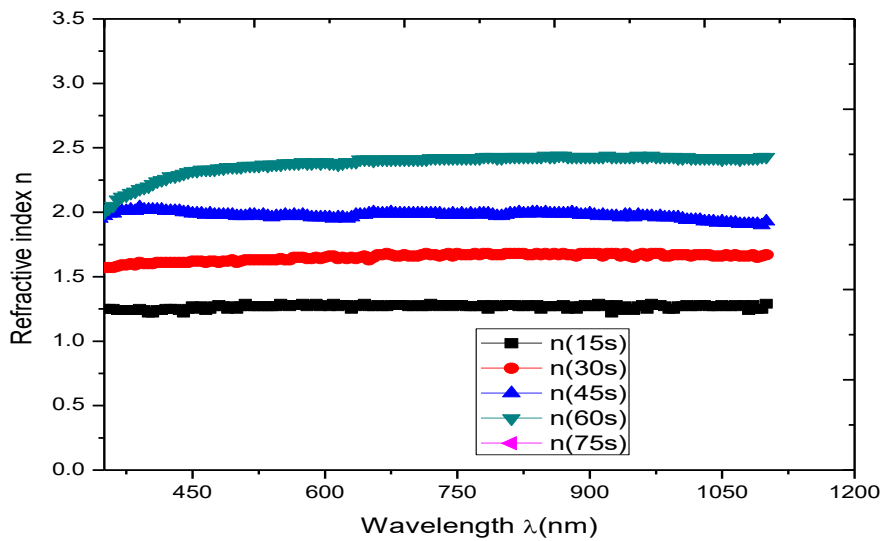


Figure 4.166: Variation of refractive index with wavelength for AgCoO_2 nanofilms for different deposition times.

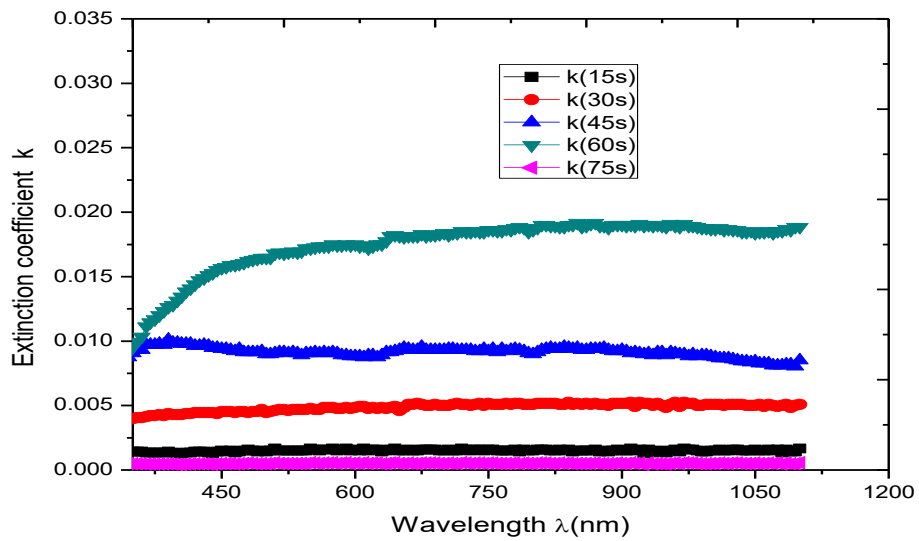


Figure 4.167: Variation of extinction coefficient with wavelength for AgCoO₂ nanofilms for different deposition times.

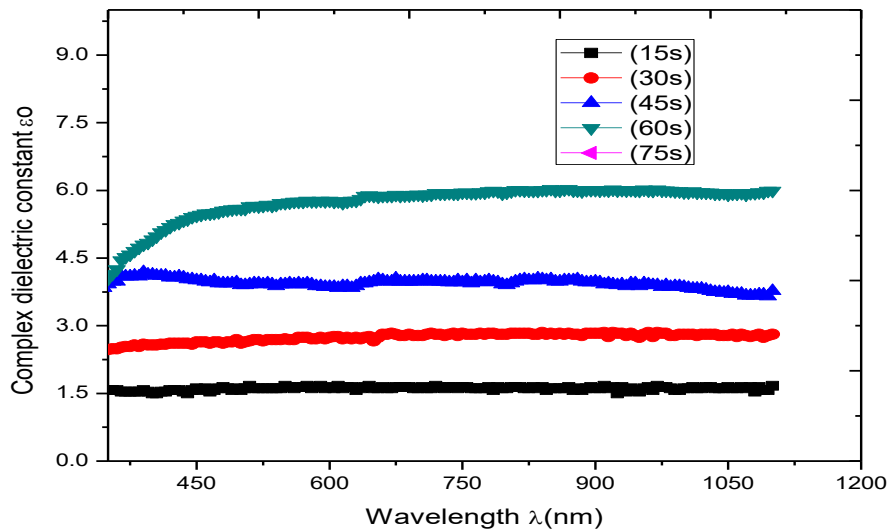


Figure 4.168: Variation of complex dielectric constant with wavelength for AgCoO₂ nanofilms for different deposition times.

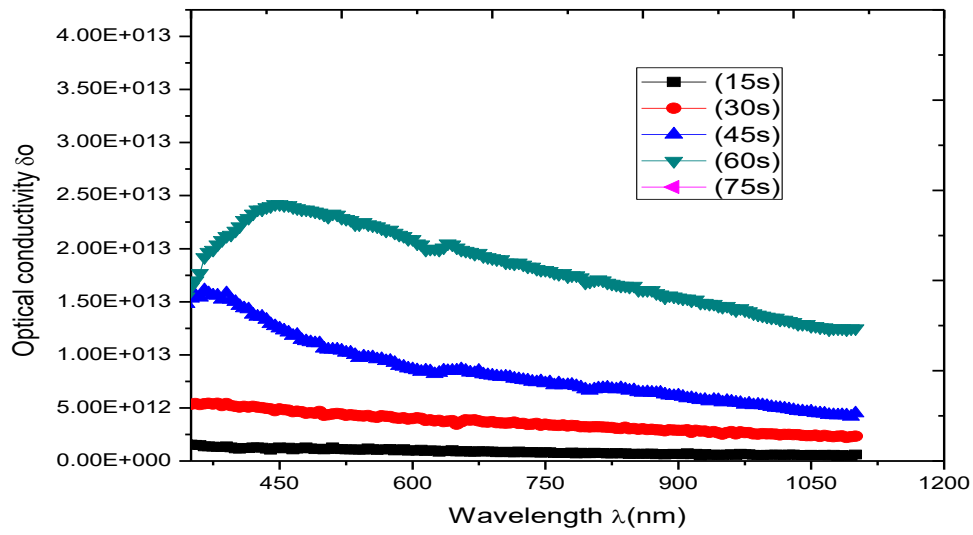


Figure 4.169: Variation of optical conductivity with wavelength for AgCoO_2 nanofilms for different deposition times.

4.4.7 Effect of deposition voltage on optical properties of silver cobalt oxide nanofilms

Figure 4.170 shows that absorbance of the film increases with increase in deposition voltage, maximum of 0.394=3.94% in VIS region for 1.5V . However, the film with deposition voltage 2V deviated from the trend due to peeling off effect whereby the film becomes thicker, peels off from the slide and starts building up afresh.

Figure 4.171 shows that transmittance of the film decreases with increase in deposition voltage, minimum of 41.36% in VIS region for 1.5V . However, the film with deposition voltage 2V deviated from the trend due to peeling off effect whereby the film becomes thicker, peels off from the slide and starts building up again.

As shown in figure 4.172, reflectance of the film increases with increase in deposition voltage, maximum of 0.19=19% for 1.5V, almost same in all the regions . However, the film with deposition voltage 2V deviated from the trend due to peeling off effect whereby the film becomes thicker, peels off from the slide and starts building up afresh.

From figure 4.173, refractive index of the film increases with increase in deposition voltage, maximum of 2.57 for 1.5V, almost same in all the regions . However, the film with deposition voltage 2V deviated from the trend due to peeling off effect whereby the film becomes thicker, peels off from the slide and starts building up afresh.

Figure 4.174 shows that extinction coefficient of the film increases with increase in deposition voltage, maximum of 0.031 in VIS region for 1.5V . However, the film with deposition voltage 2V deviated from the trend due to peeling off effect whereby the film becomes thicker, peels off from the slide and starts building up afresh.

Figure 4.175 shows that complex dielectric constant of the film increases with increase in deposition voltage, maximum of 6.76 for 1.5V, almost same in all the regions . However, the film with deposition

voltage 2V deviated from the trend due to peeling off effect whereby the film becomes thicker, peels off from the slide and starts building up afresh.

From figure 4.176, optical conductivity of the film increases with increase in deposition voltage, maximum of $4.66\text{E}+13$ in VIS region for 1.5V, . However, the film with deposition voltage 2V deviated from the trend due to peeling off effect whereby the film becomes thicker, peels off from the slide and starts building up afresh.

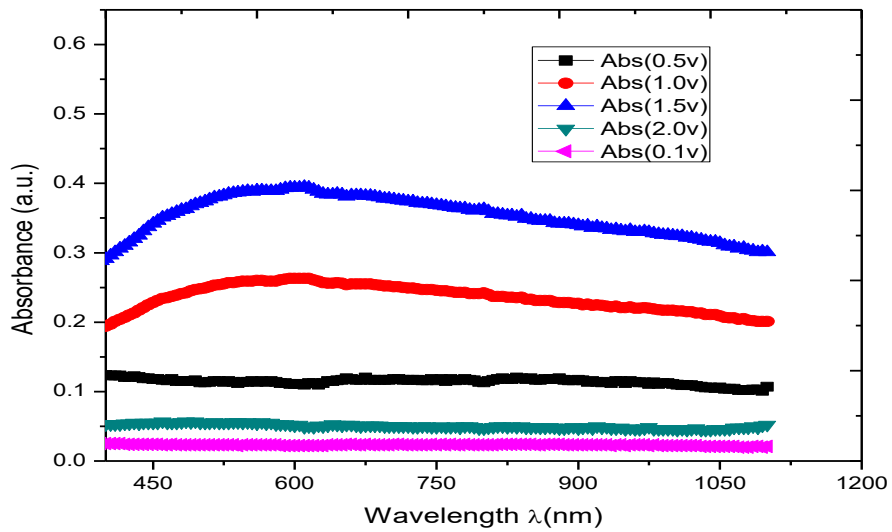


Figure 4.170: Variation of absorbance with wavelength for AgCoO_2 nanofilms for different deposition voltages.

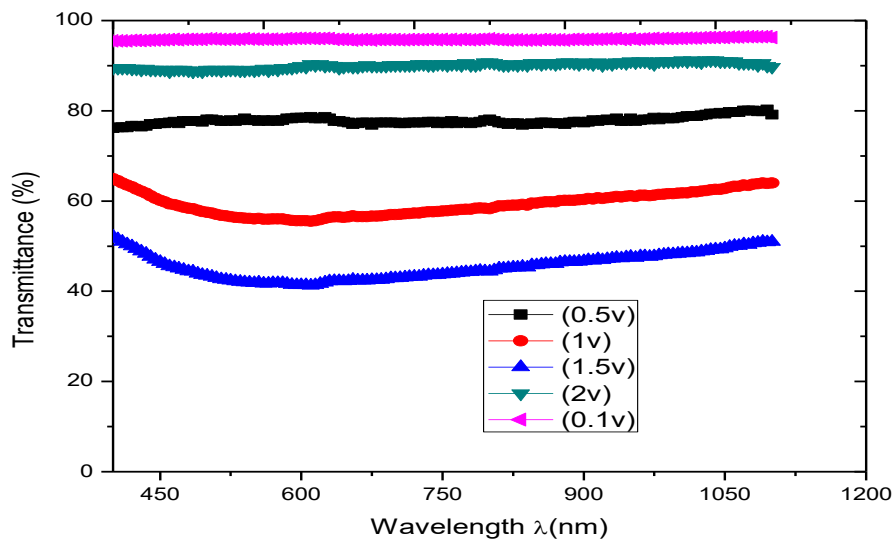


Figure 4.171: Variation of transmittance with wavelength for AgCoO_2 nanofilms for different deposition voltages.

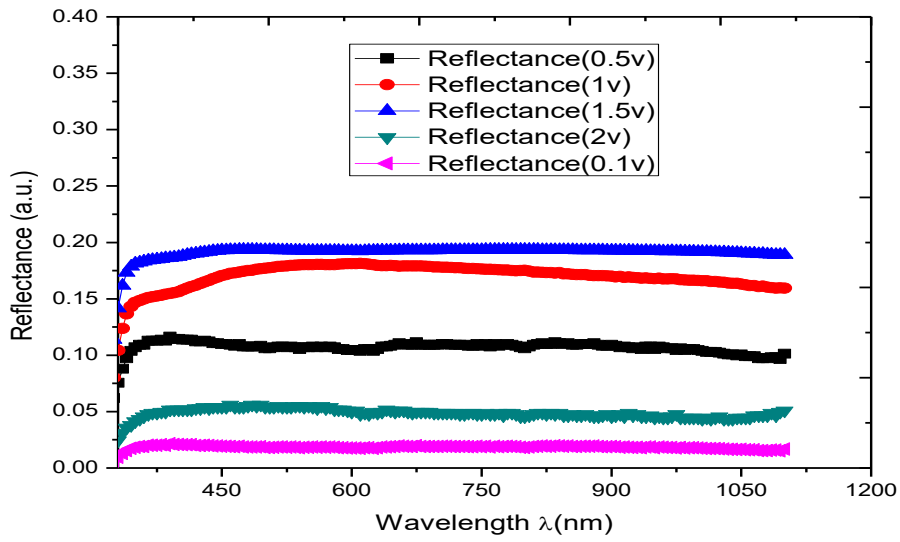


Figure 4.172: Variation of reflectance with wavelength for AgCoO_2 nanofilms for different deposition voltages.

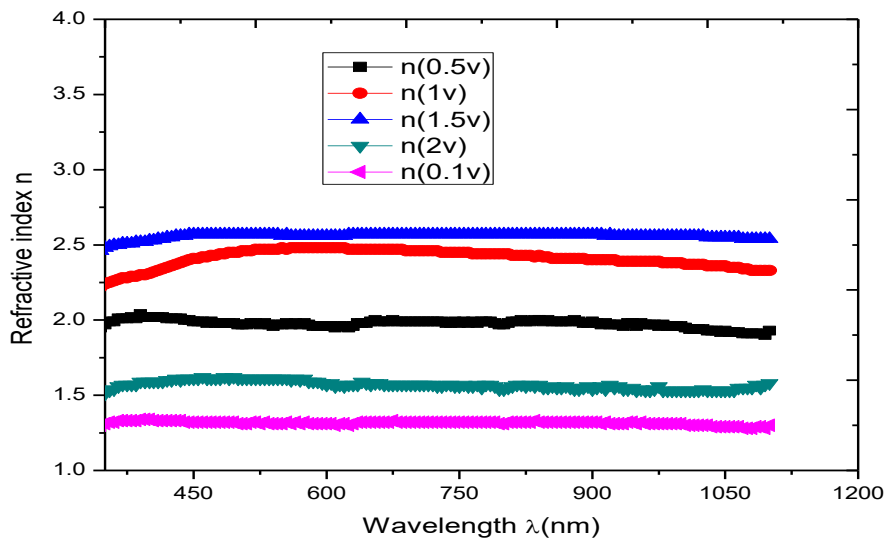


Figure 4.173: Variation of refractive index with wavelength for AgCoO_2 nanofilms for different deposition voltages.

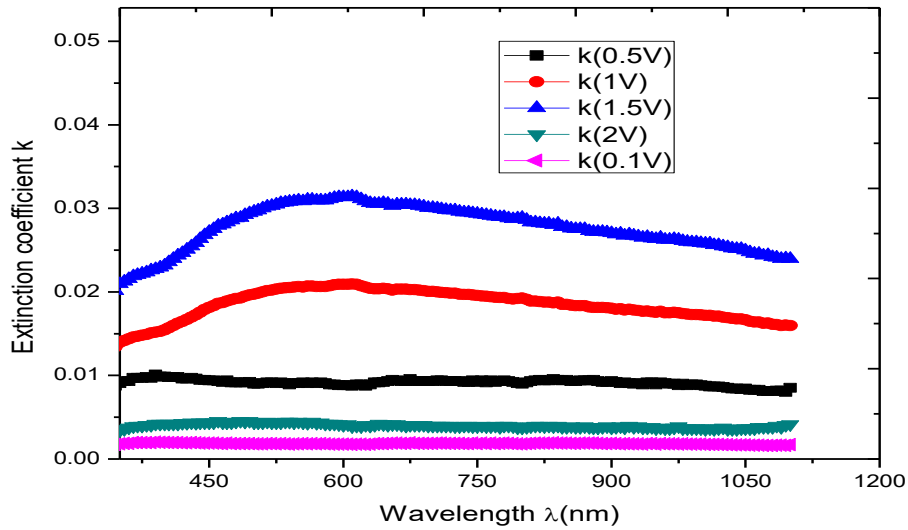


Figure 4.174: Variation of extinction coefficient with wavelength for AgCoO_2 nanofilms for different deposition voltages.

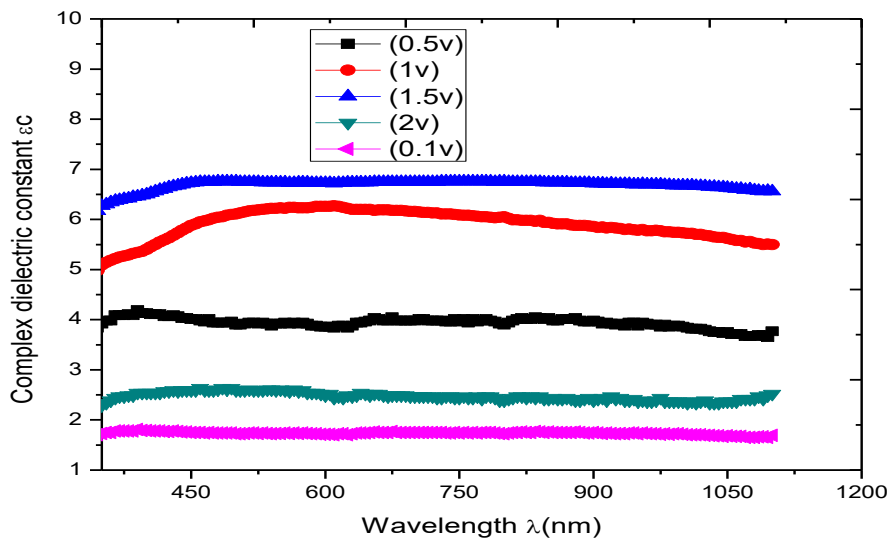


Figure 4.175: Variation of complex dielectric constant with wavelength for AgCoO_2 nanofilms for different deposition voltages.

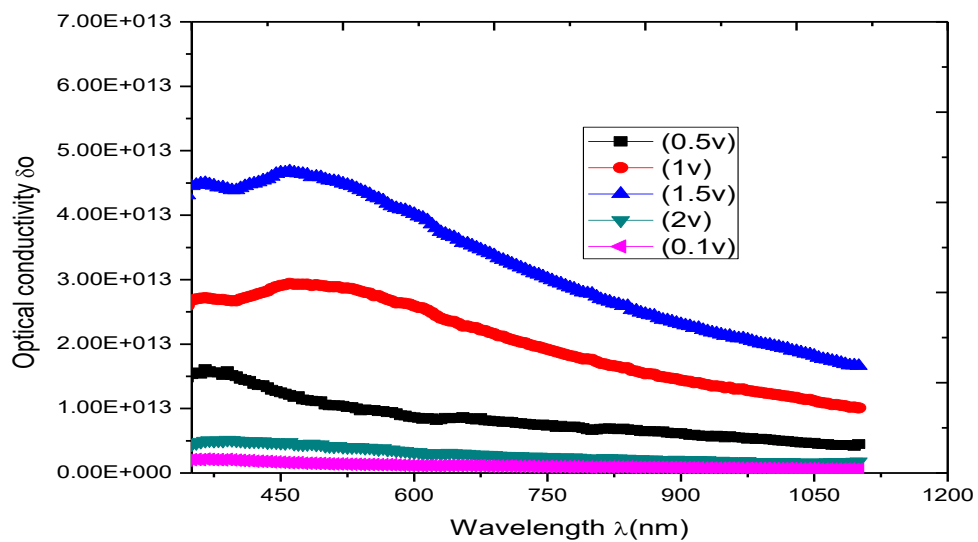


Figure 4.176: Variation of optical conductivity with wavelength for AgCoO₂ nanofilms for different deposition voltages.

4.4.8 Variation of magnetic saturation with percentage doping with cobalt for silver cobalt oxide nanofilm

Figure 4.177 shows that magnetic saturation of pinned layer for AgCoO₂ nanofilm is fluctuatory in nature. It rises to a peak value of 5.30E-04 in the lower percentage doping range , decreases to minimum in the subsequent percentages then rises to maximum of 4.89E-04 in the higher percentage doping range.

From figure 4.178, the magnetic saturation of free layer for AgCoO₂ is directly proportional to the percentage doping with cobalt in the lower percentage doping range reaching a peak value of 8.01E-04 then decreases to minimum of 7.32E-04 in the higher percentage doping range.

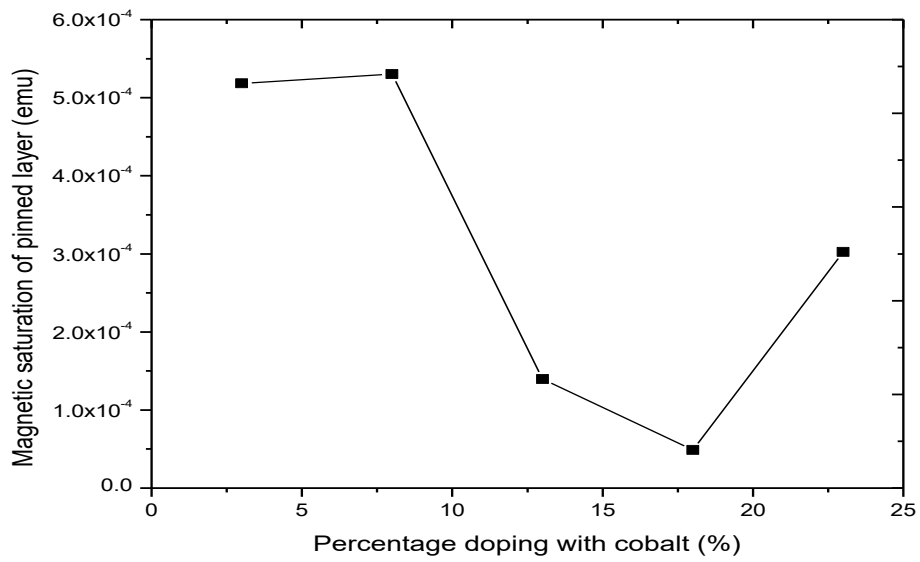


Figure 4.177: Variation of magnetic saturation of pinned layer with percentage doping with cobalt for AgCoO₂ nanofilm

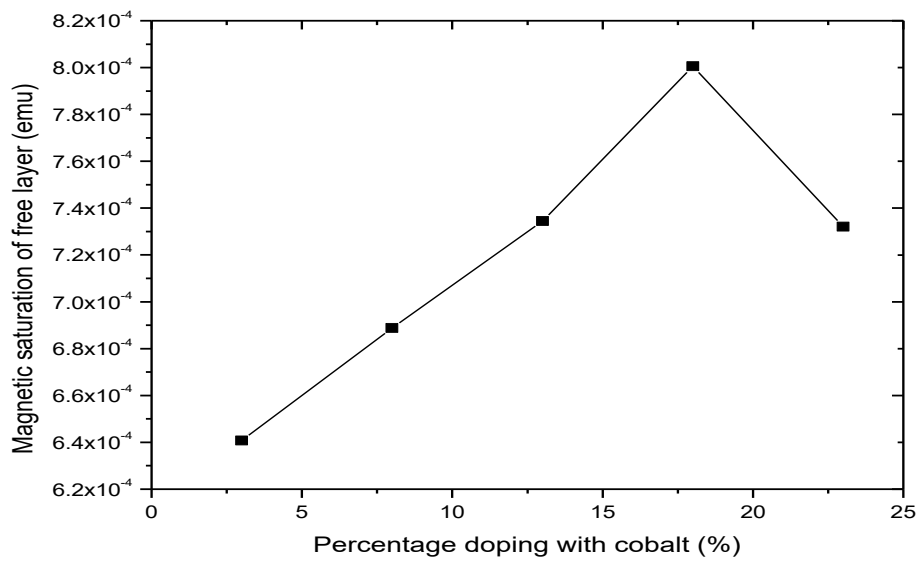


Figure 4.178: Variation of magnetic saturation of free layer with percentage doping with cobalt for AgCoO₂ nanofilm

4.4.9 Variation of magnetization with applied voltage at various percentages doping for AgCoO₂ nanofilms

Figure 4.179 shows that slope of the graph is 141.67, therefore magnetic susceptibility of 3% doped film is 141.67. From figure 4.180, slope of the graph is 144.33, therefore magnetic susceptibility of 8% doped film is 144.33. As shown in figure 4.181, slope of the graph is 147.00, therefore magnetic susceptibility of 13% doped film is 147.00. From figure 4.182, slope of the graph is 147.67, therefore magnetic susceptibility of 18% doped film is 147.67. Figure 4.183 shows that slope of the graph is 149.00, therefore magnetic susceptibility of 23% doped film is 149.00. As shown in figure 4.184, magnetic susceptibility of the film increases as percentage cobalt dopant increases. The magnetic saturation of the films are 640.752E-6emu for 3% doped, 688.791E-6emu for 8% doped, 734.449E-6emu for 13% doped, 800.587E-6emu for 18% doped and 732.098E-6emu for 23% doped. Since the film has no Fe³⁺ ion, it is not ferrimagnetic and by virtue of positive high magnetic susceptibility and magnetic saturation, the material is ferromagnetic. Applications as ferromagnetic semiconductor is as stated in 4.1.10

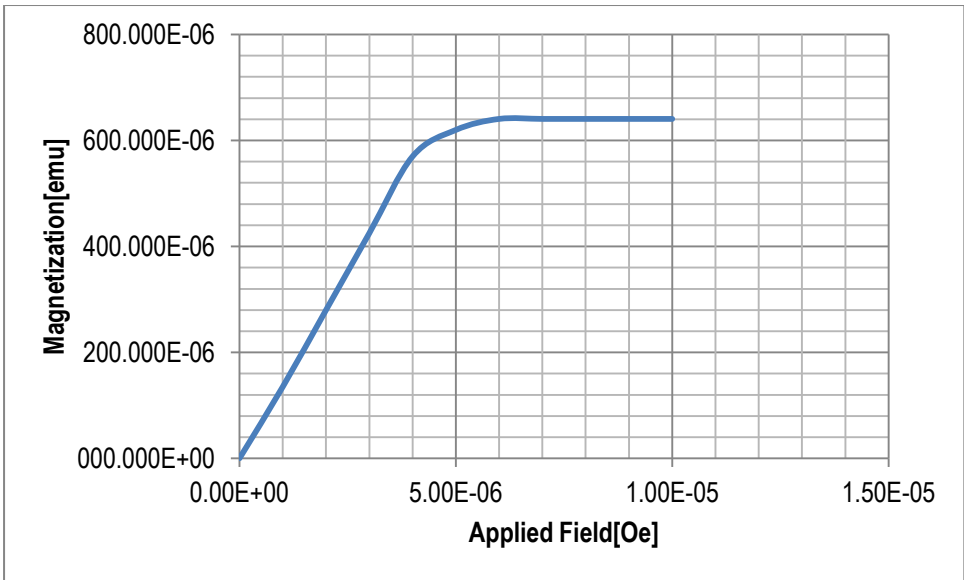


Figure. 4.179: Variation magnetization with applied voltage (3% doping)

Slope of the graph is 141.67

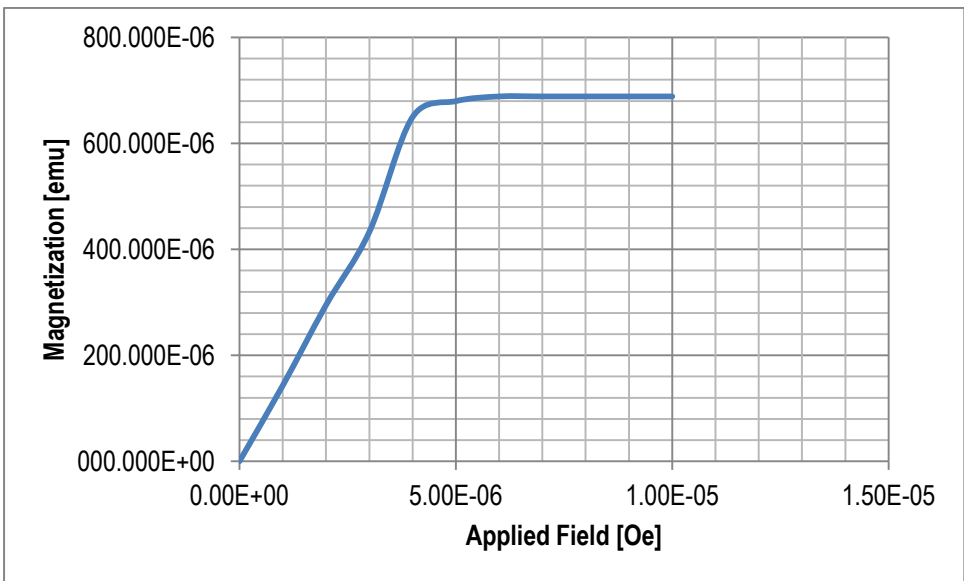


Figure. 4.180: Variation magnetization with applied voltage (8% doping)

Slope of the graph is 144.33

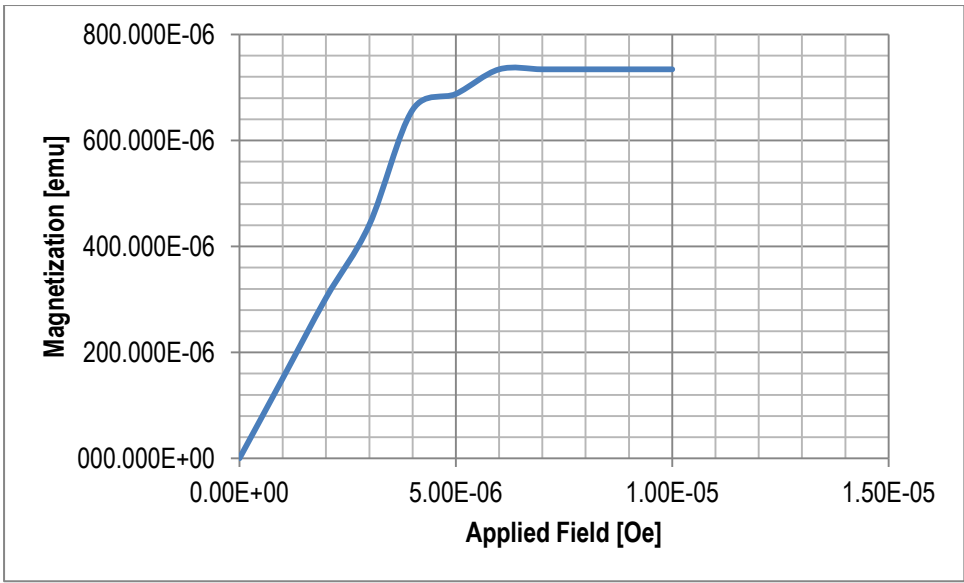


Figure. 4.181: Variation magnetization with applied voltage (13% doping)

Slope of the graph is 147.00

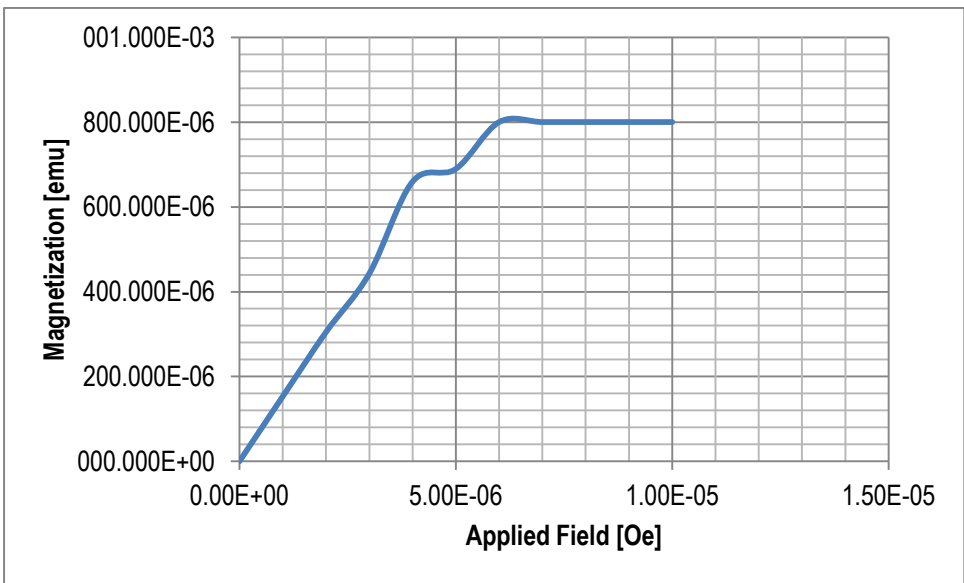


Figure. 4.182: Variation magnetization with applied voltage (18% doping)

Slope of the graph is 147.67

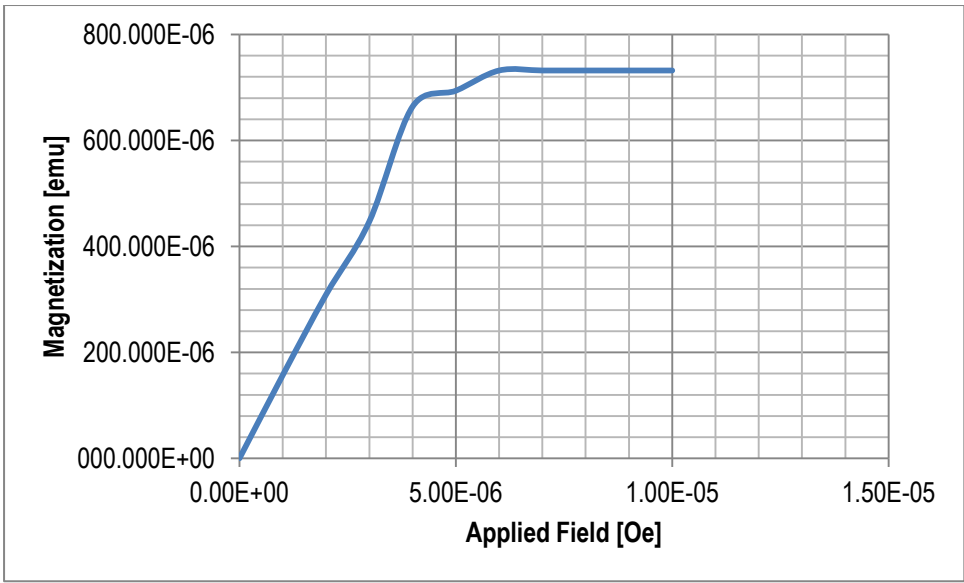


Figure. 4.183: Variation magnetization with applied voltage (23% doping)

Slope of the graph is 149.00

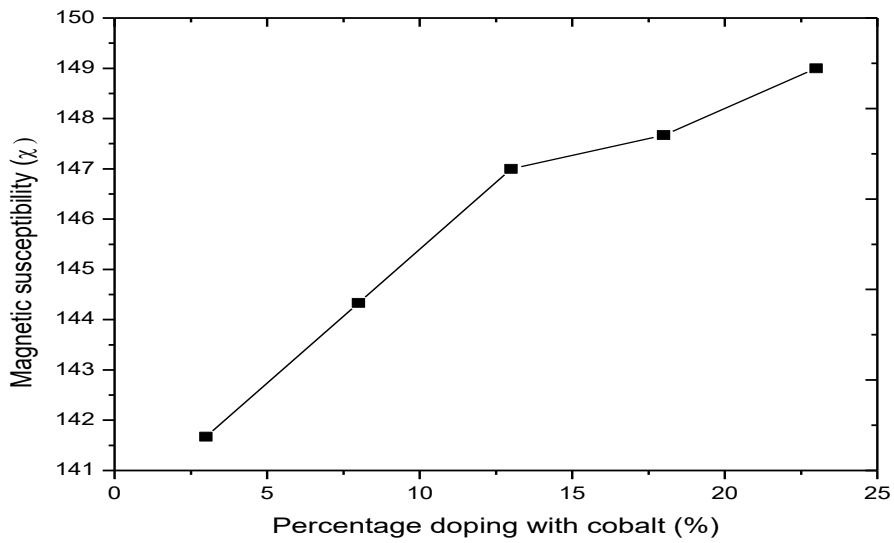


Figure 4.184: Variation of magnetic susceptibility with percentage cobalt dopant for AgCoO₂ nanofilm.

4.4.10 Compositional analysis

Table 4.8 shows that as the mass of cobalt dopant increases, mass of host metallic element(silver) decreases.

Table 4.8: Compositional analysis for AgCoO_2 at various percentage doping with cobalt

Sample	Percentage doping (%)	Ag	O	Co
N40	3	90.3103	6.8966	2.7931
N41	8	85.6550	6.8967	7.4483
N42	13	80.9999	6.8959	12.1042
N43	18	76.3462	6.8952	16.7586
N44	23	71.689	6.8961	21.4149

CHAPTER 5

SUMMARY, CONCLUSIONS AND RECOMMENDATION FOR FURTHER STUDIES

5.1 Summary

Cobalt doped nanofilms of NiCo_2O_4 , MgCo_2O_4 , CdCo_2O_4 , AgCoO_2 were grown by electrodeposition method. Percentage doping was varied from 3% to 23%, deposition voltage varied from 8.5V to 14.5V for NiCo_2O_4 , 7V to 13V for MgCo_2O_4 , CdCo_2O_4 and 0.1V to 2V for AgCoO_2 . Deposition time was varied from 5mins to 25mins for NiCo_2O_4 , MgCo_2O_4 , CdCo_2O_4 and 15s to 75s for AgCoO_2 .

Results of effect of percentage doping on optical properties show that bandgap is inversely proportional to percentage doping with cobalt for NiCo_2O_4 , MgCo_2O_4 , CdCo_2O_4 and inversely proportional in case of AgCoO_2 . Absorbance, reflectance, refractive index, extinction coefficient, complex dielectric constant and optical conductivity of NiCo_2O_4 , MgCo_2O_4 , CdCo_2O_4 films are directly proportional to percentage doping with cobalt, deposition voltage and deposition time but in case of AgCoO_2 they are directly proportional to deposition voltage and deposition time but inversely proportional to percentage doping with cobalt. Transmittance of NiCo_2O_4 , MgCo_2O_4 and CdCo_2O_4 films are inversely proportional to percentage doping with cobalt, deposition voltage and deposition time but in case of AgCoO_2 it is inversely proportional to deposition voltage and deposition time but directly proportional to percentage doping with cobalt. Thickness of the films is directly proportional to percentage doping with cobalt, deposition voltage and deposition time for NiCo_2O_4 , MgCo_2O_4 and CdCo_2O_4 but in case of AgCoO_2 it is directly proportional to deposition voltage and deposition time and inversely proportional to percentage doping with cobalt.

5.2 Conclusions

Magnetic oxide semiconductor nanofilms of NiCo_2O_4 , MgCo_2O_4 , CdCo_2O_4 , AgCoO_2 could be grown by electrodeposition method. Absorbance, reflectance, refractive index, extinction coefficient, complex dielectric constant and optical conductivity of NiCo_2O_4 , MgCo_2O_4 , CdCo_2O_4 films are directly proportional to percentage doping with cobalt, deposition voltage and deposition time but in case of AgCoO_2 they are directly proportional to deposition voltage and deposition time but inversely proportional to percentage doping with cobalt. Transmittance of NiCo_2O_4 , MgCo_2O_4 and CdCo_2O_4 films are inversely proportional to percentage doping with cobalt, deposition voltage and deposition time but in case of AgCoO_2 it is inversely proportional to deposition voltage and deposition time but directly proportional to percentage doping with cobalt. The bandgaps of the films are inversely proportional to percentage doping with cobalt except for AgCoO_2 where it is directly proportional. In case of NiCo_2O_4 , MgCo_2O_4 , CdCo_2O_4 , thickness of the films is directly proportional to percentage doping with cobalt, deposition voltage and deposition time except for AgCoO_2 where it is inversely proportional percentage doping with cobalt and directly proportional to deposition voltage and deposition time.

The films which are ferromagnetic have both optoelectronic and magneto electronic applications.

5.3 Contributions to knowledge

This research on growth of NiCo_2O_4 , MgCo_2O_4 , CdCo_2O_4 and AgCoO_2 nanofilms by electrodeposition method and study of their optical and magnetic properties are new areas of study.

5.4 Recommendations for further studies

As a way of obtaining in-depth knowledge of the doped semiconductors, we recommend as follows;

1. That further research be carried out to determine the electrical/electronic properties of the . doped semiconductors , (whether N type, P type, degenerate, isoelectronic trap)
2. That the effect of doping on the electrical properties of the semiconductors be studied
3. That the effect of temperature variation on the magnetic properties be studied.
4. That the effect of doping on the thermal properties of the semiconductors be researched

REFERENCES

- Andreas, S. (2012). Transparent conducting oxide –An up-to-date over view. *Materials*,**5**,661-683
- Animalu, A.O.E.(1977). Intermediate quantum theory of crystalline solids. New Jersey, Prentice-Hall, Inc., Eaglewood Cliffs, 231
- Archid, M. A., Ayyaz, M., Amir, S., Hafiz, M.A., Asgher, S. N. and Hussain, H. S. (2012). Doped metal oxide(ZnO) and photocatalysis-a review. *Journal of Pakistan Institute of Chemical Engineers*,**40**(1),11-19
- Atsufumi, H. (2015). Shift from electronics to spintronics opens up possibilities of faster data.*The Conversation*,1-2
- AZO optics (2014). Optical transmittance-Definition and formular.*Optics*, 101
- Balkanski, M. and Wallis, R.F. (2000). Semiconductor physics and applications. New York, Oxford University press, 487
- Banerjee, A.N. and Chattopadhyay, K.K. (2005). Recent developments in the emerging field of crystalline p-type transparent conducting oxide thinfilms. *Science Direct, Progress in Crystal Growth and Characterization of Materials*,**50**,52-105
- Beauchamp, W. T. and Tuttle-Hart, T. (1995). UV/IR reflecting solar cell cover. *Patent*,US5449413 A
- Beevi, M. M., Anusuya, M. and Saravanan, Y. (2010). Characterization of CdO thin films prepared by silar deposition technique. *International Journal of Chemical Engineering and Applications*,**1**,(20),151-154
- Begam Rigana, M., Rao Madhusudhana, N., Joshi, G. M., Kaleemulla, S., Shobana, M., Sai Krishna, N. and Kuppan, M.(2013). Structural, optical, and magnetic properties of Co doped CdTe alloy powders prepared by solid-state reaction method. *Advances in Condensed Matter Physics*, **2013** , Article ID 218659, 5
- Beneq(2010). TCO coatings for Architectural and solar glass. Beneq aerosol,www.beneq.com, 1-4
- Benramache, S., Belahssen, O. and Temam, H. B. (2014). Effect of bandgap energy on the electrical conductivity in doped ZnO thin film. *Journal of Semiconductors*,**35**(7) 20-25
- Bhosale, C.H., Kambale, A.V., Kokate, A.V. and Rajpure, K.Y.(2005). Structural, Optical and electrical properties of chemically sprayed CdO thin film. *Material Science B*,**122**,(1),67-71
- Biljana, P., Tanja, K., Metodija, N. and Ivan, G. (2000). A solution growth route to nanocrystalline NiO thin films. *Applied Surface Science*,**165**,(4),271-278

- Li, H., Winget, P. and Bredas, J. (2014). Transparent Conducting oxides of relevance to organic electronics ,electronic structures of their interfaces with organic layers, Centre for Interface Science; Solar Electric Materials. *Chemical Materials*,**26**(1), 631-646
- Bremner, S.(2009). ELEG620, Solar Electric Systems University of Delaware, *ECE Spring* .1-4
- Cemre, A. (2013). Electrodeposition of ZnO thin films: Effect of vanadium doping. MSc thesis, School of Natural and Applied Sciences, Middle East Technical University.
- Choi, H. (2012). Vapour-liquid-solid growth of semiconductor nanowires (Semiconductor nanostructures for optoelectronic devices, Nano Science and Technology). Berlin Heidelberg, Springer-Verlag, 36
- Chopra, K. L. L. and Das, S.R. (1983). Thin film solar cells. New York, Plenum press, 560
- Chun-Hai, Y., Chao, L., Don-Yan, T. and Yin-Ping, Z.(2012). Annealing effects on structural and magnetic properties of Tb and Cr co-implanted AlGaIn. *Frontiers of Materials Science*,**6**(4),366-370
- Chuu, D., Chang, Y. and Hsiesh, C. (1997). Growth of CdMnS films by pulsed laser evaporation. *Thin Solid Films*, **304**, 28-35.
- Campos-Gonzalez, E., Guillén-Cervantes, A., Santoyo-Salazar, J., Zelaya-Angel, O., Ramírez-Velázquez, L. E., Santos-Cruz, J., Mayén-Hernández, S.A., de Moure-Flores, F., Olvera, M. de la L. and Contreras-Puente, G. (2015). Growth of CdO films from CdO films by chemical bath deposition: Influence of the concentration of cadmium precursor. *Superficies Y Vacío*, **28**(1) 25-29,
- Cohen and Chelikowsky, (2012). Electronic structure and optical properties of semiconductors, Springer Science and Business Media, 264
- Coutts, T. J., Mason, T.O., Perkins, J. D. and Ginley, D. S.(1999).Transparent Conducting Oxides: Status and Opportunities in Basic Research. *Electrochem. Soc. Proc.*, **99**, 11
- Creighton, J. R. and Ho, P. (2001). Introduction to chemical vapor deposition(CVD). *ASM International; Chemical Vapor Deposition(#06682G)*. www.asminternational.org, 1-10
- Cruz, M. R. A., Zarzota, G. O., Castanon, G. A. M. and Martinez, J. R. (2012).Thin films from different material obtained by the sol-gel method; Study of the morphology through atomic force microscopy (AFM). *Current Microscopy Contributions to Advances in Science and Technology* (A. Mendez-Vilas, Ed). 1370-1376
- Cubillas, P. and Anderson, M.W. (2010). Synthesis mechanism: Crystal growth and nucleation. In Cejka, J.(Ed.), *Zeolites and Catalysis: Synthesis, Reactions and Applications*,1-55, Weinheim, Germany,Wiley-Vch Verlag GmbH & Co. KGaA.

- Das-Sarma, S. (2001). Spintronics. *American Scientist*, **89**, 516-523
- Desai, J.D., Min, S. and Joo, O. (2006). Spray pyrolytic synthesis of large area NiO_x thin films from aqueous nickel acetate solutions. *Applied Surface Science*, **253**,(4),1781-1786
- Detlef, K. (2014). Electronic materials with wide bandgap: recent developments. *IUCrJ*, **1**(pt 5), 281-290
- Diachenko, O. V., Opanasuyk, A. S., Kurbatov, D. I., Opanasuy, N.M., Kononov, O.K. Nam, D. and Cheong, H. (2016). Surface morphology, structural and optical properties of MgO films obtained by spray pyrolysis technique. *Acta Physica Polonica A*, **130**(3), 805-810
- Dinesh, C. S., Subodh, S., Vijay, Y.K. and Sharma, Y.K. (2013). Preparation and characterization of the chromium doped ZnTe thin films. *Advanced Materials Letters*, **4**(1),68-703
- Djaja, N. F., Montja, D. A. and Saleh, R. (2013).The Effect of Co Incorporation into ZnO Nanoparticles. *Advances in Materials Physics and Chemistry*, **3**, 33-41
- Dufour, J. (2006). An Introduction to metallurgy(5th edition).Cameron, **IX**, 12
- Ebru, G., Tayyar, G., Deniz, C., Abdullah, C. and Ekmel, O.(2014). Co doping induced structural and optical properties of sol–gelprepared ZnO thin films. *Applied Surface Science*, **318** , 309–313
- Edmonds, K.W., Freeman, A.A., Farley, N.R.S., Champion, R.P., Foxon, C.T., Gallagher, B.L., Van der Laan G., Johal, T.K. and Arenholz, E.(2006). Electronic structure and magnetism in dilute magnetic semiconductors. *Advanced Light Source*, Berkeley lab. US Department of Energy. 1-2
- Eisberg, R. and Resnick, R. (1974). Quantum Physics of atoms, molecules, solids, nuclei and particles. New York, John Wiley & sons, 545
- Erhaima, M. K., AL-ansari, R. A. and Habubi, N. F. (2010). Structural and optical properties of cobalt-doped zinc oxide thin films prepared by spray pyrolysis technique. *Baghdad Science Journal*, **7**(1), 1-8
- Ezekiel, D. D. and Abdullahi, M.F. (2013). Synthesis, characterization and comparative study of copper and zinc metal organic frame works. *Chem. Sci. Trans.*, **2**(4), 1386-1394
- Ezema, F.I., Ekwealor, A.B.C. and Osuji, R.U.(2008). Optical properties of chemical bath deposited nickel oxide (NiO_x) thin films. *Superficies Y Vacio*, **21**,(1),6-10
- Ezeokoye, B.A., Ezeokoye, V.A., Offor, P.O. and Utazi, S.C.(2013). Synthesis, structural and optical characterizations of cadmium oxide (CdO) thin films by chemical bath deposition (CBD) technique. *International Journal of Physical Sciences*, **8**(31), 1597-1601.

- Ezhil, R. A. M., Nehru, L.C., Jayachandran, M. and Sanjeeviraja, C.(2007). Spray pyrolysis deposition and characterization of highly (100) oriented MgO thin films. *Crystal Research and Technology Journal*,**42**,(9), 867-875
- Ezhil R. A. M., Som T., Ganesan V., Jayachandran M., Selvan G., Swaminathan V. and Sanjeeviraja C. (2008). Tailoring optical and electrical properties of MgO thin films by 1.5 MeV H⁺ implantation to fluencies. *Nuclear Instruments and Methods in Physics Research Section B: Beam Interactions with Materials and Atoms*,**266**(11),2564-2571
- Fraden, J. (2004). Hand book of modern sensors. New York, Springer-Verlag Inc. 589
- Furdyna, J., Aggarwal, R. L., Awschalom, D. D., Ehrenreich, H., Geschwind, S., Gunshor, R. L. and Wolff, P. A (1991). Diluted magnetic semiconductors. Washington DC, National Academy press, 29
- Gaur, R.K. and Gupta, S.L.(2007). Engineering physics. New Delhi, Dhanpat Rai publications (P) LTD, 1-64.19
- Girjesh, S., Shrivastava, S. B. and Ganesan, V. (2013). Effect of Co doping on structural, morphological, electrical and optical properties of nanocrystalline zinc oxide films. *Journal of Chemical Engineering and Materials Science* . **4**(1), 1-6
- Gomaa, M. M., Boshta, M., Farag, B. S. and Osman, M. B. S. (2016). Structural and optical properties of nickel oxide thin films prepared by chemical bath deposition and by spray pyrolysis techniques. *Journal of Materials Science: Materials in Electronics*, **27**(1), 711-717
- Gosavi, S.R., (2010). Growth, structural, optical and electrical properties of Cu_{2-x}Se semiconductor thinfilms for photovoltaic application. PhD thesis, Department of Physics, Dr Babasaheb Ambedkar Marathwada University, Aurangabad-431004.
- Guar, R. K. and Gupta, S. L. (2001). Engineering Physics. New Delhi, Dhanpat Rai Publications,1470
- Gulebagian, S.E., Dogan, E.K., Aycibin, M., Secut, M.N., Erdinc, B. and Akkus, H., (2014). The bowing parameters of Ca_xMg_{1-x}O ternary alloys. *Journal of Modern Physics*, **5**, 1546-1551
- Guojian, L., Huimin, W., Qiang, W., Yue, Z., Zhen, W., Jiaojiao, D. and Yonghui, M. (2015). Structure and properties of Co-doped ZnO films prepared by thermal oxidization under a high magnetic field. *Nanoscale Research Letters* ,**10**(112), 1-8
- Guojun, M. (2010). Chemical bath deposition and electrodeposition of epitaxial semiconductor materials for application in photovoltaic devices. PhD thesis, Department of Chemistry, Missouri University of Science and technology.
- Guthrie, J. M. and Ferguson, J. R. (2015). Overview of X-ray fluorescence. *Archaeometry Laboratory, University of Missouri Research Reactor*,1-5

- Guzeldir, B., Saglam, M. and Ates, A.(2012). Deposition and Characterization of CdS, CuS and ZnS thin Films Deposited by SILAR Method. *Acta Physica Polonica A*,**121**(1),33-34.
- Hakim, A., Hossain, J., and Khan, K.A.(2009). Temperature effect on the electrical properties of undoped NiO thin films. *Renewable Energy*,**34**,(12),2625-2629
- Harbeke, G.(1972). Band edge Excitons in PbI: A puzzle. *Physical Review Letters*,**28**,(24),1567-1570
- Harris, I. R. and Williams, A. J. (2009). Magnetic materials. In Rawlings, R. D. (Ed.), *Materials Science and Engineering*, Vol. II, (49-83), Oxford United Kingdom, Eolss publishers Co. Ltd,
- Hieronymi, M. (2016). Polarized reflectance and transmittance distribution functions of the ocean surface. *Optics Express*,**24**(14), A1045-A1068
- Hornyak, G.L., Moore, J. J., Tibbals, H. F. and Dutta, J. (2009). *Fundamentals of nanotechnology*. London, CRC press, 786.
- Hong-Liang, F., Xiao-Yong G., Zheng-Yuan, Z. and Jiao-Min, M. (2010). Study on the crystalline structure and the thermal stability of silver oxide films deposited by using direct current reactive magnetron sputtering method. *Journal of Korean Physical Society*,**56**,(4),1176-1179
- Honsberg, C. and Bowden, S. (2014). Absorption coefficient. PV Education.org,1-2
- MEMSnet (2013).Thin film deposition processes. *MEMSnet*,1-5
- Hufner, S.(1994). Electronic structure of NiO and related 3d-transition metal compounds. *Advanced Physics*,**43**,183-356
- Islam, M.A., Hossain, M.S., Aliyu, M.M., Yusuf, S., Razykov, T., Sopian, K. and Amin, N.(2013).Structural, optical and electrical properties of in doped CdS thin films prepared from Co-sputtering technique. *Latest Trends in Renewable Energy and Environmental Informatics*, ISBN: 978-1-61804-175-3
- Irwin, D. M., Buchholz, B. D., Hains, A. W., Chang Robert, P.H. and Marks, T. J.(2008). p-Type semiconducting nickel oxide as an efficiency-enhancing anode interfacial layer in polymer bulk-heterojunction solar cells. *Proceedings of National Academy of Science, U S A.*;**105**(8): 2783–2787
- Ivill, M., Pearton, S. J., Rawal, S., Leu, L., Sadik, P., Das, R., Hebard, A. F., Chisholm, M., Budal, J. D. and Norton, D. P. (2008). Structure and magnetism of Cobalt doped ZnO thin films. *New Journal of Physics*,**10**, 1-21
- Jlassi, M., Sta, I., Hajji, M. and Ezzaouia, H. (2014). Synthesis and characterization of nickel oxide thin films deposited on glass substrates using spray pyrolysis. *Applied Surface Science*, **308**,199-205

- John, F. S. (1996). Role of magnetic susceptibility in magnetic resonance imaging: MRI magnetic compatibility of the first and second kinds. *Medical Physics*, **23**(6),1-36
- Jones, A. C. and O'Brien, P. (1997). CVD of compound semiconductor precursor for synthesis, development and application, Weinheim Germany, VCH Verlagsgesellschaft mbH, D-69451, 329
- Kamalianfar, A., Halim, S.A., Behzad, K., Mahmoud, G.N., Navasery, M., Fasih, U.D., Zahedi, J.A.M., Lim, K.P., Chen, S.K. and Sidek, H.A.A.(2013). Effect of thickness on structural, optical, and magnetic properties of Co doped ZnO thin film by pulsed laser deposition. *Journal of Optoelectronics and Advanced Materials*, **15**,(3-4),239-243
- Katarzyna, S. (2014). Optical properties of semiconductors. Centre for Photoconversion and catalysis, University of Wyoming, www.uwyo.edu/cpac/short-course.html, July 3
- Kayo, M. (2014). What are the different types of semiconductor application. *WiseGeek*, 1
- Kern, W. and Schueggraf, K. K. (2002). Deposition technologies and applications: Introduction and overview. In Krishna, S. (Ed). Handbook of thin film deposition (2nd Ed.), (11-43), New York, Noyes publications
- King, P.D.C. and Veal, T.D. (2011). Conductivity in transparent oxide semiconductors. *Journal Of Physics-Condensed Matter*, **23** (33),4214-4219
- Kittel, C. (2005). Introduction to solid state physics. Singapore, John Willey and sons Inc., 199
- Koenraad, P.M. and Flatte, M.E. (2011). Single dopants in semiconductors. *Nature Materials* , **10**,(2), 91-100
- Kumar N., Parihar U., Kumar R., Patel K.J., Panchal C.J. and Padha N. (2012). Effect of film thickness on optical properties of tin selenide thin films prepared by thermal evaporation for photovoltaic applications. *American Journal of Materials Science*, **2**(1), 41-45
- Kuryliszyn, I., Wojtowicz, T., Liu, X., Furdyna, J. K. and Dobrowolski, W. (2002). Transport and magnetic properties of LT. annealed Ga_{1-x}Mn_xAs. *Acta Phys.Pol., A*, **102**(4-5),659-663
- Lee, K. H., Kim, H. J., Choi, J. C., Park, H. L. and Kim, T. W. (2004). Thermal annealing effects on the magnetic properties of (Ga_{1-x}Mn_x)As thin films grown on GaAs (1 0 0) substrates. *Journal of Crystal Growth*, **270**(1-2),174-178
- Lehraki, N., Aida, M.S., Abed, S., Attaf, N., Attaf, A. M. and Poulain, M. (2012). ZnO thin films deposition by spray pyrolysis: Influence of precursor solution properties. *Current Applied Physics*, **12**(5),1283-1287
- Lorenzo, M. (2013). Molecular beam epitaxy(MBE). In Robert, M. (2013). Silicon based thin film solar cells, (81-107), www.benthamsciences.com/ebooks/978/608055180

- Lyons, J. L., Janotti, A. and Van de Walle, C.G (2013). Theory and Modelling of Oxide Semiconductors. In Bengt, G. S., Stephen, J. P., Chennupati, J.(Eds.), Semiconductors and semimetals-vol.88, Oxide Semiconductors,(1-38), USA, Elsevier Inc.
- Mathieu, M. (2005). Magnetic and transport properties of $Ga_{1-x}Mn_xAs$ diluted magnetic semiconductors. PhD thesis, Katholieke Universiteit, Lauen
- Minami, T. (2005). Transparent conducting oxide semiconductors for transparent electrodes. *Semiconduc. Sci. and Technol.*, **20**(4), S35
- Moses, P. G. and Van de walle, C.G.(2010). Band bowing and band alignment in InGaN alloys. *Applied Physics Letters*,**96**, 021908,23-27
- Moss, T. S.(1961). Optical absorption edge in Ga As and its dependence on electric field. *Journal of Applied Physics*,**32**(10),2136- 2139
- Bakr, N. A., Funde, A.M., Waman, V.S., Kamble, M.M., Hawaldar, R.R., Amalnerkar, D.P., Gosavi, S.W. and Jadkar, S.R. (2011). Determination of the optical parameters of a-Si:H thin films deposited by hot wire–chemical vapour deposition technique using transmission spectrum only. *Pramana Journal of Physics*,**76**(3),519–531
- Nadana, S., Shanmugam, C., Natesan, K., Kannadasan, S. and Viruthagiri, G. (2013). Effect of annealing on the ZnS nanocrystals prepared by chemical bath precipitation method. *Journal of Nanometals*,**2013**, Article ID: 351798, 1-7
- Nadeem, M.Y. and Ahmed, W. (2000). Optical properties of ZnS thin films. *Turkish Journal of Physics*,**24**(5), 651-659
- National Nanotechnology Initiative,(2016). Benefits and applications. Nanotechnology and you, 1-3
- Nelkon, M. and Parker, P. (1982). Advanced Level Physics. London, Heinemann Educational Books Ltd., 948
- Nemade, K. R. and Waghuley, S.A.(2014). Synthesis of MgO nanoparticles by solvent mixed spray pyrolysis technique for optical investigation. *Hindawi Publishing Corporation International Journal of Metals* <http://dx.doi.org/10.1155/2014/389416>,**2014**, 1-4
- Nirmala, M. and Anukaliani, A. (2010). Structural and optical properties of undoped and Co doped ZnO nanostructured thin films. *Suranaree J. Sci. Technol.* **18**(1),81-88
- Nisha, T. J., Raveendran, R., Vaidyan, V. A. and Chithra, P.G.(2008). Optical, electrical and structural studies of nickel-cobalt oxide nanoparticles. *Indian Journal of Engineering and Material Sciences*,**15**,489-496

- Nwanya, A. C., Ugwuoke, P. E., Ezekoye, B. A., Osuji, R.U. and Ezema, F. I. (2013). Structural and Optical Properties of Chemical Bath Deposited Silver Oxide Thin Films: Role of Deposition Time. *Advances in Materials Science and Engineering* **2013**,1-8
- Muresan, L. M. and Varvara, S. C. (2005). Levelling and Brightening Mechanisms in Metal Electrodeposition. In Nunez, M. (Ed.), *Metal Electrodeposition*, (1-45), New York, Nova Science Publishers Inc.
- Okafor, P. C., Ekpunobi, A. J. and Ekwo, P.A. (2015). Effect of manganese percentage doping on thickness and conductivity of zinc sulphide nanofilms prepared by electrodeposition method. *International Journal of Science and Research (IJSR)*, **4**(12), 275-2279
- Pandiaraman, M., Soundararajan, N. and Vijayan, C. (2011). Effect of thickness on the optical band gap of Silver telluride thin films. *Journal of Ovonic Research*, **7**(1), 21 – 27
- Park, C., Kim, J., Lee, K., Oh, S. K., Kang, H. J. and Park, N. S. (2015). Electronic, optical and electrical properties of nickel oxide thin films grown by rf magnetron sputtering. *Applied Science and Convergence Technology*, **24**(3),72-76
- Parkin, S., Wolf, S. A., Harris, J.S., Zhang,S. and Smith, D.J.(2007). The applications of spintronics. *IBM* 100, 03,1-5
- Patel, K. J., Desai, M.S., Panchal, C.J. and Rehani, B. (2011). P-Type transparent NiO thin films by e-beam evaporation techniques. *Journal of Nano-Electron.Phys.***3**,*(1)*,376-382
- Patil, P. S., Bharat, N., Naik, D. B. and Shrivastava, V. S. (2011). Synthesis and characterization of Al doped CdS thin films grown by chemical bath deposition method and its application to remove dye by photocatalytic treatment. *Chalcogenide Letters*,**8** (2),117-121
- Patil, P.S. and Kadam, L.D.(2002). Preparation and characterization of spray pyrolyzed nickel oxide (NiO) thin films. *Applied Surface Science*,**199**,*(1)*, 211-221.
- Pathan, H. M., Sankapal, B. R., Desai, J. D. and Lokhande, C. D. (2002). Preparation and characterization of nanocrystalline CdSe thin films deposited by SILAR method. *Materials Chemistry and Physics*,**78**,11-14
- Perkampus, H. H. (1992). *UV-VIS Spectroscopy and its applications*. New York. Springer Verlag, 237
- Proetto, C. R. (1996). Electronic structure of delta-doped semiconductors, In Schubert, E. F.(Ed.), *Delta doping of semiconductors*, (23-68), Great Britain, Cambridge University press,
- Pushpalatha, H. L., Bellappa, S., Narayanaswamy, T. N. and Ganesha, R. (2014). Structural and optical properties of CdS thin film obtained by chemical bath deposition and effect of annealing. *Indian Journal of Pure and Applied Physics*,**52**, 545-549

- Pu-Xian, G., Paresh, S., Haiyong, G., Caihong, L., Yanbing, G., Wenjie, C., Kuo-Ting, L., Gregory, W., Zhonghua, Z., Zheng, R. and Hui-Jan, L. (2012). Hierarchical assembly of multifunctional oxide-based composite nanostructures for energy and environmental applications. *International Journal of Molecular Sciences*, **13**, 7393-7423
- Rafael, P., Araceli, G. and Olivier, P. (2005). Er-doped ZnO thin films. *Journal of Applied Physics*, **97**, 054905-054908
- Ramana, C.V., Smith, R.J. and Hussain, M.O. (2003). Grain size effects on the optical characteristics of pulsed-laser deposited vanadium oxide thin films. *Phys. Stat. Sol. (a)* **199**,(1), R4–R6 (2003) / DOI 10.1002/pssa.200309009
- Reddy, M. H. P. and Uthanna, S. (2015). Substrate temperature influenced structural and optical properties of RF magnetron sputtered pure and copper doped silver oxide thin films. *International Journal of ChemTech Research*, **7** (3), 1079-1084
- Reynard, D.L. and Andrew, A. (1996). Improvement of silicon solar cell performance through the use of thin film coatings. *Applied Optics Journal*, **5**, 23-28
- Rubby, D. and Suman, P. (2011). Comparison of optical properties of bulk and nano crystalline thin films of CdS using different precursors. *International Journal of Material Science*, **1**(1), 35-40
- Salik, J., Ferrante, J., Honey, F. and Hoffman, R. (1986). Analysis of plasma nitride steels. *NASA Technical Memorandum*, **89815**, 1-11
- Saraiva, M. (2012). Sputter deposition of MgO thin film-effect of cation substitution. PhD thesis, University of Gent. 113
- Sardela, M. R. (2014). X-Ray diffraction and reflectivity. In Sardela, M. R. (Ed.), *Practical materials characterization*, (1-42), New York, Springer Science + Business Media, 237
- Saroja, G., Vasu, V. and Nagarani, N. (2013). Optical studies of Ag₂O thin film prepared by electron beam evaporation method. *Open Journal of Metal*, **3**, 57-63
- Sato, K., Bergquist, L., Kudrnovsky, J., Dederichs, P.H., Erickson, O., Turek, I., Sanyal, B., Bouzerar, G., Katayama-Yoshida, H., Dinh V.A., Fukushima, T., Kizaki, H. and Zeller, R. (2010). First principles theory of dilute magnetic semiconductors. *Review of Modern Physics*, **82**(10), 1633-1638
- Scheffler, P., Tkatchenko, A. and Rinke, P., (2012). Theoretical material science. Fritz Haber Institute of the max Planck Society, Berlin, chapter 8. (Access; Chapter 8: http://www.itp.tu-berlin.de/fileadmin/a3233/upload/SS12/TheoFest2012/kapitel/chapter_8.pdf)
- Schubert, E. F. (1990). Delta doping of III-V compound semiconductors; Fundamentals and device applications. *Journal of Vacuum Science Technology*, **A8**(3), 2980-2996

Scribd,(2013). Basics of Semiconductors.(For access use;
<https://www.scribd.com/document/203128744/Basics-of-Semiconductors>

Shahedipour-Sandvik, F., Schubert, E. F. and Bell, D. L.(Eds.), (2009). Compound semiconductors for energy application and environmental sustainability.**1167**, *Materials Research Society (MRS) Symposium Proceedings*

Shailaja, J., Nagabhushana, H., Mrudula, K., Naveen, C.S., Raghu, P. and Mahesh, H. M. (2014). Concentration dependent optical and structural properties of Mo doped ZnTe thin films. *International Journal Of Electrochemical Science*, **9**, 2944 – 2954

Sharma, P. and Katyayal, S.C. (2007). Determination of optical parameters of a-(As₂Se₃)₉₀Ge₁₀ thin film. *Journal of Physics D*, **40**,(7), article 038, 2115–2120

Seo, D. and Hoffmann, R. (1999). Direct and indirect bandgap types in one dimensional conjugated or stacked organic materials. *Theoretical Chemistry Accounts*,**102**,23-32

Simona, L. I., Patrick, C., Philippe, L. C. and Daniela, P. (2014). Antimicrobial Activity of Thin solid films of silver doped hydroxyapatite. *The Scientific World Journal* , **2014** (2014),ID 165351,1-8

Sinclair, I. R. (2001).Sensors and transducers(3rd Ed.). ebook, ISBN;978080516998, 256

Singh, T., Pandaya, D.K. and Singh, R. (2011). Electrochemical deposition and characterization of elongated CdO nano structures. *Journal of Material Science and Engineering B*,**176**,(12),945-949

Soares, J. A. N. T. (2014). Introduction to optical characterization of materials. In Sardela, M. R. (Ed.), Practical materials characterization,(43-92), New York, Springer Science + Business Media, 237

Spinu, L., Dodrill, B.C. and Radu, C. (2013). Magnetometry measurements. *Materials Characterization- Magnetism Technology International*, 1-4.

Shimadzu, Measurement of bandgap in compound semiconductors. Spectrophotometric analysis A428,1-2

Tempus (2012). Study of semiconductors by Uv-Vis spectroscopy. Department of Energy Physics, Belarusian State University.

Terasako, T., Fujiwara, T., Nakata, Y., Masakazu, Y. and Shirakata, S.(2013). Structural and optical properties of CdO nanostructures prepared by atmospheric pressure Chemical vapour deposition.*Thin Solid Films*, **528**,237-241

- Thakur, S., Kumar, J., Sharma, J., Sharma, N. and Kumar, P. (2013). Structural and optical study of nickel doped ZnO nanoparticles and thin films for dye sensitized solar cell applications. *Journal Of Optoelectronics And Advanced Materials* ,**15**,(7- 8), 989 – 994
- Tian, Y., Hu, S., Yan, S. and Mei, L. (2013). Oxide magnetic semiconductors: Materials, properties, and devices. *Chin. Phys. B*, **22**,(8), 088505-1--88505-19
- Tsymbal, E.Y. (2015). Section 15, magnetic properties of materials. *Physics* 927,1-12
- United States National Nanotechnology Initiative, Nanotechnology 101,Nano.gov.National Nanotechnology Initiative.
- U.S. Department of Energy (2013). Wide Bandgap Semiconductors: Pursuing the Promise. *Energy Efficiency & Renewable Energy*, 1-2
- Valyukh, I., Green, S., Arwin, H., Niklasson, G.A., Wackeigard, E. and Granqvist C.G. (2010). Spectroscopic ellipsometry characterization of electrochromic tungsten oxide and nickel oxide thin films made by sputter deposition. *Solar Energy Materials and Solar Cell*,**94**,(5),724-732
- Van de walley, C.G., McCluskey, M. D., Master, C.P., Romano, L.T. and Johnson, N.M. (1999). large and composition dependent bandgap bowing in $\text{In}_x\text{Ga}_{1-x}\text{N}$ alloys. *Material Science and Engineering B59*,274-278.
- Vossen, J. L. and Kern, W.(1978). Thin film processes. New York, Academic press, 67
- Wade, T. and Clochard, M. (2017). Moules et Electrodeposition. Laboratoire Des Solides Irradies, L'Ecole Polytechnique.1
- Wang, W. B., Yang, Y., Gil-Yanguas, A., Chang, N. N., Girolami, G. S. and Abelson, J. R.(2013). Highly conformal MgO thin films by low temperature chemical vapour deposition from $\text{Mg}(\text{H}_3\text{BNMe}_2\text{BH}_3)_2$ and water. *Journal of Applied Physics Letter*,**102**,(10),101605-101609
- Wen-Wei, L. and Yen-Kuang, K. (2002) . Band structures and bandgap bowing parameters of wurtzite and zinblende III-nitrides. In Yi, L. and Yoshiaki, N. (Eds), Semiconductor Lasers and Applications, *Proceedings of SPIE* ,**4913** , 2002 SPIE-0277-786X/02/\$15.00
- Wikipedia, (13th Sept., 2013, 14.33). Doping (Semiconductor)
- Wikipedia (12th January, 2014, 21.25). Semiconductor
- Wikipedia,(8th April, 2014, 20.28). Pulsed laser deposition
- Wikipedia, (27th June, 2014, 4.31). Quantum dot

- Wolf, S. A., Awschalom, D. D., Buhrman, R. A., Daughton, J. M., Molnar, S. V., Roukes, M. L., Chtchelkanova, A. Y. and Treger, D. M. (2001). Spintronics: A spin based electronics, vision for the future. *Science*, **294**, 1488-1495.
- Wikipedia, (30th March, 2017, 16.26). Characterization(materials science)
- Xing, Z., Erjia, L., Ramanujan, R.V. and Jingsheng, C.(2012). Effects of rapid thermal annealing on structural, magnetic and optical properties of Ni doped ZnO thin films. *Current Applied Physics*, **12**, 834-840
- Xiong, D., Zhou, S., Wang, Q. and Ren, X.(2008). First-principles investigation of BAs and $B_xGa_{1-x}As$ alloys. *Chinese Physics B*, **17** (8), 3062-05
- Xi-Yao, Z., Pan, X., Zhang, Q., Xu, B., Jiang, H., Liu, C., Gong, Q. and Wu, J. (2003). Synthesis of Silver Oxide nanoscale thinfilms and Photoactivated dynamic luminescence from their nanoparticles by vacuum evaporation and glow discharge oxidation. *Acta Physico-Chimica Sinica*, **19**, (03), 203-207
- Xin-Zheng, L. and Jian-Bai, X. (2002). Electronic structure and optical properties of quantum rods with wurtzite structure. *Physical Review B*, **66**, 1153160-1153166
- Xue, M. and Guo, Q. (2007). Layer by layer growth of polar MgO(111) ultra thin film. *Journal of Chemical Physics*, **127**, 054705-054710
- Yacobi, B.G. (2004). Semiconductor materials: An Introduction to basic principles. Kluwer , New York, Academic publishers, 227
- Youssif, M.I., Bahgat, A.A. and Ali, I.A.(2000). AC magnetic susceptibility technique for characterization of high temperature superconductors. *Egypt J.Sol.* **23**(2), 231-250
- Yun, F., Reshchikov, M.A. and He, L. (2002). Energy band bowing parameter in $Al_xG_{1-x}N$ alloys. *Journal of Applied Physics*, **92**(8), 4832-4839
- Zaien, M., Ahmed, N.M. and Hassan, Z.(2012). Structural and optical properties of nanocrystalline CdO thin film growth by solid vapour deposition. *Advanced Materials Research* , **620**, 241-245
- Zang, S. (2008). Materials characterization techniques. United kingdom, CRC press, ISBN 1420042947, 260
- Zeghbrock, B. V. (2011). Principles of Semiconductor Devices. <http://ece-www.colorado.edu/~bart/book/>
- Zheng, N. (2008). Introduction to dilute magnetic semiconductor. Department of Physics and Astronomy, University of Tennessee, Knoxville. sces.phys.utk.edu/~dagotto/condensed/HW2_2008/DMS.pdf

- Zhi, Z. Z., Liu, Y. C., Li, B. S., Zhang, X. T., Lu, Y. M., Shen, D. Z. and Fan, X. W. (2003). Effects of thermal annealing on ZnO films grown by plasma enhanced chemical vapour deposition from Zn(C₂H₅)₂ and CO₂ gas mixtures. *J. Phys. D: Appl. Phys.* **36**(6), 719-724
- Zhiyun C., Erin F.F. and Gregory. D. C. (2011) Applications of semiconductor nanosized particles for photolithography. *Patents Docs*, 20110281221, USPC Class; 430325
- Ziatko, M. (2010). Study of diluted magnetic semiconductors, the case of transition metal doped ZnO. PhD thesis, Faculty of sciences, Laboratoire de Physique de la matiere complexe, Ecole Polytechnique Federale Lausanne, Suisse.